Lecture Notes in Applied and Computational Mechanics 80

Theodoros Triantafyllidis *Editor*

Holistic Simulation of Geotechnical Installation Processes

Benchmarks and Simulations

Springer

Lecture Notes in Applied and Computational Mechanics

Volume 80

About this Series

This series aims to report new developments in applied and computational mechanics—quickly, informally and at a high level. This includes the fields of fluid, solid and structural mechanics, dynamics and control, and related disciplines. The applied methods can be of analytical, numerical and computational nature.

More information about this series at http://www.springer.com/series/4623

Theodoros Triantafyllidis
Editor

Holistic Simulation of Geotechnical Installation Processes

Benchmarks and Simulations

Springer

Editor
Theodoros Triantafyllidis
Karlsruhe Institute of Technology (KIT)
Karlsruhe, Baden-Württemberg
Germany

ISSN 1613-7736 ISSN 1860-0816 (electronic)
Lecture Notes in Applied and Computational Mechanics
ISBN 978-3-319-23158-7 ISBN 978-3-319-23159-4 (eBook)
DOI 10.1007/978-3-319-23159-4

Library of Congress Control Number: 2015938753

Springer Cham Heidelberg New York Dordrecht London

Printed on acid-free paper

Springer International Publishing AG Switzerland is part of Springer Science+Business Media (www.springer.com)

Preface

In a previous textbook with similar title, the midterm results of the research group GEOTECH on the numerical and physical modeling of geotechnical installation processes have been presented. In this volume emphasis is given to the simulation strategies of the benchmark problems. The holistic simulation of geotechnical installation processes takes into account the entire installation of structural elements into the ground for foundation purposes and considers the serviceability of nearby structures such as excavation pit supporting systems or adjacent buildings. It refers to the nonlinear structure–soil–structure interaction.

From the engineering practice, it is well-known that the installation process itself may cause larger deformations than the excavation or dewatering of a construction pit on its shoring or the neighboring buildings. The assessment of the deformation is, on the one hand, required from the codes (EC 7) or regulations but on the other hand the high-quality prediction based on realistic and proven incrementally, highly nonlinear constitutive models for the soils under cyclic/dynamic conditions and the respective simulation tools do not offer up to now the required prediction quality.

The research group GEOTECH is dedicated to this challenging issue with the performance of fundamental and applied research starting from the modification of existing or even new development of constitutive modeling for the soil behavior, the development of new type contact elements for the cyclic/dynamic structure–soil–structure interaction and the provision of new simulation techniques or appropriate tools for the description of the vibro-installation of piles.

The research group is organized and operating at three levels:

- benchmarking projects with element-like and large-scale model tests for the calibration and validation of the developed numerical models
- theoretical fundamental research for the development of high-quality constitutive soil models and contact formulations in combination with efficient numerical implementations and algorithms
- application of the developed theoretical models to boundary value problems with parametric studies of respective geotechnical installation processes and

recommendations for further use of the numerical models in practice as well as for the practical optimization of these processes.

Furthermore the research group provides high-quality benchmarks using physical modeling and measurements on real construction sites where the installation processes of vibro-injected piles took place and produced unexpected large deformations on the shoring wall (diaphragm wall). The provision of real data from construction sites and those from experimental results on physical model tests related to the pure pile installation process in combination with the developed numerical tools offer to the interested readers a rich source of valuable information. The provided information can serve as a basis to test newly developed constitutive models or simulation tools developed elsewhere or as benchmark to check the validity or accuracy of further experimental investigations in future.

The young researches, who joined this group, obtained an incredible knowledge in testing and simulation techniques enabling them to achieve a higher level of education and to widen their view with the exchange of experience between the different disciplines. Therefore in this volume, the first authors in all contributions from the research group are not the principal investigators but the young well-educated researchers, who just obtained or are in a process to obtain their Ph.D. degree.

The editor likes to thank all his colleagues (Prof. Ehlers, Prof. Wriggers, Prof. Savidis, Prof. Rackwitz, Prof. Hettler) and coworkers (Dr. Niemunis, Dr. Osinov, Dr. Huber) for their engagement within the research group and their valuable contributions as well as their extreme efforts to make things possible within the different disciplines in order to achieve the high scientific targets within the different projects.

The contributions of our invited speakers (Prof. A. Wittle and Prof. T. Schanz) in the final GEOTECH Workshop (7 and 8 December 2015 in Karlsruhe) are very much appreciated and are also included in this volume due to their relevance to the scientific targets of the group.

Furthermore I would like to express my thanks to Mrs. Meininger for the organization of all the workshops of the research group GEOTECH and her engagement to make those events pleasant, as well as Mr. Vogelsang for the collection of the manuscripts and the help given to the editor prior to publication of this textbook.

Finally, all of us like to express our deep gratitude to German Research Council (DFG) for the generous financial support of this very interesting and challenging research topic in geotechnical engineering.

Karlsruhe
August 2015

Theodoros Triantafyllidis

Contents

Requirements, Concepts, and Selected Results for Model Tests on Pile Penetration

J. Vogelsang, G. Huber and T. Triantafyllidis

Abstract Designing and performing adapted model tests related to pile penetration is a major target of the central project of the research group GEOTECH. These tests shall allow to capture major aspects of pile penetration quantitatively and to obtain input data for numerical simulations. The tests are focused on the interaction of the pile and the soil in dry or saturated conditions. Guidelines are to keep the tests as simple as possible, realize boundary conditions that are convenient for numerical simulations, and to provide reliable information on the state of the soil at the beginning of and during the tests. Furthermore, implications induced by the measurements, e.g., lower stiffness of an instrumented pile or the use of glass walls enabling the application of digital image correlation have to be evaluated and considered in the numerical simulations as well. Examples demonstrate how the concepts have been implemented for the measurement of tip and friction force on model piles under monotonic, cyclic, and dynamic loading as well as for the evolution of pore water pressure. Based on selected results, size effects of the test devices and the role of the model material resp. its state are pointed out. The contribution includes a discussion on disturbing influences such as friction in the linear guiding system or between pile and glass wall.

Keywords Model test · Physical modeling · Benchmark · Pile driving

1 Introduction

Since the beginnings of geotechnical research, model tests (resp. physical modeling) have always played a major role for the investigation of geotechnical problems, see e.g. [5, 11] and many others. Compared to in situ experiments, model tests can be an

J. Vogelsang (✉) · G. Huber · T. Triantafyllidis
Institute of Soil Mechanics and Rock Mechanics, Karlsruhe Institute of Technology, Karlsruhe, Germany
e-mail: Jakob.Vogelsang@kit.edu

T. Triantafyllidis (ed.), *Holistic Simulation of Geotechnical Installation Processes*, Lecture Notes in Applied and Computational Mechanics 80, DOI 10.1007/978-3-319-23159-4_1

Table 1 Terminology

Term	Explanation	Synonyms
Model test	Non-element-like experiment	Model experiment
Benchmark experiment	Experiment intending the validation of numerical models via prediction or back analysis	
Test material	Soil used for the model test (here sand)	Tested soil
Test device	Test facility to perform a model test (incl. instrumentation, equipment, etc.)	Test facility, apparatus
Test setup	General concept/configuration of a test	
Test box	Repository and external boundary for the test material	Strong box, container
Region of interest (ROI)	Usually area around the pile tip	
Type A prediction	A priori prediction of experimental results	
Type C1 prediction	Back analysis of experimental results with knowledge of the results	

efficient and moderate cost alternative to perform series of tests under well-defined conditions without the usually considerable uncertainty about the in situ ground conditions. For this reason, they have often served as a basis for the formulation or justification of design approaches. During the last twenty years their role as benchmark problems for numerical simulations has become more and more important. The term "benchmark experiments" is used in this context for high quality experiments that can be interpreted as boundary value problems, see details on the terminology in Table 1. The results obtained from these tests are then used for numerical back analysis (so-called type C1 prediction) or even better to validate numerical predictions of the experimental results (type A prediction) [12].

Dealing with the penetration of pile-like structural elements, model tests are not only necessary for the validation of numerical models but still also for an ameliorated understanding of the process. A great progress in the evaluation of experiments is the development and application of digital image correlation (DIC) techniques, e.g., particle image velocimetry (PIV), to penetration problems allowing to visualize the soil displacements during the process. Nevertheless, there are still significant aspects of pile driving that have to be considered as poorly understood and often various conflicting interpretations of the same effect exist. To give only a few examples, we would like to mention the occurrence of different pile driving types (or modes), possible liquefaction effects around vibro-driven piles or the strong dependance of post-installation pile behavior on the installation method used. It is suitable to study these complex problems not only by usage of numerical tools but also on the basis of adequate experiments. Not without a good reason, researchers working on the numerical simulation of pile penetration often have an experimental mainstay and vice versa.

The approach in the experimental research of the research group GEOTECH is to combine measurements on the pile with image analysis in a visible soil region in vicinity to the pile. While in many literature examples, the measurements are focused on the pile, we strongly concentrate on the mechanisms governing the behavior of the soil around the pile. Using 1g-model tests it was tried to cover the most relevant effects occurring in penetration problems and to provide a multitude of benchmark problems all using the same test material. The intention was to gain an improved level of knowledge about the performance of up-to-date numerical methods for the simulation of pile penetration processes using numerical back analyses of the experiments (type C/C1 prediction). Once this higher level of confidence is achieved, the model validation will be pursued by switching to real predictions (type A) and by comparison with field measurements. The aim of this paper is to formulate requirements for suitable experiments, to show problems and difficulties encountered as well as some technical solutions for those arising from our own research work and from other researchers.

An alternative approach for the study of penetration problems is to use centrifuge tests. The ability of these tests to provide precious experimental data has been shown in many instances [13, 38]. However, we concentrate on general issues of model pile testing. Specific features of centrifuge model testing are not discussed here. Also, the usage of scaling laws in order to transfer the test results to a larger scale is not within our topics, see next chapter. For more details in this direction, we refer to the related literature, e.g., [10, 24, 38].

2 Requirements for Benchmark Experiments

The main requirements for benchmark experiments have already been discussed in [29] and are summarized here. A laboratory experiment will always be "synthetic" compared to the real process that is tried to be simulated. However, the most important requirement for benchmark experiments is to reproduce similar effects like in the real process. The geometry can be very simplified or even truly abstracted, but the major effects have to be modeled realistically. The great advantage of laboratory experiments is to provide clearly defined boundary conditions that are implementable in numerical simulations and a sound knowledge of the test material (parameters) and its state (stratification, density, etc.). To be qualified as a benchmark experiment, the measurements shall allow a profound interpretation and a quantitative comparison with numerical results. Information about forces/stresses on structures should be incorporated as well as about the displacements/deformations in the soil. The test material has to be characterized properly and reliable data on its state before and during the test has to be provided. If the influence of the test setup on the test results is not clear, it may be expedient to perform comparative tests using similar geometries but to modify the general test setup. Reproducibility of the test results is an absolute necessity. In order to achieve this, a homogenous soil deposition is considered to be indispensable. In the region of interest, the test setup has to provide a minimum

stress level of about a few kPa. This is important in order to minimize the influence of parasitic effects such as attraction between the particles and to ensure a sufficient stress level for a numerical simulation using barotropic constitutive models.

3 Concepts

A guideline in the central project of GEOTECH has always been to investigate different aspects of pile penetration separately. For the investigation of shaft friction or tip resistance as well as for the role of grouting adapted tests have been designed and performed. The experiments have always been designed to suit well for numerical back calculation. This includes an adapted choice of boundary conditions and geometries.

Four basic test configurations can be distinguished for model tests on pile penetration. They are schematically illustrated in Fig. 1. Generally, the pile shape should correspond to the shape of the test box. Of course, various adaptions of these idealized setups exist. For example, often rectangular base plans are used even if the pile

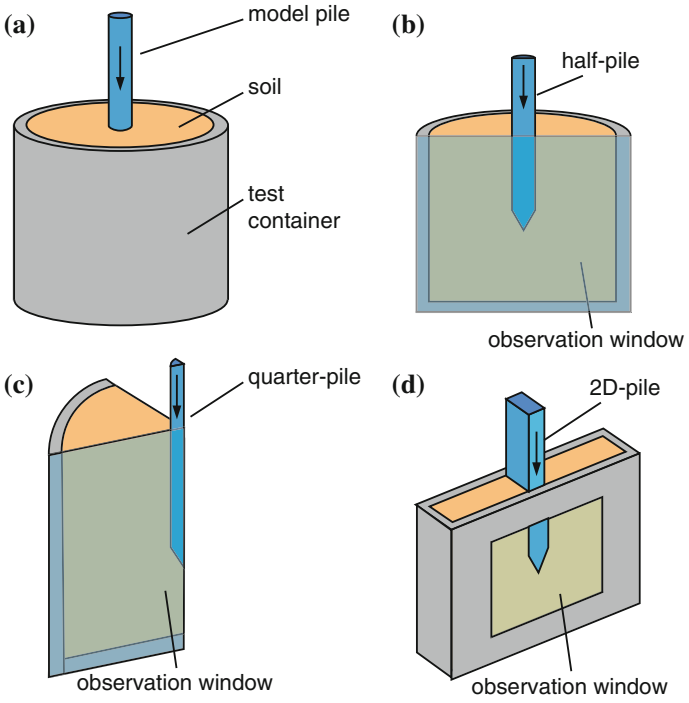

Fig. 1 Basic concepts for model tests on pile penetration: **a** full model, **b** half model, **c** quarter model, and **d** 2D-pile (sheet pile)

geometry intends axisymmetric conditions. Tests using the configurations (a), (b), and (d) have been performed in the central project.

By far the simplest test setup for pile penetration is a cylindrical full model, Fig. 1a. A circular model pile is penetrated into a test box filled with soil. Usually, the instrumentation is restricted to measurements on the pile such as pile head force or tip resistance, pile displacement and acceleration. Reliable measurements in the soil body are difficult to realize, but possible [20, 26, 39]. Advantages are the robust and simple test setup and the symmetric geometry. Some results using this test setup are given in Sect. 10.1, literature examples are, e.g., [20, 26].

The test setup shown in Fig. 1b tries to imitate axial symmetry but also to allow the investigation of soil deformation. The test device has an observation window which represents the symmetry plane. Thus, only half of the problem is modeled. The pile slides along the window and is kept visible throughout the test. Results obtained using similar setups can be found in [21, 23, 31, 33]. The soil deformation around the pile can be evaluated with digital image correlation. Strictly spoken the axial symmetry is not maintained because the deformations and stresses in the symmetry plane are not necessarily representative for the whole soil body. Friction between soil and window as well as a deflection of the window can strongly influence the test results. A discussion on these effects follows in Sect. 6.

The setup shown in Fig. 1c is quite exotic but would possibly enable the investigate pile penetration using a quarter model. The pile has a quarter circle shape and is placed in a rectangular edge of the test device. Both cut planes can be installed with observation windows to evaluate the soil deformation.

A common approach is to try to realize 2D (plane strain) conditions, Fig. 1d. The test device can now have a rectangular plan and the pile reaches over the whole width of the device (sheet pile). The pile has a relatively large base area which is beneficial for the reproducibility of the test results because the penetration resistance is an integral value over a larger soil zone. For a correct modeling of a sheet pile, the test device would need an infinite width but if the side walls are very smooth and rigid, one can obtain a realistic simulation of sheet pile penetration even with small model dimensions. If the side walls are equipped with observation windows, these setups also allow the evaluation of soil deformation with DIC. A similar test setup was used for the tests presented in [29, 33]. Literature examples are [25, 37] and others.

4 Instrumentation Techniques

4.1 Data Acquisition

The measurements are recorded using a multichannel data acquisition system with simultaneous sampling and digital filtering. The sampling rate and low-pass Bessel filtering are chosen depending on the test type (quasi-static or dynamic). Bessel

filtering is used to achieve a low distortion of the signals (constant group delay). The time delays by sensors with digital signal processing have to be considered as well as the different frequency ranges of the individual sensors.

4.2 Pressure Measurements

4.2.1 Earth Pressure Measurements

Earth pressure measurements are known to be challenging in granular soils but in the current context they can provide important data concerning, for example, the correct interpretation of boundary conditions. An overview of possible approaches is given, e.g., in [30]. It is briefly summarized here and illustrated in Fig. 2a. A detailed description of the principal techniques applied in the model tests of the central project is provided in [29].

By embedding of pressure transducers in the soil body, it is often tried to measure the stress evolution at interesting locations [26]. In reality, such measurements are not likely to produce quantitatively representative data about the soil state due to different stiffnesses of transducer and the surrounding soil. This inevitably produces arching effects around the transducer and the original stress state to be measured is modified. If cabled transducers are used, the cables can also disturb the experiments, see discussion for pore pressure measurements below. In the presented tests, the embedding technique was not used.

In contrast to this, the integration of stress transducers at soil structure interfaces is considered to give proper results if the transducers membrane is stiff enough and ends flush (in-plane) with the structures surface. Transducers of this type are implemented in the test device described in [29] to measure the evolution of vertical stress at the lower boundary of the test device. Results are also given in Fig. 13b of this contribution.

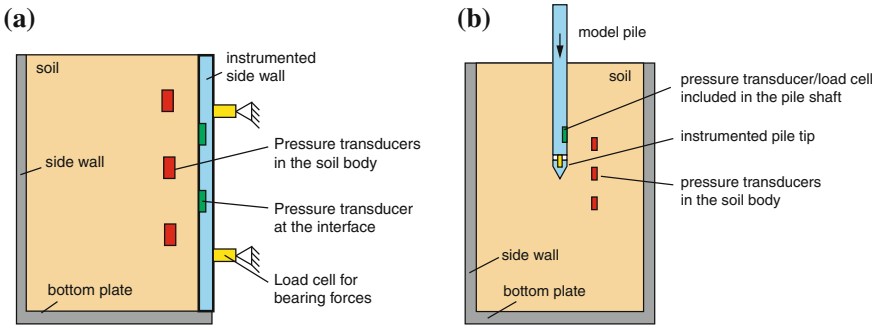

Fig. 2 **a** Instrumentation techniques for the measurement of earth pressures and **b** instrumentation techniques on and around the pile

A way to obtain quantitative information about the resulting force exerted by earth pressure is to measure the bearing forces of earth pressure-loaded sections of the test device. These sections have to be decoupled from the rest of the test device (at least in the measurement direction). Appropriate transducers have to be very stiff in order to maintain the earth pressure to be measured. An example is described in [29] in the context of the concurrent measurement of normal and tangential earth pressure on instrumented wall sections. A similar solution is described in [1].

4.2.2 Pore Pressure Measurements

For model tests in saturated soil, pore pressure measurements can provide important information about the penetration process. However, without the simultaneous measurement of total stress, the quantitative interpretation of pore pressures is limited. Thus, pore pressure measurements are suited for qualitative interpretation and local comparison with numerical simulations. They are mainly valuable for the full model test configuration, Fig. 1, because in the other configurations, the interface between pile and observation window works like a drainage. The measurement of pore pressures can either be performed by embedding of transducers at the wished location in the soil or hydraulic connection of an external transducer with this location (tube with filter at the end, see Fig. 3). Both methods influence the evolution of stress in

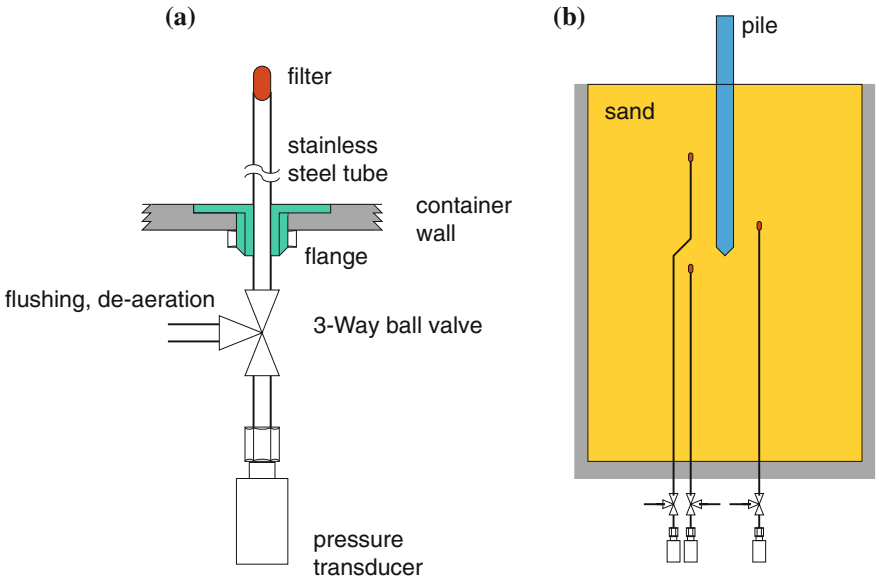

Fig. 3 Pore pressure measurement with external transducers at the *bottom* of the test device: **a** schematic detail of the connection transducer measurement location and **b** exemplary schematic overview with measurement at three locations around a pile

vicinity due to a differing stiffness of transducer or tube compared to the surrounding soil. Particular attention is required for the deaeration around the transducers and in the tube/filter in order to quantitatively measure even small pressures. The advantage of an external transducer connected to the measurement location by a tube is the more reliable information about the position of the transducer and the possibility to flush and deaerate transducer, tube, and filter. In all cases, it is preferred to route the cables (if wired transducers are used) or tubes from below in order to avoid an additional hydraulic connectivity to the free surface.

4.3 Measurements on and around the Pile

Possible instrumentation techniques on and in vicinity of a penetrating pile are illustrated in Fig. 2b. Important measurements on the pile are its motion (displacement, acceleration), the pile head force and the tip force. More advanced instrumentation allow the measurement of shaft friction as an integral over the whole shaft or for multiple smaller sections. The measurement of radial (horizontal) stress in the pile shaft is complex and therefore rarely implemented. Successful examples of such measurements are given in [13, 20, 29]. In granular soil, pore pressure measurements directly at the pile are only valuable in dynamic (vibratory) tests. If external transducers connected by a tube to the pile–soil interface are used, the fluid column in the tube is subjected to accelerations which influence the measurements and are not easy to quantify. The embedding technique described above can also be used to obtain qualitative information about the stress state in vicinity of the pile.

4.4 Evaluation of Soil Motion

Digital image correlation (DIC) and related methods (PIV) have become the most important techniques for the evaluation of displacement and deformation fields in the soil. Requirement for the application of these techniques to pile penetration tests is an appropriate configuration of the test device, see Sect. 3. Principles are concisely discussed in [36], examples using planar DIC (PIV) dealing with pile driving are given in [23, 31, 37] and many others. For the reconstruction of the off-plane motion a symmetry assumption (plane strain or axial symmetry) is necessary. A measurement of this component requires 3D-DIC which is only rarely applied (in the context of pile penetration, e.g., in [18]) and the use of transparent soil, see [8] and Sect. 7.2.

4.4.1 Slow Image Acquisition

For the image acquisition during slow processes, e.g., quasi-static pile penetration, one can achieve satisfying results with standard digital cameras. For our current

research we use NIKON Coolpix P7700 in interval mode. Their resolution of 3000 × 4000 pixel is sufficient to cover an area of about 150 × 200 mm for DIC purposes. If the region of interest is larger, multiple cameras are used (up to four). As standard, they provide an interval shooting with intervals larger than 30 s. For smaller intervals (down to 2 s) an external control system is used that synchronously triggers an image capturing for up to six cameras and passes an output signal to the data acquisition for every taken image. Video modes of the cameras offer frame rates of 30–60 images/s depending on the resolution and can be used if the interval of 2 s is not sufficient. The captured videos are subsequently split into individual images for the DIC analysis.

4.4.2 Fast Image Acquisition

The frequencies of vibratory pile driving usually range between 20 and 40 Hz. In order to capture the dynamic cyclic motion of the pile and the surrounding soil, at least 5 images have to be taken during a vibration period (better 10). Nowadays digital video cameras with full image rates of about 350 images/s and 2000 × 1000 pixels and high resolution lenses are available at comparably low costs. This resolution is sufficient for capturing the region of the pile and surrounding soil for DIC purposes. The image rate can be handled by high-speed interfaces and an adapted video grabber. The continuous data rate is about 750 MB/s for non color images with 8-bit depth. A workstation or server with 70–120 GB of memory or a high performance Raid controller with 4 or more Solid-State-Drives in Raid 0 configuration can handle this data rate continuously during the tests (>100 s). A scheme of the image data acquisition for vibratory tests is shown in Fig. 4. The maximum exposure time for each image is about 1/400 s for a frame rate of 350 images/s. Additional illumination is necessary therefore and for a sufficient depth of focus a higher aperture value is

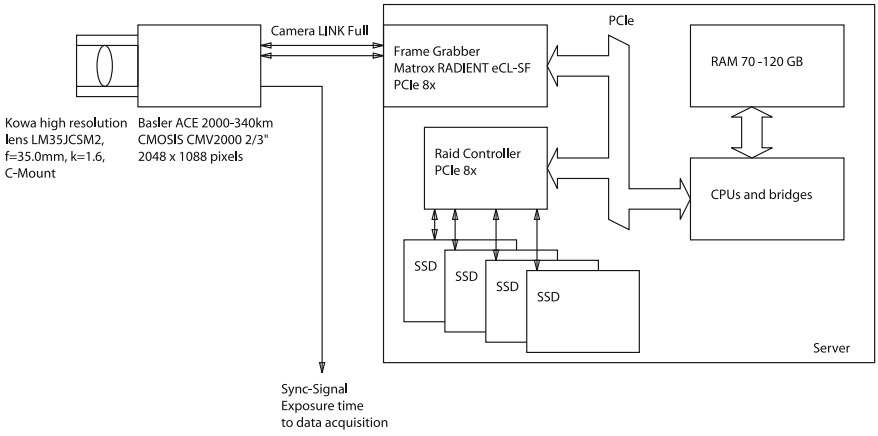

Fig. 4 Scheme of the fast image data acquisition used in vibratory pile driving tests for the evaluation of displacements with DIC

needed also. LED lamps with constant intensity and with very low IR content give good illumination uniformity and prevent heating up of the test box.

4.4.3 Evaluation of Displacements and Deformations

For present studies we use the freeware JPIV [27], that calculates occurring displacements between two images based on the PIV method. Various other softwares exist and have been shown to provide good results if the relevant guidelines, e.g. formulated in [36], are followed. In this context, it is important to mention that for quantitatively satisfactory results, an extensive experience with the software is essential. Generally, as a result of the PIV evaluation, incremental displacements between two subsequent images of a series of images are obtained. These have to be interpreted in terms of strains, usually, with respect to a reference configuration defined by the first image. The strain calculation is mostly performed analogously to the finite element method or finite difference method. Our approach is similar to the procedure in [37] and is described in detail in [34]. In [34], we also give some indications toward the summation of incremental to total displacements.

5 Construction Aspects

5.1 Structural Design of Test Devices

The construction of a test device can be kept simple in the case of a circular test setup similar to Fig. 1a. Earth pressures and pore pressures can only introduce circumferential tensile stress which is easily supported, e.g., by relatively thin metal tubes, even with very small deformation. When the geometry of the test box is rectangular or involves planar structures (e.g., for the application of planar DIC), it cannot be avoided that these parts are subjected to bending. Even with relatively small bending lengths, the deflection under bending load can be significant and require strong reinforcements. Not without a good reason, geotechnical test devices are usually equipped with reinforcing steel beams, etc., to obtain a very stiff construction [29, 37].

5.2 Pile Shape

The pile shape should correspond to the symmetry conditions intended by the general test setup. This ensures that a similar deformation mechanism in the plane of the observation window and in the inner soil body. For the test setup allowing DIC and intending axial symmetry this requires a pile cross section of half or quarter circle

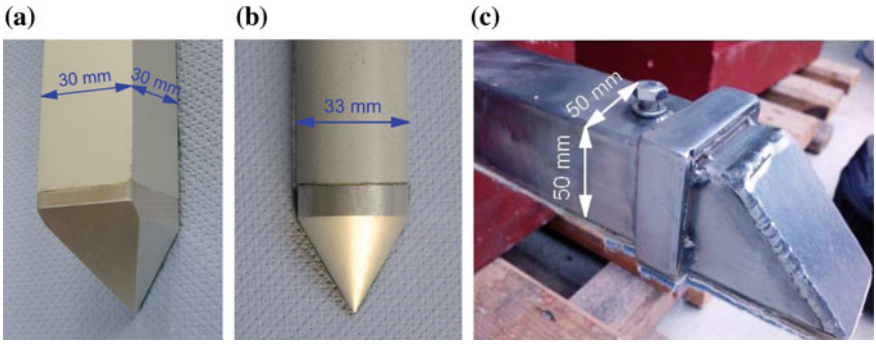

Fig. 5 *Back* view on different piles used in half model tests: **a** rectangular pile with pyramidal tip and **b** half-circular pile with conical tip (both used in the central project), **c** rectangular pile equipped for grout injection (collar and outlet of the inner injection tube) with wedge-shaped tip used in [23]

and conical or flat-ended pile tips. Pyramidal- or wedge-shaped pile tips (Fig. 5a, [31]; Fig. 5c, [23]) violate this requirement and the symmetry assumptions usually made in numerical simulations. The pile tip should either be tapered or flat-ended, see Figs. 5b and 6. If the test involves large penetration, it is helpful for most numerical simulations to give priority to tapered pile tips instead of flat-ended pile tips or at least to round the edges of the pile shoulder, see Fig. 8a, b.

5.3 Guiding the Pile

Independent of the test configuration, the model pile has to be guided properly with very low systematic friction. The guidings should ensure a smooth pile motion (usually in vertical direction) and avoid lateral movement.

5.3.1 Guidings Above the Soil Surface

In most cases, the pile can only be guided above the soil surface. For this purpose, roller guides or sleeve bearings with low friction (e.g., PTFE) are practicable solutions. Especially when the pile has to be guided along the observation window, two guidings in different vertical positions can be used to create a couple of forces that presses the pile tip against the window, see Fig. 6c. This effect is supported by the high contact pressure on an inclined pile tip. Simple pile guiding systems are shown in Fig. 6.

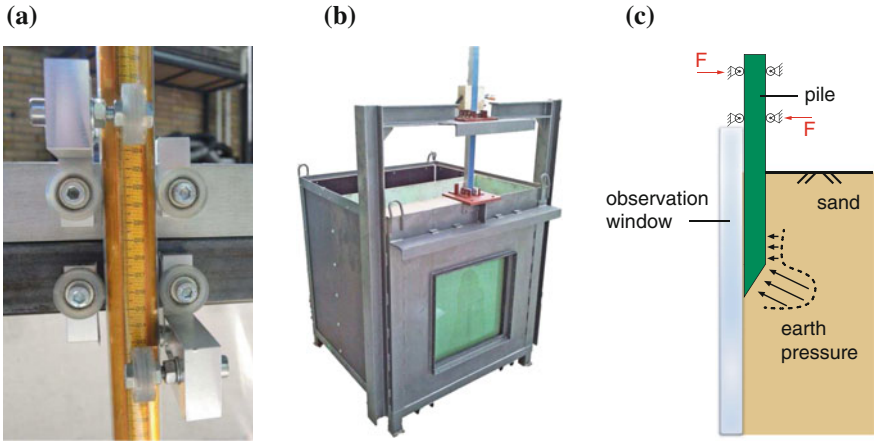

Fig. 6 Guiding techniques above the soil surface: **a** two pairs of roller guides for a cylindrical pile used in the central project and **b** model test device involving a pair of sleeve guidings (*red*) used in [23] and **c** schematic illustration of the mechanism of two guidings in different heights creating a couple of forces to press the pile tip against the observation window

5.3.2 Guidings Below the Soil Surface

Some test configurations (e.g., [29], see Fig. 12) allow a guiding of the pile even below the soil surface. Therefore, the pile has to contain a smaller pilot-pile that separates the guidings from the soil. For test configurations with half-piles, Fig. 1b, this concept can be adapted as illustrated in Fig. 7. The major advantages of this setup is the close link to numerical models of pile penetration that often use a sort of pilot-

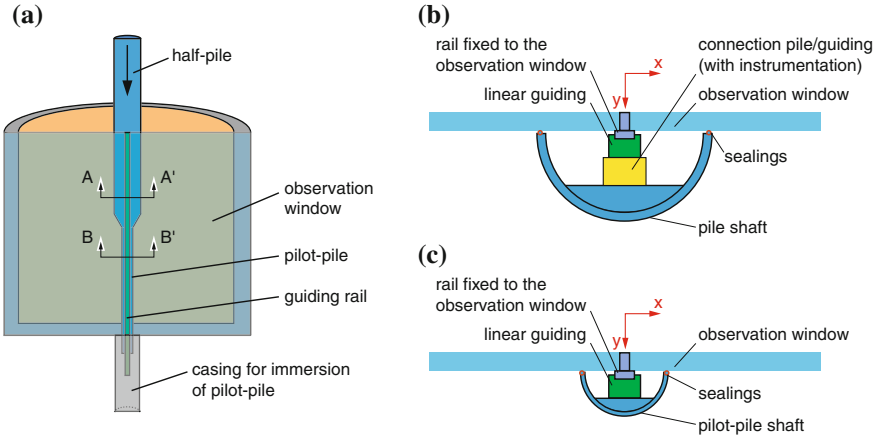

Fig. 7 Guiding technique below the soil surface: **a** concept with half-pile and pilot-pile and **b** cross section of the half-pile and **c** cross section of the pilot-pile

pile and the higher stiffness of the observation window when it is supported in the middle of the field. An important drawback arises under water-saturated conditions because the interior volume of the pile has to be filled with water. Even if the sealings prevent sand ingress, they cannot prevent a dissipation of pore pressure. The drainage conditions may therefore be completely different than in the axisymmetric case and the evolution of pore pressures around the pile may be strongly influenced.

5.4 Sealings Against Sand Ingress

For the application of DIC, the pile usually slides alongside the observation window. Therefore sealings are necessary to prevent the soil from entering between the pile and the window. Typical and effective solutions are surface seals in the form of layers of felt or carpet between the pile and the window [23, 33]. In [34], a slightly modified solution is presented using a combination of a layer of felt and PTFE stripes that ensures a stiffer contact behavior, Fig. 8a, b.

A very sophisticated sealing concept is provided in [29] using line seals fabricated with PTFE stripes that are pressed against the observation window by means of springs, (Fig. 9).

5.5 Actuator System

Practical methods for pile driving are quasi-static penetration (jacking), vibratory methods and impact driving. All these methods require different equipment. For quasi-static penetration, hydraulic actuators with position control, variable speed and sufficiently large stroke can be used. These actuators require a loading frame to carry the resulting force. The loading frame can be connected to the test device (internal driving force) or designed as separate system. This involves a sufficient

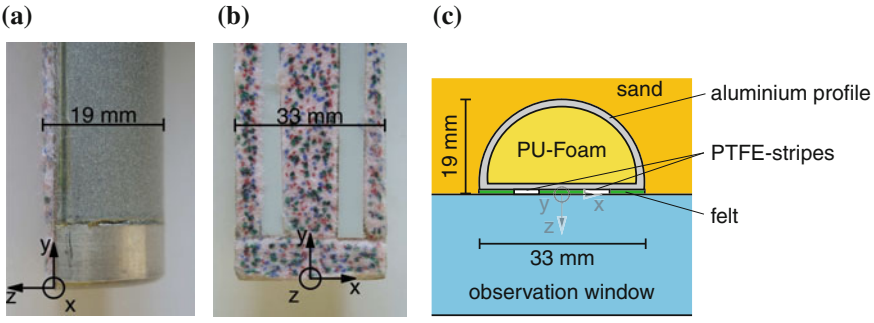

Fig. 8 Surface sealing concept against sand ingress between pile and observation window: **a** *side* view, **b** *front* view, and **c** schematic horizontal cross section of the model pile

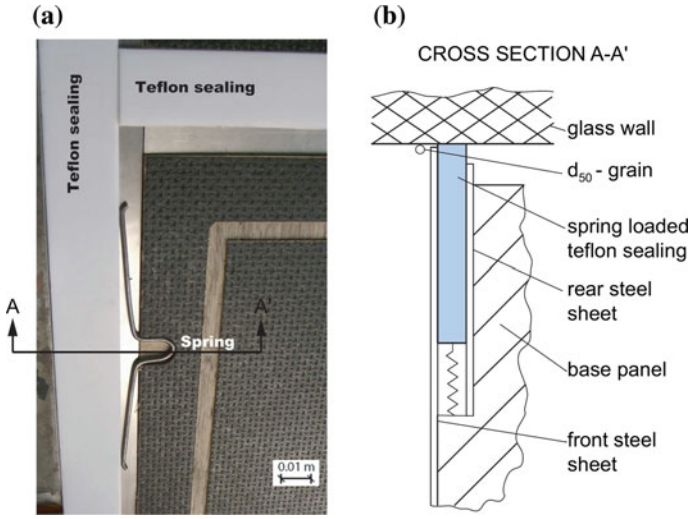

Fig. 9 Line sealings concept realized for the *interface test device* (from [29]): **a** photo without front steel sheet and **b** schematic cross section A–A'

weight or fixation of the loading frame. In any case, the loading frame has to be a stiff construction. For small driving forces, the pile load can also be applied by using a dead load. A similar setup was, e.g., described in [32] for cone penetration tests: a sufficiently large dead weight hanging on a crane and connected to the pile head is lowered with constant speed and penetrates the cone in a displacement controlled mode.

Vibratory or impact driving tests do not necessarily require a loading frame. For vibratory tests, a guideway may be desired to apply a constant static force. In this case, it has to be isolated from the vibration. Guided dead weights or hydraulic/pneumatic actuators connected to a loading frame can be used to generate the required static force. Impact driving can be performed by using adapted pile hammers mounted on the pile head (and guided if necessary) or drop weights.

5.6 Boundary Conditions for the Test Material

In general, the test material can be subjected to two basic types of boundary conditions (BC):

- Pressure BCs ensuring constant normal stress and no tangential stress at the boundary
- Displacement BCs with negligible or at least very small normal displacement of the boundary and tangential movement governed by the friction coefficient between test material and boundary

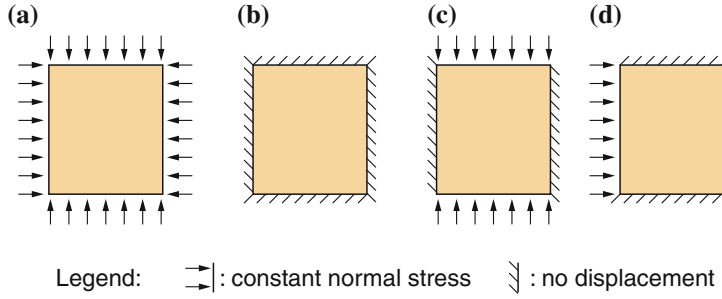

Fig. 10 Illustration of idealized BC: **a** BC1, **b** BC2, **c** BC3 and **d** BC4

Following the terminology of calibration chamber testing for penetration resistance, four idealized combinations of boundary conditions at the lateral and vertical boundaries can be distinguished [22]. They are schematically illustrated in Fig. 10.

In practice, often used BCs are combinations of the above mentioned idealized ones. These combinations and their practical implementation are illustrated in Fig. 11.

Pressure BCs can be realized using pressurized membranes. If multiple membranes are installed along the vertical sides, a pressure gradient can be modeled. Displacement BCs are usually introduced by frictional contact to a stiff outer construction (test box). In most cases, the BC at the bottom of the soil body is of displacement type because otherwise, the position of the soil body is not easy to determine, especially during vibratory tests. The BC at the upper boundary of the soil body is usually either a free surface or a constant surcharge. Both types, pressure and displacement BC, are easily implemented in a numerical model of the test as long as they are clearly defined. Problems concerning pressure BCs can arise from a not precisely defined volume of the sample. The mechanical implications induced by the BCs are discussed in Sect. 6.1.

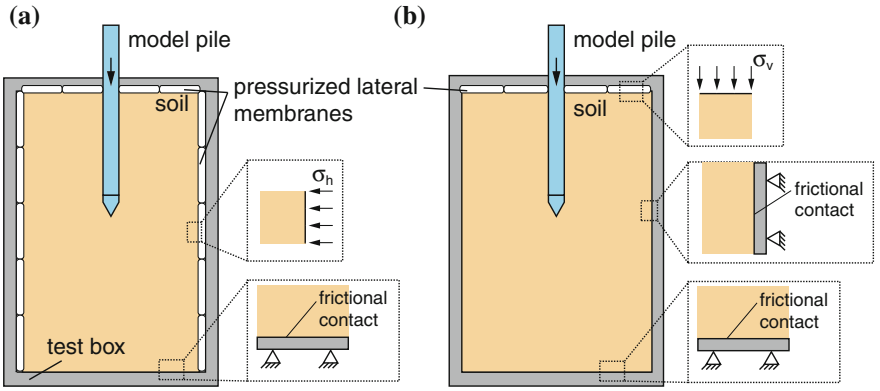

Fig. 11 Illustration of idealized often used combinations of BC: **a** pressure BC and **b** displacement BC with frictional contact

5.7 Structural Prerequisites for Water-Saturated Conditions

Tests performed with moist soil or even under water-saturated conditions involve important modifications of the test device. The inner construction has to be impervious to water and noncorrosive. Welded stainless or epoxy-coated/galvanized steel sheets are typically used for this purpose. All connections (e.g., for the application of pressure transducers or bolted connections) have to be constructed watertight.

6 Influences of the Test Device on the Results

A model test device will always interact with the test material and influence the test results. The main focus of interest of the experimentalist is to keep these influences as low as possible, to describe the occurring interactions and, when the influences are not negligible, to take them into account. Relevant aspects are influences related to silo effects, the deformation behavior of the test device during the tests, systematic friction and—if DIC is used—the role of the observation window.

6.1 Size Effects

It is nearly impossible to achieve free field conditions and penetration behavior in a test device restricted in size for various reasons (space limitation, investment costs, etc.). The test results are influenced by the type of the boundary condition and the size of the test box. In the case of lateral displacement BCs, especially the initial stress state may be influenced by silo effects which have an impact on the test results. The evolution of stresses during the test, for example due to the penetration process, can also be strongly influenced by size effects. The strategy in the central project has always been to give qualitative indications toward the influence of BCs, to quantify their mechanical behavior and in case of necessity to quantify their influence based on numerical simulations.

6.1.1 Silo Effects

Silo effects are well-known to occur in containers filled with granular material that have large heights compared to their widths (or diameters). The underlying mechanism is the mobilization of friction on the side walls and arching between the sides [5, 11]. Silo effects are likely to occur in many types of geotechnical experiments and can potentially strongly influence the initial stress distribution in the test box and thereby, the subsequent test, see e.g. [3, 19, 32] and Sect. 9. The major consequence of silo effects is an underlinear increase of geostatic stress with depth. In a given depth, the influence is mainly governed by the ratio of depth to effective radius

(distance to the boundary) and the contact friction angle between test material and boundary. A discussion on the evaluation of silo effects and their investigation using the FEM can be found in [32]. Dynamic effects that can occur during the emptying of a silo are usually not of primordial importance for model tests since they occur after the actual test.

6.1.2 Other Size Effects

The model dimensions can also have a direct effect on the evolution of stresses during the penetration process. Probably the greatest efforts have been made to quantify the influences of the BC on the evolution of penetration resistance with regard to the interpretation of cone penetration tests (CPT), a similar process to pile penetration [3, 15, 19, 22]. The magnitude of the influence is related to the ratio of diameter of the test box d_{box} and pile diameter d_{pile}: $\eta = d_{box}/d_{pile}$. Beyond a certain threshold of $\eta = \eta_0$, the influence of the BC can be neglected and the response is similar to what would be expected under free field conditions. The threshold value is mainly a function of the BC type and the soil type and state (stress and density). A pressure BC with $\eta < \eta_0$ reduces the penetration resistance. In contrast to that, a displacement BC that is located too close to the penetrating pile induces a jamming effect and increases the penetration resistance.

6.1.3 Dynamic Boundary Effects

In dynamic experiments like vibratory tests, the BC can significantly influence the test results compared to free field behavior, e.g., by reflections at the boundaries. Options to estimate or even quantify these influences are to variate the BC type or to perform comparative quasi-static tests. Redundant measurements at different locations are helpful for a better understanding of the process. However, such dynamic effects are incorporated in a simulation of the model test as well so the comparison of experimental and numerical results is still possible.

6.2 Deformation of the Test Device

Stiffness requirements for transducers have already been the subject in Sect. 4. This section discusses the influences on the test results related to deformations of the test device and the pile structure.

Generally, it is aimed to minimize the deformation of the test device. For pressure BCs this is not of primordial importance as long as the BC on the exterior boundaries of the soil body is correctly applied. For a correct application of displacement BCs, a deformation of the test device is absolutely to be avoided. Otherwise, a deflection can lead to significant changes in the stress state (relaxation) that are difficult to

quantify. Therefore, they cannot be easily taken into account in a numerical simulation of the test. In order to achieve a sufficient structural stiffness of the test device, usually, solid reinforcements are used. Often, an inner construction containing the soil body is supported by an exterior strong box or steel framework, [29, 37]. If there are doubts whether a test device provides a sufficient stiffness, measurements of the deformations occurring during the tests may bring some clarity. For the test device described in [29], such measurements have been performed showing that the deflection of the observation window is about 0.4 mm.

A too low pile stiffness is not desirable for several reasons. If the pile deforms considerably, it can no longer be treated like a rigid body. As a consequence, a pile displacement measured at the pile's head cannot be considered as representative for the whole pile and force measurements can be significantly influenced. In vibratory tests, a axial flexibility of the pile or parts of the pile (e.g., pile tip) can lead to wave phenomena that disturb the measurements. A simple "rule of thumb" for the validation of the axial rigidity assumption is provided in [28].

6.3 System Friction

System friction can be a relevant problem that needs to be tackled when the measured forces contain both, earth pressure or soil resistance forces and friction forces resulting from the apparatus. Principal sources of system friction in this context are linear guidings and sealings. Systematic friction forces should not exceed about ten percent of the typical force measured during the tests in order to be neglected. A first impression of occurring system friction is gained by performing empty runs before and after the test (translating the pile structure in the empty test device). However, things can considerably change when the soil comes into play. Even single grains jammed, e.g., between pile and window can significantly influence the magnitude of friction. In order to avoid this, it has to be ensured that seals work properly throughout the whole test.

6.4 Observation Window

It is evident that the modification of the test setup necessary to implement an observation window has an impact on the test results. Possible influences of the observation window are:

- a relaxation of effective stress (primarily in normal direction) in the soil directly adjacent to the window due to a deflection of the window
- friction between soil and window inhibiting the soil motion in tangential directions
- a higher hydraulic conductivity in the interface soil-window leading to preferred flow paths

All these influences violate the symmetry that is actually intended for the tests and assumed in numerical back analysis of these. The windows are therefore tried to be kept as small as possible but should still provide a sufficiently large region of interest. Material providing low friction in combination with the soil should be applied, smooth glass surface are the best choice. Like for the surfaces of internal boundaries, it is always a good idea to evaluate the coefficient of friction between the two materials, e.g., by means of modified direct shear tests.

7 Test Materials

7.1 Suitable Test Materials and Their Characterization

The focus of our present studies is on pile driving in granular soil. Uniform medium to coarse sands are appropriate materials for such tests because they provide a sufficient particle size to minimize the influences of particle attraction, their size is large enough compared to the roughness of the side walls and they are easy to handle in combination with sealings, see Sect. 5.4. Their grains sizes are not to large even compared to small diameter piles (typically 15–50 mm) so that continuum approaches are justified for the numerical modeling and with regard to the DIC analysis, typical search patches of about 2–3 mm contain a sufficient number of particles. It is also beneficial that uniform sands eliminate effects related to erosion. A negative aspect to mention is the high permeability which complicates the realistic observation of effects related to partially drained conditions (pore pressure changes in dynamic tests, liquefaction, etc.).

Without a detailed description of the test material, the best experiment is worthless. The characterization of the test material has to include the granulometric properties but also the limit void ratios, the permeability and the mechanical behavior in oedometric and triaxial tests. As the experimentalist has the best knowledge about the test material it is beneficial to give also indications toward the parameter choice for often-used constitutive models.

7.2 Transparent Granular Soils

The requirements for a soil to be transparent are transparent particles in a transparent pore fluid. Both should have the same light refractive index. The displacement fields in the soil can be captured all over the soil with digital image correlation (DIC). Laser sheets select individual plains of soil model through the transparent boundaries.

The mechanical properties of the material should be similar to real soil. A promising approach for a soil and pore fluid is found in [8] with fused quartz particle. The size of the setup is limited due to transparency degradation of soil and fluid to about

Table 2 Some properties of *Karlsruhe sand*

Mean grain size	d_{50}	[mm]	0.55
Coefficient of uniformity	C_U	[–]	1.5
Critical friction angle	φ_c	[°]	32.8
Min. void ratio	e_{min}	[–]	0.549
Max. void ratio	e_{max}	[–]	0.851
Grain shape			Sub-rounded

150 mm in depth and also affected by the light refractive index of the transparent container walls.

7.3 Karlsruhe Sand

In all tests performed in the central project, the same test sand was used, the so-called *Karlsruhe Sand*. The sand is received in big bags à 800 kg as a composition of two grain fractions delivered from the same manufacturer. Since important quantities are needed for the tests, it has to be ensured that the sand remains the same throughout the test series. Therefore, a sieve analysis is performed for each big bag. If the grain size distribution differs to much from the average, the sand of this charge is only used for pretests.

Table 2 shows some important properties of Karlsruhe sand, detailed information can be found in [29, 34]. Additional test results, e.g., from triaxial tests, have been distributed to our project partners on request.

8 Deposition Methods

A thorough soil deposition method is an indispensable prerequisite for a homogeneous soil sample and is therefore of utmost importance for benchmark experiments. Sample preparation, particularly for large samples, is a science of its own. Here, we only mention the most important aspects and refer to the related literature, [4, 6, 9, 14, 35].

8.1 Dry Samples

In most cases, pluviation techniques are used to prepare dry samples. Depending on the size and shape of the test devices, different setups exist. Most of them pluviate the soil by means of diffusers that create soil rains for example on a band-shaped or circular base area. By variation of the deposition intensity and the drop height, different relative densities can be achieved (from medium dense to dense). Usually,

it is tried to build up the soil body in horizontal layers similar to a real sedimentation process. A technique to prepare dry samples in loose state is to build up a cone of soil like it is done in standard laboratory tests to evaluate the minimum density [2, 7]. A comparable procedure is used in the Interface test device, for details see [29].

8.2 Saturated Samples

Samples with high degrees of saturation can be obtained by pluviation of dry material into deaerated water. This approach is followed in the central project, see [34]. The drop height should be kept constant and the sedimentation distance under water should be sufficient for the particles to reach their ultimate descent rate. This procedure results in relative densities from loose to medium dense. Higher densities can be achieved by subsequent cyclic excitation of the test device (e.g., by placing it on a shaking table). The preparation of large dry samples and subsequent flushing with water from bottom to top is considered to provide lower degrees of saturation [16, 17]. An advantage of this method is that dense samples can be prepared using the methods of dry pluviation without the need for further densification (and possibly a disturbance of the sample).

8.3 Uniformity Control

For each preparation method that is applied for the tests, the ability to achieve a homogeneous density distribution has to be demonstrated. Cone penetration tests (CPT) are considered to be an appropriate tool for this purpose since the cone resistance is very sensitive to density changes. A discussion on the interpretation of CPT in dry soil is provided in [32], other results can be found in [6, 14]. Results of CPTs under water-saturated conditions are given, e.g., in [34]. At best, after selected tests, the uniformity of the relative density should be checked via CPTs. Of course, the soundings can not be performed in the direct region of interest (pile) but only in a certain distance beside and are likely to be influenced by the preceding tests. However, significant nonuniformities (e.g., in terms of a stratification) are still detectable.

9 Evaluation and Modeling of the Initial Soil State

A realistic implementation of the initial soil state is indispensable for a successful numerical simulation of a model test. Only for some experiments, a simple but nevertheless realistic description of the initial state is possible, e.g. using a K_0-state with homogeneous density distribution. However, in general, the initial state is more

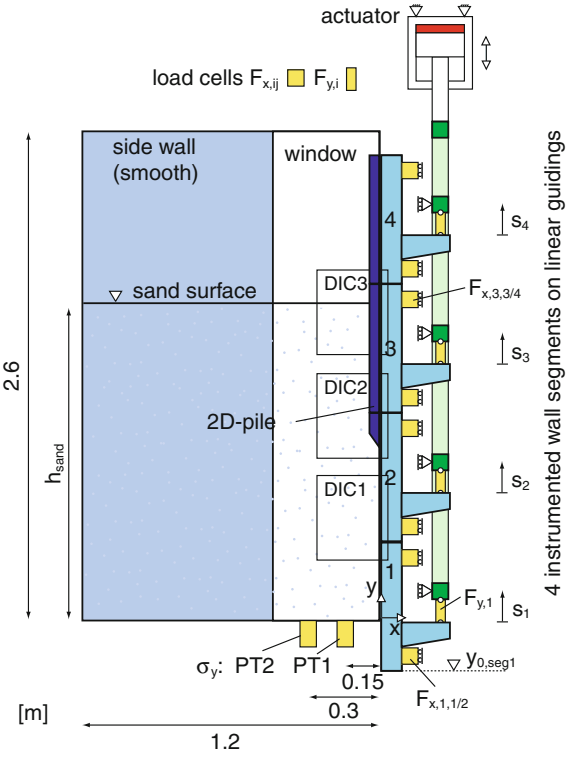

Fig. 12 Schematic illustration of the setup and the instrumentation installed in the interface test device

complex and its influence on the test results has to be evaluated. A discussion on reasons therefore is provided in Sect. 6.

9.1 Observation of the Deposition Procedure

The so-called *interface test device* is used for different test series in the central project of GEOTECH, see Fig. 12. It provides a sophisticated instrumentation but involves significant boundary effects on the test results, see [32]. Notably, during sand deposition, strong influences of the silo effect are observed. These effects cannot be avoided but they can be quantified by recording the deposition procedure with the available instrumentation schematically displayed in Fig. 12.

Results gained during the sand deposition are given in Fig. 13. Figure 13a summarizes some important information regarding the test configuration and the averaged soil state after sand deposition. The vertical position of the bottom of the lowest segment $y_{0,seg1}$ determines the starting position of the wall segments. Stress and force measurements are shown as functions of the current filling height in Fig. 13b–d. A sand deposition in horizontal layers is indispensable for this presentation. For more

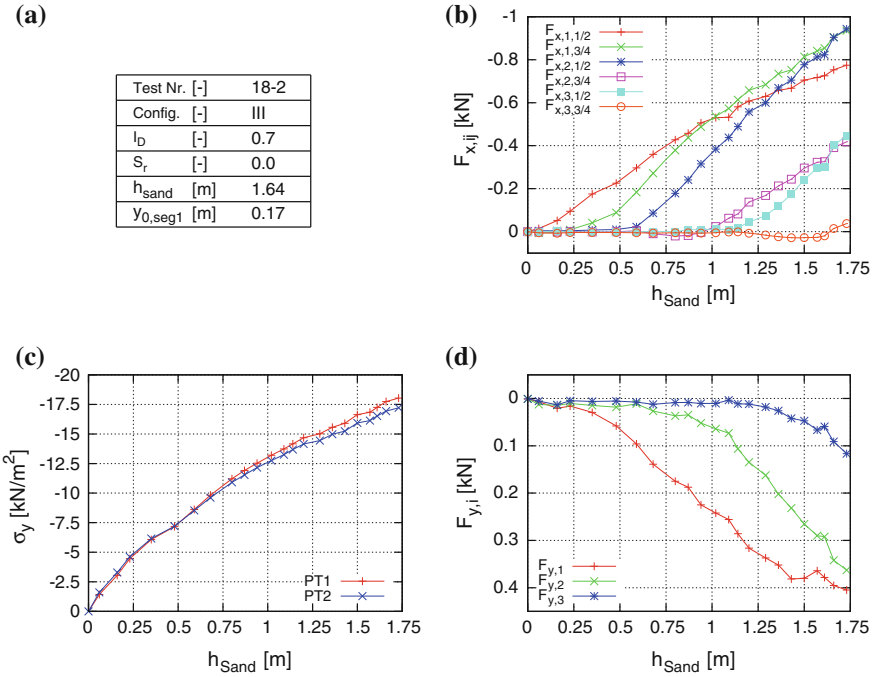

Fig. 13 Measurements during sand deposition for a test in the interface test device: **a** general information, **b** vertical stress σ_y at two locations on the *bottom* plate (PT1 and PT2 in Fig. 12), **c** normal bearing forces $F_{x,ij}$ on the wall segments and **d** tangential bearing forces $F_{y,i}$ on the wall segments (all plotted over filling height h_{sand}, explanation of symbols in Fig. 12)

information about the instrumentation, see Fig. 12 and [29]. The sand was filled in up to a sand height of 1.64 m. Therefore, only measurements on the lower three wall segments are shown, the highest wall segment is not in contact with the sand.

Figure 13 describes quantitatively the evolution of stresses during the sand deposition and the situation before the test start. Similar results are provided for all tests of the central project that are simulated by the other subprojects. They can be used to check an assumed initial state and to estimate discrepancies between test and simulation results.

9.2 Soil Deposition as a Boundary Value Problem

A better way for obtaining a realistic initial soil state for the simulation of a model test is to consider the sand deposition procedure as a boundary value problem and to simulate it previously to the simulation of the actual test. Guidelines for such simulations are given in [32]. The described simulation technique bases on

a layer-by-layer increase of soil weight from the bottom to the top of the soil body starting from a very low stress level. In [32], its applicability for almost all types of test devices is shown. In many cases, this approach can lead to a more realistic initial stress state and to better accordance between test and simulation results.

10 Selected Results

In this section, we want to emphasize some of the aspects discussed above with some experimental results. The results illustrate the role of pile and test box geometry and the state of the test material in monotonic penetration tests. For detailed results of vibratory tests, we refer to [34] in this book.

10.1 Size Effects on the Penetration Resistance

In order to demonstrate how size effects can influence the test results depending on the soil state and the geometry, Fig. 14 compares some results of simple penetration tests using a full model test setup as illustrated in Fig. 1a. The cylindrical test box has a diameter of 0.94 m and the sand body has a height of 0.85 m in all tests. Figure 14a

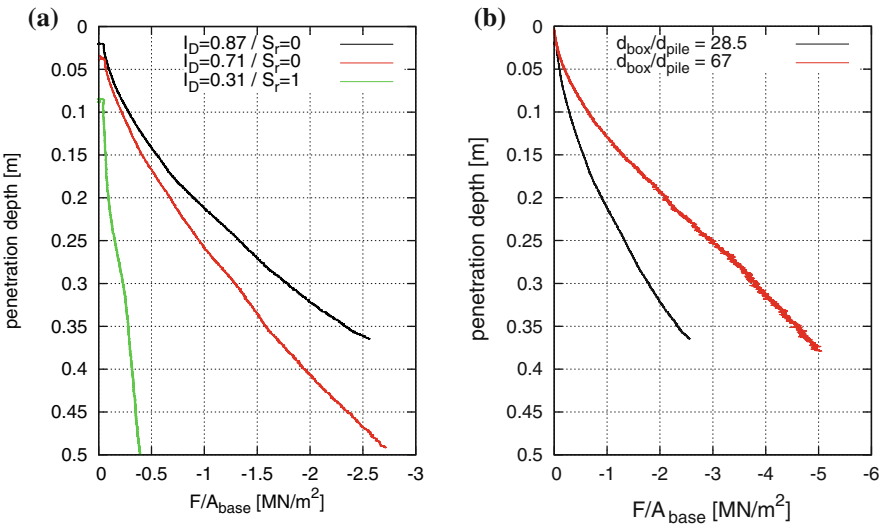

Fig. 14 Measurements of penetration resistance (pile head force F divided by the cross section of the tip) in a full model test device: **a** variation of relative density and saturation ($d_{\text{pile}} = 33$ mm) and **b** comparison of two pile diameters, *red line* $d_{\text{pile},1} = 14$ mm and $I_{\text{D}} = 88\,\%$; *black line* $d_{\text{pile},2} = 33$ mm and $I_{\text{D}} = 87\,\%$

shows results from tests with a pile diameter of 0.033 m ($d_{box}/d_{pile} = 28.5$) and different relative densities for dry and saturated conditions. The tip shape is tapered with 60° angle of aperture. The evolution of measured pile head force with the penetration depth is plotted. The measured force is interpreted as an averaged vertical stress below the pile tip (penetration resistance similar to q_c in CPT). Figure 14b compares for a similar relative density ($I_D = 87$ % resp. 88 %, dry sand) the penetration resistance for two different pile diameters.

Figure 14a clearly indicates the strong influence of relative density on boundary effects. In loose to medium dense and saturated sand, no significant boundary effects are observed. The penetration resistance increases with depth which can be probably attributed to the higher stress level. In dense sand however, a parabolic increase of the penetration resistance is observed which can only be explained by a jamming effect due to the fixed boundaries. This jamming leads to smaller penetration depths in dense sand.

Figure 14b illustrates how the geometry can influence the magnitude of penetration resistance on the one hand but also how the diameter ratio influences the evolution of penetration resistance on the other hand. The smaller pile leads to higher localized stresses below the pile tip (about twice as large as for the larger pile). This geometric effect may be of great importance when the test results shall be transferred to a larger (prototype) scale, like it is often done based of centrifuge test results. The other interesting observation is that obviously boundary effects lead to a qualitatively different penetration behavior. While the larger pile shows a parabolic increase of penetration resistance with depth as discussed above, for the small diameter pile this behavior is observed only on the first 20 cm of penetration. In about this depth, the penetration resistance reaches an inflection point and increases only sub-linearly afterward. The BC plays only a minor role compared to the larger pile.

10.2 Influence of the Tip Shape

In the majority of numerical models for the simulation of pile penetration, the pile tip is modeled with a conical shape or even streamlined with curved edges to ensure a smooth penetration behavior. In practice, many pile types have flat-ended pile tips which are generally not suitable for most numerical methods. Although some pile types are installed with a conical pile tip, from a practical point of view this is not indispensable. Experience shows that anyhow, kinds of wedges form under flat-ended piles and work as pile tips (bearing capacity mechanism of flat surface). This observation is used as a justification of the geometrical modeling of pile tips. The fact that a tip formed in the soil shows a completely different contact behavior to the surrounding soil than a tapered steel or concrete tip is often omitted in the discussion.

Figure 15 compares results of the penetration resistance in a half model test device. One of the tested piles is flat-ended, Fig. 8a, b, and the other has a tapered pile tip, Fig. 5b. Both have the same horizontal cross section, Fig. 8c. With the flat-ended pile

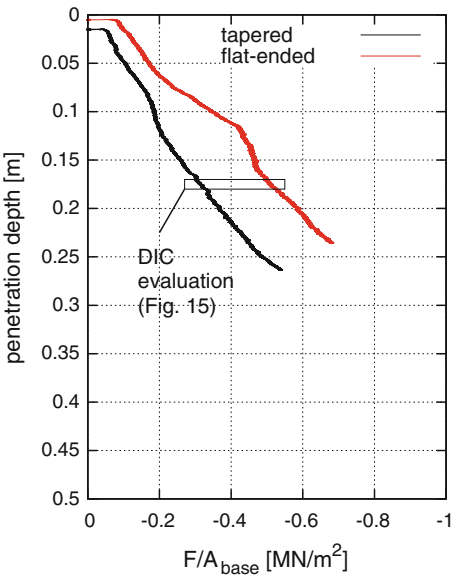

Fig. 15 Comparison of measured penetration resistance in a half model test device for a flat-ended and a tapered pile (*both tests* $d_{\text{pile}} = 33$ mm, $I_{\text{D}} = 56\,\%$ and $S_{\text{r}} \approx 1$)

only a penetration depth of 0.25 m was reached due to sand ingress between sealing and observation window, see discussion above. Both tests are performed in saturated sand with $\text{I}_{\text{D}} = 56\,\%$.

The global evolution of penetration resistance is similar in both cases. The tendency is a linear increase of resistance with depth. Some small variations can be observed indicating slight inhomogeneities of relative density. While the qualitative penetration behavior is similar for both tests, the magnitude of stress below the pile tip differs significantly. In a given depth, the stress below the flat-ended pile tip is about twice as large as for the tapered pile tip. This indicates that when it comes to the evaluation of pile forces from numerical simulations, special considerations have to be taken into account for the modeling of the pile.

In order to compare both tests in more detail, the displacements are evaluated with DIC for a representative section of 10 mm penetration occurring from a depth of 0.17–0.18 m. This section is highlighted in Fig. 15. Figure 16 shows the evaluated incremental horizontal and vertical displacement fields around the pile tip. The position of the pile tip is plotted in solid line.

In the observed plane, all displacement fields show satisfactory symmetry conditions with respect to the pile center line. Some problems with the DIC evaluation of the tapered pile can be seen in Fig. 16b where the pattern painted on the pile does not provide sufficient contrast. In both cases, the soil below the pile tip is pushed laterally downward. Horizontal displacements concentrate on two ear-shaped zones vertically below the pile shoulders. The zone of large vertical displacements is located centrally below the pile tip and has a bubble shape. For the flat-ended pile a soil zone with large displacements downwards can be seen. This zone works as a tip for the flat-ended

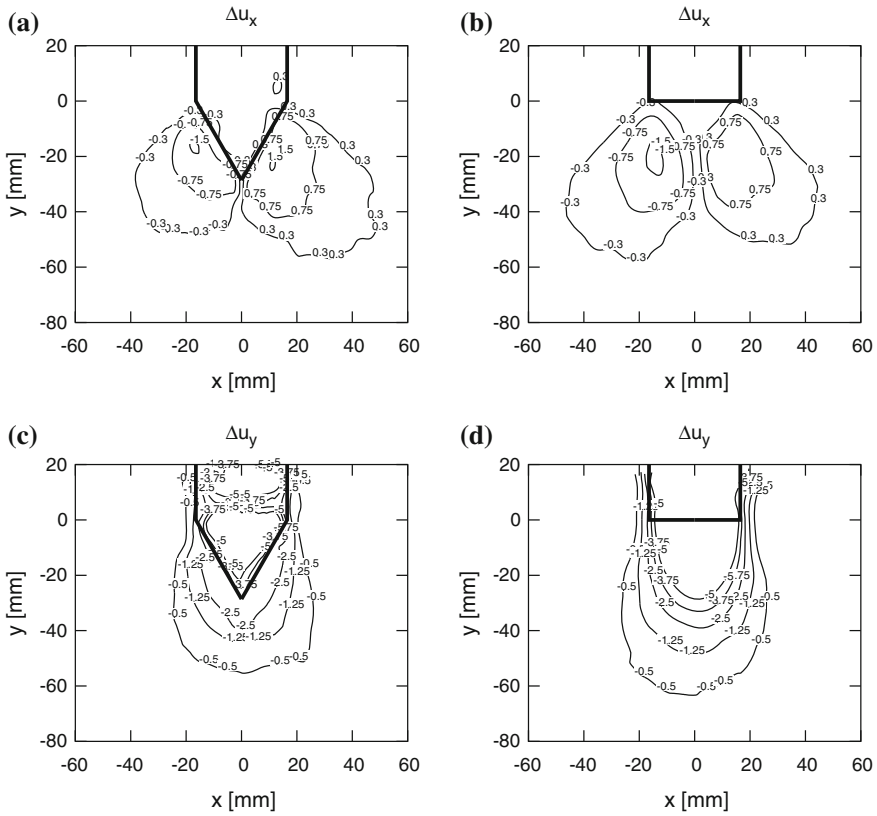

Fig. 16 DIC results of monotonic penetration tests: **a** horizontal and **b** vertical displacements for a test with tapered pile tip and **c**, **d** with flat-ended pile tip (*both tests* $d_{\text{pile}} = 33$ mm, $I_{\text{D}} = 56\,\%$ and $S_{\text{r}} \approx 1$)

pile. It can be seen that significant differences are observed only directly below the pile tip. Outside of this zone, the displacement fields are similar which indicates a qualitatively similar penetration behavior. This experimental observation justifies the geometrical simplification often used in geometrical models for the simulation of penetration processes.

11 Final Remarks

In this contribution we have tried to give an overview of the experimental approach pursued in the central project aiming to provide valuable experimental data for the validation of numerical simulation techniques. On the basis of long-term experience in this field, we formulate requirements for the design and performance of the

experiments and show exemplary solutions to the problems encountered. It was pointed out that the suitability for comparison with numerical simulations should always be kept in mind when performing benchmark tests and that the feedback obtained from this comparison can also lead to an improved interpretation of the experiments. Last but not least, it is also worth mentioning that redundant measurements, repeated tests and comparative tests, e.g., using another test setup, are crucial in order to obtain quantitatively reliable test data.

Important issues of future work will be the investigation of vibratory pile driving in water-saturated sand. Of particular interest is the explanation of the occurrence of different types of pile driving and modes of vibration. The study will be performed using half-scale models and an equivalent axisymmetric full-scale model including an instrumented model pile in order to evaluate the effects of the test setup on the results.

References

1. Arnold, M., Franke, D., Bartl, U.: A solution to concurrent measurement of the normal and tangential earth pressure in model tests. Proceedings of the International Symposium Geotechnical Measurements and Modeling, Karlsruhe (2003)
2. ASTM Standard D4254–91: Standard Test Method for Minimum Index Density and Unit Weight of Soils and Calculation of Relative Density, Annual Book of ASTM Standards, ASTM International, West Conshohocken, PA (2006)
3. Bolton, M.D., Gui, M.W.: The Study of Relative Density and Boundary Effects for Cone Penetration Tests in Centrifuge. Report CUED/D-SOILS/TR256 (1993)
4. Choi, S.-K., Lee, M.-J., Choo, H., Tumay, M.T., Lee, W.: Preparation of a large size granular specimen using a rainer system with a porous plate. Geotech. Test. J. **33**(1), 45–54 (2009)
5. Darwin, G.H.: On the horizontal thrust of a mass of sand. Proc. Inst. Civil Eng. **71**, 350–378 (1883)
6. Dave, T.N., Dasaka, S.M.: Assessment of a portable traveling pluviator to prepare reconstituted sand specimen. Geomech. Eng. **4**(2), 407–423 (2012)
7. DIN 18126: Bestimmung der Dichte nichtbindiger Böden bei lockerster und dichtester Lagerung (1996)
8. Ezzein, F.M., Bathurst, R.J.: A transparent sand for geotechnical laboratory modeling. Geotech. Test. J. **34**(6), 1–12 (2011)
9. Fretti, C.: Lo Presti, D.C.F., Pedroni, S.: A pluvial deposition method to reconstitute well-graded sand specimens. Geotech. Test. J. **18**(2), 292–298 (1995)
10. Holzlöhner, U.: Techniques of model testing. Contribution to the Symposium "Messtechnik im Erd- und Grundbau", Karlsruhe, pp. 119–126 (1983)
11. Janssen, H.A.: Versuche über Getreidedruck in Silozellen. Zeitschrift Verein deutscher Ingenieure, Band XXXIX., pp. 1045–1049 (1895)
12. Lambe, B.M.: Predictions in soil engineering. Géotechnique **23**(2), 151–202 (1973)
13. Lehane, B.M., White, D.J.: Lateral stress changes and shaft friction for model displacement piles in sand. Can. Geotech. J. **42**, 1039–1052 (2005)
14. Maier, C.: Herstellung trockener Großproben mit verschiedenen Lagerungsdichten. Diploma Thesis at the Institute of soil mechanics and rock mechanics, Karlsruhe Institute of Technology (2011)
15. Mayne, P.W., Kulhawy, F.H.: Calibration chamber database and boundary effects correction for CPT data. Proceedings of the 1st International Symposium on Calibration Chamber Testing, pp. 257–264. Potsdam and New York (1991)

16. Negro, P., Verzeletti, J. a. S. a. P. D., Molina, G., Pedroni, S.: TRISEE: 3D site effects and soil-foundation interaction in earthquake and vibration risk evaluation—Task 3 Large-scale geotechnical experiments on soil-foundation interaction. Technical report, Special Pub. No. I.98.73, ELSA Lab., JRC, Ispra, Italy (1998)
17. Negro, P., Paolucci, R., Pedretti, S., Faccioli, E.: Large scale soil-structure interaction experiments on sand under cyclic loading. In: Proceedings of the 12th World Conference on Earthquake Engineering, Auckland, New Zealand, volume, Bd. 14, Paper No. 1191. A.A. Balkema (2000)
18. Ni, Q., Hird, C.C., Guymer, I.: Physical modeling of pile penetration in clay using transparent soil and particle image velocimetry. Géotechnique **60**(2), 121–132 (2009)
19. Parkin, A., Lunne, T.: Boundary effects in the laboratory calibration of a cone penetrometer in sand. In: Proceedings of the 2nd European Symposium on Penetration Testing, vol. 2, Balkema, Amsterdam, pp. 761–768 (1982)
20. Rimoy, S.P.: Ageing and axial cyclic loading studies of displacement piles in sands. Dissertation,Imperial College London(2013)
21. Robinsky, E.I., Morrison, C.F.: Sand displacement and compaction around model friction piles. Can. Geotech. J. **I**(2), 81–93 (1964)
22. Salgado, R., Mitchell, J.K., Jamiolkowski, M.: Calibration chamber size effects on penetration resistance in sands. J. Geotech. Geoenviron. Eng. **124**(9), 878–888 (1998)
23. Savidis, S.A., Aubram, D., Rackwitz, F.: Vibro-Injection pile installation in sand: Part II - Numerical and experimental investigation. In: Triantafyllidis, Th (ed.) Holistic simulation of geotechnical installation processes—numerical and physical modeling, pp. 103–131. Springer, Heidelberg (2015)
24. Schofield, A.N.: Cambridge geotechnical centrifuge operations. Géotechnique **30**(3), 227–268 (1980)
25. Thanh Chi, N., Thuy Loi, D.h., Viet Nam, H.N.: Investigation into soil displacement near a jacked-in pile in sand. Master thesis at the Delft University of Technology (2008)
26. Thomas, S., Kempfert, H.-G.: Experimentelle Erkenntnisse zum zyklisch axialen Pfahltragverhalten, Geotechnik 36. Heft **3**, 169–179 (2013)
27. Vennemann, P.: JPIV-software package for particle image velocimetry, (2007), http://www.jpiv.vennemann-online.de
28. Viking, K.: The vibratory pile installation technique. TRANSVIB 2006, Gonin, Holeyman et Rocher-Lacoste (ed.), Editions du LCPC, Paris, pp. 65–82 (2006)
29. Vogelsang, J., Huber, G., Triantafyllidis, Th: A large scale soil-structure interface testing device. Geotech. Test. J. **36**(5), 613–625 (2013)
30. Vogelsang, J., Huber, G., Triantafyllidis, Th.: Zur Erfassung von Erddruckkräften auf Wand- und Pfahlstrukturen im Modellversuch. Messen in der Geotechnik 2014, publications of the Institut für Grundbau und Bodenmechanik of the University of Braunschweig—Institute of Technology, vol. 98, pp. 401–420 (2014)
31. Vogelsang, J., Chrisopoulos, S.: Experimentelle und numerische Untersuchungen zum Vibrationsrammen in nichtbindigem Boden. Technical papers of the special session "Forum for young geotechnical engineers", 33. Baugrundtagung in Berlin, pp. 195–202 (2014)
32. Vogelsang, J., Zachert, H., Huber, G., Triantafyllidis, Th.: Effects of soil deposition on the initial stress state in model tests: Experimental results and FE simulation. In: Triantafyllidis, Th. (ed.) Holistic simulation of geotechnical installation processes—numerical and physical modeling, pp. 1–21. Springer, Heidelberg (2015)
33. Vogelsang, J., Huber, G., Triantafyllidis, Th.: On soil deformation and stress redistribution around pressed-in and vibrated displacement pile tips. In: Triantafyllidis, Th. (ed.) Holistic simulation of geotechnical installation processes—numerical and physical modeling, pp. 44–59. Springer, Heidelberg (2015)
34. Vogelsang, J., Huber, G., Triantafyllidis, Th., Bender, T.: Interpretation of vibratory pile penetration based on Digital Image Correlation. In: Triantafyllidis, Th. (ed.) Holistic simulation of geotechnical installation processes—Benchmarks and numerical results. Springer, Heidelberg (2015)

35. Walker, B.P., Whitaker, T.: An apparatus for forming uniform beds of sand for model foundation tests. Géotechnique **17**(2), 161–167 (1967)
36. White, D.J., Take, W.A., Bolton, M.D.: Soil deformation measurement using particle image velocimetry (PIV) and photogrammetry. Géotechnique **53**(7), 619–631 (2003)
37. White, D.J., Bolton, M.D.: Displacement and strain paths during plane-strain model pile installation in sand. Géotechnique **54**(6), 375–397 (2004)
38. White, D.J.: Contributions to géotechnique 1948–2008: physical modeling. Géotechnique **58**(5), 413–421 (2008)
39. Woods, R., Athanasopoulos-Zekkos, A., Gkrizi, A., Pietrangelo, A., Zimmerman, A.: Measurement of ground motion near piles during driving. Geotech. Spec. Publ. **233**, 512–521 (2014)

Interpretation of Vibratory Pile Penetration Based on Digital Image Correlation

J. Vogelsang, G. Huber, T. Triantafyllidis and T. Bender

Abstract A combined interpretation of force measurements together with the evaluation of dynamic motion around the pile based on digital image correlation (DIC) is performed to identify soil deformation during vibratory pile driving in model tests. The tests are executed under water-saturated 1g-conditions. We prove the occurrence of the so-called cavitational pile driving but without the experimental evidence of the forming of a cavity under the pile tip. Using the DIC results, first attempts are made to evaluate the volumetric cyclic deformation of soil around the pile tip during the vibro-penetration. The results show an alternation of contractancy and dilatancy in proximity of the pile tip with volumetric peak-to-peak strain amplitudes up to 2 %. They indicate drained or at least partially drained conditions. Based on the test results, existing phenomenological interpretations of soil deformation due to pile penetration are reviewed.

Keywords Model pile · Tip resistance · Vibratory pile driving · Slow and fast vibratory pile driving · Cavitational and non-cavitational pile driving

1 Introduction

The penetrating pile tip is generally considered to be the principal excitation source of ground vibrations during vibratory pile driving. This is particularly true when vibro-injection piles are used. In this case, the grout material around the pile shaft acts as a lubrication layer and reduces the shear wave propagation from the pile shaft into the surrounding soil. The pile tip, however, undergoes strong impacts and transmits pressure and shear waves into the ground. These can provoke densification around the pile or in water-saturated conditions the tendency of a pore pressure build-up

J. Vogelsang (✉) · G. Huber · T. Triantafyllidis · T. Bender
Institute of Soil Mechanics and Rock Mechanics,
Karlsruhe Institute of Technology, Karlsruhe, Germany
e-mail: Jakob.Vogelsang@kit.edu

T. Triantafyllidis (ed.), *Holistic Simulation of Geotechnical Installation Processes*, Lecture Notes in Applied and Computational Mechanics 80, DOI 10.1007/978-3-319-23159-4_2

if the soil is not too dense. In both cases, neighbouring structures can be affected by the pile installation process [13]. With regard to the prognosis of settlements of adjacent structures, the mechanisms of pile driving and especially the interaction with the surrounding soil around the pile tip have to be understood and analysed. This pertains also to numerical simulations, where only very few valuable methods exist to quantitatively investigate pile penetration processes. Notably, for pile driving in water-saturated conditions, no numerical method is available that which could be considered as validated and recommendable for practical applications [9].

Usually, for both, theoretical and practical description two basic types of pile penetration can be distinguished: cavitational (slow) and non-cavitational (fast) pile driving [2–5, 10]. The distinction relies directly on the evolution of the tip force. Slow or cavitational vibro-penetration is a term for vibratory pile driving with large displacement amplitudes. Measurements show that during phases with pile displacement upwards the contact tip force vanishes and at least for pile driving above the phreatic level, it was concluded that a cavity forms below the pile tip [2, 3, 12, 16]. The soil mechanical interpretation of this type of pile driving is that the soil below the pile tip undergoes large cyclic deformation and eventually reaches swept-out-of-memory states (SOM) [3]. As a consequence, the following penetration phase resembles a virgin loading for the soil below the pile tip and the response is very soft. Figure 1a shows the evolution of tip force during cavitational pile driving measured in high-quality in-situ tests. During non-cavitational (fast) vibro-driving the tip force does not vanish in the phase of upward motion, see Fig. 1b. In every repeated penetration phase, the soil response is very stiff and after small penetration a limit value of tip resistance is reached. The maximum tip resistance is higher than during cavitational pile driving.

Another interesting observation, especially during laboratory tests on vibratory pile driving, is the occurrence of different pile driving modes, e.g. shown in [15]. The distinction is made on the basis of the comparison of the period of characteristic motion compared to the excitation frequency. Higher modes show more complex motions and generally lower penetration rates. This topic will not be discussed in

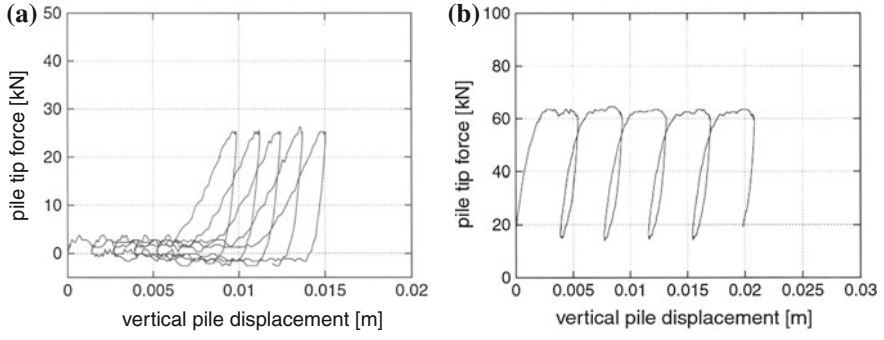

Fig. 1 Field data of the evolution of tip force during **a** cavitational and **b** non-cavitational pile driving (from [5])

this contribution because for practical applications the simple modes are of principal interest.

Although various measurements show the described phenomena, there is still a lack of information about soil behaviour related to these. Their interpretation, e.g. provided in [3], is based on coherent and comprehensive reflections about soil behaviour in triaxial tests, but it is not validated by measurements of soil deformation during pile driving. One approach for obtaining such data are digital image correlation methods (DIC).[1] However, to the authors best knowledge, an application of DIC for the evaluation of cyclic soil deformation in the vicinity of a vibrating pile is not available (e.g. [11] or [19] suffer a lack of time resolution), while a great number of examples can be found for slow, monotonic pile penetration ([7, 19, 20] and many others). This can be probably attributed to the far greater effort required for the DIC investigation of cyclic, dynamic processes compared to slow processes. The camera used has to provide a frame rate of at least 10 images per vibration cycle. For typical vibration frequencies of about 30 Hz, this results in a required frame rate of 300 or more images per second, which involves substantial investment costs compared to usual digital cameras that can be used for the observation of slow processes.

2 Test Set-Up

The basic test set-up for the experiments presented here has already been presented in [17, 19] and is schematically illustrated in Fig. 2. The test device has a half-circular base area and an acrylic glass panel. It has been used as observation window in the symmetry plane of the pile. During the test the panel is reinforced with a steel beam attached in front to minimize deflection. Information concerning the test material and the deposition method can be found in Appendix 2.

2.1 Model Piles

In previous test series, as well as in many other model pile tests that can be found in the literature, piles with a rectangular cross section were used. A pile tip of this type (called pile type I) is shown in Fig. 3a, b. However, with regard to a numerical back analysis of the tests that often assume axial symmetry this pile geometry causes problems with the transferability of the results. One could argue that for comparison of forces the same base area should used while the deformation in the observation window probably depends more on the pile geometry in this plane.

[1] The term particle image velocimetry (PIV) is considered to be more appropriate to hydromechanical applications. In the geotechnical context where groups of grains of the grain skeleton are used as markers and not individual particles the authors prefer the general term DIC. However, the evaluation procedures are usually based on the PIV-method.

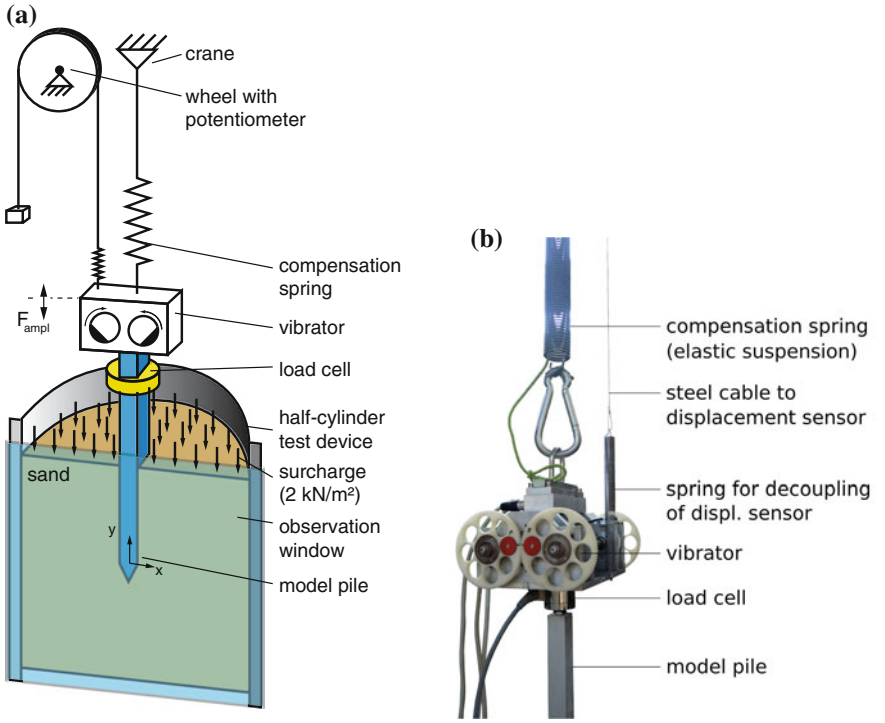

Fig. 2 **a** Schematic test set-up and **b** detail photo of the vibrator system with connection to the pile, elastic suspension from the crane and displacement measurement

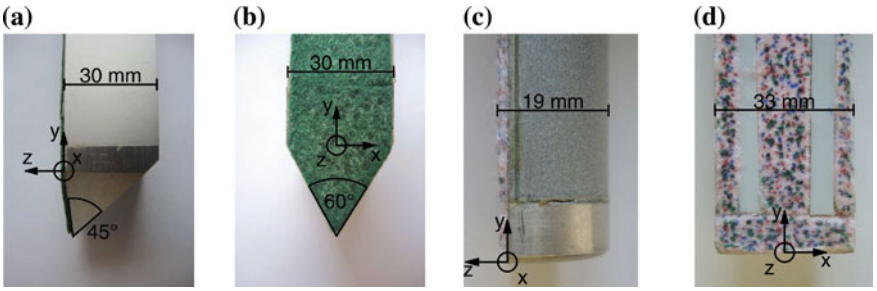

Fig. 3 Geometry of the pile tip: **a** side view, **b** front view of pile type I and **c** side view, **d** front view of pile type II

In order to overcome these drawbacks, model piles with almost half-circular horizontal cross section (pile type II) were used in the recent tests. They are manufactured using the aluminium profiles of a cable channel system. They consist of two parts that are clipped and bonded together, installed with a head and pile tip and filled with 2-K-PU-foam. In the "symmetry plane" (contact to the observation window), two PTFE-stripes ensure a stiff normal contact with the observation window and low

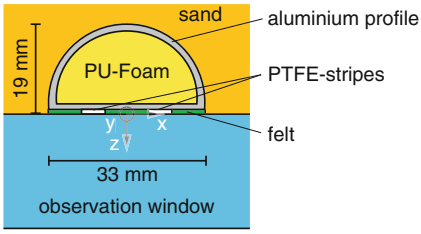

Fig. 4 Schematic cross section of pile type II

friction. Around the two stripes, a layer of felt acts as a sealing against the penetration of sand grains between PTFE and window. Figure 4 shows a schematic sketch of this feature. A random pattern is painted on the felt in order to provide sufficient contrast for the evaluation of pile displacement using the DIC method (so-called seeding). The pile visible width in the "symmetry plane" (x–y-plane, Fig. 2a) is 33 mm. Together with the PTFE, the width into the sand body (y–z-plane) is 19 mm. Thus the cross section of pile type II is 937.5 mm^2, compared to 855 mm^2 of a half-circle with 16.5 mm radius. The pile tip of type II is shown in Fig. 3c, d. A schematic cross section of this pile is given in Fig. 4.

2.2 Vibrator System

A small vibrator mounted on top of the model piles is used in the experiments, Fig. 2b. The vibrator has a mass of $m_{\mathrm{vib}} = 6734.5$ g and four pairwise counter-rotating eccentric masses with 37 g each. The static moment is 0.005476 kgm. The vibrator is servo controlled and the excitation frequency can be adjusted continuously in the range of 0–50 Hz. It is also possible to record the eccenter position. Using a photoelectric light barrier, the digital output signal varies between two extremes depending on whether the vertical centrifugal force is oriented downwards or upwards.

2.3 Instrumentation and Data Acquisition

The following instrumention is used in recent tests:

- The force acting between vibrator and pile is measured using a load cell with 10 kN measuring range and linearity errors smaller than 0.5 % (HBM Type U2A). It has a stiffness of approximately 200 kN/mm, its natural frequency in combination with the pile is about 10 times higher than the highest vibration frequency. The load cell is connected between the bottom plate of the vibrator and the pile head.
- The global penetration is measured with a potentiometric displacement sensor connected to an impeller. A thin steel cable is fastened with a spring to the vibrator and runs over the rim of the impeller. On the other side, a counterweight of 0.4 kg

tauts the cable, see Fig. 2. The sensor is isolated from the vibrations by a spring connected in series (low-pass filtering). Using this set-up, the sensor records only the trend of displacement. The measurement range is about 1.5 m with approximate resolution of 0.25 mm.
- The eccenter position is recorded using a light barrier as described in Sect. 2.2.
- An acceleration sensor is attached to the vibrator. It is assumed that the connections and the pile are stiff enough to consider this measurement at the base of the vibrator as representative for the pile. A PCB 321 A02 acceleration sensor with a range of ±50 g is used.
- Image data of the tests are obtained using a high-speed camera with high-resolution lens (Basler ACE acA2000-340 km). It captures up to 352 images per second with 2040 × 1088 pixel resolution. The region of interest is chosen in such a way that one pixel corresponds to approx. 0.1 mm and 5 pixel to a d_{50} grain. The incremental displacements (displacements between one image and the following) are evaluated using the PIV software JPIV [14]. The utilized settings as well as information about the summation of incremental displacements and strain calculation are given in Appendix 1.

The measurements are recorded with a multichannel data acquisition system (HBM MGCplus) with simultaneous sampling and digital filtering. A sampling rate of 1200 Hz and 200 Hz low-pass Bessel filtering was used in the tests.

3 Test Results

We concentrate on a detailed description of cyclic soil behaviour around the vibrating pile tip on the basis of a selected section of a test with pile type II. In additional tests, similar results were obtained. The soil is considered to be nearly fully saturated and has an initial void ratio of $e_0 = 0.691$ which corresponds to a medium density ($I_D = 0.53$). The sand body has a height of 0.85 m and the pile tip is initially located 0.35 m below the sand surface. A vibration frequency of 24 Hz is used. The vibration is applied only for a few seconds. In doing so, the global penetration is kept small because the test results serve as a basis for the validation of FE simulations similar to those presented in [8] where the simulation technique is restricted to very small pile penetrations.

3.1 Penetration Mode—Identification of "Cavitational" Pile Driving?

Figure 5 shows the evolution of measured pile head force plotted over the pile displacement evaluated with DIC for a selected time period. Only three characteristic cycles of pile motion are plotted. The second period of motion is highlighted with

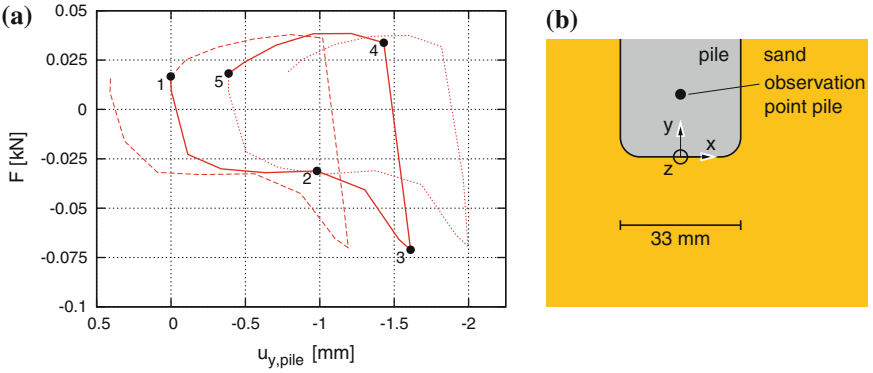

Fig. 5 **a** Typical pile head force-displacement-curve for three selected cycles—the pile displacements are obtained from DIC analysis for a representative observation point illustrated in (**b**)

a solid line. The pile displacement is set to zero an the beginning of the highlighted cycle (highest pile position in this cycle). Important curve points are marked with numbers and referred to in the subsequent figures.

All cycles in Fig. 5 are comparable and the period of motion corresponds to the excitation period. The pile head force changes between tension and compression during each cycle and the compression force increases significantly towards the end of the downward motion between the points nr. 2 and 3. The pile penetrates with approximately 0.4 mm per cycle. The evolution of pile head force indicates cavitational pile driving. In contrast to the tip force, the head force does not vanish in the phases of upward motion because it also contains the shaft friction and inertia forces.

In Fig. 5, between the moments 1 and 2 resp. 4 and 5, distinct phases with constant force can be observed. These phases indicate that the pile tip loses contact to the soil and a small gap (cavity) forms below the tip. Therefrom the term *cavitational* pile driving [3, 4, 16] has been deducted. The tip force vanishes and the measured force at the pile head contains only inertial and shaft friction forces (and, possibly, a resulting pore pressure force for saturated soil). Considering the image data, the forming of a cavity is not evident. In order to investigate a possible opening and closure of such kind of cavity, Fig. 6 compares the pile displacements to the displacements of a material point in the soil 7.5 mm below the pile tip for the same time periods like in Fig. 5.

The zero value of the pile displacements is also used for the soil displacement to visualize the initial offset. Points closer to the pile tip cannot be evaluated reliably by DIC. Reasons therefore are the large deformations in this zone and mainly the material transition involving problems with overlapping DIC search patches.

From Fig. 6a, it can be seen that pile and soil move almost in phase in both modes. The displacement amplitudes of the pile are larger, but the evolution is very similar. The different amplitudes are at least partly contributed to a deformation of

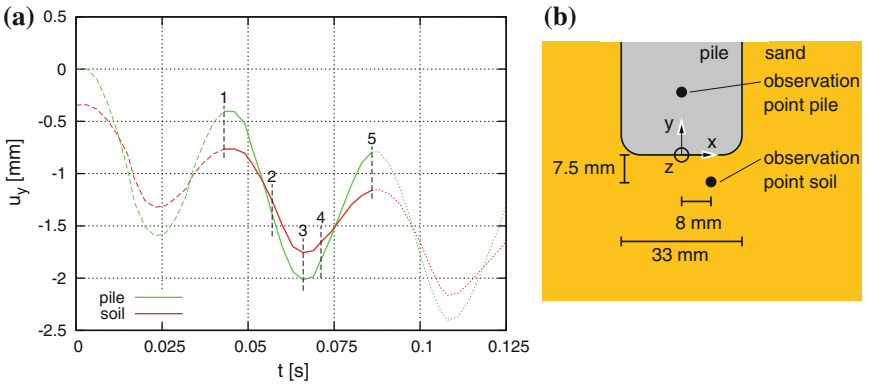

Fig. 6 **a** Chronological evolution of displacements of the pile and a point below the pile tip for three selected cycles from DIC and **b** location of the observation points

the soil between the considered point and the pile tip. Even without this deformation the amplitude difference of about 0.35 mm cannot justify the displacement of about 1 mm necessary to mobilize tip resistance (between the moments 1 and 2 in Fig. 5). In the case of a formation of a cavity below the pile tip, one could also expect to detect the subsequent impact as a sharp bend in the displacement curve of the soil. In Fig. 6a nothing like this can be observed, the soil displacements follow the pile displacements without visible delay. The results indicate that the occurrence of a cavity is not a prerequisite of the cavitational type of pile driving in saturated soil.

3.2 Deformation Mechanism During Vibro-Penetration

3.2.1 Incremental Displacement Fields

Figure 7 shows the isolines of the incremental horizontal and vertical displacement fields obtained from the DIC analysis. The incremental displacements are separately calculated for the time periods between the characteristic curve points already marked in the preceding figures. The current pile position is indicated with thick solid line.

During the first downward phase of pile motion (from 1 to 2), the soil under the pile is pushed horizontally out- and vertically downwards, Fig. 7a. Vertical displacements dominate below the pile tip, whereas horizontal displacements occur also beside and above. The maximum horizontal displacements occur directly below the pile shoulders. The contours of vertical displacement downwards have a bubble shape of roughly one pile diameter, located centrally below the pile tip. Also laterally, above the pile shoulders, some displacements occur. The displacements are directed upwards, apart from the pile shaft and are more pronounced on the left-hand side of the pile. From 2 to 3, in the phase where tip resistance is mobilized, only under

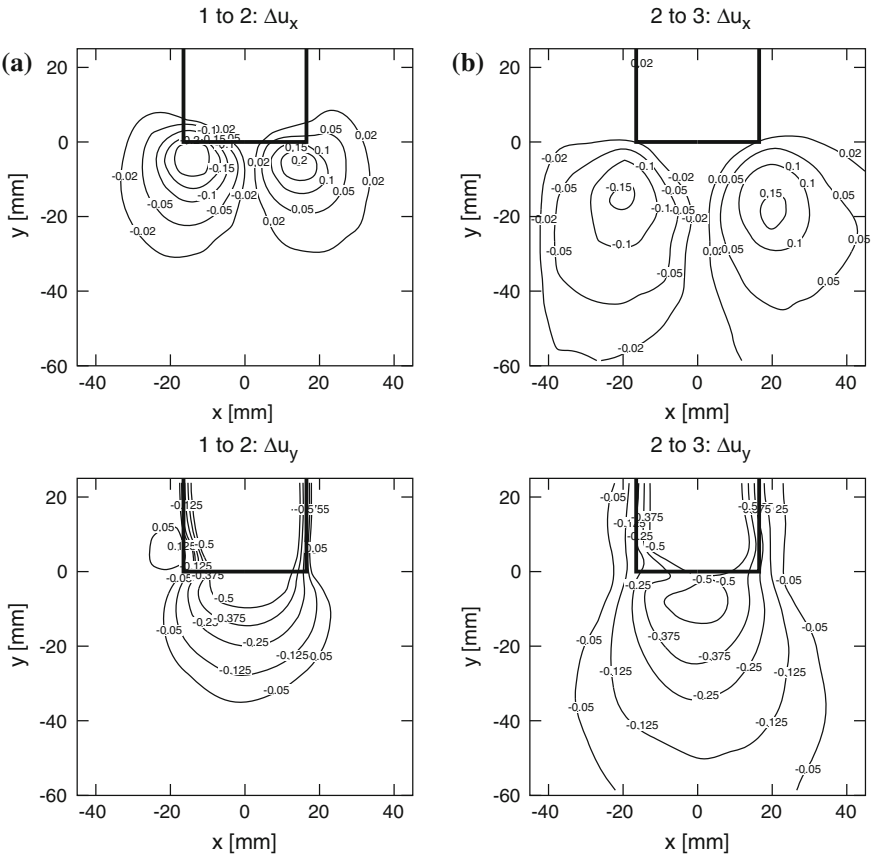

Fig. 7 Isolines of incremental in-plane *horizontal* and *vertical* displacements Δu_x, Δu_y (*top down*) in vicinity to the pile tip obtained from DIC analysis: column **a** phase 1 to 2, **b** 2 to 3 (all values in mm)

the pile tip significant displacements are observed, Fig. 7b. Compared to Fig. 7a, a larger soil zone is affected. The zone with significant displacement gradients extends approximately over twice the pile diameter into the depth. The maximum horizontal displacements are now located at about half the pile diameter under the pile shoulders. During upward pile motion, the displacements reverse, Fig. 8c, d. Both qualitatively and quantitatively, the horizontal and vertical displacements in the phase 4 to 5, Fig. 8d, resemble to the displacements in the very first phase, from 1 to 2, but with reversed sign. Compared to the phase 2 to 3, Fig. 7b, the displacements during upward pile motion concentrate on the direct vicinity of the pile tip.

Considering Figs. 7 and 8, an important result is the symmetry of the displacement field with respect to the y-axis (pile centre line) in the plane of the observation window. This symmetry is indispensable for the calculation of volumetric strain under assumption of axial symmetry (results are given below, Sect. 3.4).

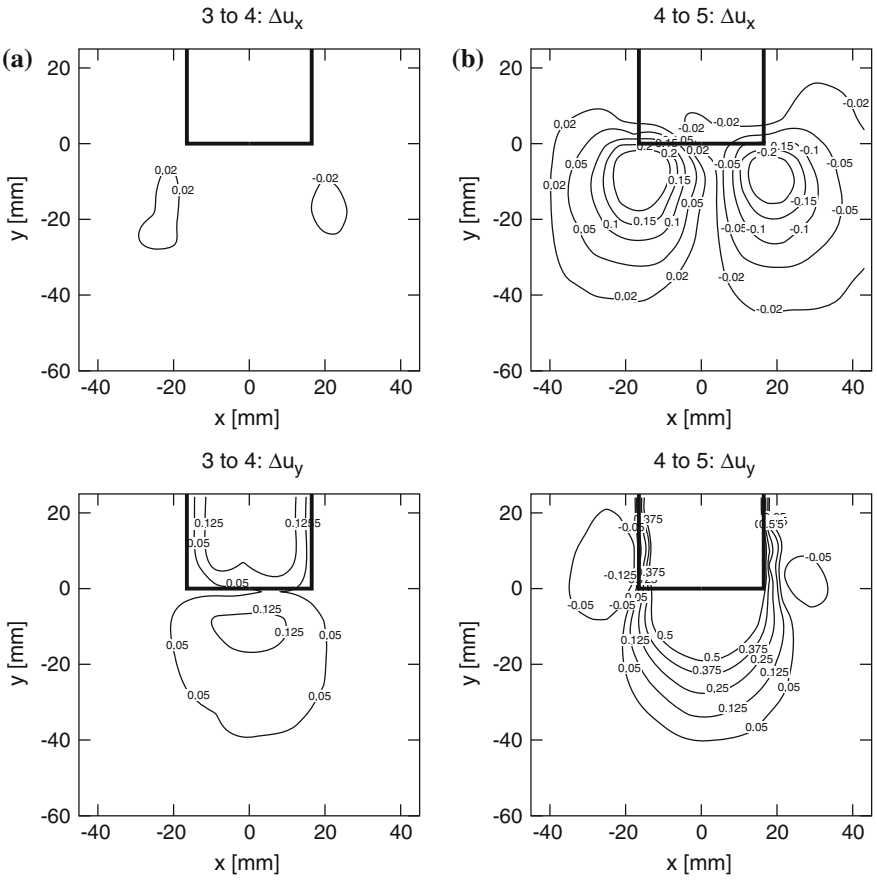

Fig. 8 Isolines of incremental in-plane *horizontal* and *vertical* displacements Δu_x, Δu_y (*top down*) in vicinity to the pile tip obtained from DIC analysis: column **c** phase 3 to 4 and **d** 4 to 5 (all values in mm)

In Figs. 7 and 8, some problems related to the DIC evaluation of pile displacements can be observed. Generally, the pile should move like a rigid body but for some phases displacement gradients can be seen along the pile contours. These problems are mainly attributed to the displacement jump at the interface pile–soil. Such discontinuity disturbs the DIC evaluation in this zone. Also overlapping search patches containing information of pile and soil can occur where usually the sand provides more contrast and determines the evaluation of a mixed patch. The evaluation in the sand should not be affected by these problems. In the literature, the pile region is often omitted. This indicates that the difficulty related to the observation of such zones is quite common.

3.2.2 Incremental Deformation Fields

Figures 9 and 10 show the incremental in-plane strain fields obtained from DIC analysis. Each columns corresponds to one phase with horizontal, vertical and maximum shear strains $\Delta\varepsilon_{xx}$, $\Delta\varepsilon_{yy}$, $\Delta\gamma_{\max}$ (top down). The mechanical sign convention is used (compression negative). Figure 9 contains the two phases of downward pile motion and Fig. 10 the upward pile motion.

The calculation of strain is performed basing on the incremental displacement fields (slightly smoothed using a spline method) according to the procedure described in Appendix 1.

The incremental strains occurring during the first downward phase of motion from 1 to 2 are plotted in Fig. 9a. In this phase, a bubble-shaped region is subjected to large shear deformations (greater than 4 %). Vertical compression and horizontal extension are observed directly below the pile tip. On the sides below, the soil is mainly compressed in horizontal direction. Above the pile tip, horizontal and vertical compression occurs. The centre of the almost circular region around the pile tip that undergoes large shear deformation is located a few mm below the pile tip and spreads also into the zone above the pile shoulder. The consequences of this observation will be discussed later on. In the phase from 2 to 3, Fig. 9b, only below the pile tip significant deformation is observed. The extension of the deformed region is larger compared to phase 1 to 2. The deformation pattern is in accordance to other results, e.g. [19, 20]. In the short phase of upward motion from 3 to 4, only small deformations occur, Fig. 10a. In the main observation zone, vertical extension and horizontal compression below the pile tip have been measured. The shear deformation concentrates on this bubble-shaped zone. The deformations occurring in the phase 4 to 5, Fig. 10b, are similar to those in phase 1 to 2 but with reversed sign.

The problems with the evaluation of the pile, already detected in Figs. 7 and 8, are even more evident after strain calculation. However, the focus of this study lies on the soil region that provides an excellent speckle and is much better evaluated. Only a small zone of a few mm vertically below the pile tip is disturbed and cannot be interpreted. If an improved evaluation of the pile itself is desired, this could be achieved by two separate evaluations: one for the pile and one for the soil region.

3.3 Displacements Trajectories During Vibro-Penetration

In Fig. 11, the displacement trajectories of selected material points around the pile tip are presented. Figure 11e shows a schematic overview of the initial position of the four points with regard to the pile tip. The initial position of the pile and its current position at the beginning of the highlighted cycle (point 1) are illustrated as well. Point A is located below the pile tip while the points B, C and D are chosen slightly beside the pile at different vertical positions. Figure 11a plots the displacement trajectories together for all four points for a time period of one second after the start of the

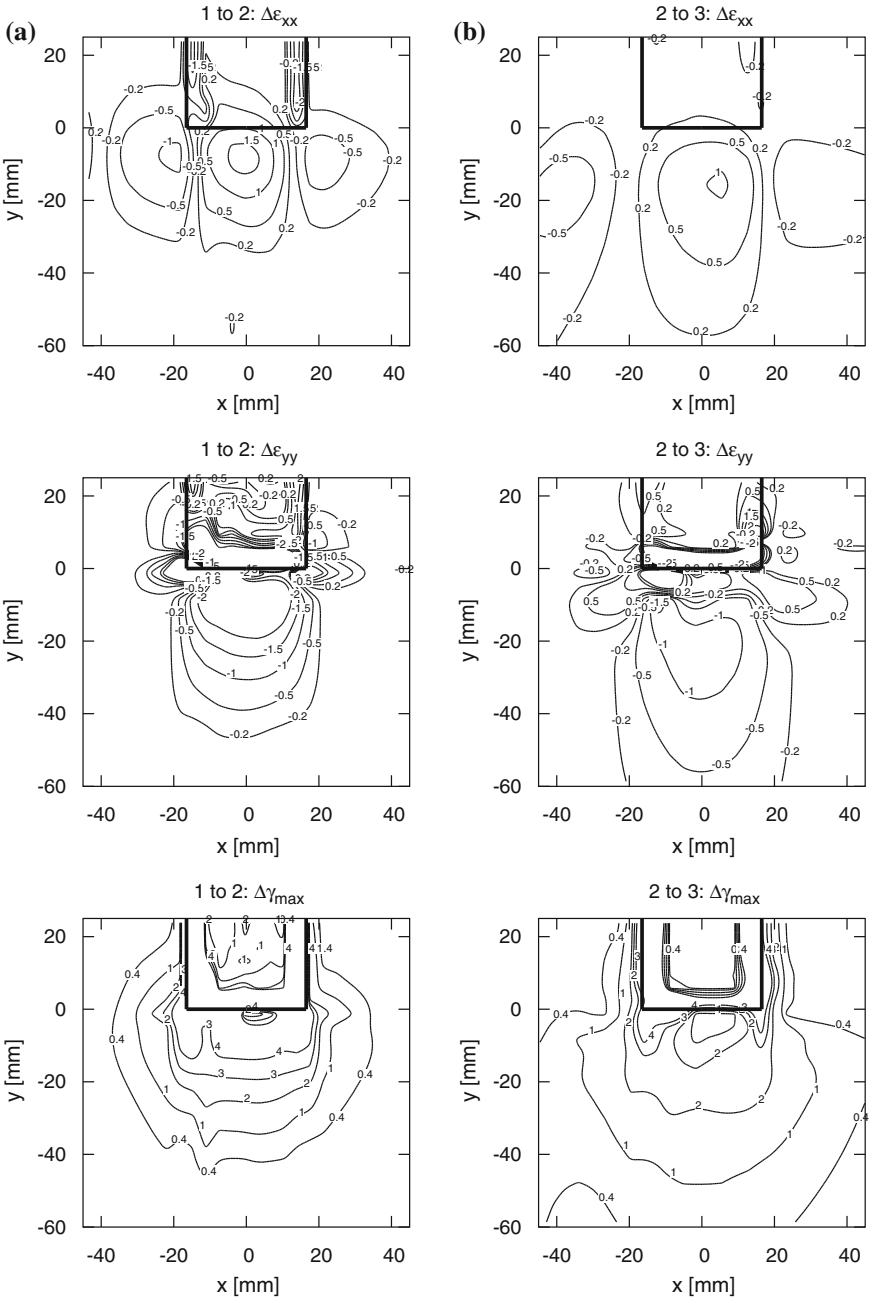

Fig. 9 Isolines of logarithmic incremental in-plane *horizontal*, *vertical* and *maximum shear* strains $\Delta\varepsilon_{xx}$, $\Delta\varepsilon_{yy}$, $\Delta\gamma_{\max}$ (*top down*) in vicinity to the pile tip during the downwards motion of the pile calculated on the basis of DIC results: column **a** phase 1 to 2, **b** 2 to 3 (all values in %)

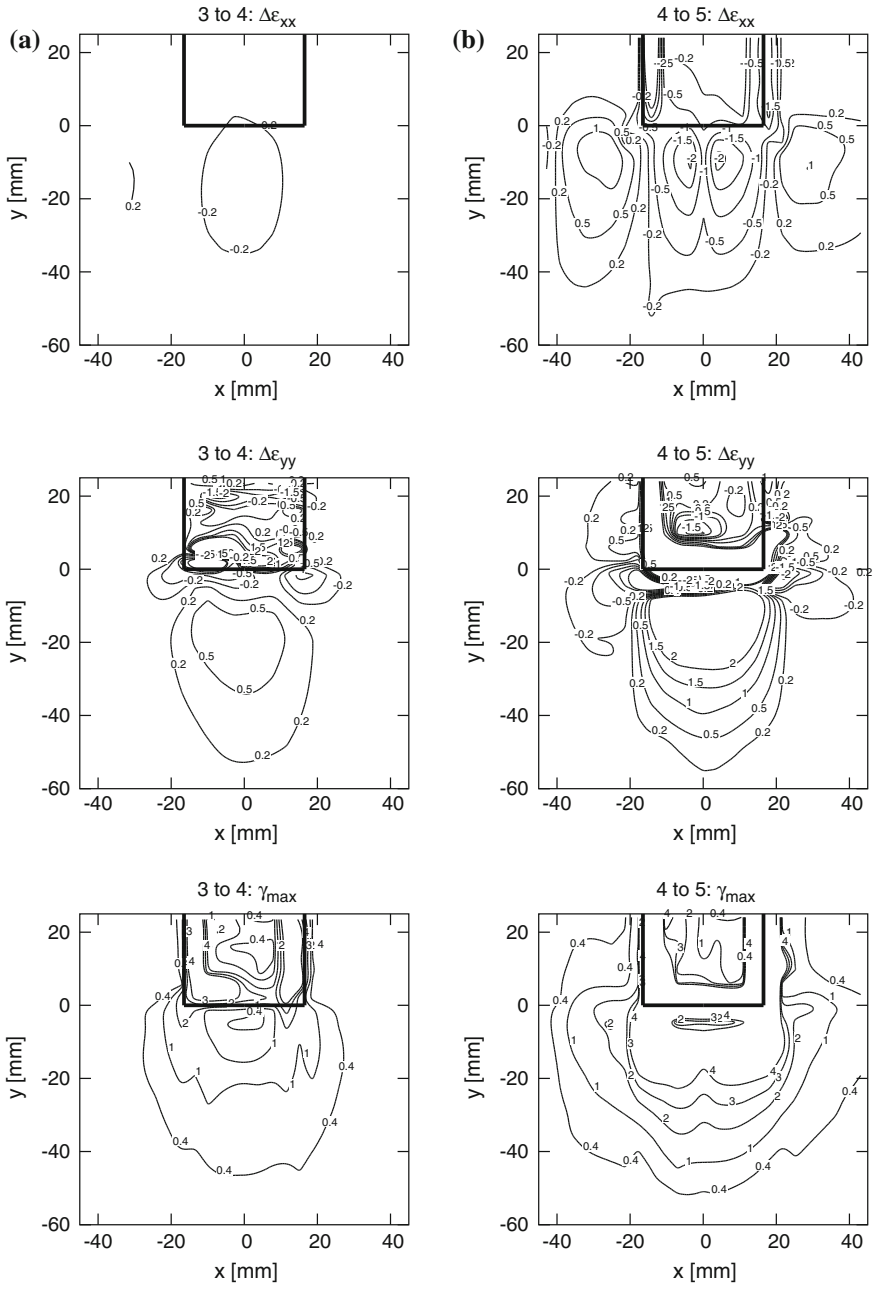

Fig. 10 Isolines of logarithmic incremental in-plane *horizontal*, *vertical* and *maximum shear* strains $\Delta\varepsilon_{xx}$, $\Delta\varepsilon_{yy}$, $\Delta\gamma_{\max}$ (*top down*) in vicinity to the pile tip during the upwards motion of the pile calculated on the basis of DIC results: column **c** phase 3 to 4 and **d** 4 to 5 (all values in %)

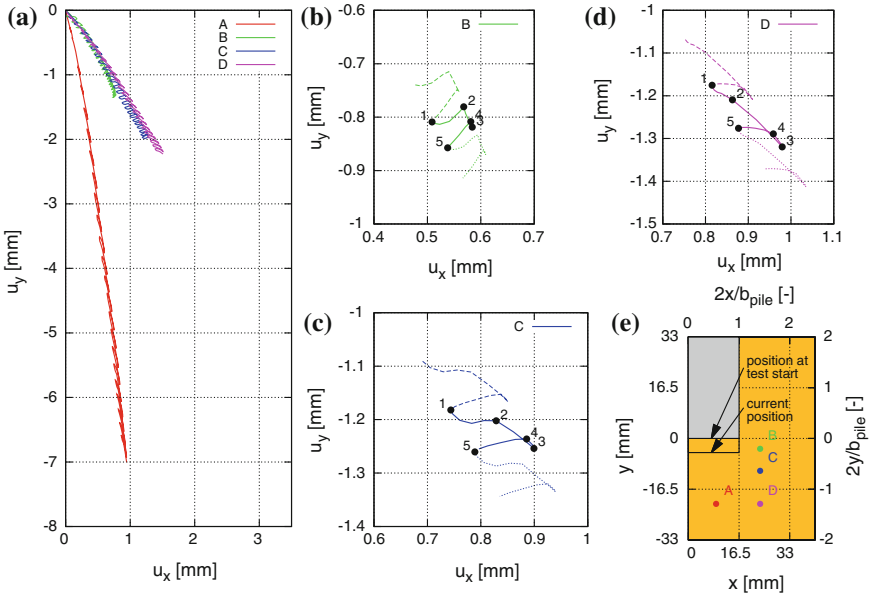

Fig. 11 Displacement trajectories of selected points in vicinity to the pile tip: **a** overview, **b–d** individual graphs for each point during three selected cycles and **e** location of the selected points

vibration. Figure 11b–d plot the trajectories of B, C and D separately for the same time period as in Figs. 5 and 6. Although different axis ranges are used the trajectories are equally scaled in size. Point A is omitted because the point moves mainly in vertical direction and a displacement trajectory is not an appropriate visualization for such kind of displacement.

From Fig. 11a, it can be seen that the point A moves primarily in vertical direction and is pushed downwards by the pile. The other points undergo significantly smaller displacements with stronger horizontal component and larger horizontal amplitudes. They have a very similar displacement trend. Considering the evolution of cyclic displacements in Fig. 11b–d, a clear relation to the phases identified in the evolution of pile head force during each cycle can be observed. In the first downward motion phase, points nr. 1–2, the soil moves outwards, apart from the pile tip. This means a displacement upwards for point B, sidewards for C and diagonally downwards for D. In the tip resistance phase, nr. 2 to 3, all points are pushed almost linearly down- and sidewards. During the short-time increment from 3 to 4, the displacements reverse and the soil moves along a short section of the path followed before. Subsequently, the displacement kinks and the soil moves towards the pile tip: B and C side- and downwards and D only sidewards.

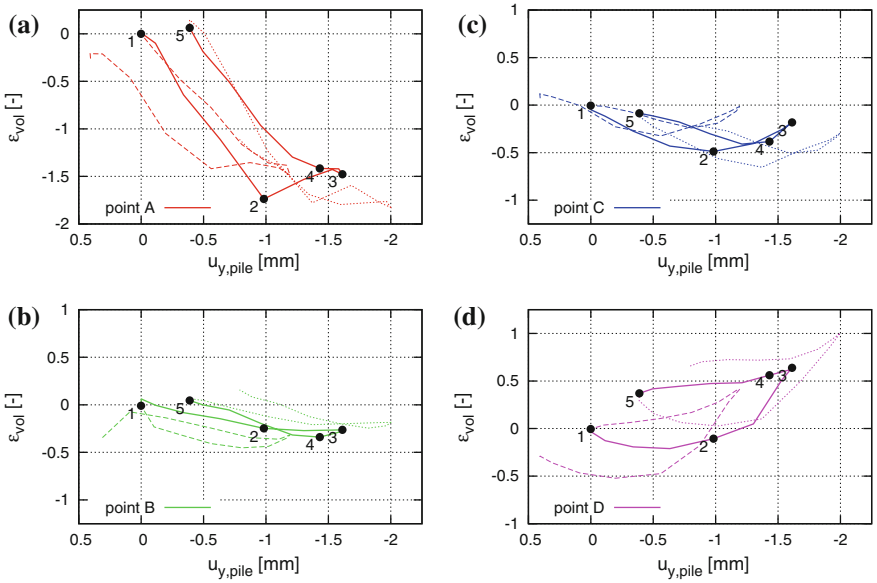

Fig. 12 Logarithmic volumetric strain ε_{vol} calculated on the basis of DIC results assuming axial symmetry plotted versus the pile displacement u_{pile} for four points during three selected vibration cycles

3.4 Cyclic Volumetric Soil Behaviour During Vibro-Penetration

Figure 12 illustrates the volumetric soil deformation ε_{vol} around the pile tip exemplary for the points A–D defined in Fig. 11. Assuming axial symmetry, ε_{vol} is calculated according to the procedure given in Appendix 1. The volumetric strain is plotted over the pile displacement to visualize the connection to the force-displacement curve and to keep the points comparable. Pile displacement and volumetric strain are set to zero at the beginning of the highlighted cycle.

In all four cases, the volumetric strain oscillates considerably during every cycle, which proves at least partially drained conditions. This is an important result because it shows that a numeric code suitable for a simulation of the experiment has to deal with dynamic consolidation. The largest peak-to-peak amplitude of volumetric strain is observed for points A (1.7 %). The others points show smaller amplitudes of 0.3–0.9 %. Almost always a reversal of the pile motion is accompanied by a strain reversal and contractant soil behaviour. Towards the end of each downward and upward motion, the tendency to dilatancy is observed. During downward pile motion, the mobilization of dilatancy corresponds to the phases with strong increase of tip resistance (between the points 2 and 3 in Fig. 12).

4 Interpretation and Postulated Mechanism

During cavitational pile driving, the increase of tip resistance is slow compared to non-cavitational pile driving. The explanation given in [3] is that in the upward motion of the pile, the soil is subjected to large deformation with change of sign of the shear stress compared to the preceding penetration phase. The ratio of principal stress reverses and the horizontal stress is greater than the vertical stress. As a consequence of this, the soil response in the new penetration phase is very soft. The assumption for the phases without tip force is the opening and closure of a cavity. The time when the tip force is restarting to increase is interpreted as the moment of establishing new contact.

This explanation seems reasonable and comprehensive for pile driving in dry soil but it is found that the qualitative evolution of pile head force measured in our experiments under water-saturated conditions is very similar. As described above the opening and closure of a cavity below the pile tip is unlikely to occur in the experiments and cannot explain the long phases without tip resistance (phases 1 to 2 resp. 4 to 5). Such cavity would also stand in contrast to the fact that significant soil deformation is observed in these phases (especially in the region laterally above the pile tip). When tip resistance is mobilized (phase 2 to 3), the soil deformation concentrates on the region below the pile tip.

A possible explanation for this deformation mechanism is a type of pumping effect. When the pile performs large displacements upwards, it frees some space under the pile tip which provokes suction. The pore fluid has the tendency to fill this space and flows towards the pile tip. This creates drag forces in the soil and the grains have to follow the fluid motion. When the pile motion reverses, also the drag forces reverse and the soil is pushed radially apart by the pore fluid. During these phases, the effective stress in the soil in direct vicinity to the pile tip is very low and the soil-water mixture behaves more like a viscous fluid. The pile tip does not necessarily have effective contact with the grain skeleton. The process is very similar to the closure and expansion of a spherical cavity. Then suddenly, the grain skeleton is reformed, load transfer between pile and soil is enabled and tip resistance is mobilized. A large zone below the pile tip is sheared and can mobilize dilatancy. Necessary conditions for this mechanism are large displacement amplitudes and partially drained conditions.

5 Conclusions and Outlook

Vibratory pile driving was investigated using model tests in a half-cylinder-shaped test device with an observation window in the symmetry plane. The pile motion along this window was recorded using a high-speed digital camera. The pile displacements and deformation of saturated soil were evaluated by means of DIC.

Important conclusions from the experimental results are:

- The evolution of tip resistance observed in the test results presented above indicates cavitational pile driving. The characteristic points on the piles' force-displacement curve correlate with sudden changes in the directions of displacement/deformation in the soil.
- Under water, the forming of a gap or cavity is not a necessary condition for the occurrence of slow or cavitational pile driving. A sufficient pile displacement upwards and the vanishing of the tip force as a result of this seems to be a more appropriate condition. However, it is of course possible that a cavity forms below the pile under different conditions (drainage, displacement amplitude, etc.).
- On the basis of the displacement and deformation fields around the pile tip evaluated by DIC in the observation plane, the symmetry of the process with respect to a plane perpendicular to the observation plane through the centre line of the pile was confirmed. Assuming axial symmetry with respect to the centre line of the pile, the calculation of volumetric strains was performed and the occurrence of the alternation of contractant and dilatant behaviour was demonstrated.
- In the phases with negligible tip resistance—usually contributed to the opening and closure of a cavity—the pile can be in contact with the soil, but without significant effective load transfer. The deformation mechanism in these phases is similar to a spherical cavity expansion. A possible explanation is the occurrence of a pumping effect induced by the cyclic pile motion. This provokes cyclic pore fluid flow that drags and pushes the soil simultaneously to the pile motion. The increase of tip resistance coincides with a dilatant soil behaviour below the pile tip.

Important topics of future work are the direct measurements of tip resistance together with pore pressure in vicinity to the vibrating pile tip. Related to these measurements, the actual degree of saturation obtained from the sample preparation method has to be reviewed. The work presented here concentrates on the so-called cavitational pile driving. Further studies will be carried out on other types of vibratory pile driving such as non-cavitational pile driving. Using the current test set-up, a surcharge load has to be applied therefore in order to reduce the upward pile motion. Another interesting field of research is the investigation of higher vibration modes. It is of practical interest to avoid these modes, therefore the reasons for their occurrence will be studied using the approach described in this contribution.

Appendix 1: Summation of Incremental Displacements and Strain Calculation Procedure

The DIC procedure evaluates a series of images and calculates the incremental displacements $\Delta \mathbf{u}_{DIC}^{(i)}$ (displacements occurring between image i-1 and i) for a fixed grid in eulerian coordinate system. Search patches of 32×32 pixel that are detected in zones four times as large are used for this evaluation. In order to obtain the total

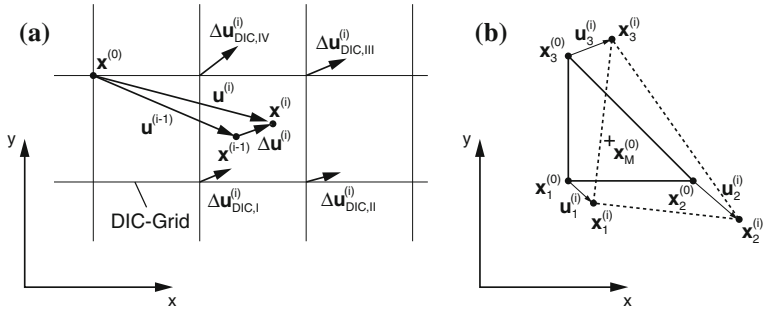

Fig. 13 **a** Interpolation of incremental displacements $\Delta\mathbf{u}$ from DIC results $\Delta\mathbf{u}_{DIC}$ and summation to total displacements $\mathbf{u}$ and **b** 3-Node element for strain calculation

displacements $\mathbf{u}^{(i)} = \mathbf{u}(\mathbf{X}, t_i)$ with respect to a reference configuration defined in the first image, the incremental displacements have to be summed. Therefore, material points $\mathbf{X}$ defined in the reference configuration are followed throughout the image series. Since a material point of the reference configuration lies generally not on a mesh point of the current configuration, its incremental displacement $\Delta\mathbf{u}^{(i)}$ has to be interpolated using the information of the four surrounding points, $\Delta\mathbf{u}^{(i)}_{DIC,I-IV}$. Linear interpolation functions are used. The incremental displacements $\Delta\mathbf{u}^{(i)}$ are then added to the total displacement of the preceding step to obtain the current total displacement $\mathbf{u}^{(i)}$. This procedure is illustrated in Fig. 13a.

Similar to [20], for strain calculation a triangular 3-node element with linear interpolation functions is used, Fig. 13b.

For this element the deformation gradient $\mathbf{F}$ is calculated as the derivative of the current position $\mathbf{x}^{(i)} = [x^{(i)}, y^{(i)}]^T$ with regard to the reference configuration $\mathbf{X} = \mathbf{x}^{(0)} = [X, Y]^T$. Linear interpolation functions N_j are used for the approximation of the current configuration.

$$\mathbf{F} = \frac{\partial \mathbf{x}^{(i)}}{\partial \mathbf{X}} = \sum_{j=1}^{3} \frac{\partial N_j}{\partial \mathbf{X}} \mathbf{x}_j^{(i)} \tag{1}$$

The derivatives of the interpolation functions can be calculated from the nodal coordinates in the reference configuration:

$$\frac{\partial N_1}{\partial X} = \frac{1}{2A_e}(Y_2 - Y_3); \qquad \frac{\partial N_1}{\partial Y} = \frac{1}{2A_e}(X_3 - X_2) \tag{2}$$

$$\frac{\partial N_2}{\partial X} = \frac{1}{2A_e}(Y_3 - Y_1); \qquad \frac{\partial N_2}{\partial Y} = \frac{1}{2A_e}(X_1 - X_3) \tag{3}$$

$$\frac{\partial N_3}{\partial X} = \frac{1}{2A_e}(Y_1 - Y_2); \qquad \frac{\partial N_3}{\partial Y} = \frac{1}{2A_e}(X_2 - X_1) \tag{4}$$

With the element area A_e:

$$A_e = 1/2[X_1(Y_2 - Y_3) + X_2(Y_3 - Y_1) + X_3(Y_1 - Y_2)] \tag{5}$$

The Right Cauchy-Green-deformation tensor $\mathbf{U}$ is obtained as follows:

$$\mathbf{U} = (\mathbf{F}^T \cdot \mathbf{F})^{1/2} \tag{6}$$

The principal in-plane (Hencky-)strains and the maximum in-plane shear strain are obtained from the eigenvalues $U_{I/II}$ of $\mathbf{U}$. Therefrom, the volumetric strain ε_{vol} is calculated assuming axial symmetry ($u_x \hat{=} u_r$).

$$\varepsilon_I = \ln U_I; \qquad \varepsilon_{II} = \ln U_{II}; \tag{7}$$

$$\gamma_{\max} = \varepsilon_I - \varepsilon_{II}; \qquad \varepsilon_{\text{vol}} = \varepsilon_I + \varepsilon_{II} + \ln(1 + u_x/X) \tag{8}$$

Appendix 2: Test Sand, Deposition Method and Uniformity Control

A poorly graded medium quartz sand with sub-rounded grains is used in the tests. A typical grain size distribution and some granulometric properties are given in Fig. 14a. The minimum and maximum void ratios at negligible stress level are $e_{\min} = 0.549$ and $e_{\max} = 0.851$. From permeability tests with constant head, the dependence of the coefficient of permeability k on the porosity n was evaluated. Results are given in

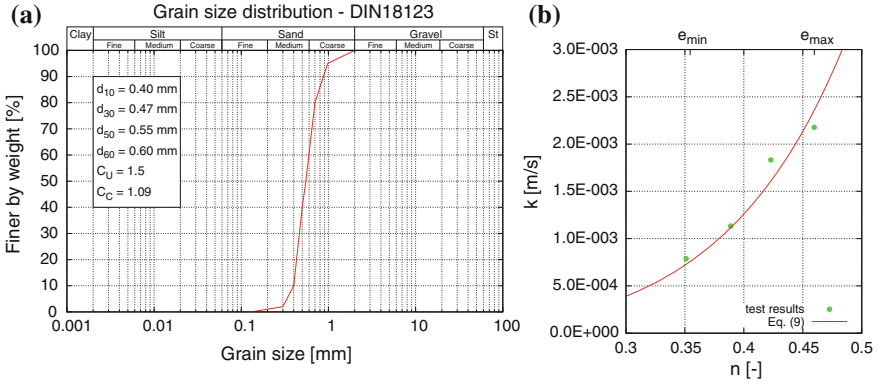

Fig. 14 **a** Grain size distribution of the test sand (Karlsruhe Sand) and **b** results of permeability tests with constant head for different porosities

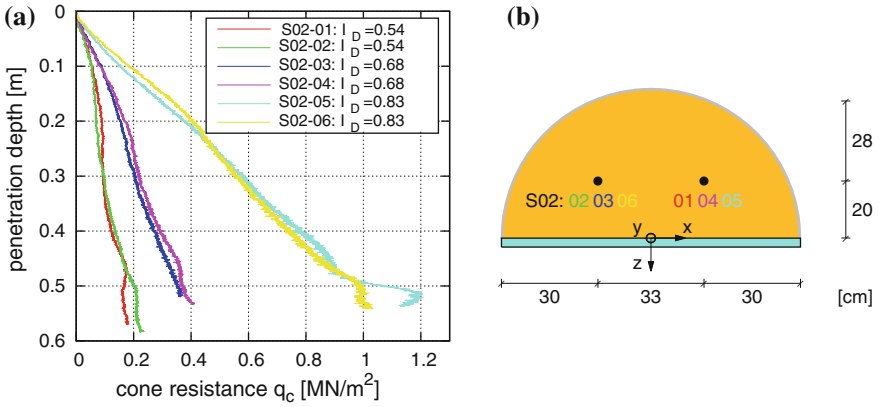

Fig. 15 CPT for uniformity control: **a** measurements and **b** position of the CPTs

Fig. 14b. For a rough estimation of the permeability k as a function of the porosity n, the well-known Kozeny/Carman-equation [1, 6] was fitted to the test results, Eq. 9:

$$k(n) = \frac{1}{308} \cdot \frac{\gamma_w}{\eta_w} \cdot \frac{n^3}{(1-n)^2} \cdot d_w^2 \tag{9}$$

with the specific weight of water $\gamma_w = 10\,\text{kN/m}^3$, the dynamic viscosity of water $\eta_w = 1.137 \times 10^{-3}\,\text{kNs/m}^2$ and the effective grain size $d_w = 0.5\,\text{mm}$.

For the preparation of the vibratory pile driving tests, the model pile is fixed in the starting position and approximately half of the test device is filled with deaired water. The dry sand is pluviated onto the water surface using a travelling diffusor which is manually operated in such a way that the sand sediments in horizontal layers. This procedure results in relative densities of about 40 %. Higher densities are achieved by dynamic excitation of the test device, e.g. by applying multiple hammer blows against the base.

For numerical simulation of the tests it is essential to obtain a homogeneous density distribution. In order to control the uniformity of the sample after the described deposition and densification method a series of cone penetration tests (CPT) was conducted. The same set-up like in [18] was used. The results are shown in Fig. 15a and the position of the CPTs in Fig. 15. The same sample was used for all six CPTs. The sample was densified step-wise and after each densification two opposited CPTs with respect to the symmetry plane y–z were performed. As expected, the cone resistance q_c increases for higher relative densities. The three CPT-pairs show very similar results although one could expect that the second CPT for each density is influenced by the preceding. The results indicate that the preparation method provides homogeneous samples and can be used for benchmark experiments.

References

1. Carman, P.C.: Permeability of saturated sands, soils and clays. J. Agric. Sci. **29**, 263–273 (1937)
2. Cudmani, R.O., Huber, G., Gudehus, G.: Zyklische und dynamische Penetration nichtbindiger Böden, Contribution to Workshop "Boden unter fast zyklischer Belastung", Bochum (2000)
3. Cudmani, R.O.: Statische, alternierende und dynamische Penetration in nichtbindigen Böden. Diss., Publications of the Institute of Soil Mechanics and Rock Mechanics, University of Karlsruhe, vol. 152 (2001)
4. Dierssen, G.: Ein bodenmechanisches Modell zur Beschreibung des Vibrationsrammens in körnigen Böden. Diss., Publications of the Institute of Soil Mechanics and Rock Mechanics, University of Karlsruhe, vol. 124 (1994)
5. Huber, G.: Vibrationsrammen: Großmaßstäbliche Versuche. Contribution to the Workshop "Vibrationsrammen", Karlsruhe (1997)
6. Kozeny, J.: Ueber kapillare Leitung des Wassers im Boden. Sitzungsbericht Akademie der Wissenschaften, Wien **136**(2a), 271–306 (1927)
7. Ni, Q., Hird, C.C., Guymer, I.: Physical modelling of pile penetration in clay using transparent soil and particle image velocimetry. Gotechnique **60**(2), 121–132 (2009)
8. Osinov, V.A., Chrisopoulos, St., Triantafyllidis, Th.: Numerical study of the deformation of saturated soil in the vicinity of a vibrating pile. Acta Geotech. (2012). doi:10.1007/s11440-012-0190-7
9. Osinov, V.A.: Numerical modelling of the effective-stress evolution in saturated soil around a vibrating pile toe. In: Triantafyllidis, Th. (ed.) Holistic Simulation of Geotechnical Installation Processes—Numerical and Physical Modelling, pp. 138–154. Springer, Heidelberg (2015)
10. Rodger, A.A., Littlejohn, G.: A study of vibratory pile driving in granular soils. Gotechnique **30**(3), 269–293 (1980)
11. Savidis, S.A., Aubram, D., Rackwitz, F.: Vibro-Injection pile installation in sand: Part II—Numerical and experimental investigation. In: Triantafyllidis, Th. (ed.) Holistic Simulation of Geotechnical Installation Processes—Numerical and Physical Modelling, pp. 103–131. Springer, Heidelberg (2015)
12. Schönit, M.: Online-Abschätzung der Rammguttragfähigkeit beim langsamen Vibrationsrammen in nichtbindigen Böden. Diss., Publications of the Institute for Technology and Management in Construction, University of Karlsruhe (2009)
13. Triantafyllidis, Th: Neue Erkenntnisse aus Messungen an tiefen Baugruben am Potsdamer Platz in Berlin, Bautechnik, 75. Heft **3**, 133–154 (1998)
14. Vennemann, P.: JPIV-software package for Particle Image Velocimetry (2007). http://www.jpiv.vennemann-online.de
15. Vielsack, P., Storz, M.: Dynamics of vibratory pile driving. Workshop "Vibrationsrammen", pp. 3–12, Karlsruhe (1997)
16. Viking, K.: The vibratory pile installation technique. TRANSVIB 2006, Gonin, Holeyman et Rocher-Lacoste (ed.), Editions du LCPC, pp. 65–82, Paris (2006)
17. Vogelsang, J., Chrisopoulos, S.: Experimentelle und numerische Untersuchungen zum Vibrationsrammen in nichtbindigem Boden. Beitrag zur Spezialsitzung "Forum für junge Geotechnik-Ingenieure", 33. Baugrundtagung in Berlin (2014)
18. Vogelsang, J., Zachert, H., Huber, G., Triantafyllidis, Th.: Effects of soil deposition on the initial stress state in model tests: Experimental results and FE simulation. In: Triantafyllidis, Th. (ed.) Holistic Simulation of Geotechnical Installation Processes—Numerical and Physical Modelling, pp. 1–21. Springer, Heidelberg (2015)
19. Vogelsang, J., Huber, G., Triantafyllidis, Th.: On soil deformation and stress redistribution around pressed-in and vibrated displacement pile tips. In Triantafyllidis, Th. (ed.) Holistic Simulation of Geotechnical Installation Processes—Numerical and Physical Modelling, pp. 44–59. Springer, Heidelberg (2015)
20. White, D.J., Bolton, M.D.: Displacement and strain paths during plane-strain model pile installation in sand. Gotechnique **54**(6), 375–397 (2004)

Dynamic Problem for the Deformation of Saturated Soil in the Vicinity of a Vibrating Pile Toe

S. Chrisopoulos, V.A. Osinov and T. Triantafyllidis

Abstract A numerical study conducted recently by the authors showed that the vibration of a pile in saturated granular soil leads to the formation of a zone with nearly zero effective stresses (liquefaction zone) around the pile toe. The dynamic problem was solved with the finite-element program Abaqus/Standard using a hypoplasticity model for soil with the assumption of zero soil permeability and without a mass force. A question which still remained open was the influence of the soil permeability and the gravity force on the solutions. In the present study, the problem is solved with nonzero permeability and gravity, and the solutions are compared with those obtained earlier. For this purpose, a user-defined element has been constructed in Abaqus to enable the dynamic analysis of a two-phase medium with nonzero permeability. The solutions show that high permeability and gravity do not prevent the formation of a liquefaction zone around the pile toe in spite of the fact that a build-up of the pore pressure is inhibited by the pore pressure dissipation.

Keywords Saturated soil · Vibratory pile driving · Liquefaction

1 Introduction

Vibratory pile driving produces cyclic deformations in the surrounding soil and may bring about unexpectedly large displacements of neighbouring structures. An example can be found in [8], where a significant displacement of a retaining wall in an excavation pit was observed after—and presumably as a consequence of—the installation of vibratory driven piles in saturated soil at the base of the pit.

To model the deformation of saturated soil in the vicinity of a vibrating pile, numerical studies were recently carried out with the use of two types of constitutive models [2–4, 6]. A numerical analysis of the first 20–30 cycles of vibration was

S. Chrisopoulos (✉) · V.A. Osinov · T. Triantafyllidis
Institute of Soil Mechanics and Rock Mechanics, Karlsruhe Institute of Technology, Karlsruhe, Germany
e-mail: Stylianos.Chrisopoulos@kit.edu

T. Triantafyllidis (ed.), *Holistic Simulation of Geotechnical Installation Processes*, Lecture Notes in Applied and Computational Mechanics 80, DOI 10.1007/978-3-319-23159-4_3

performed with a hypoplasticity model (low-cycle problem) and showed that the vertical vibration of a pile in saturated soil leads to the formation of a zone with nearly zero effective stresses (referred to as liquefaction zone) in the immediate vicinity of the pile toe [2]. The further evolution of the incipient liquefaction zone for a large number of cycles (high-cycle problem) was simulated numerically with the use of a so-called explicit cyclic constitutive model. It was shown how the liquefaction zone grows in size with the increasing number of cycles [3, 4] and how the stress state near a concrete wall may be changed by a vibrating pile [6].

In the method presented in [3, 4, 6], input data for the high-cycle problem (an initial stress state and stress amplitudes around the pile) are estimated from the solutions to the low-cycle problem. The latter was solved in [2] with the finite-element program Abaqus/Standard with the assumption of locally undrained conditions (zero soil permeability) and without a mass force. The question still remained open as to how nonzero soil permeability and the gravity force would influence the solutions. Abaqus does not provide a built-in procedure for the dynamic analysis of fluid-saturated solids with nonzero permeability. These limitations can be overcome by the construction of a user-defined element [7] or by other means as proposed, for instance, in [5, 9].

The objective of the present study is to construct a user-defined finite element in Abaqus for the solution of the dynamic problem for a fluid-saturated solid with nonzero permeability, to solve the low-cycle problem with nonzero permeability and gravity and to compare the solutions with those obtained in [2]. The problem will be solved, as in [2], in the two-dimensional axisymmetric formulation.

2 Governing Equations

Saturated soil is considered here as a two-phase continuum consisting of a solid skeleton and a pore fluid. The skeleton material is assumed to be incompressible. The dynamic problem is formulated within the framework of the so-called *u-p* approximation [10, 11]. In this approximation, the difference in the accelerations of the solid and fluid phases is neglected, while the difference in the displacements and velocities is not. Furthermore, the material time derivative of the pore pressure with respect to the fluid phase is replaced with the material time derivative with respect to the solid phase. The equations of motion for the whole continuum and for the fluid phase are written as:

$$\operatorname{div} \boldsymbol{\sigma} - \operatorname{grad} p + \varrho \mathbf{g} = \varrho \ddot{\mathbf{u}}, \tag{1}$$

$$-\operatorname{grad} p + \varrho_f \mathbf{g} - \frac{1}{k} \varrho_f g \mathbf{w} = \varrho_f \ddot{\mathbf{u}}, \tag{2}$$

where $\boldsymbol{\sigma}$ is the effective stress tensor (the normal components are negative for compression), p is the pore pressure (positive for compression), $\mathbf{u}$ is the displacement vector of the skeleton, ϱ is the bulk density of the medium, ϱ_f is the density of the fluid phase, $\mathbf{g}$ is the mass force vector, g is the acceleration due to gravity, k is the soil

permeability (m/s), **w** is the seepage velocity (the fluid velocity relative to the solid phase multiplied by the porosity) and the dot stands for the material time derivative with respect to the solid phase. The fluid density, ϱ_f, and the bulk density of the medium,

$$\varrho = (1-n)\varrho_s + n\varrho_f, \tag{3}$$

are treated as constants. Here ϱ_s is the density of the solid phase and n is the porosity. In the numerical calculations in this paper, $\varrho_s = 2650\ \mathrm{kg/m^3}$ and $\varrho_f = 1000\ \mathrm{kg/m^3}$.

The constitutive equation for the pore pressure reads

$$\dot{p} = -\frac{K_f}{n}\,\mathrm{div}\,(\mathbf{w} + \dot{\mathbf{u}})\,, \tag{4}$$

where K_f is the bulk modulus of the pore fluid.

The system (1), (2), (4) should be complemented by a constitutive equation for the effective stresses. In this study, we use a hypoplasticity model with intergranular strain [1] with the constitutive parameters of Karlsruhe sand. The constitutive parameters can be found in [2, 4].

The numerical solution of the problem with the hypoplasticity model requires two supplements to the calculation of stresses: a small-stress correction and viscous stresses. The tensile deformation of a hypoplastic material results in zero mean stress at a finite strain. The numerical integration of the hypoplasticity equation in this case will yield a positive (tensile) stress, which will stop the computation. For this reason, the following small-stress correction is introduced in the numerical algorithm: if the current effective stress tensor $\boldsymbol{\sigma}$ is such that $\mathrm{tr}\,\boldsymbol{\sigma}/3 > \sigma^*$, where $\sigma^* < 0$ is a prescribed small stress (e.g. -0.01 kPa), a hydrostatic stress $\Delta\boldsymbol{\sigma}$ is added to $\boldsymbol{\sigma}$, where $\Delta\boldsymbol{\sigma}$ is such that $\mathrm{tr}(\boldsymbol{\sigma} + \Delta\boldsymbol{\sigma})/3 = \sigma^*$.

Although the small-stress correction prevents the mean stress from being positive, the computation may still stop because of the loss of convergence during the implicit time integration. Convergence is maintained by introducing an additional viscous stress

$$\boldsymbol{\sigma}^{\mathrm{vis}} = \lambda\,\mathbf{I}\,\mathrm{tr}\,\dot{\boldsymbol{\varepsilon}} + 2\mu\,\dot{\boldsymbol{\varepsilon}}, \tag{5}$$

where $\dot{\boldsymbol{\varepsilon}}$ is the strain rate, **I** is the unit tensor, and λ, μ are viscosity coefficients. The values of λ, μ in the calculations were in the range between 0.002 and 0.02 kPa · s. These values provide convergence and, at the same time, do not strongly influence the solution.

3 Weak Form of the Equations

The unknown nodal variables in the finite-element formulation of the problem are the displacement components and the pore pressure. To obtain a weak form of the equations, we write the scalar product of (1) and a test function $\delta\mathbf{u}$ and integrate over

a domain Ω. After integrating by parts, we obtain

$$\int_{\Omega} \left[\boldsymbol{\sigma} : \operatorname{grad} \delta\mathbf{u} - p \operatorname{div} \delta\mathbf{u} + \varrho \left(-\mathbf{g} + \ddot{\mathbf{u}}\right) \cdot \delta\mathbf{u} \right] \mathrm{d}\Omega - \int_{\Gamma_t} \mathbf{t}^{\mathrm{tot}} \cdot \delta\mathbf{u} \, \mathrm{d}\Gamma = 0, \tag{6}$$

where Γ_t is the part of the boundary where the total traction $\mathbf{t}^{\mathrm{tot}}$ acting on the body is prescribed. On the rest of the boundary, the displacements are prescribed and $\delta\mathbf{u} = 0$.

Similarly, multiplying (4) by a test function δp and integrating over the domain Ω, then integrating by parts and using (2) to eliminate $\mathbf{w}$ in the volume integral, we arrive at

$$\int_{\Omega} \left[\left(\frac{n}{K_f} \dot{p} + \operatorname{div} \dot{\mathbf{u}} \right) \delta p + \frac{k}{g} \left(\frac{1}{\varrho_f} \operatorname{grad} p - \mathbf{g} + \ddot{\mathbf{u}} \right) \cdot \operatorname{grad} \delta p \right] \mathrm{d}\Omega$$
$$- \int_{\Gamma_q} q \, \delta p \, \mathrm{d}\Gamma = 0, \tag{7}$$

where Γ_q is the part of the boundary where the fluid flux $q = -\mathbf{w} \cdot \mathbf{n}$ is prescribed ($\mathbf{n}$ is the outer normal vector). On the rest of the boundary, the pore pressure is prescribed and $\delta p = 0$.

Equations (6), (7) were used to construct a user-defined finite element. The discrete form of the equations and the time integration scheme are described in Appendix.

4 Numerical Verification of the User Element

In order to verify the user-defined finite element, a spherically symmetric problem has been solved with two different numerical methods: with the finite-element method as a two-dimensional axisymmetric problem using the present user element and with the finite-difference method as a one-dimensional problem. The boundary of the computational domain consists of an inner and an outer spheres with radii of 15 cm and 5 m, respectively. The initial stress state is homogeneous and hydrostatic with a mean effective stress of -50 kPa and a pore pressure of 50 kPa. The problem is solved with an initial void ratio of 0.6 and a soil permeability of 10^{-3} m/s. The bulk modulus of the pore fluid, K_f, is taken to be 100 MPa. The inner boundary is impermeable with the prescribed radial displacement

$$u_r(t) = u_{\mathrm{amp}} \left[1 - \cos\left(2\pi f t\right)\right], \tag{8}$$

with $u_{\mathrm{amp}} = 0.1$ mm and $f = 34$ Hz. The outer boundary is impermeable with zero displacement. The size of the finite elements in the two-dimensional finite-element mesh varies from 1.2 cm near the inner boundary to 20 cm near the outer boundary. The time increment is equal to 10^{-4} s. Figure 1 shows the stress components obtained

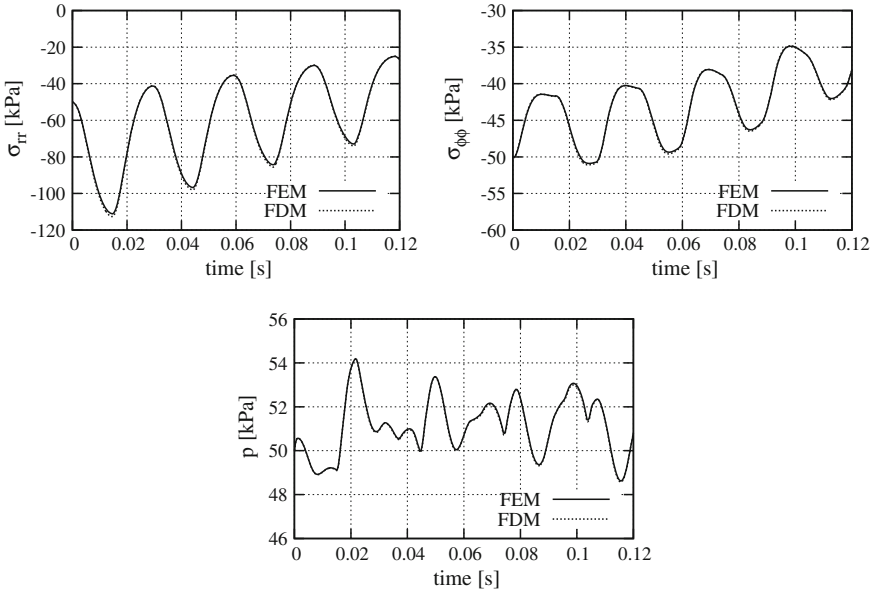

Fig. 1 Verification of the user element. The radial (σ_{rr}) and circumferential ($\sigma_{\phi\phi}$) effective stress components and the pore pressure (p) are shown as functions of time at a point with a radius of 20 cm. *FEM* the finite-element method with the user element, *FDM* the finite-difference method

with the two methods at a point located at a distance of 20 cm from the centre of the spheres. The two solutions coincide with good accuracy.

5 Boundary Value Problem

Consider a cylindrical closed-ended pile with a diameter of 0.3 m embedded in saturated soil as shown in Fig. 2. The initial stress state and the shape of the computational domain depend on whether the problem is solved with or without a mass force (gravity). In the problem without gravity, the initial effective stress is hydrostatic and homogeneous with a mean stress of −50 kPa. The pore pressure is also homogeneous and equal to 50 kPa. The outer boundary of the computational domain is a half-circle with a radius of 10 m and a centre near the pile toe. In the problem with gravity, both the initial effective stresses and the pore pressure satisfy static equilibrium and change linearly with depth, with the effective stresses being hydrostatic. The computational domain is rectangular with a depth of 15 m and a width of 10 m. The upper boundary corresponds to a free ground surface. The pile length (from the

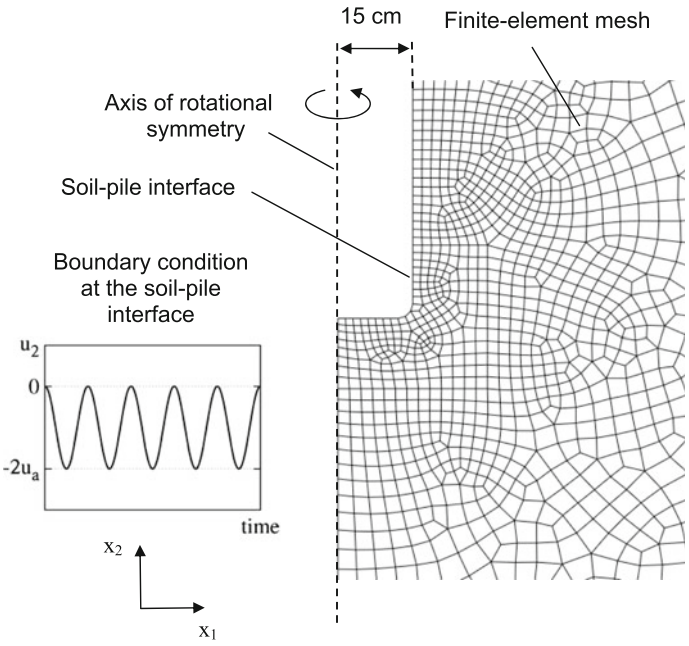

Fig. 2 Boundary conditions and finite-element mesh near the pile toe

toe to the free surface) is 5 m. This gives approximately the same value of the initial mean effective stress near the pile toe (−50 kPa) as in the case without gravity. The size of the finite elements in the mesh varies from 1.5 cm near the pile toe to about 35 cm near the outer boundary. The initial void ratio is in all cases homogeneous and equal to 0.6. The bulk modulus of the pore fluid is taken to be equal to that of pure water: $K_f = 2.2$ GPa.

The pile is assumed to vibrate in the vertical direction about a fixed position without penetration. The pile vibration is simulated by prescribing a time-harmonic vertical displacement with a given amplitude u_a and a frequency of 34 Hz as a boundary condition for the soil at the pile-soil interface, see Fig. 2. Furthermore, this boundary is taken to be impermeable. The outer boundary, except for the free surface in the case with gravity, is also impermeable and equipped with the dynamic infinite elements of Abaqus in order to minimize wave reflection from the boundary. The elastic parameters required for the infinite elements are calculated from the small-strain stiffness of a saturated hypoplastic solid with zero intergranular strain for given stresses and void ratio at the corresponding points of the boundary. The time increment is equal to 10^{-4} s and corresponds to 300 increments per cycle.

6 Numerical Results

As mentioned in Introduction, the objective of the present study is to investigate the influence of the soil permeability and the gravity force on the solutions as compared to those obtained in [2] with locally undrained conditions and without a mass force. We begin with the gravity-free case and solve the problem for a pile vibration amplitude of 2 mm with three values of permeability: $k = 0$, 10^{-4} and 10^{-3} m/s. Figures 3, 4 and 5 show the distributions of the mean effective stress near the pile toe after 5 and 20 cycles. The darkest area in figures is a low-stress zone (liquefaction zone) in which the mean effective stress lies between 0 and −1 kPa, i.e. does not exceed 2 % of the initial value (−50 kPa). Similar to the solutions with locally undrained conditions ($k = 0$) obtained in [2], the effective stress around the pile toe is reduced to a nearly zero level also in the case of nonzero permeability. Even a high value of permeability (10^{-3} m/s) does not prevent the formation of a liquefaction zone around the pile toe.

Although the distributions of the effective stress for different values of permeability are similar, it is reasonable to expect differences in the pore pressure evolution, namely that the increase in the pore pressure around the pile in the case of high soil permeability will be inhibited by the pore pressure dissipation. This conjecture is confirmed by the calculations. Consider a point in the low-stress zone beneath the pile toe (point P in Fig. 6 with $\theta = 5°$). Figure 7 shows the pore pressure and the mean total stress at this point as functions of time for the same problem as in Figs. 3, 4 and 5. In the locally undrained case, the pore pressure increases from 50 to 100 kPa within a short transient phase of 0.1 s and then oscillates about this level. Since the effective

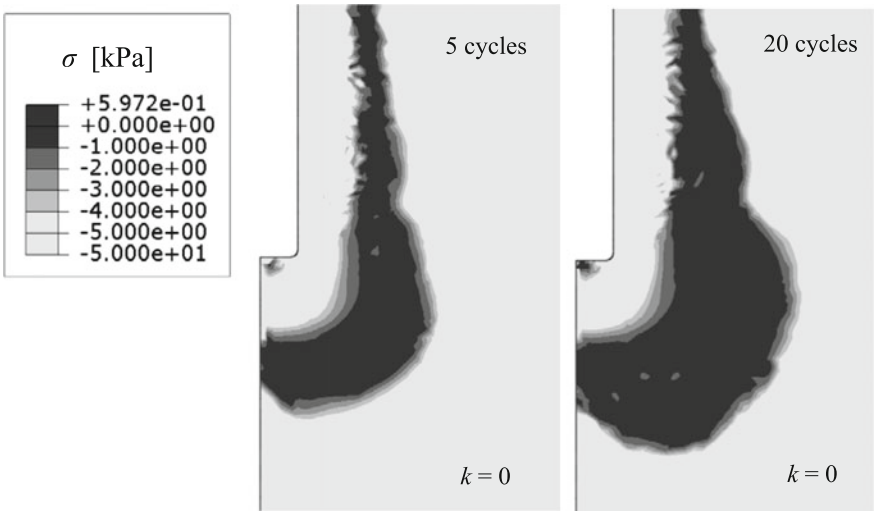

Fig. 3 Mean effective stress near the pile toe after 5 and 20 cycles. $k = 0$, $u_a = 2$ mm

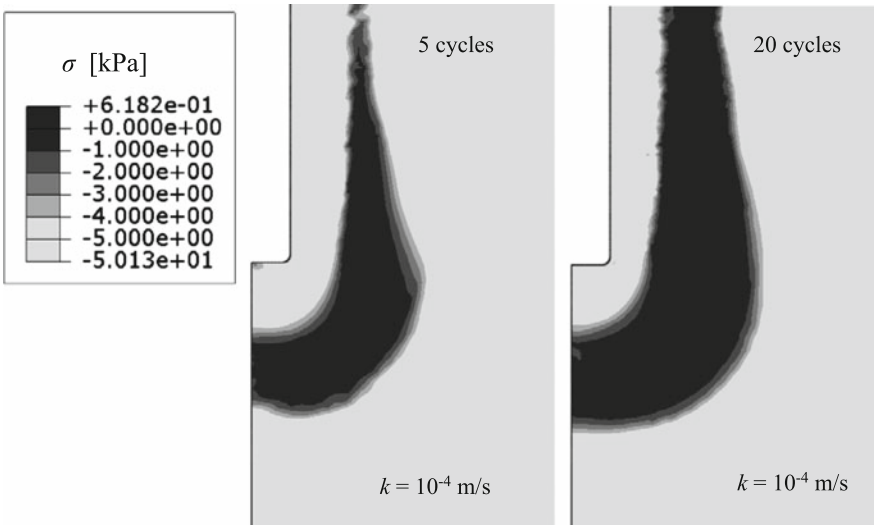

Fig. 4 The same as in Fig. 3 for $k = 10^{-4}$ m/s

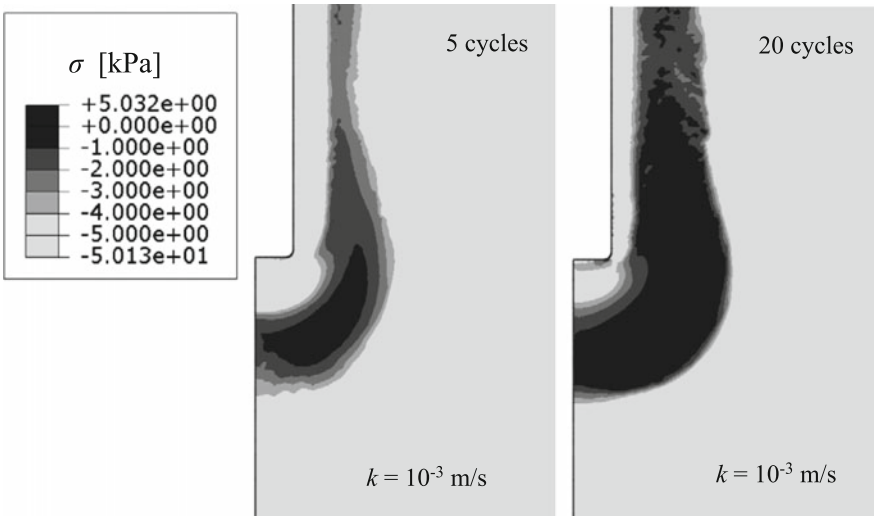

Fig. 5 The same as in Fig. 3 for $k = 10^{-3}$ m/s

stress is reduced to zero, the total stress oscillated about −100 kPa. The average total stress in the liquefaction zone thus remains at the same level as before the vibration. The situation changes in the case of high permeability. For $k = 10^{-3}$ m/s, the pore pressure does not increase as much as before and eventually oscillates about 55 kPa. The excess pore pressure amounts to only 5 kPa. Accordingly, the average total stress

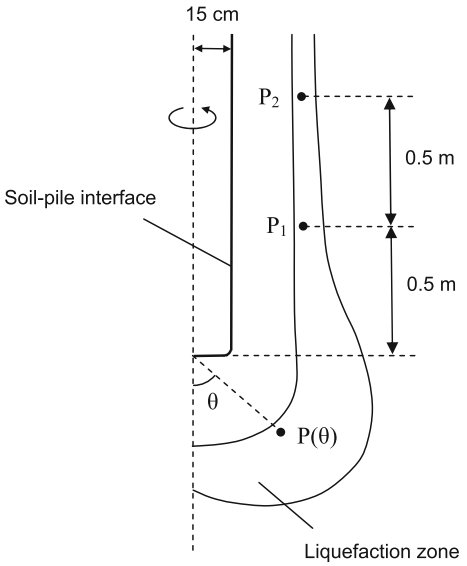

Fig. 6 Control points P(θ), P_1, P_2 in the liquefaction zone

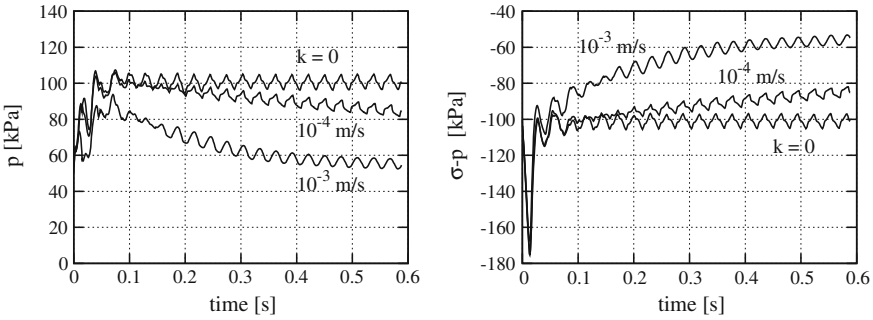

Fig. 7 Pore pressure (p) and mean total stress ($\sigma - p$) in the liquefaction zone beneath the pile toe as functions of time for different values of the soil permeability. $u_a = 2$ mm

is reduced to −55 kPa. Thus, the influence of the soil permeability on the solution is that it reduces the total stress level around the pile.

To estimate the stress amplitude around the pile, a number of control points in the liquefaction zone were introduced in [2] as shown in Fig. 6. Each point is characterized by an angle θ and a distance from the pile tip. Note that the distances are different for different pile displacement amplitudes u_a, see [2] for detail. Here we consider the same control points as in [2] and plot the amplitude of the mean total stress, σ_a, at these points as a function of θ for various values of permeability. Figure 8 shows the result. Generally, the stress amplitude decreases with increasing permeability. The influence of permeability is weak for a small pile displacement

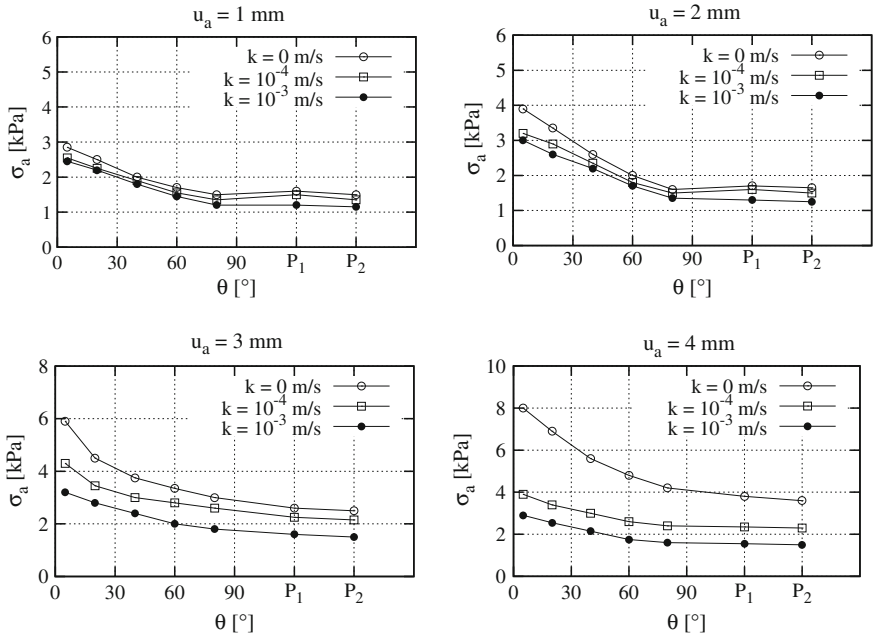

Fig. 8 Amplitude of the mean total stress, σ_a, at the control points in the liquefaction zone (Fig. 6) for different values of the soil permeability, k, and the pile displacement amplitude, u_a

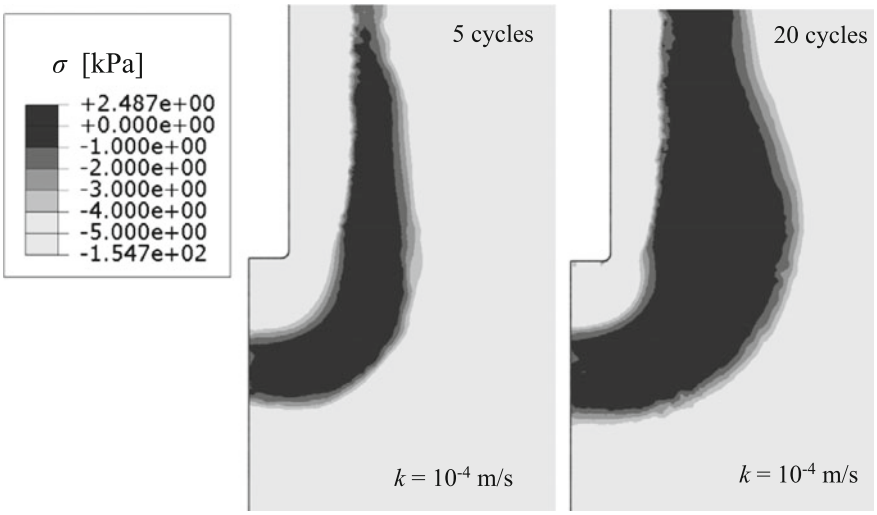

Fig. 9 Mean effective stress near the pile toe after 5 and 20 cycles in the problem with the gravity force. $k = 10^{-4}$ m/s, $u_a = 2$ mm

amplitude u_a and becomes stronger for larger values of u_a. The estimation of the stress amplitude in the liquefaction zone is needed for the solution of the high-cycle problem with the use of an explicit cyclic model, see [3, 4, 6].

The problem with gravity has been solved for a pile displacement amplitude of 2 mm and two values of permeability: 10^{-4} and 10^{-3} m/s. Figures 9 and 10 show the distributions of the mean effective stress after 5 and 20 cycles. A comparison of Figs. 9 and 10 with Figs. 3, 4 and 5 reveals that there is no significant difference in stress distribution between the solutions with and without gravity. Soil liquefaction near the pile toe occurs in the presence of the mass force as well. A difference is only observed in the stress amplitudes beneath the pile toe. A comparison of Fig. 11 with the corresponding plot in Fig. 8 shows that the total stress amplitude beneath the pile toe increases from about 3 to 5 kPa if gravity is taken into account.

Numerical solutions obtained in [2] with locally undrained conditions revealed the accumulation of permanent displacements in the form of rotation about a stationary centre located in the liquefaction zone (rotational drift). The condition for the

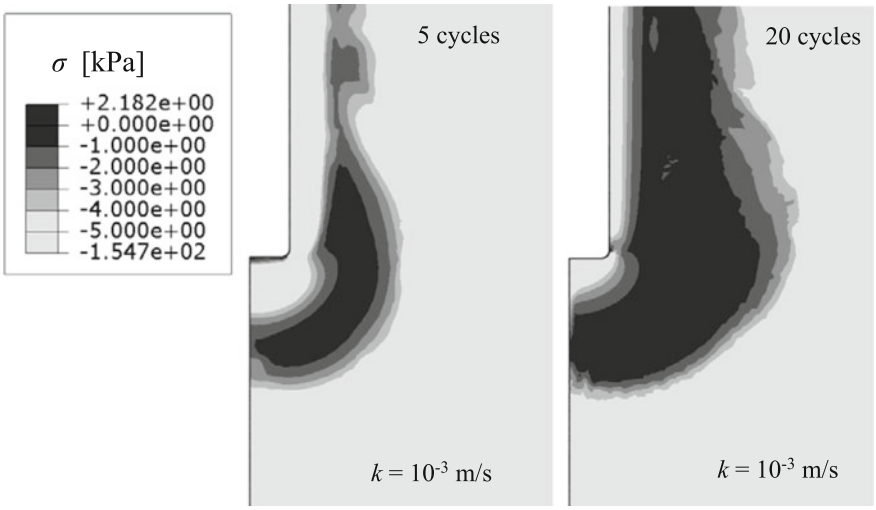

Fig. 10 The same as in Fig. 9 for $k = 10^{-3}$ m/s

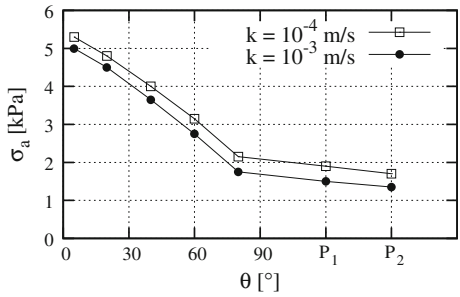

Fig. 11 Amplitude of the mean total stress, σ_a, at the control points in the problem with the gravity force. $u_a = 2$ mm

rotational drift to occur was found to be a sufficiently high frequency. Calculations made in the present study have shown that the rotational drift becomes weaker with increasing soil permeability and practically disappears at $k = 10^{-3}$ m/s. Therefore, a sufficiently low value of the soil permeability is also a condition for the rotational drift.

7 Conclusion

The problem of deformation of saturated soil in the vicinity of a vibrating pile toe investigated numerically in [2] with locally undrained conditions has been extended in the present study to the case of nonzero soil permeability. For this purpose, a user-defined element has been constructed within the finite-element program Abaqus to enable the dynamic analysis of a two-phase medium in the *u-p* approximation. In addition, the gravity force has been included in the analysis. The main result obtained in [2] is that the effective stress near the pile toe is reduced to zero after several cycles of vibration and the soil thus becomes liquefied. The present study has shown that this holds true for the problem with gravity and nonzero soil permeability (up to 10^{-3} m/s) as well. The difference is that, in the case of high permeability, a build-up of the pore pressure that accompanies the effective stress reduction is small because of the pore pressure dissipation, so that the total stresses are reduced as well as the effective stresses. Nonzero soil permeability also reduces the amplitude of the total stress oscillation near the pile toe to an extent that depends on the pile displacement amplitude.

Acknowledgments The study was financed by the Deutsche Forschungsgemeinschaft as part of the Research Unit FOR 1136 'Simulation of geotechnical construction processes with holistic consideration of the stress strain soil behaviour', Subproject 6 'Soil deformations close to retaining walls due to vibration excitations'. The authors are grateful to A. Niemunis for helpful discussions.

Appendix: Finite-Element Discretization and Time Integration

The unknown functions $\mathbf{u}$ and p are approximated with the help of shape functions N_I^u, N_J^p:

$$\mathbf{u} = N_I^u \mathbf{u}_I, \quad p = N_J^p p_J, \tag{9}$$

where $\mathbf{u}_I$ is the nodal displacement vector at node I, and p_J is the nodal value of the pore pressure at node J. The same shape functions are used for the test functions:

$$\delta\mathbf{u} = N_I^u \delta\mathbf{u}_I, \quad \delta p = N_J^p \delta p_J. \tag{10}$$

Substituting (9), (10) into (6), (7) yields a system which contains the nodal variables $\mathbf{u}_I$, p_J and their time derivatives:

$$\int_\Omega \left(\boldsymbol{\sigma} \cdot \operatorname{grad} N_I^u - \varrho N_I^u \mathbf{g}\right) \mathrm{d}\Omega - p_J \int_\Omega N_J^p \operatorname{grad} N_I^u \, \mathrm{d}\Omega$$
$$+ \ddot{\mathbf{u}}_K \int_\Omega \varrho N_I^u N_K^u \mathrm{d}\Omega - \int_{\Gamma_t} \mathbf{t}^{\mathrm{tot}} N_I^u \mathrm{d}\Gamma = 0, \tag{11}$$

$$\dot{p}_L \int_\Omega \frac{n}{K_f} N_L^p N_J^p \mathrm{d}\Omega + \dot{\mathbf{u}}_K \cdot \int_\Omega N_J^p \operatorname{grad} N_K^u \, \mathrm{d}\Omega$$
$$+ p_L \int_\Omega \frac{k}{g \varrho_f} \operatorname{grad} N_L^p \cdot \operatorname{grad} N_J^p \, \mathrm{d}\Omega - \int_\Omega \frac{k}{g} \mathbf{g} \cdot \operatorname{grad} N_J^p \, \mathrm{d}\Omega$$
$$+ \ddot{\mathbf{u}}_I \cdot \int_\Omega \frac{k}{g} N_I^u \operatorname{grad} N_J^p \, \mathrm{d}\Omega - \int_{\Gamma_q} q N_J^p \mathrm{d}\Gamma = 0. \tag{12}$$

Let U_t be a column vector of the nodal variables u_{Ii}, p_J at time t, and $\dot{U}_t$, $\ddot{U}_t$ be its time derivatives. With these vectors being known, Abaqus solves a system

$$F\left(U_{t+\Delta t}\right) = 0 \tag{13}$$

for $U_{t+\Delta t}$, where a column vector F is a (generally nonlinear) function of $U_{t+\Delta t}$ to be specified by the user. The function F also involves $\dot{U}_t$ and $\ddot{U}_t$. The solution proceeds iteratively. If $U_{t+\Delta t}^i$ is an ith approximation, the next approximation is

$$U_{t+\Delta t}^{i+1} = U_{t+\Delta t}^i + C^{i+1}, \tag{14}$$

where the correction term C^{i+1} is found from the linear system

$$A\left(U_{t+\Delta t}^i\right) C^{i+1} = -F\left(U_{t+\Delta t}^i\right) \tag{15}$$

with a matrix $A = \partial F / \partial U_{t+\Delta t}$. Equation (15) is obtained by expanding (13) in a Taylor series about $U_{t+\Delta t}^i$.

Now we show how the time integration of (11), (12) leads to (13). Equations (11), (12) can be written as

$$M\ddot{U} - G = 0, \tag{16}$$

with a constant mass matrix M and a vector G which depends on $\dot{U}$, U and the stress field $\boldsymbol{\sigma}$. Note that the elements of M which are multiplied by $\ddot{p}_J$ are equal to zero because Eqs. (11), (12) do not contain $\ddot{p}_J$. According to the Hilber–Hughes–Taylor integration scheme employed in Abaqus/Standard, (16) is written as

$$M\ddot{U}_{t+\Delta t} - (1+\alpha)G_{t+\Delta t} + \alpha G_t = 0, \tag{17}$$

where α is a parameter ($-1/3 \leq \alpha \leq 0$). The implicit time integration scheme for U is

$$U_{t+\Delta t} = U_t + \Delta t\, \dot{U}_t + \Delta t^2 \left[\left(\frac{1}{2} - \beta \right) \ddot{U}_t + \beta \ddot{U}_{t+\Delta t} \right], \tag{18}$$

$$\dot{U}_{t+\Delta t} = \dot{U}_t + \Delta t \left[(1-\gamma)\, \ddot{U}_t + \gamma \ddot{U}_{t+\Delta t} \right], \tag{19}$$

with parameters $\beta = (1-\alpha)^2/4$, $\gamma = 1/2 - \alpha$. With known U_t, $\dot{U}_t$, $\ddot{U}_t$, relations (18), (19) give $\dot{U}_{t+\Delta t}$ and $\ddot{U}_{t+\Delta t}$ as functions of $U_{t+\Delta t}$. These allows us to write $\ddot{U}_{t+\Delta t}$ and $G_{t+\Delta t}$ in (17) as functions of $U_{t+\Delta t}$. It remains to express $\boldsymbol{\sigma}_{t+\Delta t}$ in $G_{t+\Delta t}$ also as a function of $U_{t+\Delta t}$. We write

$$\boldsymbol{\sigma}_{t+\Delta t} = \boldsymbol{\sigma}_t + \Delta \boldsymbol{\sigma}, \tag{20}$$

where $\boldsymbol{\sigma}_t$ is known. The increment $\Delta\boldsymbol{\sigma}$ is obtained from the strain increment $\Delta\boldsymbol{\varepsilon}$ by the use of the constitutive model, whereas $\Delta\boldsymbol{\varepsilon}$ can be expressed through the derivatives of the shape functions and the difference $U_{t+\Delta t} - U_t$. This finally makes the left-hand side of (17) a function of $U_{t+\Delta t}$ and the known quantities U_t, $\dot{U}_t$, $\ddot{U}_t$, $\boldsymbol{\sigma}_t$. The differentiation of this function with respect to $U_{t+\Delta t}$ yields the matrix A.

The user-defined element is constructed with the help of the user subroutine `UEL`. The subroutine is called for each element and receives the nodal values $U^i_{t+\Delta t}$, $\dot{U}^i_{t+\Delta t}$, $\ddot{U}^i_{t+\Delta t}$ of the element as input. The subroutine uses the displacement increments contained in $U^i_{t+\Delta t} - U_t$ to compute the strain increment $\Delta\boldsymbol{\varepsilon}$ and calls the user subroutine `UMAT` to obtain the stress increment $\Delta\boldsymbol{\sigma}$ and the material Jacobian $\partial\Delta\boldsymbol{\sigma}/\partial\Delta\boldsymbol{\varepsilon}$. The latter is needed for the matrix A. The `UEL` calculates contributions of the element to the matrix A and the vector F and saves them in the arrays `AMATRX` and `RHS` as output. Abaqus collects contributions from all elements, forms global matrix A and vector F and finds a correction vector C^{i+1} by solving (15). The next approximation $U^{i+1}_{t+\Delta t}$ is given by (14), and $\dot{U}^{i+1}_{t+\Delta t}$, $\ddot{U}^{i+1}_{t+\Delta t}$ are calculated from (18), (19).

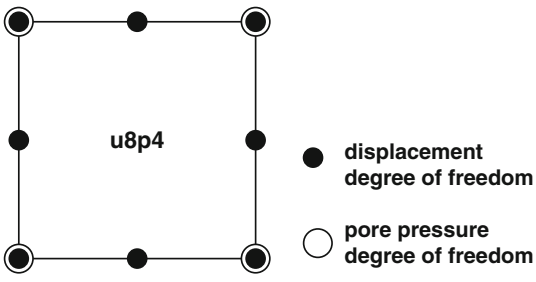

Fig. 12 User element

The user element shown in Fig. 12 is constructed as a two-dimensional quadrilateral u8p4 element for axisymmetric problems with a biquadratic interpolation of the displacements and a bilinear interpolation of the pore pressure.

References

1. Niemunis, A., Herle, I.: Hypoplastic model for cohesionless soils with elastic strain range. Mech. Cohesive-frict. Mater. **2**(4), 279–299 (1997)
2. Osinov, V.A., Chrisopoulos, S., Triantafyllidis, T.: Numerical study of the deformation of saturated soil in the vicinity of a vibrating pile. Acta Geotechnica **8**, 439–446 (2013)
3. Osinov, V.A.: Application of a high-cycle accumulation model to the analysis of soil liquefaction around a vibrating pile toe. Acta Geotech. **8**, 675–684 (2013)
4. Osinov, V.A.: Numerical modelling of the effective-stress evolution in saturated soil around a vibrating pile toe. In: Triantafyllidis, T. (ed.), Holistic Simulation of Geotechnical Installation Processes. Numerical and Physical Modelling, pp. 133–147. Springer International Publishing Switzerland (2015)
5. Osinov, V.A., Grandas-Tavera, C.: A numerical approach to the solution of dynamic boundary value problems for fluid-saturated solids. In: Triantafyllidis, T. (ed.), Holistic Simulation of Geotechnical Installation Processes. Numerical and Physical Modelling, pp. 149–162. Springer International Publishing Switzerland (2015)
6. Osinov, V.A., Chrisopoulos, S., Grandas-Tavera, C.: Vibration-induced stress changes in saturated soil: a high-cycle problem. In: This volume (2015)
7. Schümann, B., Grabe, J.: FE-based modelling of pile driving in saturated soils. In: De Roeck, G., Degrande, G., Lombaert, G., Müller, G. (eds.), Proceedings of the 8th International Conference on Structural Dynamics, EURODYN 2011, pp. 894–900 (2011)
8. Triantafyllidis, T.: Neue Erkenntnisse aus Messungen an tiefen Baugruben am Potsdamer Platz in Berlin. Bautechnik **75**(3), 133–154 (1998)
9. Ye, F., Goh, S.H., Lee, F.H.: Dual-phase coupled u-U analysis of wave propagation in saturated porous media using a commercial code. Comput. Geotech. **55**, 316–329 (2014)
10. Zienkiewicz, O.C., Chang, C.T., Bettess, P.: Drained, undrained, consolidating and dynamic behaviour assumptions in soils. Géotechnique **30**(4), 385–395 (1980)
11. Zienkiewicz, O.C., Chan, A.H.C., Pastor, M., Schrefler, B.A., Shiomi, T.: Computational Geomechanics with Special Reference to Earthquake Engineering. John Wiley, Chichester (1999)

Vibration-Induced Stress Changes in Saturated Soil: A High-Cycle Problem

V.A. Osinov, S. Chrisopoulos and C. Grandas-Tavera

Abstract Numerical modelling of the cyclic deformation of soil can be performed with the use of two types of constitutive models: incremental plasticity models and so-called explicit cyclic models. The present study deals with the application of a model of the second type—the high-cycle accumulation model for sand—to the analysis of vibration-induced stress changes in saturated soil. The application of the model requires the concurrent solution of two coupled boundary value problems: a dynamic problem for the determination of strain amplitude and a quasi-static problem for the calculation of stress evolution. The coupling of the two problems has been implemented in a two-dimensional axisymmetric formulation with the finite-element program Abaqus. The model is applied to the analysis of stress changes near a concrete wall caused by a vibrating pile. The numerical results show that a large-amplitude vibration, e.g. during the installation of vibratory driven piles, may substantially reduce both the effective and the total stresses in front of the wall. The effective stress may be reduced to zero resulting in soil liquefaction.

Keywords Cyclic deformation · Saturated soil · Vibratory pile driving

1 Introduction

Soil is a plastic material which does not generally return to the same stress state when subjected to a closed deformation cycle. Similarly, a closed stress cycle results in a residual deformation. Permanent changes in stress or deformation may play a role even for small strain amplitudes of the order of 10^{-5} if they accumulate over a large number of cycles.

The numerical study of the cyclic deformation of soil can be based on two types of constitutive models: incremental plasticity models and so-called explicit cyclic

V.A. Osinov (✉) · S. Chrisopoulos · C. Grandas-Tavera
Institute of Soil Mechanics and Rock Mechanics, Karlsruhe Institute of Technology, Karlsruhe, Germany

T. Triantafyllidis (ed.), *Holistic Simulation of Geotechnical Installation Processes*, Lecture Notes in Applied and Computational Mechanics 80, DOI 10.1007/978-3-319-23159-4_4

models. The choice of the model type is dictated by the strain amplitude and the number of cycles. Although the incremental models can, in principle, describe the soil behaviour for any amplitude, the use of such models for small strain amplitudes (below 10^{-3}) and large numbers of cycles may be problematic. First of all, it may be difficult or impossible to calibrate an incremental model with respect to the weak accumulation effects (the accumulation of residual stresses or deformations) for small strain amplitudes and, at the same time, to preserve the correct behaviour for large amplitudes. This concerns the complicated dependence of the accumulation on the strain amplitude, the relative soil density, the current stress state and the cyclic deformation history. Besides the calibration problems, there may be purely numerical difficulties in using an incremental model for very small amplitudes when the residual change in stress or deformation in one cycle becomes comparable with the numerical error resulting from the incremental integration of the cycle. In this case, the computation of permanent changes will lead to erroneous results even if the model itself is correct. It is also important to mention that the incremental models entail high computational costs because of the necessity to integrate each cycle incrementally.

The present paper deals with the application of a model of the other type—the high-cycle accumulation model for granular soils developed in [2, 7]. The model belongs to the class of explicit cyclic models and considers the stresses and deformations as explicit functions of the number of cycles (this explains the name 'explicit models'). The number of cycles is treated as a real number. The stresses and density, understood as quantities averaged over a cycle, undergo gradual changes due to small-amplitude cyclic deformation. The model is constructed in such a way that the constitutive parameters control directly the dependence of the accumulation effects on the strain amplitude, the void ratio, the stress state and the cyclic deformation history. Owing to this structure, the model is able to describe correctly the accumulation effects, and because of its explicit type, it allows us to calculate a large number of cycles within a relatively short computing time. The model has been thoroughly verified and calibrated by a large number of cyclic element tests on various sands [10–12, 14, 15] and used for the finite-element simulation of the permanent displacements of foundations subjected to quasi-static high-cycle loading [8, 9, 13].

Recently, the cyclic model [2, 7] was applied to saturated soil under dynamic loading to analyse effective-stress changes produced by a vibrating pile during vibratory pile driving [4, 5]. To gain a first insight into the stress evolution, the boundary value problem for the vicinity of a pile toe was solved in a simplified spherically symmetric formulation. The approach proposed in [4, 5] is extended in the present study to two-dimensional axisymmetric problems and implemented numerically with the finite-element program Abaqus. The objective of the study is to estimate the influence of a vertically vibrating pile on the stress state in the soil near a retaining wall. The consideration of the pile-wall problem is motivated by the results of measurements made in an instrumented excavation pit during successive construction stages reported in [6]. The measurements showed that the installation of vibratory driven piles in the saturated soil at the base of the pit produced significant displacements of the retaining wall. These displacements may be brought about by vibration-induced

changes in the stress state of the soil and, specifically, by a reduction in the effective pressure. This explanation is suggested by the results of numerical simulations of the stress evolution around a vibrating pile. The simulations reveal a reduction in the effective pressure to a nearly zero value around a vibrating pile in a large-amplitude low-cycle problem [1, 3] and the subsequent growth of the low-stress zone in a high-cycle problem [4, 5].

2 High-Cycle Accumulation Model

The high-cycle accumulation model developed in [2, 7] is aimed at describing the rate-independent behaviour of granular soils subjected to small-amplitude cyclic deformation with a large number of cycles (up to hundreds of thousands). The stresses and strains in a soil element within one cycle of deformation are considered as the sum of an average value and a varying part. A quantity averaged over a cycle can thus be viewed as a function of the number of cycles. Treating the number of cycles N as a real number allows us to introduce the rates $\mathrm{d}(\,)/\mathrm{d}N$ and to write a constitutive equation for the average stress tensor in rate form in which the number of cycles plays the role of time. If the soil is deformed with a constant frequency, the rate $\mathrm{d}(\,)/\mathrm{d}N$ and the time derivative $\mathrm{d}(\,)/\mathrm{d}t$ are connected by the relation

$$\frac{\mathrm{d}(\,)}{\mathrm{d}t} = \frac{\omega}{2\pi}\frac{\mathrm{d}(\,)}{\mathrm{d}N}, \tag{1}$$

where ω is angular frequency.

The use of the cyclic model requires the knowledge of a scalar strain amplitude $\varepsilon^{\mathrm{amp}}(\mathbf{x}, t)$ in the soil as a function of space and time. For time-harmonic deformation, the scalar strain amplitude is defined as

$$\varepsilon^{\mathrm{amp}} = \sqrt{\varepsilon_{ij}^{\mathrm{amp}}\varepsilon_{ij}^{\mathrm{amp}}}, \tag{2}$$

where $\varepsilon_{ij}^{\mathrm{amp}}$ are the amplitudes of the strain components in a rectangular coordinate system [2, 7]. Note that the amplitudes $\varepsilon_{ij}^{\mathrm{amp}}$ are not components of a tensor, except for the case where there are no phase shifts between the components $\varepsilon_{ij}(t)$. Nevertheless, it can be shown that definition (2) is objective in the sense that $\varepsilon^{\mathrm{amp}}$ is invariant to the change of the coordinate system. If the cyclic model is used for the solution of a boundary value problem, the strain amplitude in the soil as a function of space and time is not known in advance. Finding $\varepsilon^{\mathrm{amp}}(\mathbf{x}, t)$ in this case constitutes a separate boundary value problem which is independent of the cyclic model and has to be solved each time when the strain amplitude is expected to change. This boundary value problem may be solved with any appropriate constitutive model in dynamic or quasi-static formulation depending of the loading rate in the problem under study.

Table 1 Constitutive parameters of the cyclic model

C_{amp}	$\varepsilon_{\text{ref}}^{\text{amp}}$	C_{N1}	C_{N2}	C_{N3}	C_e	e_{ref}	C_p	p_{ref} (kPa)	φ_c (°)
1.6	10^{-4}	3.6×10^{-3}	0.016	1.05×10^{-4}	0.48	0.829	0.44	100	32

Sand L12 from [12]

The cyclic model establishes a relation between the strain amplitude ε^{amp} and the rate $\mathrm{d}\boldsymbol{\varepsilon}^{\text{acc}}/\mathrm{d}N$, where the tensor $\boldsymbol{\varepsilon}^{\text{acc}}$ is the accumulated strain of dry soil deformed in such a way that the average stress tensor is kept constant. The relation is written as

$$\frac{\mathrm{d}\boldsymbol{\varepsilon}^{\text{acc}}}{\mathrm{d}N} = f_{\text{amp}} f'_N f_e f_p f_Y f_\pi \mathbf{m}, \tag{3}$$

where the tensor $\mathbf{m}$ and the scalar factors f_{amp}, f'_N, f_e, f_p, f_Y, f_π describe the dependence of the strain accumulation rate on the strain amplitude ε^{amp}, the average void ratio e and the average stress tensor $\boldsymbol{\sigma}$ (the factor f_π is not used in this study). The cyclic deformation history is taken into account through a state variable g^A which enters (3) and is to be found from the solution of a differential equation as a function of the number of cycles. For detailed discussion of (3) and calibration, see [2, 7, 10, 15]. Parameters of (3) used in the present study are given in Table 1.

Taking (1) into account and writing a dot for the time derivative, (3) can be represented as

$$\dot{\boldsymbol{\varepsilon}}^{\text{acc}} = \dot{\boldsymbol{\varepsilon}}^{\text{acc}}(\varepsilon^{\text{amp}}, e, \boldsymbol{\sigma}, g^A). \tag{4}$$

A constitutive equation for the average stress tensor $\boldsymbol{\sigma}$ is written in the form

$$\dot{\boldsymbol{\sigma}} = \mathsf{E}(\sigma) : (\dot{\boldsymbol{\varepsilon}} - \dot{\boldsymbol{\varepsilon}}^{\text{acc}}) \tag{5}$$

with an elastic stiffness tensor E, where $\boldsymbol{\varepsilon}$ is the average strain tensor [2, 7]. In the case of saturated soil, $\boldsymbol{\sigma}$ denotes the effective stress tensor. In order to better reproduce the stiffness of granular soil, the tensor E is made a function of the mean stress $\sigma = \operatorname{tr}\boldsymbol{\sigma}/3$. Equation (5) has been calibrated by the comparison of the results of drained and undrained cyclic tests [11, 14]. The tensor E is taken as in an isotropic elastic solid with a Poisson ratio of 0.2 and a pressure-dependent bulk modulus

$$K(\sigma) = A\, p_{\text{atm}}^{1-n}\, (-\sigma)^n, \tag{6}$$

where A, p_{atm} and n are parameters.

The use of elasticity equation (5) can lead to unlimited principal-stress ratios and is justified only if the stress states do not deviate far from the hydrostatic axis. Otherwise, it may be necessary to correct the stress rate given by (5). In this study, the correction is made by projecting the stress state on a given bounding surface in the stress space if the stress state falls outside the surface. The bounding surface is defined by the Matsuoka–Nakai yield condition with a given friction angle. For the

numerical calculations, this angle is taken to be equal to the angle φ_c of the cyclic model, see Table 1. The projection is made in the direction to the hydrostatic axis in such a way that the mean stress does not change. Equation (5) then takes the form

$$\dot{\boldsymbol{\sigma}} = \mathsf{E}(\sigma) : (\dot{\boldsymbol{\varepsilon}} - \dot{\boldsymbol{\varepsilon}}^{\mathrm{acc}}) + \dot{\boldsymbol{\sigma}}^{\mathrm{cor}} \tag{7}$$

with a correction term $\dot{\boldsymbol{\sigma}}^{\mathrm{cor}}$. This modification can also be viewed as an additional plastic strain rate introduced into (5) as proposed in [2, 7].

The use of Eqs. (5), (6) for the solution of boundary value problems requires a further correction to these equations if the mean stress σ approaches zero. This may happen in saturated soil under cyclic deformation if volumetric changes are inhibited by the low soil permeability. Apart from cyclic deformation, the mean effective stress in saturated soil may vanish because of the expansion of the skeleton caused by the pore water flow. In both cases, Eqs. (5), (6) written for the mean effective stress reduce to the equation

$$\dot{\sigma} = K(\sigma)\dot{\varepsilon}_v \tag{8}$$

with a volumetric strain rate $\dot{\varepsilon}_v = \mathrm{tr}(\dot{\boldsymbol{\varepsilon}} - \dot{\boldsymbol{\varepsilon}}^{\mathrm{acc}}) > 0$. Integration of (8) shows that the evolution of σ as a function of ε_v depends on the parameter n in (6). If $0 < n < 1$, which is the case for granular soils, σ reaches zero at a finite ε_v. If $n \geq 1$, σ approaches zero asymptotically as $\varepsilon_v \to +\infty$. Zero σ and, as a consequence, zero skeleton stiffness E make a boundary value problem ill-posed in both quasi-static and dynamic cases (except for certain one-dimensional problems for saturated soils). This fact does not allow us to use Eqs. (5), (6) directly for problems where the effective stress vanishes. In order to avoid zero effective stress, we modify (6) and write it as

$$K(\sigma) = A\, p_{\mathrm{atm}}^{1-n}\, (-\sigma)^n \left[1 - \exp\left(-\frac{\sigma}{\sigma_\zeta}\right)\right]^{\zeta - n} \tag{9}$$

with a parameter $\zeta > 1$ and a reference stress $\sigma_\zeta < 0$. For $\sigma/\sigma_\zeta \gg 1$, (9) turns into (6). For $\sigma \to 0$, $K(\sigma) \sim (-\sigma)^\zeta$ and, because $\zeta > 1$, σapproaches zero asymptotically as ε_v increases. The parameters of Eq. (9) used in the numerical calculations are given in Table 2. The function $\sigma(\varepsilon_v)$ with $\sigma(0) = -10$ kPa obtained with (6) and (9) is shown in Fig. 1.

Table 2 Parameters of Eq. (9)

A	n	p_{atm}(kPa)	ζ	σ_ζ(kPa)
467	0.46	100	2	−1

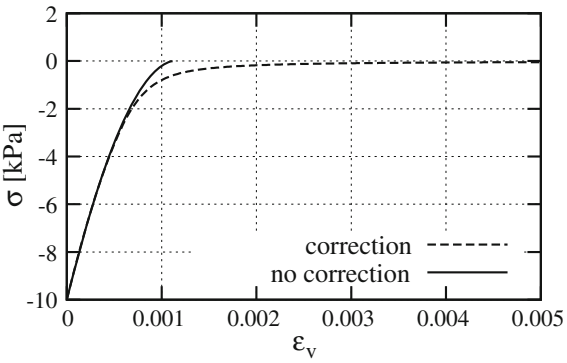

Fig. 1 Mean stress as a function of the volumetric deformation calculated with (6) (*no correction*) and with the modified Eq. (9) (*correction*). $\zeta = 2$, $\sigma_\zeta = -1$ kPa

3 Boundary Value Problem

Cyclic models of the explicit type are based on the concept of gradually changing average stress and deformation. Since this concept is inapplicable to large-amplitude loading, the high-cycle model is valid only for small strain amplitudes (below 10^{-3}) and cannot be used for the immediate vicinity of a vibrating pile where cyclic deformations are large. This inevitable drawback does not allow us to formulate directly a boundary value problem for the modelling of vibratory pile driving. To overcome these limitations, it is proposed in [4, 5] to introduce an auxiliary surface (boundary) in the soil around the pile in such a way that the strain amplitudes outside the enclosed region are small enough for the cyclic model to be applicable. The computational domain of the boundary value problem is then bounded by the auxiliary surface and a remote boundary.

The main difficulty in the formulation of the problem is the specification of boundary conditions at the auxiliary boundary. These conditions are not known from the physical problem under study, e.g. from the pile vibration amplitude, and their determination constitutes a separate problem. In the numerical study in [4, 5], the location of the auxiliary boundary and the corresponding boundary conditions are inferred from the solution of a low-cycle problem, i.e. a dynamic boundary value problem for a vibrating pile solved with an incremental plasticity model for a small number (a few tens) of cycles. This solution also provides an initial stress state for the high-cycle problem. The auxiliary boundary may be introduced in a zone of small (nearly zero) effective stress that is formed in the soil around the pile toe after several cycles of vibration. As the low-cycle solutions show, the varying part of the total stress in this zone is nearly hydrostatic. This suggests a simple boundary condition for the high-cycle problem as a given pressure amplitude.

To illustrate this idea, consider the low-cycle problem for a cylindrical closed-ended pile situated in saturated soil with a homogeneous initial stress state. Assume the pile starts to vibrate in the vertical direction with a constant displacement amplitude. Numerical simulations reveal that the effective stresses near the pile are rapidly reduced within the first several cycles of vibration resulting in the formation of a zone

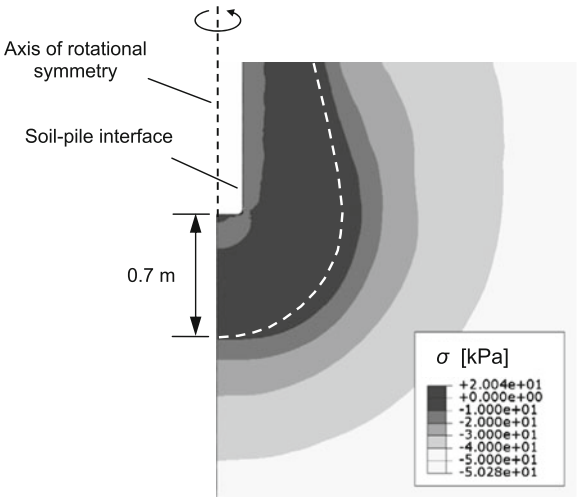

Fig. 2 Mean effective stress in saturated dense sand around a cylindrical pile after 20 cycles of vibration calculated with a hypoplasticity model with a pile diameter of 0.3 m, a pile displacement amplitude of 2 mm, a vibration frequency of 34 Hz, a hydrostatic initial effective stress of −50 kPa, a soil permeability of 10^{-4} m/s and a pore water bulk modulus of 2.2 GPa

with nearly zero effective stresses. Figure 2 shows the mean effective stress around the pile toe after 20 cycles of vibration calculated with a hypoplasticity model as described in [1]. The mean effective stress in the darkest area in Fig. 2 is between 0 and −10 kPa, with the initial value being equal to −50 kPa. Note that increasing the soil permeability does not prevent the effective-stress reduction, see examples in [1]. The dashed line in Fig. 2 shows the possible location of an auxiliary boundary for the high-cycle problem in the general three-dimensional case when considering a vibrating pile near a retaining wall.

For the two-dimensional axisymmetric formulation adopted in the present paper, the auxiliary boundary is taken as a spherical surface with a radius which corresponds to the lower part of the surface shown in Fig. 2. For a pile diameter of 0.3 m, the radius of the sphere is taken to be 0.7 m. The spherical auxiliary boundary allows the pile-wall problem to be considered in an approximate manner as shown in Fig. 3, with a concrete wall being placed at a distance L from the centre of the sphere. The computational domain is bounded by a remote boundary.

Given initial distributions of the effective stresses, pore pressure and void ratio, assume that a cyclic pressure with a constant amplitude acts on the auxiliary boundary. This cyclic load together with the pore pressure dissipation due to local drainage produce the gradual change in the effective stress $\boldsymbol{\sigma}(\mathbf{x}, t)$, pore pressure $p_f(\mathbf{x}, t)$ and void ratio $e(\mathbf{x}, t)$ considered as average values in the sense of the cyclic model. The numerical simulation of this process with the cyclic model consists in the concurrent solution of two coupled boundary value problems.

The calculation for a time step between t and $t + \Delta t$ begins with the determination of the strain amplitude field $\varepsilon^{\mathrm{amp}}(\mathbf{x}, t)$ required for the cyclic model. The strain amplitude field is found from the *first* boundary value problem formulated as a steady-state dynamic problem for an elastic medium with spatially inhomogeneous stiffness for time-harmonic displacements and stresses with complex amplitudes $\mathbf{u}^0$

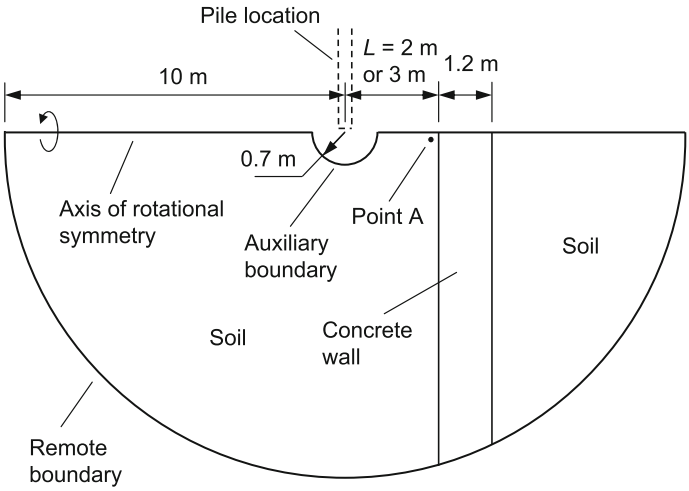

Fig. 3 Computational domain for the high-cycle boundary value problem

and $\boldsymbol{\sigma}^0$, respectively. The amplitudes must satisfy the equation of motion

$$\operatorname{div} \boldsymbol{\sigma}^0 = -\omega^2 \varrho \mathbf{u}^0 \tag{10}$$

and the constitutive equation

$$\boldsymbol{\sigma}^0 = \mathsf{C}(\sigma) : \boldsymbol{\varepsilon}^0, \tag{11}$$

where $\boldsymbol{\varepsilon}^0$ is the complex strain amplitude, ω is the angular frequency, and ϱ is the soil density. The strain amplitude $\varepsilon^{\mathrm{amp}}$ for the cyclic model is given by (2) with $\varepsilon_{ij}^{\mathrm{amp}} = |\varepsilon_{ij}^0|$.

The stiffness tensor C in (11) is assumed to be a function of the current mean effective stress $\sigma(\mathbf{x}, t) = \operatorname{tr} \boldsymbol{\sigma}(\mathbf{x}, t)/3$ and correspond to an isotropic elastic medium with the Lamé constants

$$\lambda = \lambda_0 \left(\frac{\sigma + \sigma^*}{\sigma_0} \right)^m + \frac{K_f}{n}, \quad \mu = \mu_0 \left(\frac{\sigma + \sigma^*}{\sigma_0} \right)^m, \tag{12}$$

where K_f is the bulk modulus of the pore water, n is the porosity of the skeleton, and σ^*, λ_0, μ_0, σ_0, m are parameters. A small stress σ^* is added to σ in (12) in order to avoid zero shear stiffness at zero effective stress and thus to avoid ill-posedness of the boundary value problem. Although the mean effective stress does not reach zero due to the correction term in (9) and the problem is therefore always well-posed, too small shear stiffness, as compared with the compression modulus ($\mu \ll K_f$), can cause numerical instability. Besides a constant-amplitude pressure acting on the auxiliary boundary, non-reflecting boundary conditions available in Abaqus are

Table 3 Parameters of the steady-state problem

σ^* (kPa)	λ_0 (MPa)	μ_0 (MPa)	σ_0 (kPa)	m	K_f (GPa)	$\omega/2\pi$ (Hz)	ϱ (kg/m^3)	E (GPa)	ν	ϱ_c (kg/m^3)
−2	120	80	−100	0.6	2.2	34	2021	40	0.2	2400

prescribed at the remote boundary. Parameters of the steady-state problem are given in Table 3 including the Young modulus E, the Poisson ratio ν and the density ϱ_c of the concrete wall.

The strain amplitude field obtained from the first boundary value problem determines the tensorial strain accumulation rate $\dot{\boldsymbol{\varepsilon}}^{\mathrm{acc}}(\mathbf{x}, t)$ according to (3), (4). With this rate assumed to be constant within the time increment Δt, changes in the effective stress $\boldsymbol{\sigma}(\mathbf{x}, t)$, pore pressure $p_f(\mathbf{x}, t)$ and void ratio $e(\mathbf{x}, t)$ are found from the *second* boundary value problem formulated as a quasi-static deformation problem for a fluid-saturated porous solid with the additional external term $\dot{\boldsymbol{\varepsilon}}^{\mathrm{acc}}$ in the constitutive equation (5). The system of equations for this problem consists of the constitutive equation (5), the total-stress equilibrium

$$\operatorname{div} \boldsymbol{\sigma} - \operatorname{grad} p_f = 0 \tag{13}$$

($p_f > 0$ for compression), the pore pressure equilibrium (Darcy's law)

$$\operatorname{grad} p_f + \frac{1}{k} \varrho_f g n (\mathbf{v}_f - \mathbf{v}_s) = 0 \tag{14}$$

and the mass conservation with incompressible solid and fluid phases

$$\operatorname{div} \left[(1 - n)\, \mathbf{v}_s + n \mathbf{v}_f \right] = 0, \tag{15}$$

where $\mathbf{v}_s, \mathbf{v}_f$ are the velocities of the solid and fluid phases, respectively, k is the soil permeability (m/s), and g is the acceleration due to gravity. Boundary conditions at the auxiliary boundary are impermeability and zero displacements. The remote boundary is equipped with the infinite elements of Abaqus in combination with a constant pore pressure. The time step is completed by the calculation of changes in the state variable g^A, see (4).

4 Numerical Implementation with Abaqus

The boundary value problem described above is solved with the finite-element program Abaqus/Standard. The solution procedure is implemented as two Abaqus jobs running concurrently. The first job consists of a number of steady-state problems (the first boundary value problem in Sect. 3). The solution of each steady-state prob-

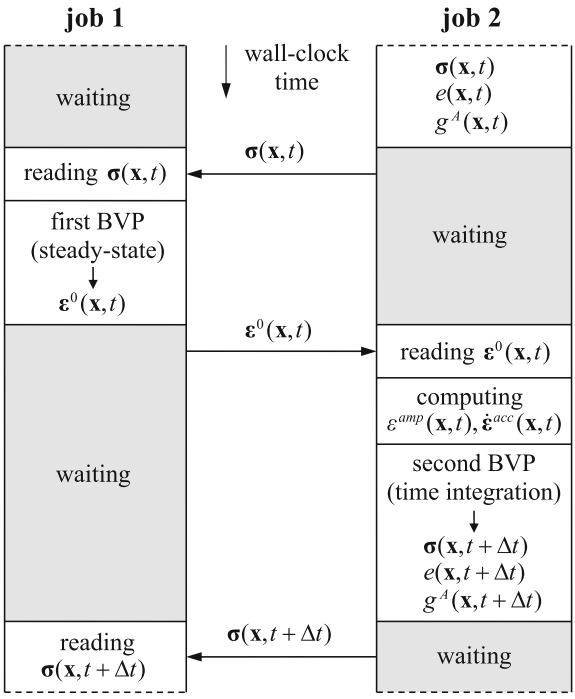

Fig. 4 Two parallel Abaqus jobs for the solution of the two coupled boundary value problems (BVP)

lem is initiated by the second job—a porous-medium deformation analysis with a user-defined material (the second boundary value problem in Sect. 3). Both boundary value problems have the same mesh but different element types: the first problem has ordinary solid elements, while the second one has elements for the porous-medium analysis with pore pressure as an additional degree of freedom. The two jobs have separate input files and user subroutines.

The key requirement of the solution algorithm is the possibility of interrupting the calculation, waiting, reading results of the other job and continuing the calculation. This possibility is provided in Abaqus through the user subroutine `UEXTERNALDB`, which allows the user to introduce waiting and reading phases. The solution scheme is shown in Fig. 4. During a reading phase, results of the other job are read from the Abaqus result file (`*.fil`) and saved in a global Fortran module accessible to the user subroutines. In particular, the first job reads the current effective stress field $\boldsymbol{\sigma}(\mathbf{x}, t)$ calculated in the second job, solves the steady-state problem, saves the strain amplitude field $\boldsymbol{\varepsilon}^0(\mathbf{x}, t)$ and waits for the next initiation. The second job reads $\boldsymbol{\varepsilon}^0(\mathbf{x}, t)$ calculated in the first job, computes $\dot{\boldsymbol{\varepsilon}}^{\mathrm{acc}}(\mathbf{x}, t)$, solves the second boundary value problem for a time increment Δt, saves the new field $\boldsymbol{\sigma}(x, t + \Delta t)$ and initiates the solution of the steady-state problem for time $t + \Delta t$. The constitutive equations of the two boundary value problems are implemented in the user subroutines `UMAT`.

The time increment Δt varies during the calculation. Abaqus controls force equilibrium and, if necessary, reduces or increases the current time increment. At the

same time, the user sets maximum allowable values for the time increment and for the change in the mean effective stress in one increment. If the change exceeds the allowable value, the time increment is reduced. This is achieved through the Abaqus variable `pnewdt` in the `UMAT` subroutine of the second job.

5 Numerical Results

The objective of the numerical analysis presented below is to evaluate changes in the stress state in the soil near a concrete wall caused by the vibration of a pile located at a short distance L from the wall. Two cases with $L = 2$ and 3 m are considered, see Fig. 3. The thickness of the wall is 1.2 m. The pile vibrates with a frequency of 34 Hz. A spherical auxiliary boundary with a radius of 0.7 m is introduced around the pile toe. As mentioned in Sect. 3, boundary conditions at the auxiliary boundary cannot be obtained immediately from given pile vibration parameters such as the displacement or force amplitude. They can only be estimated numerically from the solution of a boundary value problem with an incremental plasticity model. Solutions obtained with a hypoplasticity model can be found in [1, 3]. In the present study, a constant pressure amplitude σ_a (for the total stress) in the range from 3 to 6 kPa is prescribed at the auxiliary boundary. In the numerical simulations in [1, 3], this range approximately corresponds to pile vibration amplitudes from 2 to 4 mm.

The initial state of the soil prior to the pile vibration is assumed to be homogeneous with a hydrostatic effective stress of -50 kPa and a pore pressure of 50 kPa. As discussed above, a homogeneous initial stress state changes significantly at the very beginning of the vibration. It is therefore reasonable to take an initial state for the high-cycle problem similar to that shown in Fig. 2, i.e. with reduced effective stresses near the auxiliary boundary. The initial effective stress for the high-cycle problem is taken to be hydrostatic with the spatial distribution shown in Fig. 5. To satisfy static equilibrium for the total stress, the initial pore pressure distribution is prescribed in such a way that the total stress is homogeneous and equal to -100 kPa.

The initial void ratio is taken to be homogeneous and equal to 0.616. For the sand considered (Table 1), this void ratio corresponds to a relative soil density of 0.6. The calculations are made for two values of the soil permeability: $k = 10^{-4}$ and 10^{-3} m/s.

The size of the finite elements in the mesh varies from 2 cm near the inner boundary to 40 cm near the remote boundary. Quadrilateral bilinear elements with full and reduced integration and biquadratic elements with full integration were used for the calculations. Biquadratic elements perform better in most cases but produce a larger data file (`*.fil`) that has to be saved on a hard disc for exchange purposes during calculations as described in Sect. 4. The maximum allowable values for the time increment and for the change in the mean effective stress in one time increment were, respectively, 0.05 s and 0.05 kPa.

Figure 6 shows the effective stress distribution after 22 s of vibration for $\sigma_a = 5$ kPa, $k = 10^{-4}$ m/s and $L = 2$ m. As seen in the figure, the cyclic loading of the

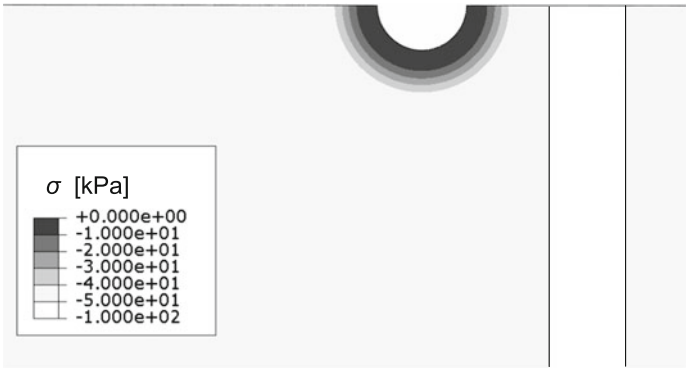

Fig. 5 Initial mean effective stress in the high-cycle problem

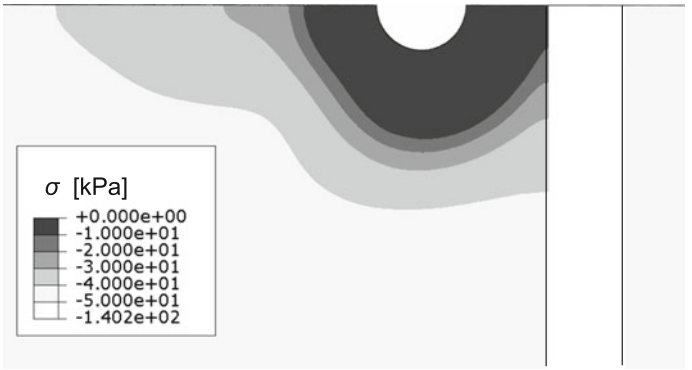

Fig. 6 Mean effective stress at time $t = 22$ s. $\sigma_a = 5$ kPa, $k = 10^{-4}$ m/s, $L = 2$ m

soil leads to the growth of the initial low-stress zone. In particular, the effective stress near the wall is reduced in absolute value from 50 to 10 kPa.

In what follows we will be interested in the evolution of the stress state in front of the wall (Point A in Fig. 3) in comparison with the stress state behind the wall. Figure 7 shows the evolution of the mean effective stress at Point A during 300 s of vibration for different loading amplitudes σ_a, two values of the permeability and two distances between the wall and the pile. A rapid change of a few kilopascals during the first few seconds, which all curves have in common, is of no importance but should be explained. Any change in the effective stress is governed by two processes: the cyclic deformation and the pore water flow due to pore pressure gradients. Cyclic deformation under locally undrained conditions leads to the reduction of the effective stress. Nonzero permeability allows local drainage and thus reduces the gradients of both pore pressure and effective stress. This can reduce the effective stress in one place and increase in another. Since the initial pore pressure distribution has in our case sufficiently high gradients, the second process—effective-stress changes due

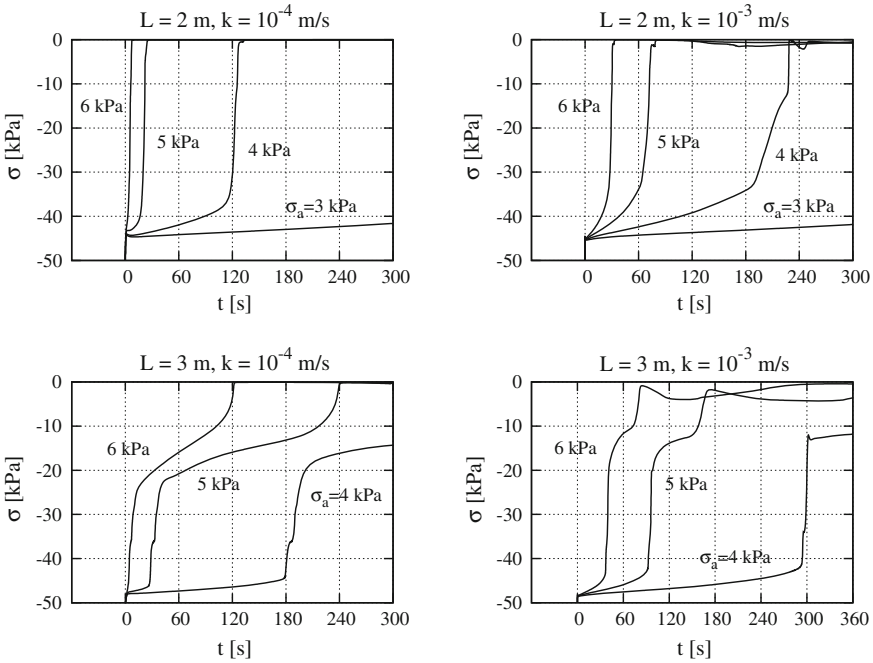

Fig. 7 Mean effective stress at Point A (see Fig. 3) as a function of time for different pressure amplitudes σ_a, different values of the soil permeability, k, and the distances between the wall and the pile, L

to pore water flow—dominates during the first few seconds. As a result, the mean effective stress slightly increases in absolute value near the auxiliary boundary and decreases near the wall. This rapid change may be considered as a correction to the initial stress state.

The solutions presented in Fig. 7 reveal that the effective stress near the wall is reduced. A reduction in the effective stress means a reduction in the soil stiffness and, in the case of zero stress, soil liquefaction. If the loading amplitude σ_a is large enough, the effective stress is reduced to zero within a short time. For smaller amplitudes, a gradual decrease at the beginning is followed by an abrupt fall to zero ($L = 2$ m) or to an intermediate nonzero stress with a further slower reduction ($L = 3$ m). For example, in the case with $L = 2$ m, $k = 10^{-4}$ m/s and $\sigma_a = 4$ kPa, the effective stress gradually changes to -35 kPa within 120 s and then falls to zero in a few seconds. The abrupt reduction of the effective stress is a consequence of a resonance-like increase in the strain amplitude in the soil for a certain spatial distribution of the effective stress with a constant pressure amplitude at the boundary. This property of the solutions was observed earlier in a spherically symmetric problem [4] and, as we have seen in the present study, manifests itself in the two-dimensional case as well. Another feature of the solutions is their high sensitivity to the loading amplitude

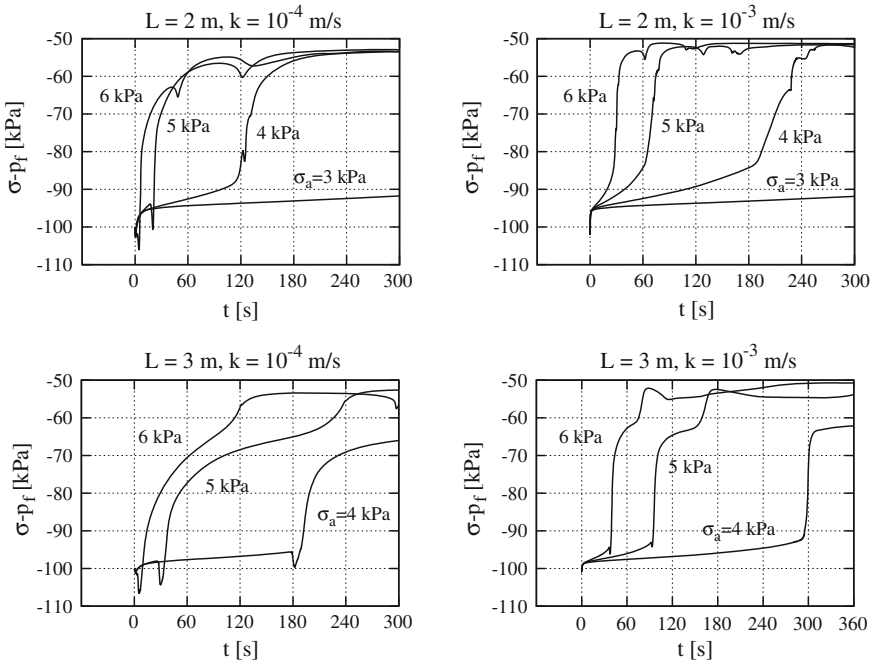

Fig. 8 The same as in Fig. 7 for the mean total stress

σ_a: the curve for $L = 2$ m, $k = 10^{-4}$ m/s and $\sigma_a = 3$ kPa, in contrast to that for $\sigma_a = 4$ kPa, shows only a slight reduction from -45 to -42 kPa after 300 s.

Leaving aside the strong dependence of the solution on the soil density, constitutive parameters and other factors, the features inferred from Fig. 7 suggest that it may be impossible to make a more or less definite prediction about the stress evolution in a real situation. Suppose we have estimated the loading amplitude σ_a to be in the range between 3 and 4 kPa, and the vibration time is about 180 s. Then, according to the solutions for $L = 2$ m and $k = 10^{-4}$ m/s, the effective stress may either remain practically unchanged or be reduced to zero.

Figure 8 shows the mean total stress at Point A for the same parameters as in Fig. 7. The changes in the pore pressure in front of the wall turn out to be insignificant, so that the changes in the total stress correspond approximately to the changes in the effective stress. Note that a higher value of soil permeability (10^{-3} vs. 10^{-4} m/s) does not prevent the stress reduction.

A question important for applications is that of the difference in the stress states in front of and behind the wall. In all numerical solutions presented here, the mean effective stress behind the wall during 300 s lies in the range between -50 and -46 kPa for $L = 2$ m and between -50 and -47 kPa for $L = 3$ m. The pore pressure remains practically at the same level of 50 kPa. In other words, both the mean effective stress and the mean total stress behind the wall are reduced in absolute value by no

more than 3–4 kPa. At the same time, as we have seen, the total stress in front of the wall is reduced in the worst case by 40 kPa. The difference is carried by the wall. In the present two-dimensional problem with an infinite wall, the deformation (bending) and the corresponding displacement of the wall caused by the stress difference are negligibly small because of the high stiffness of the concrete. However, in a real three-dimensional situation with a finite wall, the stress difference together with the reduced soil stiffness in front of the wall may produce a large wall displacement.

6 Conclusion

The problem of vibration-induced deformation of saturated granular soil is formulated and solved numerically with the high-cycle accumulation model of the explicit type. The numerical implementation realized with the finite-element program Abaqus/Standard consists in the concurrent solution of two coupled boundary value problems. The first problem is a dynamic steady-state problem solved at each time step in order to find the strain amplitude field required for the high-cycle model. The second problem, which gives the stress evolution, is a quasi-static deformation problem for a fluid-saturated solid with an additional accumulation term in the constitutive equation.

The high-cycle model is applied to the analysis of stress changes near a concrete wall caused by the large-amplitude vibration of a pile. The numerical results have shown that the vibration of a pile in saturated soil near a wall may reduce the effective stress in front of the wall to zero and thus lead to soil liquefaction. The total stress is substantially reduced as well because of the absence of a pore pressure build-up. The total-stress reduction in the case of liquefaction approximately equals the initial effective stress and should therefore increase with increasing depth. The stress state behind the wall remains practically unchanged. The reduction of both the effective and the total stresses in front of the wall may cause a large wall displacement during the installation of vibratory driven piles near the wall.

Acknowledgments The study was financed by the Deutsche Forschungsgemeinschaft as part of the Research Unit FOR 1136 ‘Simulation of geotechnical construction processes with holistic consideration of the stress strain soil behaviour’, Subproject 6 ‘Soil deformations close to retaining walls due to vibration excitations’.

References

1. Chrisopoulos, S., Osinov, V.A., Triantafyllidis, T.: Dynamic problem for the deformation of saturated soil in the vicinity of a vibrating pile toe. In: This volume (2015)
2. Niemunis, A., Wichtmann, T., Triantafyllidis, T.: A high-cycle accumulation model for sand. Comput. Geotech. **32**, 245–263 (2005)

3. Osinov, V.A., Chrisopoulos, S., Triantafyllidis, T.: Numerical study of the deformation of saturated soil in the vicinity of a vibrating pile. Acta Geotech. **8**, 439–446 (2013)
4. Osinov, V.A.: Application of a high-cycle accumulation model to the analysis of soil liquefaction around a vibrating pile toe. Acta Geotech. **8**, 675–684 (2013)
5. Osinov, V.A.: Numerical modelling of the effective-stress evolution in saturated soil around a vibrating pile toe. In: Triantafyllidis, T. (ed.) Holistic Simulation of Geotechnical Installation Processes. Numerical and Physical Modelling, pp. 133–147. Springer International Publishing, Switzerland (2015)
6. Triantafyllidis, T.: Neue Erkenntnisse aus Messungen an tiefen Baugruben am Potsdamer Platz in Berlin. Bautechnik **75**(3), 133–154 (1998)
7. Wichtmann, T.: Explicit accumulation model for non-cohesive soils under cyclic loading. Dissertation, Publications of the Institute of Soil Mechanics and Foundation Engineering, Ruhr-University Bochum, vol. 38 (2005)
8. Wichtmann, T., Niemunis, A., Triantafyllidis, T.: Differential settlements due to cyclic loading and their effect on the lifetime of structures. In: Stangenberg, F., Bruhns, O.T., Hartmann, D., Meschke, G. (eds.) Lifetime-Oriented Design Concepts, pp. 357–364. Aedificatio Publishers, Freiburg (2007)
9. Wichtmann, T., Niemunis, A., Triantafyllidis, T.: Prediction of long-term deformations for monopile foundations of offshore wind power plants. In: Mlynarek, Z., Sikora, Z., Dembicki, E. (eds.) Geotechnics in Maritime Engineering, vol. 2, pp. 785–792. Polish Committee on Geotechnics & Gdansk University of Technology, Gdansk (2008)
10. Wichtmann, T., Niemunis, A., Triantafyllidis, T.: On the determination of a set of material constants for a high-cycle accumulation model for non-cohesive soils. Int. J. Numer. Anal. Meth. Geomech. **34**, 409–440 (2010)
11. Wichtmann, T., Niemunis, A., Triantafyllidis, T.: On the 'elastic' stiffness in a high-cycle accumulation model for sand: a comparison of drained and undrained cyclic triaxial tests. Can. Geotech. J. **47**(7), 791–805 (2010)
12. Wichtmann, T., Niemunis, A., Triantafyllidis, T.: Simplified calibration procedure for a high-cycle accumulation model based on cyclic triaxial tests on 22 sands. In: Gourvenec, S., White, D. (eds.) Frontiers in Offshore Geotechnics II, pp. 383–388. Taylor & Francis, London (2011)
13. Wichtmann, T., Niemunis, A., Triantafyllidis, T.: Towards the FE prediction of permanent deformations of offshore wind power plant foundations using a high-cycle accumulation model. In: Gourvenec, S., White, D. (eds.) Frontiers in Offshore Geotechnics II, pp. 635–640. Taylor & Francis, London (2011)
14. Wichtmann, T., Niemunis, A., Triantafyllidis, T.: On the 'elastic stiffness' in a high-cycle accumulation model—continued investigations. Can. Geotech. J. **50**(12), 1260–1272 (2013)
15. Wichtmann, T., Niemunis, A., Triantafyllidis, T.: Improved simplified calibration procedure for a high-cycle accumulation model. Soil Dyn. Earthquake Eng. **70**, 118–132 (2015)

Peak Stress Obliquity in Drained and Undrained Sands. Simulations with Neohypoplasticity

Andrzej Niemunis, Carlos E. Grandas Tavera and Torsten Wichtmann

Abstract The difference between undrained and drained peak friction angle is considerable (up tp 10°), despite identical densities and pressures (at peak). This cannot be explained using the elastoplastic formalism. An attempt is made to describe this effect with neohypoplasticity. For this purpose two types of nonlinearity are used, the well-known term $Ym_{ij}\|\dot{\epsilon}\|$ and the novel skew-symmetric correction tensor which is added to the elastic stiffness.

Keywords Constitutive modelling · Sand · Dilatancy · Peak friction angle · Cyclic mobility

1 Introduction

Dense sand samples reach much lower stress obliquities, say $\varphi_U \approx 34°$, in the undrained triaxial compression than in the conventional drained compression with $\varphi_{\text{peak}} \approx 42°$ or more at similar pressure and density, Fig. 1 left: black and blue stress paths. This has been confirmed by numerous tests like the ones in Fig. 3. For a fair comparison of φ_U and φ_{peak} the densities and pressures at the peak should be equal (not just the ones from the initial isotropic state). Similarly, for loose samples, the undrained strength, say $\varphi_U \approx 25°$, is smaller than the drained strength, $\varphi_c \approx 32°$, Fig. 1 middle: black and blue stress paths.

The aim of this paper is to examine experimentally, whether the low undrained stress ratio is caused by inhomogeneities (shear bands) or whether it is a constitutive issue. Having demonstrated the latter case, we implement the effect to neohypoplasticity.

A. Niemunis (✉) · C.E.G. Tavera · T. Wichtmann
Institute of Soil Mechanics and Rock Mechanics, Karlsruhe Institute of Technology, Karlsruhe, Germany
e-mail: andrzej.niemunis@kit.edu, fuenteslacouture1@gmail.com

T. Triantafyllidis (ed.), *Holistic Simulation of Geotechnical Installation Processes*, Lecture Notes in Applied and Computational Mechanics 80, DOI 10.1007/978-3-319-23159-4_5

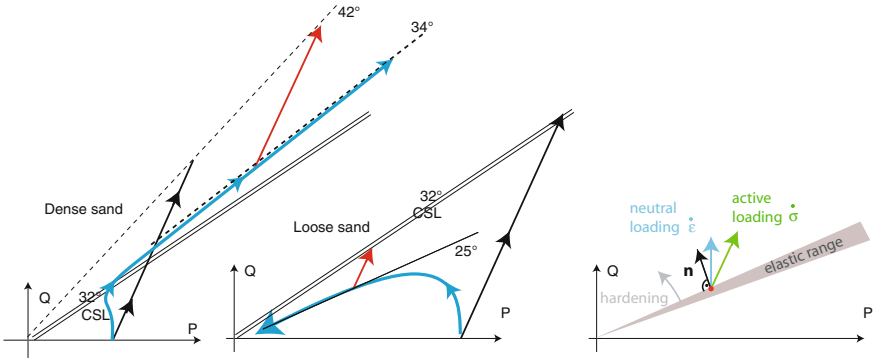

Fig. 1 At the same void ratio different maximal friction angles can be measured: φ_U in undrained tests (*blue stress paths*) and φ_{peak} in drained tests (*black paths*). The undrained strength is significantly smaller

1.1 Notation

A fixed orthogonal Cartesian coordinate system x_1, x_2, x_3 is used. A repeated (dummy) index implies summation. According to Gibbs notation $\sqcup\!\sqcup$ denotes a dyadic product, $\sqcup \cdot \sqcup$ is a product with a single dummy index and $\sqcup : \sqcup$ with two dummy indices of two tensorial quantities $\sqcup$. The Kronecker's symbol is δ_{ij}. The fourth-order identity tensor is $(\mathsf{J})_{ijkl} = \delta_{ik}\delta_{jl}$ and its symmetrizing part is $I_{ijkl} = \frac{1}{2}(\delta_{ik}\delta_{jl} + \delta_{il}\delta_{jk})$. Proportionality of tensors is denoted by tilde, $\sim$. The components of diagonal matrices (with zero off-diagonal components) are written as $\text{diag}(\,,\,,\,)$, e.g. $\mathbf{1} = \text{diag}(1, 1, 1)$. The operator $(\sqcup)^{\rightarrow}$ or $\vec{\sqcup}$ denotes normalization of $\sqcup$, e.g. $\vec{\epsilon}_{ij} = \epsilon_{ij}/\sqrt{\epsilon_{kl}\epsilon_{kl}}$. The superposed dot $\dot{\sqcup}$ denotes the material time derivative of $\sqcup$. The superscript $\sqcup^*$ denotes the deviatoric part of $\sqcup$. The superscripts $\sqcup^{\text{acc}}$, $\sqcup^{\text{av}}$ and $\sqcup^{\text{ampl}}$ denote the cumulative part of $\sqcup$, its average value and its amplitude. Several frequently used variables are listed below.

E_{ijkl} or E	$= \partial\sigma_{ij}/\partial\epsilon_{kl}$ elastic stiffness
$\dot{\epsilon}_{ij}$ or $\dot{\boldsymbol{\epsilon}}$	strain rate (tension positive)
σ_{ij} or $\dot{\boldsymbol{\sigma}}$; $R = \sqrt{\sigma_{ij}\sigma_{ij}}$	stress (tension positive) and its norm
$\psi(\boldsymbol{\epsilon})$, $\bar{\psi}(\boldsymbol{\sigma})$	elastic and complementary energy density
$P = -\sigma_{ii}/\sqrt{3}$; $Q = \sigma^*_{ij}\sigma^*_{ij}$	isomorphic pressure and deviatoric stress
$H = \sigma_{ii}\ \sigma^{-1}_{jj} - 9$	a stress invariant for Matsuoka and Nakai criterion
$h = Q/P$	stress obliquity similar to $\eta = q/p$
$\epsilon_P = -\epsilon_{ii}/\sqrt{3}$; $\epsilon_Q = \epsilon^*_{ij}\epsilon^*_{ij}$	isomorphic volumetric strain and deviatoric strain
$\mathbf{m}$, $\mathbf{n}$, K	flow rule and loading direction, hardening module
m, m_i	homogeneity order, direction of sedimentation
$\vec{\mathbf{1}} = \frac{1}{\sqrt{3}}\,\text{diag}(1, 1, 1)$	basis tensor $P = -\vec{\mathbf{1}} : \boldsymbol{\sigma}$ on the PQ plane
$\vec{\mathbf{1}}^* = -\frac{1}{\sqrt{6}}\,\text{diag}(-2, 1, 1)$	basis tensor $Q = \vec{\mathbf{1}}^* : \boldsymbol{\sigma}$ on the PQ plane

The invariants $P, Q, \epsilon_P, \epsilon_Q$ are not only work conjugate $\boldsymbol{\sigma} : \dot{\boldsymbol{\epsilon}} = P\dot{\epsilon}_P + Q\dot{\epsilon}_Q$ but also, unlike the Roscoe invariants, they are isomorph, i.e. $\boldsymbol{\sigma} : \boldsymbol{\sigma} = P^2 + Q^2$ and $\boldsymbol{\epsilon} : \boldsymbol{\epsilon} = \epsilon_P^2 + \epsilon_Q^2$. For axial symmetric tensors $\boldsymbol{\sigma}$ and $\boldsymbol{\epsilon}$ we introduce *signed* invariants $Q = \vec{\mathbf{1}}^* : \sigma$ and $\epsilon_Q = \vec{\mathbf{1}}^* : \epsilon_Q$ so that the initial tensors can be recovered, e.g. $\boldsymbol{\sigma} = -\vec{\mathbf{1}}P + \vec{\mathbf{1}}^* Q$.

2 Elastoplastic Approach

One may expect difficulties with contemporary elastoplastic models for soils like *Severn Trent* [7] or *Sanisand* [3, 21] in simulating the difference between φ_U and φ_{peak}. These models introduce a conical yield surface with the sharp apex at the origin of the coordinate system, Fig. 1 right. Hardening corresponds to the rotation of such cone about the origin towards larger stress obliquity $h = Q/P$. Starting from the mobilized friction angle φ_U, we want to enable hardening for drained compression (with strong dilatancy and increase of h) but to preclude hardening for undrained compression.

In elastoplastic models, the hardening is driven by the plastic multiplier.[1] This multiplier must be positive for hardening and hence $\mathbf{n} : \mathsf{E} : \dot{\boldsymbol{\epsilon}} > 0$ must hold. The loading direction $\mathbf{n}$ is perpendicular to the yield surface. Moreover, $\mathbf{n} : \boldsymbol{\sigma} = 0$ holds in the above-mentioned models [3, 7, 21]. Using a reasonable elastic stiffness,[2] the neutrality of elastic undrained shearing $\mathsf{E} : \dot{\boldsymbol{\epsilon}}^*$ seems to be impossible.

The problem with elastoplastic models is illustrated in Fig. 2, where the so-called response envelopes are used. A response envelope (RE) is a polar representation of

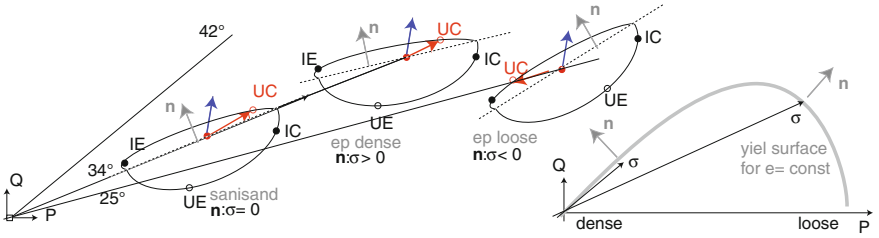

Fig. 2 The undrained stress rate corresponds to the point UC on the response envelope. The response envelope of the sanisand model corresponds to the flattened ellipse with the loading direction $\mathbf{n} \perp \boldsymbol{\sigma}$. If there is hardening for drained direction (*blue arrow*) there should be also hardening for undrained direction UC. A differently inclined yield surface (*dashed lines*) with $\mathbf{n} : \boldsymbol{\sigma} > 0$ for dense and with $\mathbf{n} : \boldsymbol{\sigma} > 0$ for loose sand is required. The rotation of the points UC, UE is necessary

[1] For strain controlled tests, the plastic multiplier is $\dot{\lambda} = \mathbf{n} : \mathsf{E} : \dot{\boldsymbol{\epsilon}} / (K + \mathbf{n} : \mathsf{E} : \mathbf{m})$ with the hardening modulus K, flow rule $\mathbf{m}$ and the loading direction $\mathbf{n}$.

[2] We will use the hyperelastic stiffness E obtained from numerous high-quality small-strain tests [6, 13], see Sect. 4.1.

stiffness [10], also known as the stiffness locus [2]. We consider the RE on the PQ plane only. Mathematically the RE can be written as a parametric expression

$$\begin{aligned} P(\theta) &= P^{\mathrm{av}} + \Delta P(\Delta\epsilon_P(\theta), \Delta\epsilon_Q(\theta)) \\ Q(\theta) &= Q^{\mathrm{av}} + \Delta Q(\Delta\epsilon_P(\theta), \Delta\epsilon_Q(\theta)), \\ \text{for} \quad \Delta\epsilon_P(\theta) &= 0.001\cos\theta \ \text{ and } \Delta\epsilon_Q = 0.001\sin\theta \end{aligned} \tag{1}$$

with parameter $-\pi < \theta < \pi$. The stress increments $\Delta P(\Delta\epsilon_P(\theta), \Delta\epsilon_Q(\theta))$ and $\Delta Q(\Delta\epsilon_P(\theta), \Delta\epsilon_Q(\theta))$ are constitutive functions obtained from $\dot{\boldsymbol{\sigma}}(\dot{\boldsymbol{\epsilon}})$ with $\dot{P} = -\vec{\mathbf{1}} : \dot{\boldsymbol{\sigma}}$ and $\dot{Q} = -\vec{\mathbf{1}}^* : \dot{\boldsymbol{\sigma}}$. Isotropic compression (IC) and extension (IE) correspond to $\theta = 0$ and $\theta = \pi$, whereas undrained (=isochoric) compression (UC) and extension (UE) correspond to $\theta = \pi/2$ and $\theta = -\pi/2$.

In the elastoplastic framework the dilemma with $\varphi_U < \varphi_{\mathrm{peak}}$ may be solved with a different shape of the elastic range, so that $\mathbf{n} : \boldsymbol{\sigma} > 0$, see the RE denoted as 'ep dense' in Fig. 2. For loose sand we need $\mathbf{n} : \boldsymbol{\sigma} < 0$. For a usual yield surface, however, the opposite inequalities hold, namely $\mathbf{n} : \boldsymbol{\sigma} < 0$ for dense and $\mathbf{n} : \boldsymbol{\sigma} > 0$ for loose sand, see Fig. 2 right.

3 Shear Band Hypothesis

The difference between φ_U and φ_{peak} might be attributed to the formation of shear bands with much lower density (and hence lower strength) inside the shear band (SB). They could explain the phenomenon, provided that SBs indeed appear during undrained but not during drained tests. Here, this hypothesis will be refuted experimentally. In the consequence, the difference between φ_U and φ_{peak} will be treated as a constitutive matter.

Suppose that the low stress obliquity of an undrained dense sand sample was caused by the formation of a system of SBs with locally very loose arrangement of grains within the thickness $10d_{50} \approx 3$mm of the SBs. Let us assume that for some reasons such system is developed during undrained but not during drained tests. Spectacular SB patterns inside the superficially homogeneous looking samples have been first experimentally shown by Desrues et al. [5] on computer tomography pictures. Under global undrained conditions, we may have strong local dilatancy inside the narrow SBs. They may dilate at the cost of slight densification of large blocks between them so that the total volume remains unchanged. Eventually, extremely loose and weak shear zones form a system that dictates the overall strength φ_U of the sample.

The question arises, whether the shear bands indeed appear earlier (at lower stress obliquities) during the undrained compression than during the drained one and why. To give a definitive answer, triaxial tests with expensive computer tomography evaluation would be necessary. Additionally, bifurcation conditions should be theoretically examined using good constitutive models.

Here we will refute the hypothesis of shear bands with the following *experimentum crucis*. A usual undrained triaxial compression of a dense sample will be stopped after a monotonic deformation which is believed to be sufficiently long for the formation of the SB.[3] Without any disturbance of the effective stress, the valve of the drainage system will be opened and the triaxial compression will be continued in the drained manner, Fig. 1 left: red arrow. If SBs were indeed responsible for the low φ_U value, then similarly low strength would be held for the *drained continuation* of undrained loading. The usual peak $\varphi_{\text{peak}} \approx 42°$ could not be attained.

It turns out, however, that the drained strength of $\varphi_{\text{peak}} \approx 42°$ or more can be reached, irrespectively of the long undrained pre-shearing, see Sect. 3.1. Hence, the difference between φ_{peak} and φ_U cannot be attributed to the existence of SBs. We conclude that this difference should be described by a constitutive model for homogeneous stress and strain fields.

3.1 Triaxial Tests Showing $\varphi_U < \varphi_{\text{peak}}$

The tests on achievable stress ratios under drained or undrained conditions were performed on Karlsruhe fine sand (d_{50} = 0.14 mm, $C_u = d_{60}/d_{10}$ = 1.5, $e_{\min}$ = 0.677, $e_{\max}$ = 1.054, ϱ_s = 2.65 g/cm^3). The samples (diameter d = 100 mm, height h = 100 mm) were prepared by air pluviation. Tests on both loose and dense samples were performed. All tests begin with an undrained loading commenced from the isotropic stress[4] p = 100 kPa.

Figure 3a, b compares the effective stress paths and the $\eta(\varepsilon_1)(= q/p)$ relationships of two dense samples (I_{D0} = 0.89 or 0.92). The first one (green curve) was sheared undrained throughout the whole test reaching $\varphi_U = 35°$. The resulting path serves as the reference. In the second test (red curve) the drainage was opened during the dilatant phase, when the excess pore pressure had become zero again, i.e. the effective lateral stress had regained its initial value 100 kPa. During the subsequent drained phase the stress path follows the dashed line (inclination 1:3 on pq-plane) that would have been measured in a drained test started at p = 100 kPa. During that drained phase the mobilized friction angle climbed from 35.2° to 44.3°.

In a third test on a dense sample (I_{D0} = 0.91, Fig. 3c, d, blue curve), two undrained phases encompass a drained one. In the drained phase, the mobilized friction angle increased considerably from $\varphi_{\text{mob}} = 35.6°$ to $\varphi_{\text{mob}} = 42.9°$. During the third, undrained phase, the effective stress path ran almost parallel to the referential undrained path with similar initial density (green curve). The mobilized friction angle slightly decreased back to $\varphi_{\text{mob}} = 38.9°$ at the end of the test at $q \approx 2000$ kPa.

[3] Note that the pictures in [5] were taken after several percent of axial deformation.

[4] In the description of experimental results, we use the conventional Roscoe invariants $p = \frac{1}{3}(\sigma_1 + 2\sigma_2)/3$ and $q = \sigma_1 - \sigma_2$ with geotechnical sign convention for principal stresses σ_i and strains ε_i.

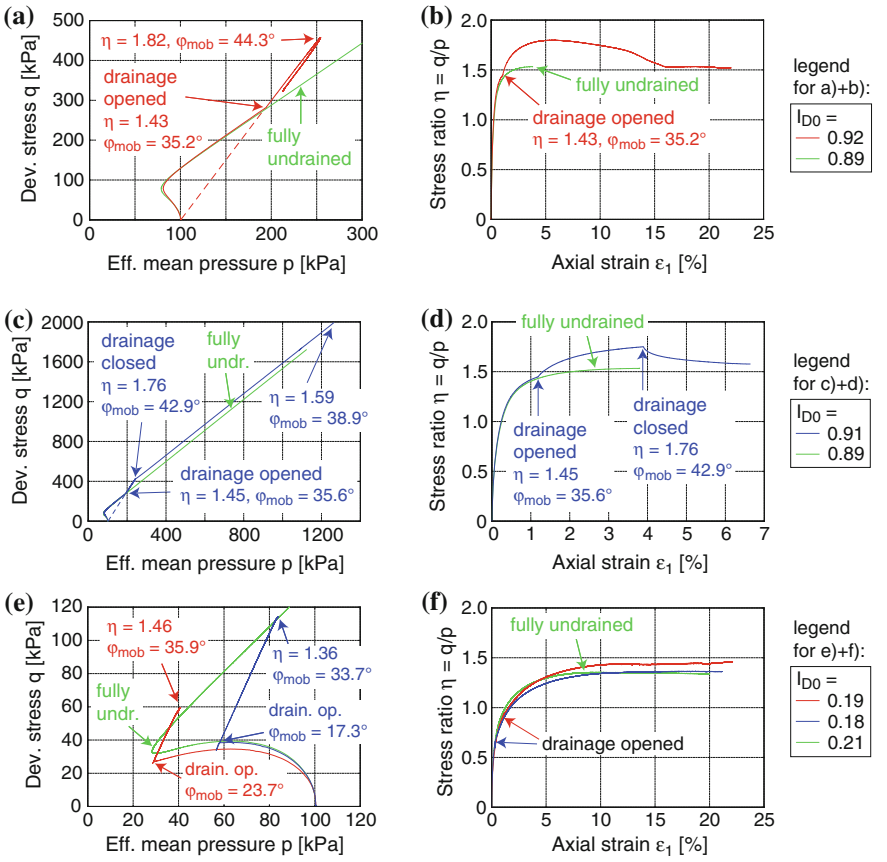

Fig. 3 Effective stress paths in the p–q plane and $\eta(\varepsilon_1)$ relationships in tests with combination of undrained and drained loading stages. **a, b** dense sand sheared under undrained conditions followed by drained triaxial compression test. **c, d** dense sand sheared under undrained, drained and again undrained triaxial conditions. **e, f** loose sand sheared under undrained conditions followed by drained triaxial compression. Fully undrained test is depicted as a reference.

Also loose samples (I_{D0} = 0.18 or 0.19, see red and blue curves in Fig. 3e, f) showed a strong increase in the mobilized friction angle during the drained phase, even if the drainage was opened after the onset of softening. The maximum value of the mobilized friction angle reached during the drained phase was similar to the value $\varphi_{\mathrm{mob}} \approx 34°$ observed during the dilatant phase in a purely undrained test performed on a loose sample (I_{D0} = 0.21, green curve in Fig. 3e).

4 Hypoplastic Modelling of φ_U

The hypoplastic constitutive equation describes the stress rate $\dot{\sigma}_{ij}$ as a nonlinear function of the strain rate $\dot{\epsilon}_{kl}$ in the following form:

$$\dot{\sigma}_{ij} = E_{ijkl}(\dot{\epsilon}_{kl} - m_{kl} Y \|\dot{\boldsymbol{\epsilon}}\|), \tag{2}$$

wherein E_{ijkl}, m_{kl}, Y are carefully designed functions of stress and void ratio. The elastic stiffness E_{ijkl} will be obtained from a complementary energy function $\bar{\psi}(\boldsymbol{\sigma})$ formulated to fit the resilient portion of the material stress response. The nonlinear part $m_{kl} Y \|\dot{\boldsymbol{\epsilon}}\|$ is responsible for irreversible effects. The yield condition $\dot{\sigma}_{ij} = 0$ at $\dot{\epsilon}_{kl} \neq 0$ corresponds to $Y = 1$ and $(\dot{\epsilon}_{kl})^{\rightarrow} = m_{kl}$, wherein m_{kl} is the flow rule (a unit tensor). Equation (2) leads to elliptic response envelopes, similarly like the ones from elasticity but shifted by $Y E_{ijkl} m_{kl}$ in the stress space. If $Y < 1$ holds, the origin $(P^{\text{av}}, Q^{\text{av}})$ of the RE described by (1) lies inside the ellipse. For $Y = 1$, the origin lies on the surface of the ellipse. Since the undrained stress path cannot surpass the obliquity

$$Q/P = M_U \quad \text{with} \quad M_U = \frac{\sqrt{2}}{3} \frac{6 \sin \varphi_U}{3 - \sin \varphi_U} \tag{3}$$

we have to enforce the proportionality

$$\dot{\sigma}_{ij} \sim \sigma_{ij} \quad \text{for} \quad \dot{\epsilon}_{kl} \sim \sigma^*_{kl} \quad \text{or} \quad \sigma_{ij} \sim E_{ijkl}(\vec{\sigma^*_{kl}} - m_{kl} Y) \tag{4}$$

Besides (4), also $Y < 1$ should be satisfied. This enables an increase in Q/P upon the usual drained compression with $\dot{Q}/\dot{P} = \sqrt{2}$. On the PQ-space (4) takes the form

$$\begin{Bmatrix} 1 \\ M_U \end{Bmatrix} \sim \begin{bmatrix} E_{PP} & E_{PQ} \\ E_{QP} & E_{QQ} \end{bmatrix} \left(\begin{Bmatrix} 0 \\ 1 \end{Bmatrix} - Y \begin{Bmatrix} m_P \\ m_Q \end{Bmatrix} \right) \tag{5}$$

and can be depicted with the help of the REs, Fig. 4 (left).

If the elastic response envelopes are overly stretched or overly rotated with respect to the P-axis in the PQ space, then the desired proportionality (4) cannot be satisfied.

The difference between φ_U and φ_{peak} depends on the shape and orientation of the response envelope and therefore on the elastic part E_{ijkl} of the hypoplastic model and not only on the flow rule m_{kl}. If the elastic ellipse obtained from E_{ijkl} is too slender or if its major diameter excessively deviates from the isotropic position (along the P axis), then the difference $\varphi_{\text{peak}} - \varphi_U$ may be too small. The experiments [6, 13] show that the ellipses of the elastic response are moderately slender with the major diameter twice larger than the minor one which is the PQ-space,[5] which corresponds to isotropic elasticity with the ratio of bulk and shear modulus $3K/(2G) \approx 2$ or the

[5] This ratio is not constant and about 1.8 for triaxial compression and 2.4 for triaxial extension.

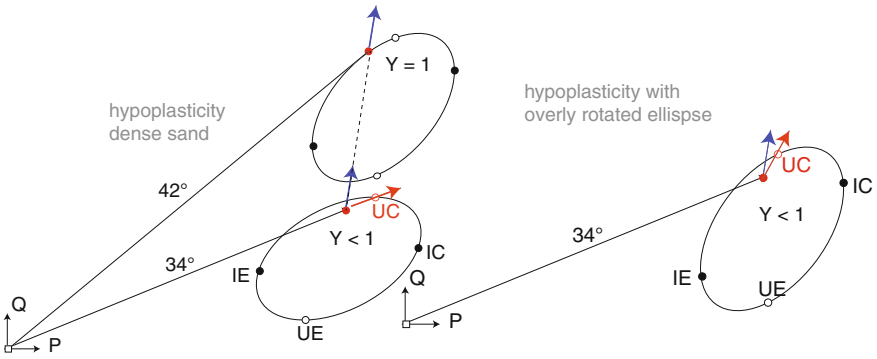

Fig. 4 The undrained stress rate corresponds to the point UC on the response envelope. Although the yield surface has not been reached yet, i.e. $Y < 1$ and the current stress (*red point*) lies inside the ellipse, the inclination of stress cannot increase anymore (*left*). However, for the same void ratio, the drained stress rate (inclined under $\dot{Q}/\dot{P} = \sqrt{2}$) can increase until $Y = 1$, i.e. until the origin stress lies on the ellipse. If the major diameter of the ellipse is too strongly rotated off the isotropic position (*right*), both undrained and drained stress rates increase the stress obliquity

Poisson number $\nu \approx 0.2$ on the P-axis.[6] The same experiments show that the inclination of the major diameter to the P-axis is roughly Q/P for both triaxial compression and extension.

As illustrated in Fig. 5, the proportionality condition (4) should be satisfied for dense sand at $\varphi_U \approx 34°$ with the stress rate going to the right and for loose sand at $\varphi_U \approx 25°$ with the stress rate going to the left. This proportionality poses a difficult problem for constitutive modelling, when a reasonable elastic stiffness like the one measured in Sect. 4.3 is used. It turns out that one cannot meet the requirement (4) for both loose and dense sand by adjusting the shift $Y E_{ijkl} m_{kl}$ only. Therefore an additional modification is proposed. It consists in rotation of the undrained response UC,UE as shown in Fig. 5. This, what we call, "U-rotation" is evident comparing the positions of the undrained response UC,UE on the blue and on the green ellipse. As we can see, the considerable difference between φ_{peak} and φ_U has a subtle origin and requires a non-symmetric stiffness. However, this difference may be of practical importance and hence it is worth some additional effort in modelling. The "U-rotation" is presented in detail in Sect. 4.5.

4.1 Hyperelastic Part of the Model

We propose an expression $\bar{\psi}(\boldsymbol{\sigma})$ for the complementary energy from which the strain function $\epsilon_{ij}(\boldsymbol{\sigma})$ and the compliance $C_{ijkl}(\boldsymbol{\sigma})$ are obtained as partial derivatives,

[6]The hyperelastic stiffness E_{ijkl} is comparable to the isotropic elastic stiffness (using the Poisson number ν) on the P-axis only.

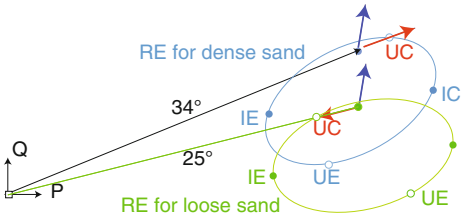

Fig. 5 The elastic stress envelope should be strongly modified between the friction angle $\varphi_U = 25°$ for loose sand (*green ellipse*) and $\varphi_U = 34°$ for dense sand (*blue*) because the desired proportionality (4) cannot be obtained by modifying just the shift $Y E_{ijkl} m_{kl}$ of the response envelope. The stiffness E corresponding to the green ellipse is not symmetric, as discussed in Sect. 4.5

$$\epsilon^{\mathrm{el}}_{ij} = \frac{\partial \bar{\psi}}{\partial \sigma_{ij}} \quad \text{and} \quad \dot{\epsilon}^{\mathrm{el}}_{ij} = \frac{\partial^2 \bar{\psi}}{\partial \sigma_{ij} \partial \sigma_{kl}} \dot{\sigma}_{kl} = C_{ijkl} \dot{\sigma}_{kl} \tag{6}$$

In geotechnical materials, the tangential compliance $C_{ijkl}(\boldsymbol{\sigma})$ should decrease with pressure. For this purpose we postulate that the tangential stiffness $E_{ijkl} = C^{-1}_{ijkl}$ is a homogeneous stress function of order $n \approx 0.6$, i.e. $\forall \lambda > 0 : \mathsf{E}(\lambda \boldsymbol{\sigma}) = \lambda^n \mathsf{E}(\boldsymbol{\sigma})$, and hence $C_{ijkl}(\boldsymbol{\sigma})$ is homogeneous of order $-n$.

Analogously to Euler's theorem about the first derivative of an mth order homogeneous function,

$$m \bar{\psi} = \frac{\partial \bar{\psi}}{\partial \boldsymbol{\sigma}} : \boldsymbol{\sigma}, \tag{7}$$

we formulate[7] a similar relation with the second derivative,

$$m(m-1)\bar{\psi} = \boldsymbol{\sigma} : \frac{\partial^2 \bar{\psi}}{\partial \boldsymbol{\sigma} \partial \boldsymbol{\sigma}} : \boldsymbol{\sigma} = \boldsymbol{\sigma} : \mathrm{C} : \boldsymbol{\sigma} \tag{8}$$

Judging by the product on the right-hand side of (8) our potential $\bar{\psi}$ should be homogeneous of order $2 - n$. This condition is sufficient (but not necessary) for the nth order homogeneous stiffness. The related degrees of homogeneity are given in the following table:

Function	$\mathsf{E}(\boldsymbol{\sigma})$	$\mathsf{C}(\boldsymbol{\sigma})$	$\mathsf{E}(\boldsymbol{\epsilon})$	$\mathsf{C}(\boldsymbol{\epsilon})$	$\boldsymbol{\epsilon}(\boldsymbol{\sigma})$	$\boldsymbol{\sigma}(\boldsymbol{\epsilon})$	$\bar{\psi}(\boldsymbol{\sigma})$	$\bar{\psi}(\boldsymbol{\sigma})$	$\psi(\boldsymbol{\epsilon})$	$\psi(\boldsymbol{\epsilon})$
Degree of homogeneity	n	$-n$	$\frac{n}{1-n}$	$\frac{-n}{1-n}$	$1-n$	$\frac{1}{1-n}$	$2-n$	$2-n$	$\frac{2-n}{1-n}$	$\frac{2-n}{1-n}$

[7] We substitute $\boldsymbol{\tau} = \boldsymbol{\sigma}\lambda$ into $\bar{\psi}$ and then differentiate the equation $\bar{\psi}(\boldsymbol{\tau}) = \lambda^m \bar{\psi}(\boldsymbol{\sigma})$ twice with respect to λ using the chain rule on the left-hand side. The resulting equation $\boldsymbol{\sigma} : \frac{\partial^2 \bar{\psi}(\boldsymbol{\tau})}{\partial \boldsymbol{\tau} \partial \boldsymbol{\tau}} : \boldsymbol{\sigma} = m(m-1)\lambda^{m-2}\bar{\psi}(\boldsymbol{\sigma})$ holds for any λ. In particular, it holds for $\lambda = 1$ and hence (8) can be concluded.

We propose the complementary energy of the general form

$$\bar{\psi}(\boldsymbol{\sigma}) = \sum_{\alpha} c_\alpha P^\alpha R^{2-n-\alpha} \quad \text{with} \quad \alpha \in \mathcal{R} \tag{9}$$

The degree of homogeneity of each summand is $2-n$, as desired. Note that the hyperelastic model [22] can be obtained as a special case with just one summand and with $\alpha = 0$. For the neohypoplasticity we decided to take just one summand in (9) and just three material constants, namely

$$\bar{\psi} = c P^\alpha R^{2-n-\alpha} \quad \text{with} \quad \begin{array}{|c|c|c|} \hline n & c & \alpha \\ \hline 0.6 & 1.517 \times 10^{-4} & 0.100 \\ \hline \end{array} \tag{10}$$

The calibration of material constants n, c, α requires high-quality tests [6, 13], see Sects. 4.3 and 4.4. The total elastic strain $\epsilon_{ij}^{\mathrm{el}}$ is

$$\epsilon_{ij}^{\mathrm{el}} = \frac{\partial \bar{\psi}}{\partial \sigma_{ij}} = \alpha P^{\alpha-1} R^{2-n-\alpha}(-\vec{\delta}_{ij}) + (2-n-\alpha) P^\alpha R^{1-n-\alpha} \vec{\sigma}_{ij} \tag{11}$$

and the compliance results from $\mathsf{C} = (\partial^2 \bar{\psi}/\partial\boldsymbol{\sigma}\partial\boldsymbol{\sigma})$, viz.

$$\mathsf{C} = A_\alpha \vec{\mathbf{1}}\vec{\mathbf{1}} + B_\alpha(\vec{\mathbf{1}}\vec{\boldsymbol{\sigma}} + \vec{\boldsymbol{\sigma}}\vec{\mathbf{1}}) + C_\alpha \vec{\boldsymbol{\sigma}}\vec{\boldsymbol{\sigma}} + D_\alpha \mathsf{I} \quad \text{or} \tag{12}$$

$$C_{ijkl\alpha} = A_\alpha \vec{\delta}_{ij}\vec{\delta}_{kl} + B_\alpha(\vec{\delta}_{ij}\vec{\sigma}_{kl} + \vec{\sigma}_{ij}\vec{\delta}_{kl}) + C_\alpha \vec{\sigma}_{ij}\vec{\sigma}_{kl} + D_\alpha I_{ijkl}, \tag{13}$$

wherein

$$A_\alpha = c(\alpha-1)\alpha P^{\alpha-2} \mathrm{R}^{2-n-\alpha} \tag{14}$$

$$B_\alpha = -c\alpha(2-n-\alpha) P^{\alpha-1} \mathrm{R}^{1-n-\alpha} \tag{15}$$

$$C_\alpha = c(2-n-\alpha)(-n-\alpha) P^\alpha \mathrm{R}^{-n-\alpha} \tag{16}$$

$$D_\alpha = c(2-n-\alpha) P^\alpha \mathrm{R}^{-n-\alpha} \tag{17}$$

Using the basis tensors $\vec{\mathbf{1}} = \frac{1}{\sqrt{3}}\,\mathrm{diag}(1,1,1)$ and $\vec{\mathbf{1}}^* = -\frac{1}{\sqrt{6}}\,\mathrm{diag}(-2,1,1)$ of the PQ plane for triaxial (axialsymmetric) rates $\dot{\boldsymbol{\sigma}}$ and $\dot{\boldsymbol{\epsilon}}$ we obtain $\dot{\epsilon}_P = -\vec{\mathbf{1}} : \dot{\boldsymbol{\epsilon}}$, $\dot{\epsilon}_Q = \vec{\mathbf{1}}^* : \dot{\boldsymbol{\epsilon}}$, $\dot{P} = -\vec{\mathbf{1}} : \dot{\boldsymbol{\sigma}}$ and $\dot{Q} = \vec{\mathbf{1}}^* : \dot{\boldsymbol{\sigma}}$ or vice versa $\dot{\boldsymbol{\sigma}} = -\vec{\mathbf{1}}\dot{P} + \vec{\mathbf{1}}^*\dot{Q}$ and $\dot{\boldsymbol{\epsilon}} = -\vec{\mathbf{1}}\dot{\epsilon}_P + \vec{\mathbf{1}}^*\dot{\epsilon}_Q$. Hence, the isomorphic components of C_{ijkl} are

$$\begin{Bmatrix} \dot{\epsilon}_P \\ \dot{\epsilon}_Q \end{Bmatrix} = \left[\begin{array}{c|c} \vec{\mathbf{1}} : \mathsf{C} : \vec{\mathbf{1}} & \vec{\mathbf{1}} : \mathsf{C} : \vec{\mathbf{1}}^* \\ \hline \vec{\mathbf{1}}^* : \mathsf{C} : \vec{\mathbf{1}} & \vec{\mathbf{1}}^* : \mathsf{C} : \vec{\mathbf{1}}^* \end{array}\right] \cdot \begin{Bmatrix} \dot{P} \\ \dot{Q} \end{Bmatrix} \tag{18}$$

The expressions for components of the compliance matrix are

$$C_{PP} = \vec{\mathbf{1}} : \mathsf{C}_\alpha : \vec{\mathbf{1}} = A_\alpha + 2B_\alpha(-P)R^{-1} + C_\alpha P^2 R^{-2} + D_\alpha \quad (19)$$

$$C_{PQ} = \vec{\mathbf{1}} : \mathsf{C}_\alpha : \vec{\mathbf{1}}^* = B_\alpha(-Q)R^{-1} + C_\alpha PQR^{-2} \quad (20)$$

$$C_{QP} = \vec{\mathbf{1}}^* : \mathsf{C}_\alpha : \vec{\mathbf{1}} = B_\alpha(-Q)R^{-1} + C_\alpha QPR^{-2} \quad (21)$$

$$C_{QQ} = \vec{\mathbf{1}}^* : \mathsf{C}_\alpha : \vec{\mathbf{1}}^* = C_\alpha Q^2 R^{-2} + D_\alpha \quad (22)$$

Additionally, one may take into account the void ratio introducing the empirical factor [19]

$$F(e) = \frac{(2.97 - e)^2}{1 + e} \quad (23)$$

The constant 2.97 may need modifications, however.

4.2 Scaling of Stiffness for Transversel Isotropy

The elastic properties of soils are often different in the direction of sedimentation m_i than in the cross directions. This can be described by the transverse isotropic (TI) stiffness. In Voigt notation such TI stiffness has the form $\mathsf{E} =$

$$\begin{bmatrix} \gamma E_h(1-\nu_{hv}\nu_{vh}) & \gamma E_h(\nu_h+\nu_{hv}\nu_{vh}) & \gamma E_h(\nu_{vh}+\nu_h\nu_{vh}) & & & \\ \gamma E_h(\nu_h+\nu_{hv}\nu_{vh}) & \gamma E_h(1-\nu_{hv}\nu_{vh}) & \gamma E_h(\nu_{vh}+\nu_h\nu_{vh}) & & & \\ \gamma E_v(\nu_{hv}+\nu_h\nu_{hv}) & \gamma E_v(\nu_{hv}+\nu_h\nu_{hv}) & \gamma E_v(1-\nu_h^2) & & & \\ & & & G_h & & \\ & & & & G_v & \\ & & & & & G_v \end{bmatrix} \quad (24)$$

with $\gamma = 1/\left[1 - \nu_h^2 - 2\nu_{hv}\nu_{vh} - 2\nu_h\nu_{hv}\nu_{vh}\right]$ and with the symmetry axis along x_3, i.e. $\mathbf{m} = \{0, 0, 1\}$. The number of material constants is reduced to five by the additional relations $G_h = E_h/(2+2\nu_h)$ and $\nu_{vh}/E_v = \nu_{hv}/E_h$. The indices $\sqcup_h$ and $\sqcup_v$ denote the horizontal and the vertical direction (the latter along m_i, i.e. along x_3).

For practical purposes Graham and Houlsby [9] introduced a simplified version of the TI stiffness with three material constants instead of five. They proposed a TI stiffness H_{ijkl} for the special case

$$a = G_h/G_v = (E_h/E_v)^{1/2} = (\nu_h/\nu_{vh}) \quad (25)$$

with just three material constants a, E_v, ν_h, because $G_h = E_h/(2 + 2\nu_h)$. After some manipulations one may notice that the simplified TI stiffness H_{ijkl} proposed in [9] can be obtained from a special *scaling transformation* of the isotropic elastic stiffness E_{abcd}, namely

$$H_{ijkl} = Q_{ijab} E_{abcd} Q_{cdkl}\,, \tag{26}$$

$$\text{where} \quad Q_{ijkl} = \mu_{ik}\mu_{jl} \quad \text{with} \quad \mu_{ij} = \sqrt{a}\delta_{ij} + (1-\sqrt{a})m_i m_j \tag{27}$$

and where m_i is the unit vector along the sedimentation axis. The scaling (26) has one major advantage over (25): it can be applied to *any* hyperelastic stiffness. From the existence of the function, $\bar{\psi}(\boldsymbol{\sigma})$, and from the 1–1 elastic relation $\boldsymbol{\sigma}(\boldsymbol{\epsilon})$ we may conclude the existence of the elastic energy $\psi(\boldsymbol{\epsilon}) = \sigma_{ij}(\boldsymbol{\epsilon})\ \epsilon_{ij} - \bar{\psi}(\boldsymbol{\sigma}(\boldsymbol{\epsilon}))$ with the help of Legendre transformation. The scaling (26) can be interpreted in the following way: we define a scaled strain with

$$\bar{\epsilon}_{ij} = Q_{ijkl}\epsilon_{kl} = \mu_{ik}\epsilon_{kl}\mu_{lj} \tag{28}$$

and we write the elastic energy with the new argument $\psi(\bar{\boldsymbol{\epsilon}})$. Using twice the chain rule $(\partial \sqcup/\partial\epsilon_{ij}) = (\partial \sqcup/\partial\bar{\epsilon}_{ab})(\partial\bar{\epsilon}_{ab}/\partial\epsilon_{ij})$ we obtain (26). The function $\psi(\bar{\boldsymbol{\epsilon}})$ is a new potential taking into account a and m_i. The advantage of the above method is that we can "add" some a-type anisotropy to an arbitrary hyperelastic stiffness *a posteriori*, without spoiling the conservation of energy, etc.

4.3 Measurement of Elastic Stiffness

The small-strain triaxial tests on Karlsruhe fine sand have been performed with local strain measurements by means of LDTs (strips of phosphore bronze equipped with strain gauges, [8, 12]) mounted on prismatic specimens (dimensions $a \times b \times h = 90 \times 90 \times 180$ mm). Two lateral faces of the sample were equipped with eight LDTs for horizontal strain measurements (Fig. 6). The other two faces faces were equipped with four LDTs for axial strain measurements. Samples of different densities were prepared. Various average stresses were tested in succession. At each average stress, stress cycles in six different directions were applied. All tests were stress controlled. The cycles of lateral effective stress were applied via pore air pressure, while the cell pressure was kept constant in order to prevent thermal disturbances of extremely sensitive LDT measurements. All samples were dry. The pore pressure and the cell pressure were applied pneumatically.

In order to investigate purely elastic material response at each average stress, 100 preconditioning cycles with larger stress amplitudes were applied in all six directions. They were intended to induce a shakedown. The essential test cycles of smaller amplitudes consisted of 30 cycles per stress point and 5 cycles per polarization. The usual accumulation of plastic strains was almost absent after the preconditioning. The material response was therefore nearly elastic during the essential test cycles. The data from the smaller cycles have been used for the analysis of the response envelopes following the procedure described in Sect. 4.4. Typical stain paths obtained for the smaller cycles are provided in Fig. 6.

Figure 7 presents the response envelopes derived from the experimental data for three different densities, three average mean pressures and seven average stress ratios. Due to the larger stiffness, the response envelopes grow with increasing values of pressure and density. Furthermore, their principal axes rotate with the average stress ratio η^{av}. The green points in Fig. 7 denote the average stresses of the tests. The points on the response envelopes corresponding to purely deviatoric or purely volumetric strain cycles are marked by the red or blue points, respectively.

4.4 Calibration of Hyperelasticity

The stiffness matrix E is found after inversion of the compliance matrix

$$\mathsf{E} = \begin{bmatrix} E_{PP} & E_{PQ} \\ E_{QP} & E_{QQ} \end{bmatrix} = \begin{bmatrix} C_{PP} & C_{PQ} \\ C_{QP} & C_{QQ} \end{bmatrix}^{-1} \tag{29}$$

Initially, the hyperelastic constants α, c and n have been calibrated by minimizing the difference between the components E_{PP}, E_{PQ}, E_{QQ} of the theoretical stiffness matrix E from (29) and the respective components $\breve{E}_{PP}$, $\breve{E}_{PQ}$, $\breve{E}_{QQ}$ from laboratory tests. As described in Sect. 4.3, a set of such values has been obtained in the vicinity of a fixed average stress P_K^{av}, Q_K^{av} optimizing the coefficients of linear relation between strain and stress increments applied in different directions there. This requires a refined smoothing filter of the strain and stress paths. Moreover, a sophisticated algorithm for automatic detection of reversals [14] was necessary. The cumulative effects as well as some small-strain nonlinearity have to be sorted out [14]. Having such "purified" stiffnesses at $K = 1, \ldots N$ (here $N = 23$) different average states (P^{av}, Q^{av}) we can find α, c and n which minimize the following function:

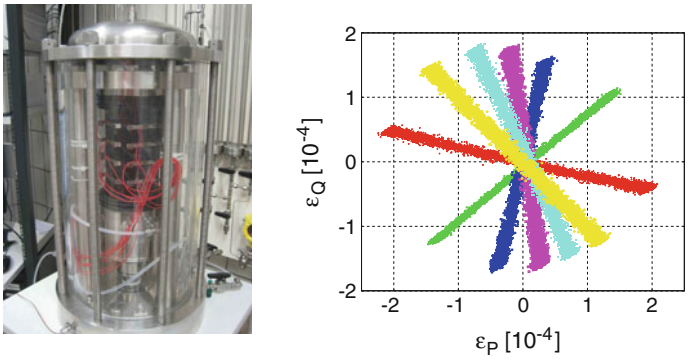

Fig. 6 *Left* Prismatic sample with LDTs [6, 13]. *Right* Strain paths measured for the cycles applied in six different directions [13]

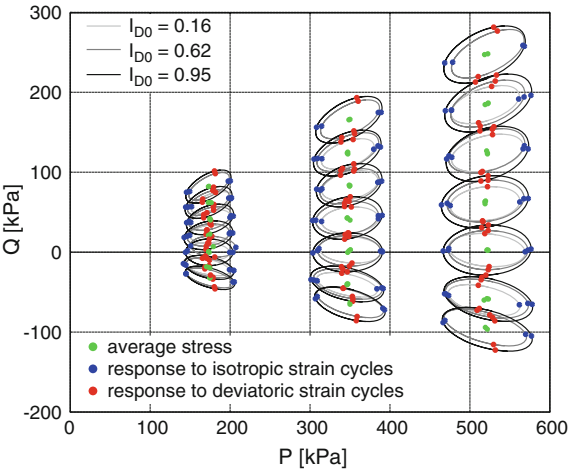

Fig. 7 Response envelopes obtained experimentally for the strain span $\|\Delta\epsilon\| = 10^{-4}$ at different densities and average stresses [13]

$$F = \sum_{K=1}^{N} \left(\check{E}^K_{PP} - E^K_{PP}\right)^2 + 2\left(\check{E}^K_{PQ} - E^K_{PQ}\right)^2 + \left(\check{E}^K_{QQ} - E^K_{QQ}\right)^2 \tag{30}$$

All increments of stresses and strains have been measured at a fixed distance $\|\Delta\epsilon\| \approx 1 \times 10^{-4}$ from the recent strain path reversal to obtain comparable values, not spoiled by small-strain variability of stiffness. We cannot claim, however, that the measured values correspond to the maximum small-strain stiffness (dynamic stiffness). Unfortunately, function (30) turns out to be a poor indicator for the calibration. As an alternative, we rewrite (8) in the form

$$(1-n)(2-n)\bar{\psi}(\boldsymbol{\sigma}) = \boldsymbol{\sigma} : \mathsf{C} : \boldsymbol{\sigma}, \tag{31}$$

and define from it another error function

$$F_B = \frac{1}{N}\sum_{K=1}^{N}\sqrt{\left(\frac{L_K - H_K}{L_K}\right)^2} \tag{32}$$

$$\text{with} \quad L_K = \boldsymbol{\sigma}^{\text{av}}_K : \check{\mathbf{C}}^K : \boldsymbol{\sigma}^{\text{av}}_K \quad \text{and} \quad H_K = (1-n)(2-n)\bar{\psi}(\boldsymbol{\sigma}^{\text{av}}_K) \tag{33}$$

This time, the discrepancies in stiffness are weighted by the underlying average stress. The symmetry of the resulting compliance is enforced, similarly as in (30). Using the results from the set of $N = 23$ experiments on medium dense sand loaded in different directions amplitude of we obtain the constants $\alpha = -0.3516$ and $c = 1.517 \times 10^{-4}$ (the homogeneity order $n = 0.6$ was set) by minimizing (32). The error of the calibration was small, $F_B = 0.02567$, however the resulting response envelopes were significantly slenderer than the experimental ones.

In a further refinement of the calibration, we kept $c = 1.517 \times 10^{-4}$ and $n = 0.6$ but adjusted α manually, until the RE from (10) coincided with the experimental ones. After this manual refinement, the resulting parameters were $\alpha = 0.1$, $c = 1.54 \times 10^{-4}$ and $n = 0.6$. The average error of calibration slightly increased to $F_B = 0.0306$. A comparison of the hyperelasticity and the laboratory results is shown in Fig. 8.

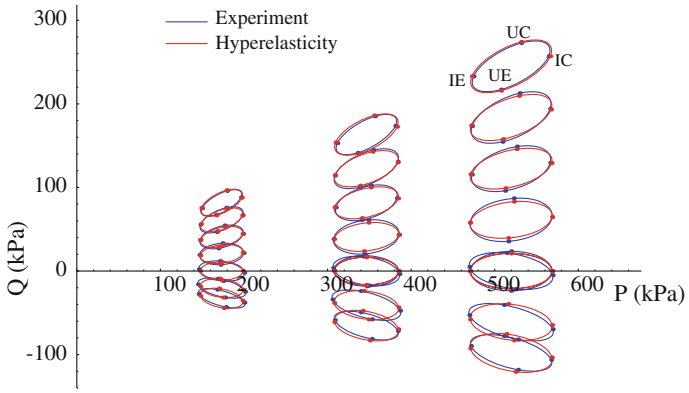

Fig. 8 Comparison between the response envelopes of the 23 experiments (*blue*) on medium dense sand evaluated for $\|\Delta\boldsymbol{\epsilon}\| = 10^{-1}$ and the theoretical response envelopes from (10) with adjusted constants $\alpha = 0.1$, $c = 1.54 \times 10^{-4}$, and $n = 0.6$

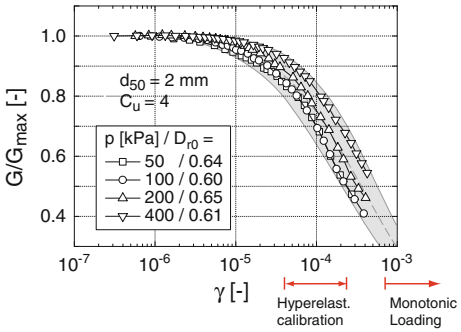

Fig. 9 Dependence of small-strain stiffness on amplitude [25]

For simulations of monotonic tests the overall compliance constant $c = 1.54 \times 10^{-4}$ has been temporarily increased to $c = 0.001$. This was necessary due to the fact that the paraelastic (PE) part of neohypoplasticity was not used in the simulations. The reduced stiffness for long monotonic deformations corresponds to the shear strain $\gamma > 0.1\,\%$, i.e. it lies beyond the range shown in Fig. 9, whereas the measurements correspond to the small strains of $\epsilon^{\text{ampl}} \approx 0.01\,\%$. For the PE part, on the other hand,

we need to *decrease* the measured value of c to obtain $G = G_{\max}$ corresponding to $\gamma \approx 10^{-6}$ in Fig. 9.

4.5 Skew-Symmetric Modification of the Elastic Stiffness

It is not possible to rotate the undrained points UC,UE of the response envelope in Fig. 10 from the elastic stiffness E keeping the shape of the ellipse and the position of isotropic points IC and IE unchanged. The original hyperelastic stiffness must be symmetric $E_{PQ} = E_{QP}$, Fig. 10 (left). Applying the modification with L from Fig. 10 (right), we break this symmetry. The position of undrained points must be rotated clockwise for dense and counterclockwise for loose sand. To this end, we propose to add to E_{ijkl} a skew-symmetric part of a dyad of isotropic direction and deviatoric direction (both unit tensors). For the PQ-plane, the new matrix has the form

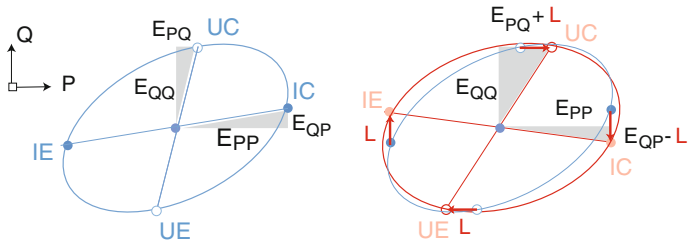

Fig. 10 Interpretation of elastic off-diagonal components of stiffness E with the response envelope. *Left* hyperelasticity with $E_{PQ} = E_{QP}$. *Right* modification with a skew-symmetric matrix with $L > 0$. This modification is further called U-rotation. Such clockwise U-rotation is used at $Q > 0$ for dense sand

$$\begin{bmatrix} E_{PP} & E_{PQ} \\ E_{QP} & E_{QQ} \end{bmatrix} + \begin{bmatrix} 0 & L \\ -L & 0 \end{bmatrix} \quad \text{with} \quad |L| \le E_{QQ} \tag{34}$$

with

$$L = \operatorname{sign}(Q)\ \left[|Q|/(M_{\text{peak}}\,P)\right]^{n_L} \cdot \begin{cases} c_{LL}\ (e - e_c)/(e_i - e_c) & \text{for} \quad e > e_c \\ c_{LD}\ (e_c - e)/(e_c - e_d) & \text{for} \quad e < e_c \end{cases} \tag{35}$$

and with material constants

c_{LD}	c_{LL}	n_L
0.2	−0.5	1

. The characteristic void ratios e_i, e_c, e_d for loose, critical and dense sand, respectively, are well known from the older versions of hypoplasticity [1, 23], see also Eq. (42).

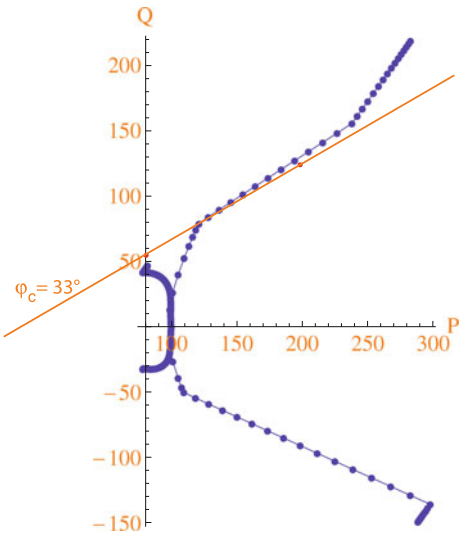

Fig. 11 With the help of the rotation L the difference between φ_U and φ_{peak} could be simulated. Four simulations with neohypoplasticity are presented in which undrained loading is followed by drained loading. The undrained dense samples follow the mobilized friction angle of 34.9° in shearing. They can significantly increase this angle in drained continuation of loading, as desired. Similar results show simulations with loose sand

The following remarks can be made to the function $L(\boldsymbol{\sigma}, e)$:

- For triaxial compression, $Q > 0$, we obtain $L < 0$ for loose, and $L > 0$ for dense sand as desired. For $e = e_c$ we have $L = 0$.
- The nonsymmetry is small for small $Q/(PM_{\text{peak}})$
- The nonsymmetry should not be used in paraelastic (PE) modelling [17] of small cycles[8]
- The modified stiffness matrix $\begin{bmatrix} 1 & c + Lb \\ c - Lb & b \end{bmatrix}$ is invertible for $1 > b > c^2 > 0$ for any L (Fig. 11).

The general (tensorial) form of the skew-symmetric portion is proposed in the form

$$S_{ijkl} = L\,(\vec{T}^*_{ij}\vec{\delta}_{kl} - \vec{\delta}_{ij}\vec{T}^*_{kl}) \tag{36}$$

and the modified stiffness is denoted as

$$\bar{E}_{ijkl} = E_{ijkl} + S_{ijkl} \tag{37}$$

4.6 Nonlinear Part Y of Neohypoplasticity

Let us introduce the following stress invariant:

[8]This prevents a violation of the Second Law of thermodynamics.

$$H(\boldsymbol{\sigma}) = \sigma_{ii}\ \ \sigma_{jj}^{-1} - 9 \qquad \in (0, \infty), \tag{38}$$

valid in the one octant of the principal stress space where all principal stresses are negative, $\sigma_i < 0$. In σ_{jj}^{-1} we should first inverse the tensor and then calculate the trace, of course. The yield criterion by Matsuoka and Nakai [15] takes with $H(\boldsymbol{\sigma})$ a simple form

$$F_{M-N}(\boldsymbol{\sigma}) = H(\boldsymbol{\sigma}) - \phi \le 0 \qquad \text{with} \quad \phi = 8\tan^2\varphi \tag{39}$$

If any principal stress vanishes, $\sigma_i = 0$, then $H(\boldsymbol{\sigma}) = \infty$. Working on the PQ plane,[9] we may express $H(\boldsymbol{\sigma})$ in the form $H = 9\sqrt{2}(h + \sqrt{2})/[(\sqrt{2} - h)(2h + \sqrt{2})] - 9$, where $h = Q/P$ is the stress obliquity from the range $h \in (-\frac{\sqrt{2}}{2}, \sqrt{2})$.

It is not a good idea to define the degree of nonlinearity Y equal to H/ϕ. At first glance, such definition may seem quite promissing: $Y = 0$ on the hydrostatic axis and $Y = 1$ corresponds to (39) as desired. Moreover, one can easily propose a function $\phi = \phi(e, P)$ that matches the peak friction angle φ_{peak} depending on void ratio and pressure. The problem with such Y is subtle: we need a longer range of $h = Q/P$ for which the degree of nonlinearity is close to unity, say $Y \in (0.9, 1)$. If the degree of nonlinearity were simply H/ϕ, then the triaxial compression curves would arrive at peak after an unrealistically small shear deformation. Moreover, serious problems with the simulation of $\varphi_{\text{peak}} - \varphi_U$ could be expected, cf. Sect. 4.

A better degree of nonlinearity is given by the following function:

$$Y(x) = A_Y \exp(-1/(B_Y x^{n_Y} + C_Y)) \qquad \text{with} \quad x = H/\phi(e, P) \quad \text{and} \quad Y(1) = 1 \tag{40}$$

From four material constants A_Y, B_Y, C_Y, n_Y only three B_Y, C_Y, n_Y are available for fitting whereas A_Y is determined from the constraint $Y(1) = 1$, i.e. from $A_Y = \exp(1/(B_Y + C_Y))$. A reasonable estimation could be

B_Y	C_Y	n_Y
20	0.3	2

, where:

- larger B_Y elongates the range of h with $Y \approx 1$
- larger C_Y increases the minimal value $Y_{\min} = Y(0)$
- larger n_Y increases the range of h with $Y \approx Y_{\min}$

Expression (40) returns the values $Y(x)$ close to unity over a long range of x, as demonstrated in Fig. 14 (middle). This helps to simulate the difference between φ_U and φ_{Peak}. A rough[10] estimation of the material constants can be conveniently per-

[9] For Roscoe invariants p, q we have the obliquity $\eta = q/p \in (-\frac{3}{2}, 3)$ and $H = 27(\eta + 3)/[(3 - \eta)(2\eta + 3)] - 9$. The value $H = \infty$ corresponds to $\eta = -3/2$ or $\eta = 3$ or the mobilized friction angle is $\arcsin(3\eta/(6 + \eta)) = \pm 90°$.

[10] The parameters n_Y and B_Y are independent of the void ratio, for simplicity.

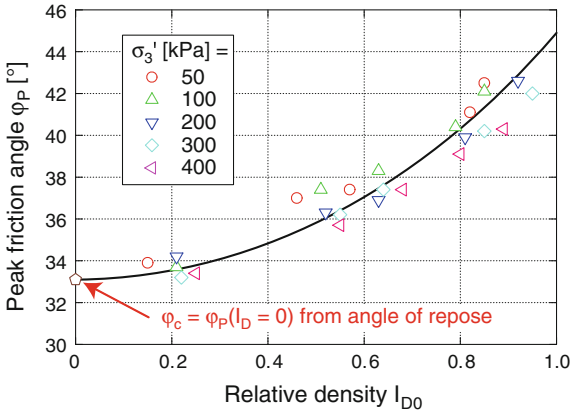

Fig. 12 Peak friction angles reached in drained tests at different void ratios

formed with the following MATHEMATICA manipulator:

Nonlinearity $Y(h)$ over $h = Q/P$

```
Manipulate[
 sq2 = Sqrt[2];
 s = 1/2;
 \[Phi] = 8 s^2 /(1 - s^2);
 Hh = 9 sq2(h + sq2)/((sq2-h)(2h + sq2 ))-9;
 x = Hh / \[Phi];
 A = 1 /Exp[ -1/(B  +  C)] ;
 Plot[{1,  A  Exp[-1/(B x^n +  C)]},
       {h, -sq2/2 + 0.01, sq2 - 0.01},
  PlotRange -> {-0.5, 2.2}] ,
 {{B, 10, "B"}, 2, 30},
 {{C, 0.1, "C"}, 0, 10.0},
 {{n, 1, "n"}, 0.5, 8}
 ]
```

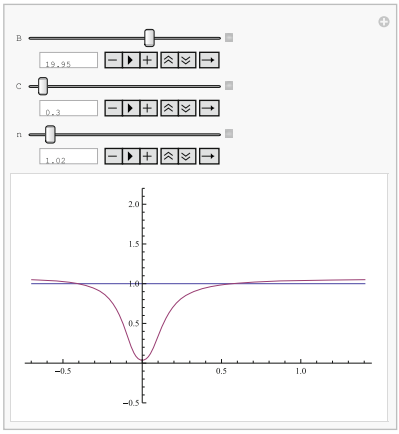

The degree of nonlinearity Y depends on stress via $H(\boldsymbol{\sigma})$ and on the void ratio via $\phi(e, P)$. In order to facilitate the calibration of the model, we introduce the peak friction angle described by the function $\varphi(e)$, Fig. 12. It will be substituted to $\phi(\varphi)$. The peak friction angle can be simply interpolated between three characteristic values given in the table

	Loose	Critical	Dense
Max. friction angle void ratio	$\varphi_i = 32°$	$\varphi_c = 33°$	$\varphi_d = 50°$
	$e_{i0} = 1.1$	$e_{c0} = 1.0$	$e_{d0} = 0.6$

using the void ratio e corrected by the barotropy function (pressure-dependent characteristic void ratios), viz.

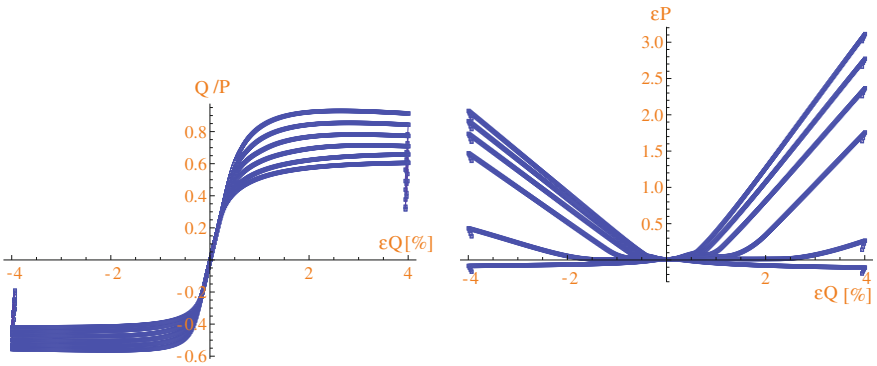

Fig. 13 Neohypoplastic simulations of isobaric ($P = 100$ kPa) shearing for different initial void ratios: $e = \{0.542, 0.621, 0.701, 0.781, 0.861, 0.992\}$ (*upwards*). The peak friction angle (*left*) and the dilatancy (*right*) increase with density according to (40)

$$\varphi(e, P) = \varphi_c + \begin{cases} (\varphi_d - \varphi_c)\frac{e_c - e}{e_c - e_d} \\ (\varphi_c - \varphi_i)\frac{e - e_c}{e_i - e_c} \end{cases} \tag{41}$$

taking the positive fraction. The characteristic void ratios $e_i(P), e_c(P), e_d(P)$ are found after [1] from

$$e_{\sqcup}(P) = e_{\sqcup 0} \exp\left[-(\sqrt{3}P/h_s)^{n_B}\right] \quad \text{with} \quad \sqcup = d, i, c \tag{42}$$

with the material constants

e_{i0}	e_{c0}	e_{d0}	h_s	n_B
1.1	1.0	0.6	5.8×10^5	0.28

calibrated[11] in [11]. Using $\varphi(e, P)$ from interpolation (41) we obtain finally

$$\phi = 8 \tan^2[\varphi(e, P)] \tag{43}$$

The simulations with the neohypoplastic model, Fig. 13, reproduce the required dependence of the peak friction angle on the void ratio. Moreover, contrarily to the old versions of the hypoplastic model, the peak friction angle is reached after a few percent deformation (and not after a few permille). This deformation at peak can be easily increased choosing a larger value of B_Y.

[11] For the old hypoplastic model [23, 24].

4.7 Flow Rule m_{ij}

The flow rule is an element of the hypoplastic model which is always active. Contrarily to elastoplasticity, m_{ij} is used inside the yield surface and also upon unloading. The flow rule is described by the unit tensor m_{ij} so it dictates just the direction of plastic flow. The intensity of plastic flow is proportional to $Y\|\dot{\epsilon}\|$.

Apart from usual notation $\phi_\sqcup = 8\tan^2\varphi_\sqcup$ for $\sqcup = i, c, d$, we introduce a mobilized friction angle φ_a, above which the associated flow rule (AFR) holds. We also denote $\phi_a = 8\tan^2\varphi_a$ for this new angle. The flow rule is formulated for three special cases

$$m_{ij} = \begin{cases} m^a_{ij} = (\partial H/\partial\sigma_{ij})^{\rightarrow} = \left[\delta_{ij}\ \ \sigma^{-1}_{kk} - \sigma_{kk}\,\sigma^{-2}_{ij}\right]^{\rightarrow} & \text{if} \quad H \geq \phi_a \\ m^c_{ij} = \left[\delta_{ij}\ \ \sigma^{-1}_{kk} - \sigma_{kk}\,\sigma^{-2}_{ij}\right]^{*\rightarrow} & \text{if} \quad H = \phi_c \\ m^i_{ij} = (\delta_{ij})^{\rightarrow} & \text{if} \quad H = 0 \end{cases} \tag{44}$$

corresponding to AFR, isochoric flow and purely volumetric flow, respectively. The following interpolations (with respect to H) between them give reasonable dilatancy and contractancy

$$\mathbf{m} = x\mathbf{m}^c + (1-x)\mathbf{m}^i \qquad \text{with} \quad x = (H/\phi_c)^{n_1} \tag{45}$$

$$\mathbf{m} = x\mathbf{m}^a + (1-x)\mathbf{m}^c \qquad \text{with} \quad x = [(H - H_c)/(\phi_a - \phi_c)]^{n_2}\,, \tag{46}$$

wherein the following material constants

φ_a	n_1	n_2
36°	0.1	1.0

have been used.

For simplicity, the presented dilatancy and contractancy are functions of stress only, i.e. $m_{ij}(\boldsymbol{\sigma})$. In the literature, e.g. [20], also the void ratio and the length of the shear strain path are taken into account. Such enhanced contractancy is discussed in Sect. 4.8. The differences in the dilatancy diagram, Fig. 13 (right), obtained from simulations with the neohypoplastic model do not result from the direct dependence $m_{ij}(e)$. Such dependence has not been implemented. The reason for larger dilatancy at smaller void ratio e is the higher obliquity Q/P enabled by small e. For higher

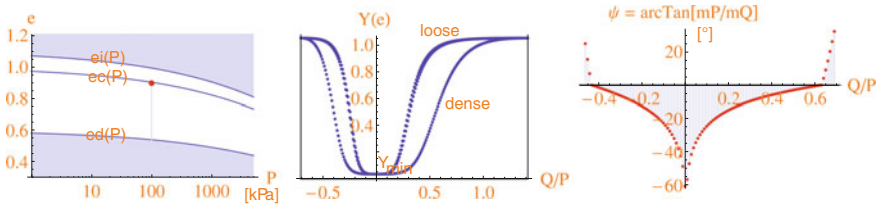

Fig. 14 *Left* the compression diagrams $e_i(P)$, $e_c(P)$ and $e_d(P)$ from [1], Eq. (42). *Middle* the degree nonlinearity (40) for loose and for dense sand as a function of $h = Q/P$. *Right* the dilatancy angle from the flow rule (45) and (46) used in the simulations

Q/P the function $m_{ij}(\boldsymbol{\sigma})$ is more dilatant. This aspect was similarly modelled in the old hypoplasticity. It should be noticed, however, that the dilatancy was significantly smaller, especially for triaxial extension. Such underestimated dilatancy caused poor FE predictions of strip foundations. The predicted failure mechanism at maximum loading was always punching, independently of the density of the sand. Besides, the bearing capacity was strongly overestimated. For dense sand, the dilatancy should activate the well-known log-spiral mechanism with bulging on both sides of the foundation. Therefore, the present dilatancy curve increases rapidly beyond the critical value of Q/P for both compression and extension, Fig. 13 (right).

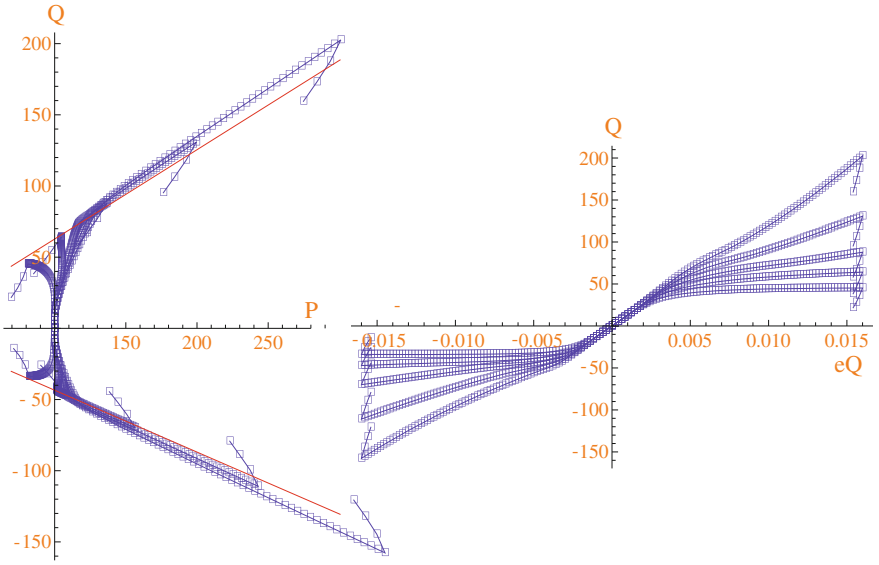

Fig. 15 Neohypoplastic simulations of undrained shearing for different void ratios

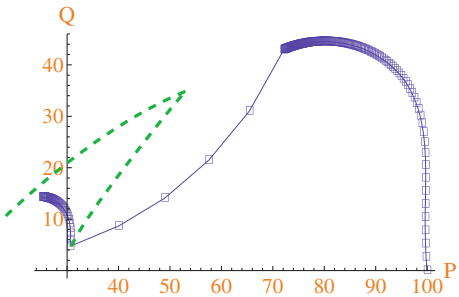

Fig. 16 Neohypoplastic simulation of an undrained shearing interrupted by a small undrained unloading and then continued. The *green dashed line* corresponds qualitatively to the material response observed during reloading in the laboratory

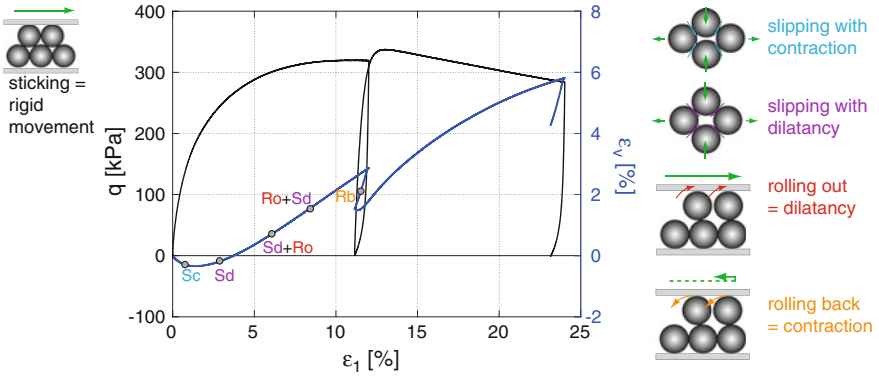

Fig. 17 Micromechanical interpretation of drained triaxial shear deformation for different states on the conventional stress–strain–dilatancy diagram

The flow rule m_{ij} and the skew-symmetric portion of the stiffness, see Sect. 4.5, influence collectively the undrained paths. The simulations of undrained shearing are shown for different void ratios in Fig. 15. Under undrained conditions, the maximum stress obliquities should not strongly differ despite different void ratios, see Sect. 4. The simulations from Fig. 15 show the desired behaviour. Each path (at different void ratio) ends with a small unloading. An interesting defect of the new model reveals the simulation of an undrained reloading shown in Fig. 16.

4.8 Butterfly Trajectory from Undrained Stress Cycles

A significant improvement of the undrained simulations can be obtained introducing an additional contractancy. Some authors, e.g. [4], attribute this contractancy to the rolling of grains during shearing at large stress obliquity, Fig. 17. After a 180° reversal of shearing the direction of rolling changes. Such backwards rolling is associated with strong contractancy. On the microscopic level one can think of grains which roll into the holes from which they have been rolled out. During undrained shearing, this contractancy manifests itself as a strong relaxation of P after stress reversals. Under undrained symmetric stress cycles, such relaxation accumulates. Finally, the stress is passing through the origin of the stress space and a characteristic shape of the stress path can be observed. This shape is sometimes called a "butterfly" and the phenomenon is known as the "cyclic mobility".

In order to describe this additional contractancy, we need information, how much dilatancy has been accumulated due to rolling. Moreover, we must know, what direction of shearing caused this accumulation. A further continuation of such shearing leads to further accumulation. Shearing in the opposite direction corresponds to rolling back and causes contractancy. For mathematical description of these phe-

nomena we introduce, similarly as in [21], a structural variable (a deviator) $\mathbf{z}$. Its norm $\|\mathbf{z}\|$ should grow during dilatant rolling and decline with contractant rolling back. Direction of the strain rate should be used as an indicator:

- rolling out with dilatancy for $\mathbf{z} : \dot{\boldsymbol{\epsilon}} > 0$
- rolling back with contractancy for $\mathbf{z} : \dot{\boldsymbol{\epsilon}} < 0$

The proposed evolution equations for $\mathbf{z}$ and for the rate of contractancy due to rolling $\dot{\epsilon}^r_P$ are

$$\dot{\mathbf{z}} = \left(1 + \frac{\|\mathbf{z}\|}{z_{\max}}\right)\left(\dot{\boldsymbol{\epsilon}}^* - \frac{\mathbf{z}}{z_{\max}}\|\dot{\boldsymbol{\epsilon}}^*\|\right) \quad \text{with} \quad z_{ii} = 0 \tag{47}$$

$$\dot{\boldsymbol{\sigma}} = \bar{\mathsf{E}} : \left(\dot{\boldsymbol{\epsilon}} - \mathbf{m}\, Y \|\dot{\boldsymbol{\epsilon}}\| - \omega\, \vec{\mathbf{1}}\, \langle -\mathbf{z} : \dot{\boldsymbol{\epsilon}}\rangle\right), \quad \text{where} \quad \bar{\mathsf{E}} = \mathsf{E} + \mathcal{S} \tag{48}$$

and where $\mathcal{S}$ is given in (36). The Macauley brackets $\langle \sqcup \rangle = \frac{1}{2}(\sqcup + |\sqcup|)$ neglect the third term on the r.h.s. of (48), if $\mathbf{z} : \dot{\boldsymbol{\epsilon}} > 0$ is satisfied (rolling out). The factor ω, initially intended as a material constant, has been rendered a barotropic function $\omega(P)$. It grows at small pressures P in accordance to the observation that the cyclic accumulation at a constant strain amplitude accelerates with decreasing P, cf. [18]. Hence we propose

$$\omega(P) = \frac{P_{\text{ref}}}{z_{\max}(P_{\min} + P)} \quad \text{with} \quad P_{\text{ref}} = 100\sqrt{3} \quad \text{and} \quad P_{\min} = 3\ \text{kPa} \tag{49}$$

The material constants are

$z_{\max}$	$P_{\min}$	P_{ref}
0.05	3	173

Given $\dot{\boldsymbol{\sigma}}$ we may ask, under what conditions the constitutive equation can be uniquely solved for $\dot{\boldsymbol{\epsilon}}$. A suitable condition of invertibility

$$\left[1 - 2\omega\,(\vec{\mathbf{1}} : \mathbf{m})(\mathbf{z} : \mathbf{m}) + \omega^2\,(\mathbf{z} : \mathbf{m})^2\right] Y^2 < 1 \tag{50}$$

has been derived in Appendix A. The jeopardy of non-unique solutions appears at $Y \approx 1$, i.e. at high Q/P. A rough estimation $(1 + \omega^2\|\mathbf{z}\|^2)Y^2 < 1$ lies on the safe side.

The stress paths from undrained stress cycles have been simulated with the neohypoplastic model at different average deviator Q^{av}, Figs. 18, 19 and 20. The cyclic mobility with the characteristic butterfly-shaped stress path is reached in nearly symmetric cycles, Fig. 20, when the stress path is passing (almost) through zero. The strain–stress plots from these tests are shown in Fig. 21. Simulations on loose sand end with a direct liquefaction. After reaching $P = 0$ the stress deviator Q is locked and no further stress cycles are possible, see Fig. 22. Strain cycles at $P = 0$ and $Q = 0$ are possible but the resulting phenomena like latent contractancy are outside the scope of the neohypoplastic model. The proposed form of description

of additional contractancy due to rolling is still provisional and may be modified in future. The following features of the novel state variable $\mathbf{z}$ are of importance:

- The evolution equation $\dot{\mathbf{z}}(\dot{\epsilon})$ is independent of stress.
- The state variable $\mathbf{z}$ is "shaken down" by symmetric strain cycles.
- No jumps in $\dot{\sigma}$ may be caused by small changes in $\dot{\epsilon}$ independently of $\mathbf{z}$.
- Unlike Y, the nonlinearity due to $\mathbf{z}$ should not vanish on the P-axis.

The paraelastic part of the model is not included in the present study. In particular, simulation of small cycles may predict excessive accumulation or, generally, the response of the model after strain path reversals may be a bit awkward. In the simulations of strain cycles (stress amplitude declines with the relaxation of P) shown in Fig. 23, the cumulative relaxation is overestimated. Nevertheless, the relaxation of P and Q is qualitatively well reproduced.

5 On Numerical Implementation of Neohypoplasticity

The neohypoplastic model has been implemented in the form of several MATHEMATICA scripts for the PQ plane. The increments can be stress-, strain- or mixed-controlled, i.e. from four increments $\Delta\epsilon_P$, $\Delta\epsilon_Q$, ΔP, ΔQ two must be prescribed

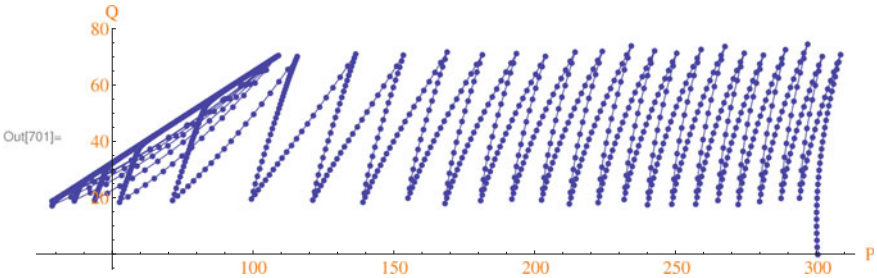

Fig. 18 Strongly asymmetric stress cycles lead eventually to "lense"-shaped closed cycles

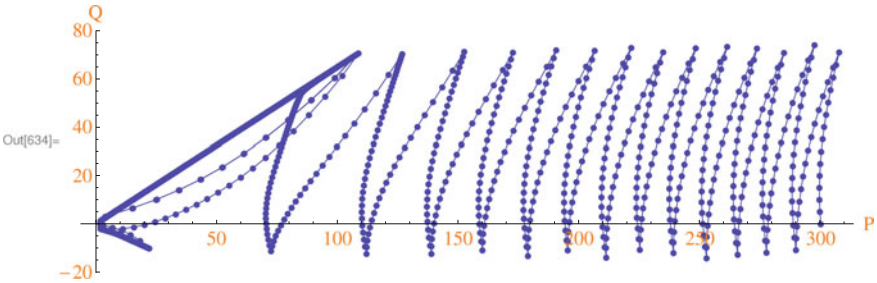

Fig. 19 Moderately asymmetric stress cycles end at "half-butterfly" with increasing strain amplitude

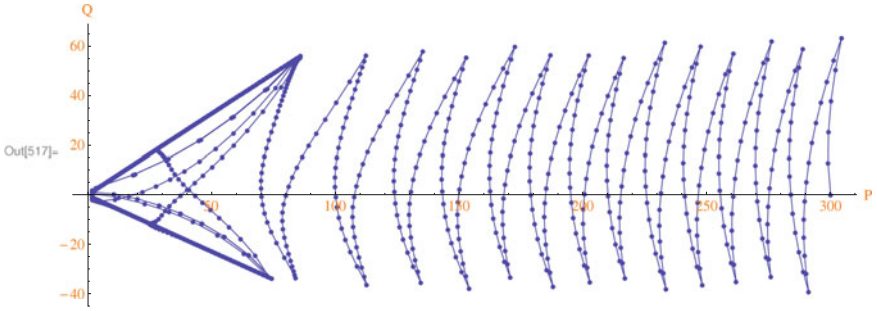

Fig. 20 Symmetric stress cycles end at "butterfly" with increasing strain amplitude

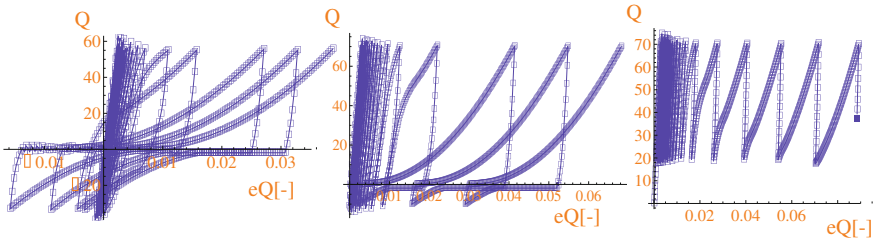

Fig. 21 Strain–stress plot for symmetric (*left*) moderately asymmetric (*middle*) and strongly asymmetric (*right*) undrained stress cycles

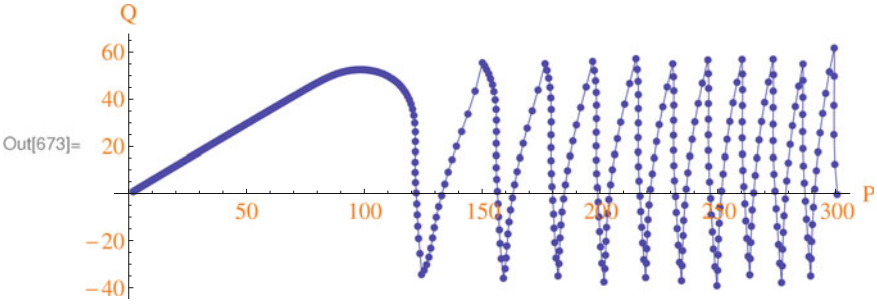

Fig. 22 No butterfly occurs in simulations with loose sand

and the other two are calculated by the constitutive model. Moreover, a special control with the prescribed value of $\Delta Q/\Delta P$ can be used. For example, in oder to simulate the drained compression with vertical strain control we can define $\Delta Q/\Delta P = \sqrt{2}$ and $\Delta\epsilon_Q = 0.001$, which enables softening.

Since the explicit time integration is used, we need sub-stepping, in particular in the vicinity of small pressures. Usually, the maximum strain increment is defined as $\Delta\epsilon_{\max} = 0.2\,\%$, so an explicit isotropic step commenced at $P < 5.6$ kPa with $\Delta P = -P$ can crash, viz.

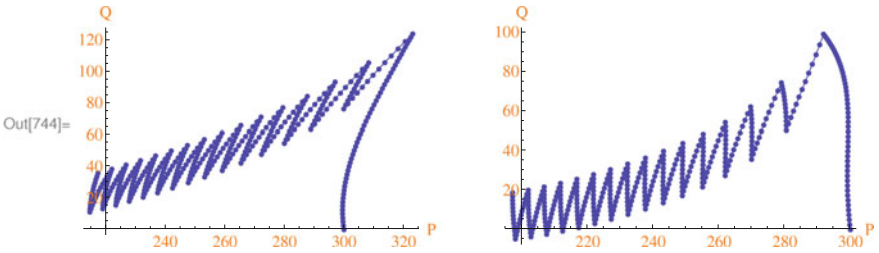

Fig. 23 Neohypoplastic simulation of undrained shearing followed by strain cycles. *Left* dense sand, *right* loose sand. In both cases, the predicted relaxation of P and Q in cycles is too fast due to the missing paraelastic part of the model

$$E_{PP} \cdot \Delta\epsilon_{\max} > P \quad \text{with} \quad E_{PP} \approx 10^3 P^{0.6} \tag{51}$$

The model cannot work with negative P and the response is unpredictable. Therefore, an artificial plasticity condition $P > 6$ kPa has been introduced. For implicit time integration, this condition is redundant, of course. Generally, one should be careful with explicit integration. As far as possible, the strain control should be used. All equations are written for prescribed strain increments. For stress increments the line search method is used. In some cases, however, in particular for states near $P = 0$ this method does not converge even for increments as small as $\|\Delta\sigma\| = 1$ kPa.

The following material constants have been used in all simulations:

Elasticity:
$n = 0.6, c = 0.001, \alpha = 0.1,$
Compression:
$h_s = 5.8 \times 10^5, n_B = 0.28, e_{i0} = 1.1, e_{c0} = 1.0, e_{d0} = 0.6$
Flow rule:
$\varphi_i = 32°, \varphi_c = 33°, \varphi_a = 36°, \varphi_d = 50°, n_1 = 0.1, n_2 = 1$
U-rotation:
$c_{LL} = -0.5, c_{LD} = 0.2, n_L = 1.0$
Nonlinearity:
$B_Y = 20.0, C_Y = 0.3, n_Y = 2$
Additional contractancy due to rolling:
$z_{\max} = 0.05, P_{\min} = 3, P_{\text{ref}} = 173$

Acknowledgments The authors are grateful to the DFG (DFG-Forschergruppe FOR 1136) for financial support.

Appendix 1: Invertibility Condition for Neohypoplasticity

If $\mathbf{z} : \dot{\boldsymbol{\epsilon}} > 0$, then the invertibility condition is $Y < 1$, identically as in the older versions of hypoplasticity, cf. [16]. In the following we examine the case $\mathbf{z} : \dot{\boldsymbol{\epsilon}} < 0$ only. First, we find two scalar variables $x = \|\dot{\boldsymbol{\epsilon}}\|$ and $y = \mathbf{z}' : \dot{\boldsymbol{\epsilon}}$, where $\mathbf{z}' = \omega\mathbf{z}$. Let us denote $\dot{\boldsymbol{\epsilon}}^{\mathrm{el}} = \mathsf{E}^{-1} : \dot{\boldsymbol{\sigma}}$ which is a known tensor. The first scalar equation is obtained multiplying the constitutive equation

$$\dot{\boldsymbol{\sigma}} = \bar{\mathsf{E}}\left(\dot{\boldsymbol{\epsilon}} - \mathbf{m}Y\|\dot{\boldsymbol{\epsilon}}\| + \vec{\mathbf{1}}\mathbf{z}' : \dot{\boldsymbol{\epsilon}}\right) \tag{52}$$

by $\mathbf{z}' : ()$

$$\mathbf{z} : \dot{\boldsymbol{\epsilon}}^{\mathrm{el}} = y - \mathbf{z}' : \mathbf{m}Yx \quad \text{because} \quad \mathbf{z}' \perp \vec{\mathbf{1}} \tag{53}$$

$$y = \mathbf{z}' : \dot{\boldsymbol{\epsilon}}^{\mathrm{el}} + \mathbf{z}' : \mathbf{m}Yx \tag{54}$$

The second scalar equation is obtained resolving the constitutive equation with substituted x, y for $\dot{\boldsymbol{\epsilon}}$ and finding $x^2 = \dot{\boldsymbol{\epsilon}} : \dot{\boldsymbol{\epsilon}}$

$$\dot{\boldsymbol{\epsilon}} = \mathsf{C} : \dot{\boldsymbol{\sigma}} + \mathbf{m}Yx - \vec{\mathbf{1}}y \tag{55}$$

$$x^2 = (\dot{\boldsymbol{\epsilon}}^{\mathrm{el}} + \mathbf{m}Yx - \vec{\mathbf{1}}y) : (\dot{\boldsymbol{\epsilon}}^{\mathrm{el}} + \mathbf{m}Yx - \vec{\mathbf{1}}y) \tag{56}$$

$$0 = \dot{\boldsymbol{\epsilon}}^{\mathrm{el}} : \dot{\boldsymbol{\epsilon}}^{\mathrm{el}} - 2\dot{\boldsymbol{\epsilon}}^{\mathrm{el}} : \vec{\mathbf{1}}y + y^2 + 2\dot{\boldsymbol{\epsilon}}^{\mathrm{el}} : \mathbf{m}Yx - 2\,\vec{\mathbf{1}} : \mathbf{m}Yxy + (Y^2 - 1)x^2, \tag{57}$$

where $\mathbf{m} : \mathbf{m} = \vec{\mathbf{1}} : \vec{\mathbf{1}} = 1$ has been used. We take y from (54) and substitute it into (57). The result is a quadratic equation $Ax^2 + Bx + C = 0$ to be solved for x. For uniqueness of the inverse solution this quadratic equation should have two roots, one positive and one negative, i.e. $x_1 x_2 < 0$ and we take the positive one because $x = \|\dot{\boldsymbol{\epsilon}}\|$. The condition $x_1 x_2 < 0$ corresponds to $C/A < 0$. Using abbreviated forms of (54) and (57), viz.

$$\begin{cases} y = \alpha + \beta x \\ 0 = ax^2 + bxy + cx + dy^2 + ey + f, \end{cases} \tag{58}$$

we obtain the quadratic equation $Ax^2 + Bx + C = 0$ with

$$\begin{cases} A = a + b\beta + d\beta^2 \\ C = f + e\alpha + d\alpha^2 \end{cases} \tag{59}$$

or

$$\begin{cases} A = (Y^2 - 1) - 2(\vec{\mathbf{1}} : \mathbf{m})(\mathbf{z}' : \mathbf{m})Y^2 + (\mathbf{z}' : \mathbf{m})^2 Y^2 \\ C = \dot{\boldsymbol{\epsilon}}^{\mathrm{el}} : \dot{\boldsymbol{\epsilon}}^{\mathrm{el}} - 2(\dot{\boldsymbol{\epsilon}}^{\mathrm{el}} : \vec{\mathbf{1}})(\mathbf{z} : \dot{\boldsymbol{\epsilon}}^{\mathrm{el}}) + (\mathbf{z} : \dot{\boldsymbol{\epsilon}}^{\mathrm{el}})^2 \end{cases} \tag{60}$$

The value C must be positive by the following argument: let us replace $\dot{\boldsymbol{\epsilon}}^{\mathrm{el}} : \dot{\boldsymbol{\epsilon}}^{\mathrm{el}}$ by $(\dot{\boldsymbol{\epsilon}}^{\mathrm{el}} : \vec{\mathbf{1}})(\dot{\boldsymbol{\epsilon}}^{\mathrm{el}} : \vec{\mathbf{1}})$, which cannot increase C and hence

$$C \geq (\dot{\boldsymbol{\epsilon}}^{\mathrm{el}} : \vec{\mathbf{1}} - \mathbf{z}' : \dot{\boldsymbol{\epsilon}}^{\mathrm{el}}) : (\dot{\boldsymbol{\epsilon}}^{\mathrm{el}} : \vec{\mathbf{1}} - \mathbf{z}' : \dot{\boldsymbol{\epsilon}}^{\mathrm{el}}) > 0 \tag{61}$$

for any $\dot{\boldsymbol{\epsilon}}^{\mathrm{el}} \neq 0$. The condition of invertibility can be therefore reduced to $A < 0$ or

$$\left[1 - (2\,\vec{\mathbf{1}} : \mathbf{m})(\mathbf{z}' : \mathbf{m}) + (\mathbf{z}' : \mathbf{m})^2\right] Y^2 < 1 \tag{62}$$

References

1. Bauer, E.: Zum mechanischen Verhalten granularer Stoffe unter vorwiegend ödometrischer Beanspruchung. PhD thesis, Institut für Boden und Felsmechanik der Universität Karlsruhe (TH), Heft, Nr. 130 (1992)
2. Bažant, Z.P.: Endochronic inelasticity and incremental plasticity. Int. J. Solids Struct. **14**, 691–714 (1978)
3. Dafalias, F., Manzari, M.T.: Simple plasticity sand model accounting for fabric change effects. J. Eng. Mech. **130**, 22–34 (2004)
4. Dafalias, Y.F.: Overview of constitutive models used in VELACS. In: Arulandan, K., Scott, R. (eds.) Verification of Numerical Procedures for the Analysis of Soil Liquefaction Problems, Proceedings of the International Conference in Davis, vol. 2, pp. 1293–1304. Balkema, California (1994)
5. Desrues, J., Chambon, R., Mokni, M., Mazerolle, F.: Void ratio evolution inside shear bands in triaxial sand specimens studied by computed tomography. Géotechnique **46**(3), 529–546 (1996)
6. Espino, E.: Quasi-statische Untersuchungen zur Elastizität von Sand als Grundlage eines neuen hypoplastischen Stoffmodells. Master's thesis, Institut für Boden- und Felsmechanik, Karlsruher Institut für Technologie, Mai (2014)
7. Gajo, A., Wood, D.M.: Severn trent sand: a kinematic hardening constitutive model: q-p formulation. Géotechnique **49**(5), 595–614 (1999)
8. Goto, S., Tatsuoka, F., Shibuya, S., Kim, Y.-S., Sato, T.: A simple gauge for local small strain measurements in the laboratory. Soils Found. **31**(1), 169–180 (1991)
9. Graham, J., Houlsby, G.T.: Anisotropic elsticity of a natural clay. Géotechnique **33**(2), 165–180 (1983)
10. Gudehus, G.: A comparison of some constitutive laws for soils under radially symmetric loading and unloading. In: Proceedings of the 3rd International Conference On Numerical Methods in Geomechanics, Balkema, Aachen (1979)
11. Herle, I.: Hypoplastizität und Granulometrie einfacher Korngerüste. PhD thesis, Institut für Boden- und Felsmechanik der Universität Karlsruhe, Nr. 142 (1997)
12. Hoque, E., Sato, T., Tatsuoka, F.: Performance evaluation of LDTs for use in triaxial tests. Geotech. Test. J. **20**(2), 149–167 (1997)
13. Knittel, L.J.: Fortgesetzte quasi-statische Untersuchungen zur Elastizität von Sand als Grundlage eines neuen hypoplastischen Stoffmodells. Master's thesis, Institut für Boden- und Felsmechanik, Karlsruher Institut für Technologie (2014)
14. Loges, I., Niemunis, A.: Neohypoplasticity—estimation of small strain stiffness. In: Triantafyllidis, Th. (ed.) Holistic Simulation of Geotechnical Installation Processes. Numerical and Physical Modelling. Springer (2014)
15. Matsuoka, H., Nakai, T.: Stress-strain relationship of soil base on the SMP, constitutive equations of soils. In: Murayama, S., Schofield, A.N. (eds.) Proceedings of the 9th International

Conference On Soil Mechanics and Foundation Engineering, Speciality Session 9. Japanese Society of Soil Mechanics and Foundation Engineering, IX ICSMFE, Tokyo (1997)
16. Niemunis, A.: Extended hypoplastic models for soils. Politechnika Gdańska, Habilitation, Monografia 34 (2003)
17. Niemunis, A., Prada-Sarmiento, L.F., Grandas-Tavera, C.E.: Paraelasticity. Acta Geotech. **6**(2), 67–80 (2011)
18. Niemunis, A., Wichtmann, T., Triantafyllidis, T.: A high-cycle accumulation model for sand. Comput. Geotech. **32**(4), 245–263 (2005)
19. Richart, F.E.Jr. , Hall, J.R.Jr., Woods, R.D.: Vibrations of Soils and Foundations. Prentice-Hall, Englewood Cliffs (1970)
20. Sands, C.M., Chandler, H.W.: Simulations of cyclic shearing of sand at low effective stress. Géotechnique **61**(11), 983–992 (2011)
21. Taiebat, M., Dafalias, Y.: Sanisand: simple anisotropic sand plasticity model. Int. J. Numer. Anal. Meth. Geomech. **32**(8), 915–948 (2008)
22. Vermeer, P.: A five-constant model unifying well established concepts. In: Constituents Relay for Soils, Proceedings of the International Workshop in Grenoble, pp. 175–198. Balkema, Holland (1982)
23. von Wolffersdorff, P.-A.: A hypoplastic relation for granular materials with a predefined limit state surface. Mech. Cohes.-Frict. Mat. **1**, 251–271 (1996)
24. von Wolffersdorf, P.-A.: Verformungsprognosen für Stützkonstruktionen. PhD thesis, Institut für Boden- und Felsmechanik der Universität Karlsruhe, Habilitationschrift, Heft Nr. 141 (1997)
25. Wichtmann, T., Triantafyllidis, T.: Influence of the grain size distribution curve of quartz sand on the small strain shear modulus $G_{\max}$. J. Geotech. Geoenviron. Eng. **135**(10), 1404–1418 (2009)

Constitutive Model for Clays Under the ISA Framework

W. Fuentes, M. Hadzibeti and Theodoros Triantafyllidis

Abstract The Intergranular Strain Anisotropy ISA framework is a novel approach to develop elastoplastic models wherein a yield surface is defined in terms of strain increments. For this purpose, the loading-unloading conditions are satisfied within the space of the intergranular strain, this latter being a state variable "following" the strain rate. With this, the model aims to improve the simulations under cyclic loading while keeping their good capabilities at monotonic loading. Within this article, a constitutive model for clays is developed under the ISA plasticity framework. The model adopts some parameters from the modified Cam-Clay model and others to describe the evolution of the integranular strain and its effect on the model response. Some illustrative simulations are provided to analyze the model performance under cyclic loading. The simulations show a qualitative behavior in agreement with some experiments. Possible improvements are discussed at the end of the article.

Keywords Clay model · ISA plasticity · Intergranular strain

1 Introduction

The intergranular strain anisotropy (ISA) plasticity, recently proposed by Fuentes and Triantafyllidis [4], is a mathematical framework useful for the development of constitutive models simulating the cyclic behavior of the material. It is based on the concept of the intergranular strain [11], being a state variable which provides information about the recent strain history. Specifically, the intergranular strain variable has information related with the change of strain rate direction $\overrightarrow{\dot{\epsilon}}$ within a strain amplitude of approximately $|| \Delta\varepsilon || \approx 10^{-3}$. Having this, the constitutive model increases the stiffness and reduces the plastic accumulation upon every change of strain rate direction $\overrightarrow{\dot{\epsilon}}$. All these effects have shown to provide a better performance of the simulations under cyclic loading.

W. Fuentes (✉) · M. Hadzibeti · T. Triantafyllidis
Institute of Soil Mechanics and Rock Mechanics, Karlsruhe Institute of Technology,
Engler-Bunte-Ring 14, 76131 Karlsruhe, Germany
e-mail: william.lacouture@kit.edu

T. Triantafyllidis (ed.), *Holistic Simulation of Geotechnical Installation Processes*, Lecture Notes in Applied and Computational Mechanics 80, DOI 10.1007/978-3-319-23159-4_6

The idea of the intergranular strain was originally proposed by Niemunis and Herle [11] in order to mitigate the excessive plastic accumulation exhibited by some Karlsruhe hypoplastic models, e.g., the model by [13]. The physical explanation attributed to this variable, even this is debatable, consists in the idea that it represents the deformations of the interface layers between the soil particles (intergranular space) and accordingly, very small deformations of these interfaces are responsible of the small strain effects, namely the stiffness increase, the reduction of the plastic strain rate, and the appearance of an elastic locus upon cyclic loading. The formulation by Niemunis and Herle [11] did simulate well some of aforementioned small strain effects except for the appearance of an elastic locus, fact which motivated the development of the recently proposed ISA formulation [3], in which an elastic locus of the material within the space of the intergranular strain and other small strain effects are truly considered.

So far with the new ISA framework, the formulation has shown to simulate well tests performing cyclic loading on sands [3, 4], but still not been tested on the simulations of fine-grained soils. Therefore, this article is committed to show the performance of the model with a direct focus on the simulation of the clay mechanical behavior. The relations presented herein are mostly based on the previous model for sands by Fuentes and Triantafyllidis [4] but modified to account for additional required effects of clays. While the evolution equation of the intergranular strain remains identical as in the previous formulation [4], some other relations have been modified for the sake of convenience, namely the compression law at isotropic conditions, the dilatancy surface which now coincides with the critical state surface and an overconsolidation factor considered to improve the simulations under these states. The details of the new relations will be provided in the next sections.

The notation of this article is as follows. Scalar quantities are denoted with italic fonts (e.g., a, b), second rank tensors with bold fonts (e.g., $\mathbf{A}$, $\boldsymbol{\sigma}$), and fourth rank tensors with Sans Serif type (e.g., E, L). Multiplication with two dummy indices, also known as double contraction, is denoted with a colon ":" (e.g., $\mathbf{A} : \mathbf{B} = A_{ij} B_{ij}$). When the symbol is omitted, it is then interpreted as a dyadic product (e.g., $\mathbf{AB} = A_{ij} B_{kl}$). The deviatoric component of a tensor is symbolized with an asterisk as superscript $\mathbf{A}^*$. The effective stress tensor is denoted with $\boldsymbol{\sigma}$ and the strain tensor with ε. The Roscoe invariants are defined as $p = -\mathrm{tr}\boldsymbol{\sigma}/3$, $q = \sqrt{3/2} \parallel \boldsymbol{\sigma}^* \parallel$, $\varepsilon_v = -\mathrm{tr}\boldsymbol{\epsilon}$ and $\varepsilon_s = \sqrt{2/3} \parallel \boldsymbol{\epsilon}^* \parallel$.

2 Intergranular Strain Model

Conventionally, constitutive models for soils propose yield functions describing a surface within the stress space. In Contrast to this, the ISA plasticity focuses on the incorporation of the elastic locus in terms of strain amplitudes (within the strain space) and not within the stress space. A yield function with such characteristics is expected to depend on a variable having information of the strain amplitude. One of the simplest idea to compute the current strain amplitude would be to subtract

from the current strain the one at the last reversal point, as by the paraelastic models [12]. Nevertheless, this operation may be numerically unstable when dealing with very small strain amplitudes $|| \varepsilon || < 10^{-4}$. On the contrary, the intergranular strain does not need the introduction of reversal points, but gives information about the strain amplitude. In the following lines, the formulation of the intergranular strain according to the ISA model is recalled [4].

Consider an elastic locus of the material within the intergranular strain space $\mathbf{h}$, described with a yield function $F_H = F_H(\mathbf{h}, \mathbf{c}) = 0$ whereby $\mathbf{c}$ is a hardening variable to be defined in the sequel. It is now established that if $F_H < 0$, the response of the material is elastic, and the intergranular strain $\mathbf{h}$ evolves identically as the strain ε does:

$$\dot{\mathbf{h}} = \dot{\epsilon} \qquad \text{for} \qquad F_H < 0 \tag{1}$$

This is a very convenient evolution equation, since any hardening variable (as the yet unknown tensor $\mathbf{c}$) remains constant under elastic conditions $F_H < 0$, and the increments of intergranular strain are equal to the increments of strain, i.e., $\Delta\mathbf{h} = \Delta\varepsilon$. This latter condition is very useful to define a yield function describing an elastic locus in terms of strain amplitude. If the strain amplitude of the elastic locus is constant, this surface looks like a sphere within the principal intergranular strain space whose center is represented with $\mathbf{c}$. Following this, the yield function can be defined as:

$$\text{IS yield surface:} \qquad F_H \equiv \| \mathbf{h} - \mathbf{c} \| - R/2 = 0 \tag{2}$$

whereby the tensor $\mathbf{c}$ has been termed the "back-intergranular strain" being actually a hardening variable, and the parameter R is a constant representing the maximum amplitude of the elastic strains. In the space of the volumetric invariant $h_v/\sqrt{3} = -\text{tr}(\mathbf{h})/\sqrt{3}$ and the deviator invariant $\sqrt{3/2}h_s = \| \mathbf{h}^* \|$, where $\mathbf{h}^*$ is the deviator intergranular strain, the IS yield surface from Eq. 2 takes exactly the form of a circle, as illustrated in Fig. 1.

Now consider the plastic case in which the intergranular strain "touches" the yield surface $F_H = F_H(\mathbf{h}, \mathbf{c}) = 0$. In that case, it is desired that after a reversal loading, the material exhibits smoothly the appearance of a plastic strain rate. Brittle materials would present a very rapid change of the stiffness when changing from elastic to plastic behavior, but most soils and some other materials show actually a smooth stiffness transition when it turns from the elastic into plastic regime. This effect can be well simulated through a hardening mechanism of the yield surface described with tensor $\mathbf{c}$. For the ISA framework, some simple relations of the bounding surface plasticity have been adopted to simulate this behavior. Hence, the model considers besides the yield surface a bounding surface within the intergranular strain space.

To formulate the behavior under plastic conditions $F_H = 0$, a plastic term is added to the intergranular strain evolution equation:

$$\dot{\mathbf{h}} = \dot{\epsilon} - \dot{\lambda}_H \mathbf{N} \qquad \text{for} \qquad F_H = 0 \tag{3}$$

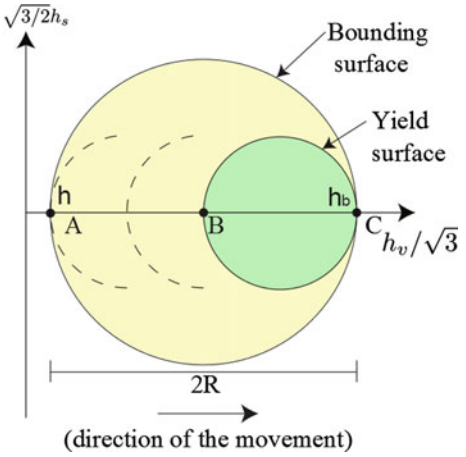

Fig. 1 Yield surface and bounding surface within the space of the intergranular strain

whereby $\dot{\lambda}_H$ is a consistency parameter and $\mathbf{N}$ is the intergranular strain flow rule being normal to the IS yield surface (see Fig. 1):

$$\mathbf{N} = (\mathbf{h} - \mathbf{c})^{\rightarrow} \tag{4}$$

In the last equation, the operator $\sqcup^{\rightarrow}$ extracts the direction of the tensor $\sqcup^{\rightarrow} = \sqcup / \parallel \sqcup \parallel$. The consistency parameter $\dot{\lambda}_H \geq 0$ in Eq. 3 is related with the yield surface function F_H and deduced considering the consistency condition $\dot{F}_H = 0$.

The bounding surface within the intergranular strain space is depicted in Fig. 1. This surface has the same shape as the yield surface but with twice its size and a center at the origin. Its function takes the following form:

$$\text{IS bounding surface:} \qquad F_{Hb} \equiv \parallel \mathbf{h} \parallel - R = 0 \tag{5}$$

The evolution equation for the back-intergranular strain $\mathbf{c}$ can be expressed as a function of the consistency parameter $\dot{\lambda}_H$:

$$\dot{\mathbf{c}} = \dot{\lambda}_H \bar{\mathbf{c}} \tag{6}$$

whereby $\bar{\mathbf{c}}$ is its hardening function. The hardening function $\bar{\mathbf{c}}$ presents the following relation:

$$\bar{\mathbf{c}} = \beta(\mathbf{c}_b - \mathbf{c})/R \qquad \text{with} \qquad \mathbf{c}_b = R/2(\dot{\boldsymbol{\epsilon}})^{\rightarrow} \tag{7}$$

whereby β is a material parameter and $\mathbf{c}_b$ is the image of $\mathbf{c}$ at the bounding surface. The consistency condition $\dot{F}_H = 0$ followed by substitution with Eqs. 2, 6, 7 and 3 yields to the consistency parameter definition $\dot{\lambda}_H$:

$$\dot{\lambda}_H = \frac{\langle \mathbf{N} : \dot{\boldsymbol{\epsilon}} \rangle}{1 + H_H} \tag{8}$$

where the operator $\langle\rangle$ are the Macaulay brackets and $H_H = -(\partial F_H/\partial \mathbf{c}) : \bar{\mathbf{c}}$ is the hardening modulus.

In the following lines, a scalar function is introduced to quantify how close is the intergranular strain $\mathbf{h}$ to the bounding surface $F_{Hb} = 0$. Similar to the image tensor $\mathbf{c}_b$, one can propose an image tensor of the intergranular strain at the bounding surface denoted by $\mathbf{h}_b$ and defined as:

$$\mathbf{h}_b = R\mathbf{N} \tag{9}$$

The distance $\| \mathbf{h}_b - \mathbf{h} \|$ provides information of how close is the intergranular strain $\mathbf{h}$ to the bounding surface $F_{Hb} = 0$. According to the proposed model, the bounding condition $\mathbf{h} = \mathbf{h}_b$ should be asymptotically reached after applying large strains in a constant direction $\overrightarrow{\dot{\epsilon}}$. At these states, $\mathbf{N}$ should reach the value of $\overrightarrow{\dot{\epsilon}}$. This particular state in which $\mathbf{N} = \overrightarrow{\dot{\epsilon}}$ and $\mathbf{h} = R\overrightarrow{\dot{\epsilon}}$ has been called the "fully mobilized" state. The scalar function ρ is introduced to consider how close is the current state to this "fully mobilized" state:

$$\rho = 1 - \frac{\| \mathbf{h}_b - \mathbf{h} \|}{2R} \tag{10}$$

This scalar function provides two important and illustrative cases. It renders $\rho = 0$ when $\| \mathbf{h}_b - \mathbf{h} \| = 2R$, which means strain reversal after fully mobilized state. On the other side, $\rho = 1$ when $\mathbf{h} = \mathbf{h}_b$ for fully mobilized state. The last case is very useful when formulating relations of the mechanical model under medium and large strain amplitudes.

3 Mechanical Model Formulation

Having defined the evolution equation of the intergranular strain $\mathbf{h}$, it is now proceeded with the description of the mechanical model which relates the rate of (effective) stress $\dot{\boldsymbol{\sigma}}$ with the rate of the strain $\dot{\epsilon}$. The constitutive relation is based on the ISA plasticity framework [3] which can be written with the following general form:

$$\dot{\boldsymbol{\sigma}} = m\bar{\mathbf{E}} : (\dot{\boldsymbol{\epsilon}} - y_h \bar{\dot{\boldsymbol{\epsilon}}}^p) \tag{11}$$

where $\bar{\mathbf{E}}$ is the residual stiffness, or with other words, the stiffness at mobilized states $\rho = 1$, the tensor $\bar{\dot{\boldsymbol{\epsilon}}}^p$ corresponds to the plastic strain rate at mobilized states $\rho = 1$ and the scalar functions m and y_h have been introduced to increase the stiffness and reduce the plastic strain rate, respectively, upon cyclic loading ($y_h < 1$). The factor y_h is proposed, such that it reduces the plastic strain rate upon unloading and guarantees the stress rate continuity between the elastic and plastic response. The simulation of these two effects are achieved through the multiplication of two factos as follows:

$$y_h = \rho^{\chi_h} \langle \mathbf{N} : \overrightarrow{\dot{\epsilon}} \rangle \tag{12}$$

whereby the factor ρ^{χ_h} reduces the plastic strain rate upon cyclic loading and the factor $\langle \mathbf{N} : \dot{\boldsymbol{\epsilon}} \rangle$ is the one responsible of the stress rate continuity. Notice that this factor also appears in the numerator of the consistency parameter Eq. 8, fact which is not a coincidence. Notice also that when $y_h = 0$, the response is (hypo-)elastic whereas $y_h = 1$ implies fully mobilized states.

The factor m responsible for the stiffness increase is a simple function interpolating between $1 \leq m \leq m_R$, whereby $m_R > 1$ is a material constant. The function from Fuentes and Triantafyllidis [4] is here adopted:

$$m = m_R + (1 - m_R) y_h \tag{13}$$

One of the main features of the ISA plasticity is that at fully mobilized states, the effect of the scalar functions m and y_h vanishes, i.e., $m = 1$ and $y_h = 1$, and the general constitutive equation yields to:

$$\begin{aligned} \dot{\boldsymbol{\sigma}} &= \bar{\mathsf{E}} : (\dot{\boldsymbol{\epsilon}} - \bar{\dot{\boldsymbol{\epsilon}}}^p) \\ &= \bar{\mathsf{E}} : (\dot{\boldsymbol{\epsilon}} - Y \mathbf{m} \parallel \dot{\boldsymbol{\epsilon}} \parallel) \end{aligned} \tag{14}$$

whereby $Y = \parallel \bar{\dot{\boldsymbol{\epsilon}}}^p \parallel / \parallel \dot{\boldsymbol{\epsilon}} \parallel$ is the degree of nonlinearity [10] and $\mathbf{m} = \overrightarrow{\bar{\dot{\boldsymbol{\epsilon}}}^p}$ is a flow rule ($\parallel \mathbf{m} \parallel = 1$). This particular form can be adjusted to the mechanical behavior exhibited by the material at medium and large strain amplitudes at which the condition $y_h = 1$ is expected. Furthermore, it recalls some constitutive equations proposed in the literature, whereby a plastic strain component is always active, such as the Karlsruhe hypoplastic models [6, 10, 13], which according to some authors, simulate well the behavior at these strain amplitudes. Hence, even this is not a must, one may adopt some existing formulations of the Karlsurhe hypoplastic model for the tensors $\bar{\mathsf{E}}$ and $\bar{\dot{\boldsymbol{\epsilon}}}^p$. To give an example, if the interest focuses on the simulation of the behavior of clays, it is possible to adopt directly the existing relations for $\bar{\mathsf{E}}$ and $\bar{\dot{\boldsymbol{\epsilon}}}^p$ from the hypoplastic model by Masin [9]. Anyway, within this work a similar formulation as the previous ISA-type model for sands by [4] is adopted as reference, and some of its functions are modified to simulate the clay behavior. These modifications are based on some conventional concepts, such as the distinction of normal consolidated and overconsolidated states which are explained within the next sections. Further steps toward the model development are still missing, such as the consideration of viscous effects and partial saturation.

3.1 Normal Consolidation and Critical State Line

As typically done with clays, this model distinguishes between normal consolidated sates and overconsolidated states. The first is identified at isotropic stress states

$q = 0$ when the void ratio is equal to $e = e_i$, whereby e_i is the maximum void ratio defined as:

$$e_i = e_{i0} - \lambda \log(p/p_{\text{ref}}) \tag{15}$$

where e_{i0} is a parameter describing the value of the maximum void ratio e_i at $p = p_{\text{ref}} = 1$ kPa, the scalar λ is the compression index and $p_{\text{ref}} = 1$ kPa is a reference (fixed) value. Notice that Eq. 15 is the relation originally proposed by the modified Cam-clay model. The Hvorlesv pressure $p = p_i$ is the maximum pressure at constant void ratio, which is obtained from Eq. 15:

$$p_i = \exp\left((e_{i0} - e)/\lambda\right) \tag{16}$$

The critical void ratio e_c follows also from the relations of the modified Cam-clay:

$$e_c = (e_{i0} - \lambda \log(2)) - \lambda \log(p/p_{\text{ref}}) \tag{17}$$

where $e_{c0} = e_{i0} - \lambda \log(2)$ is the critical void ratio at $p = 1$ kPa. The term $\lambda \log(2)$ in Eq. 17 comes from the fact, that once the critical state is reached, the mean pressure yields accordingly to a value of $p = p_i/2$.

Within the stress space, the model incorporates a bounding surface to describe some observations like the peak stress ratio of the material, and a critical state surface governing the behavior at large deformations ($|| \varepsilon || > 25\,\%$). Similar to the ISA model for sands by Fuentes [4] and some bounding surface models [1, 8], a "loading direction" tensor is introduced to project at these surfaces the current stress ratio $\mathbf{r} = \boldsymbol{\sigma}^*/p$, whereby $\boldsymbol{\sigma}^*$ is the deviator stress. The loading direction tensor is denoted by $\mathbf{n}$ and defined according to Fuentes [4]:

$$\mathbf{n} = \left[\overrightarrow{\mathbf{r}} + \langle -\overrightarrow{\mathbf{r}} : \mathbf{N}^* \rangle (\overrightarrow{\mathbf{N}^*} - \overrightarrow{\mathbf{r}})\right]^{\rightarrow} \tag{18}$$

The critical state surface is described with the condition $F_c \equiv F_c(\boldsymbol{\sigma}, \mathbf{n}) = 0$, whereby:

$$\text{Critical state surface:} \qquad F_c \equiv \mathbf{r} : \mathbf{n} - r_c = 0, \qquad r_c = \sqrt{2/3} M_c g(\theta_{\mathbf{n}}) \tag{19}$$

where M_c is the critical state slope for triaxial compression in the $p - q$ space and the scalar function $g = g(\theta_{\mathbf{n}})$ is evaluated with the Lode's angle $\theta_{\mathbf{n}}$ of the loading direction tensor $\mathbf{n}$. This function is responsible of the shape of the critical state surface seen from a deviator plane, as schematically shown in Fig. 2. It ranges between $c \leq g \leq 1$ whereby $c = M_e/M_c = 3/(3 + M_c)$ represents the ratio between the critical state slope for triaxial extension M_e and triaxial compression M_c according to Mohr-Coulomb. The function defining g follows the simple relation:

$$g(\theta) = \frac{2c}{(1 + c) - (1 - c)\cos(3\theta)} \tag{20}$$

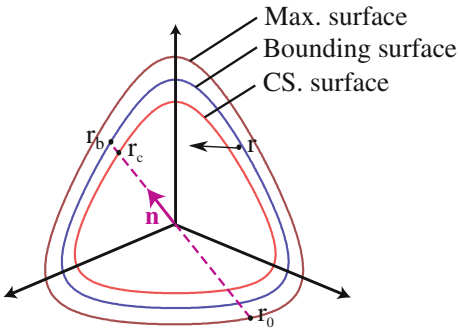

Fig. 2 Stress ratio images at the maximum surface, bounding surface, and critical state surface

The bounding surface represents the condition $\| \bar{\dot{\epsilon}}^p \| / \| \dot{\epsilon} \| = Y = 1$ within the stress space. According to Eq. 14, if the strain rate is in the same direction as the flow rule $\overrightarrow{\dot{\epsilon}} = \mathbf{m}$, the stresses would not change $\dot{\boldsymbol{\sigma}} = \mathbf{0}$ at the bounding surface. This is advantageous, because one may associate the shape of this surface as the maximum stress ratios $\| \mathbf{r} \|$ reached by the experiments. Within this model, the clay anisotropy due to the loading history is considered though the effect of the intergranular strain and not by the bounding surface. This means that, even this bounding surface does not present an additional rotational mechanism to simulate the clay anisotropy, such as in [2, 7], this latter effect is simulated through the small strain effects provided the intergranular strain formulation. The shape of the bounding surface is similar to [4], with a wedge-capped form (see Fig. 3):

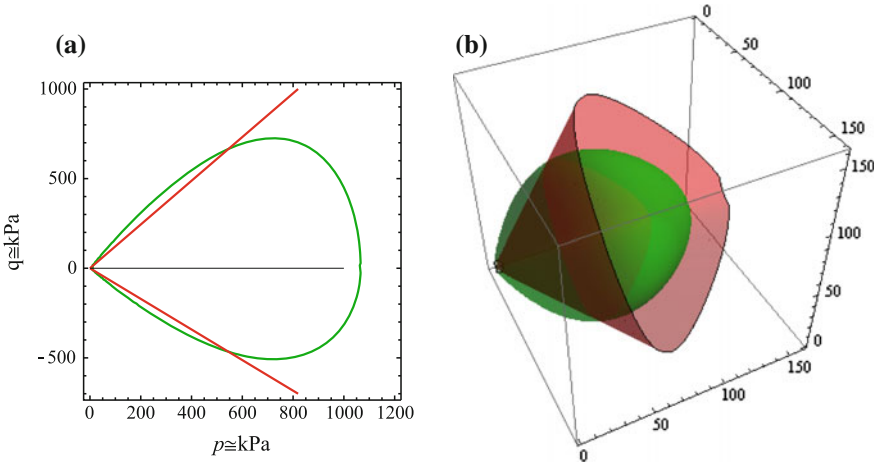

Fig. 3 **a** bounding surface within the $q - p$ space. **b** Bounding surface and critical state surface within the principal stress space

$$\text{Bounding surface:} \qquad F_b \equiv \mathbf{r} : \mathbf{n} - r_c f_b = 0 \quad \text{with} \quad f_b = f_{b0}\left(1 - \left(\frac{e}{e_i}\right)^{n_F}\right)^{1/2} \tag{21}$$

where $f_{b0} > 1$ is a material parameter defining the maximum norm of the stress ratio $\| \mathbf{r} \|$ at overconsolidated states and n_F is an exponent controlling the intersection of this surface with the critical state surface and defined as [4]:

$$n_F = \frac{\log\left((f_{b0}^2 - 1)/f_{b0}^2\right)}{\log(e_c/e_i)} \tag{22}$$

Notice that the fact that f_{b0} controls the norm of the maximum stress ratio allows to use this model for overconsolidated states. Hence, the surface described with:

$$\text{Maximum surface:} \qquad F_{b0} \equiv \mathbf{r} : \mathbf{n} - r_c f_{b0} = 0, \tag{23}$$

is the one controlling the maximum stress ratio for all states independently of the void ratio. Figure 2 gives a schematic illustration of this surface.

3.2 Stiffness Tensor

The residual stiffness $\bar{\mathbb{E}}$ is defined as in [4]:

$$\bar{\mathbb{E}} = 3\bar{K}\,\overrightarrow{\mathbf{1}}\,\overrightarrow{\mathbf{1}} + 2\bar{G}\left(\mathsf{I} - \overrightarrow{\mathbf{1}}\,\overrightarrow{\mathbf{1}}\right) - \frac{\bar{K}}{\sqrt{3}M_c}(\mathbf{1r} + \mathbf{r1}) \tag{24}$$

The bulk modulus $K = m\bar{K}$ and shear modulus $G = m\bar{G}$ are now adjusted to the behavior of clays with the following relations:

$$\bar{K} = \frac{K^L}{(1 - Y_{im})} = \frac{p}{\lambda_i}\frac{(1+e)}{(1 - Y_{im})} \tag{25}$$

$$\bar{G} = Kr \quad \text{with} \quad r = \frac{1 - 2\nu}{2(1+\nu)} \tag{26}$$

where ν is a material parameter (Poisson ratio) and the factor $Y_{im} = (r_K - 1)/(r_K + 1)$ depends on the function $r_K = \lambda/\kappa$, whereby κ is the swelling index considered as a material parameter. The details of the formulation of tensor $\bar{\mathbb{E}}$ can be found in [5, 10].

3.3 Residual Plastic Strain Rate $\bar{\dot{\epsilon}}^P$

The residual plastic strain rate tensor $\bar{\dot{\epsilon}}^P$ is proposed similar to some Karlsruhe hypoplastic models [10]:

$$\bar{\dot{\epsilon}}^P = Y\mathbf{m} \parallel \dot{\boldsymbol{\epsilon}} \parallel \tag{27}$$

whereby $Y = \parallel \bar{\dot{\epsilon}}^P \parallel / \parallel \dot{\boldsymbol{\epsilon}} \parallel$ is called the degree of nonlinearity [10] and $\mathbf{m}$ is the flow rule. This latter is defined identically as in Fuentes [4] but with a dilatancy surface equal to the critical state surface:

$$\mathbf{m} = \left(-1/2(r_c - \mathbf{r} : \mathbf{n})\mathbf{1} + \parallel \mathbf{N}^* \parallel \mathbf{n}\right)^{\rightarrow} \tag{28}$$

whereby $r_c = \sqrt{2/3}M_c g$ is the norm of the image stress ratio tensor at the critical state surface and the factor $g = g(\mathbf{n})$ has been previously defined in Eq. 20. The degree of nonlinearity Y is dictated by the relation according to [5]:

$$Y = \left(\frac{\parallel \mathbf{r} - \mathbf{r}_0 \parallel}{\parallel \mathbf{r}_b - \mathbf{r}_0 \parallel}\right)^{n_Y} \tag{29}$$

with the image stress ratio $\mathbf{r}_b = \sqrt{2/3}M_c g f_b \mathbf{n}$ and the image stress ratio at the maximum surface $\mathbf{r}_0 = \sqrt{2/3}M_c f_{b0}\mathbf{n}$, as depicted schematically in Fig. 2. As in Fuentes [4], the exponent n_Y controls the value of $Y = Y_i$ at isotropic states $q = 0$ through the relation:

$$n_Y = \frac{\log(Y_i)}{\log(f_{b0}/(f_{b0} + f_b/c))} \tag{30}$$

Whereby Y_i can be defined independently to simulate the behavior at isotropic states $q = 0$. Probably, the definition of Y_i is one of the key features of this model compared to the one for sands [4] because it now considers the effect of the overconsolidation. To do this, a factor $(p/p_i)^2$ is introduced to its definition as follows:

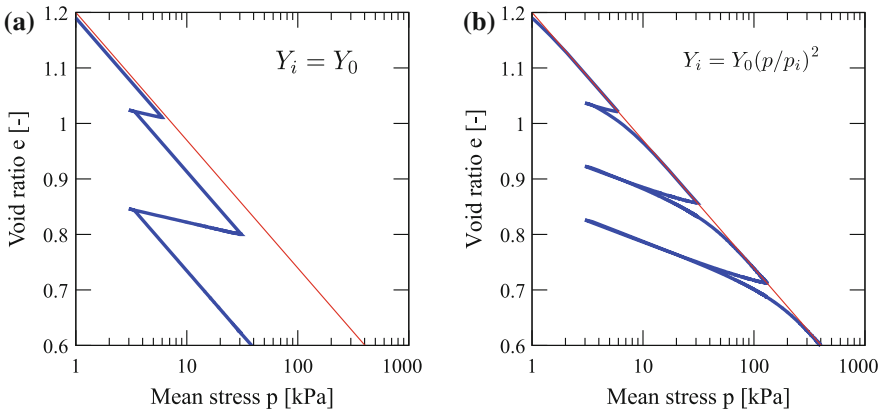

Fig. 4 Simulation of loading-unloading cycles at isotropic states $q = 0$ for different definitions of Y_i. **a** with $Y = Y_0$, **b** with $Y = Y_0(p/p_i)^2$

$$Y_i = Y_{im}(p/p_i)^2 = \left(\frac{r_K - 1}{r_K + 1}\right)(p/p_i)^2 \tag{31}$$

In order to show the influence of the factor $(p/p_i)^2$, some simulations at isotropic conditions $q = 0$ are provided in the Fig. 4. If this factor is not considered, the simulations shows ratcheting as in Fig. 4a. Simulations of the Fig. 4b shows an improvement avoiding this shortcoming.

4 Parameters and Numerical Implementation

The model requires 10 parameters listed within the Table 1. The Table presents also the description, units, approximated range, and some useful experiments for their calibration. These parameters include the basic parameters of the modified Cam-clay model namely λ, κ, e_0, ν, and M_c plus one parameter describing the maximum stress ratio f_{b0} at overconsolidated states and four additional parameters from the intergranular strain model m_R, R, β, χ_h. For their calibration, some routine tests are required, such as isotropic compression test, undrained triaxial test, drained triaxial test, and some cyclic tests.

The implementation has been performed by using a substepping explicit scheme with small strain subincrements to avoid numerical problems. The programming

Table 1 Material constants of the proposed model

Description		Units	Approx. range	Value	Useful experiments
Modified Cam-Clay					
λ	Compression index	(−)	10^{-6}−1	0.0057	IC$^{(i)}$
κ	Swelling index	(−)	10^{-6}−1	0.0057	IC$^{(i)}$
e_{i0}	Maximum void ratio	(−)	0.5−2	1.21	IC
ν	Poisson ratio	(−)	0−0.5	0.18	UTC$^{(ii)}$
M_c	CS slope	(−)	10−40	1.33	UTC, DTC
Hvorslev surface					
f_{b0}	Bounding surface factor	(−)	1−2	1.35	UTC, DTC
Intergranular strain					
m_R	Stiffness factor	(−)	1−7	5	CUTC$^{(iv)}$
R	IS yield surface radius	(−)	10^{-5}−10^{-4}	1.4×10^{-4}	−
β	IS hardening parameter	(−)	0−1	1.0	CUTC
χ_h	IS exponent	(−)	1−10	7	CUTC

(*i*) *IC* Isotropic test (loading-unloading)
(*ii*) *UTC* Undrained triaxial test
(*iii*) *DTC* Drained triaxial test
(*iv*) *CUTC* Cyclic undrained triaxial test

language corresponds to Fortran and follows the syntax of the subroutine UMAT from the software Abaqus Standard. The numerical integration of this subroutine has been performed with the software Incremental Driver which is fully compatible with the syntax of the UMAT subroutine.

5 Simulation Examples

This section presents some qualitative simulations with the proposed model. The parameters are typical for clay-like soils but has not been calibrated to any particular material. Hence, these simulations are qualitative to analyze the model response under some particular type of loading paths. For comparison purposes, some simulations with the modified Cam-clay model having the same counterpart parameters are presented. In all these simulations, the intergranular strain and back-intergranular strain where initialized with $\mathbf{h} = -R\mathbf{1}$ and $\mathbf{c} = -R/2\mathbf{1}$ to consider the effect of the initial isotropic compression before proceeding with the triaxial shearing.

Samples sheared under monotonic undrained loading were simulated and are shown in Fig. 5. Before the undrained shearing, all samples were isotropically compressed till $p = 200$ kPa reaching a void ratio of $e = 0.67$ and some of them were unloaded to different pressures. In this way, four different overconsolidated ratios OCR have been considered and correspond to OCR = {1, 2, 3, 4}. Simulations with the Modified Cam Clay model MCC have been included for comparison purposes, see Fig. 5a, c. The simulations with the MCC model show the well-known problems of this model when simulating heavy overconsolidated states (OCR $>$ 2), namely the overestimation of the peak stress ratio and the brittle transition from the elastic to plastic state. The ISA model does not present these disadvantages because the maximum stress ratio is controlled through the parameter f_{b0} and the transition from elastic to plastic states is very smoothed by the hardening of the IS yield surface.

The Fig. 6 presents the simulations of a cyclic undrained triaxial test with constant deviatoric stress amplitude and with 20 cycles. The cycles start at $p = 200$ kPa with a void ratio of $e = 0.67$. This illustrative example shows that under this cyclic loading path, the ISA model shows always plastic accumulation and finds an attractor (superimposed stress path cycles) when it reaches the critical state line, see Fig. 6b. Most of the experiments show that this attractor presents an "eight"-shape, but is attributed to the viscous effects in some plastic clays which has not been considered in the present formulation.

Figure 7 presents some simulations of cyclic undrained triaxial tests but now with constant strain amplitudes. Two simulations were included, the first with $|| \Delta\varepsilon || = 0.02$ and the second with $|| \Delta\varepsilon || = 0.005$. The cycles were performed after simulating a "large" cycle as shown in the figure. The simulations highlight the fact, that the "point attractor" (liquefaction) shape is achieved with the current model.

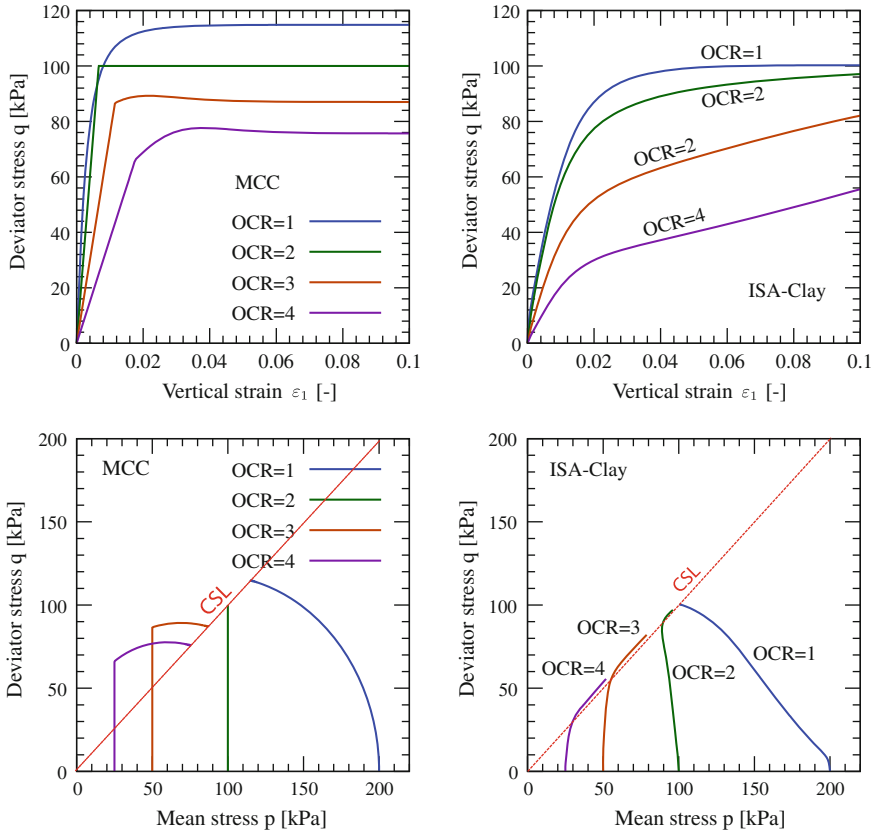

Fig. 5 Simulations of monotonic undrained triaxial test for different OCR. ISA model for clays (ISA-clay) is compared with the modified cam clay model (MCC)

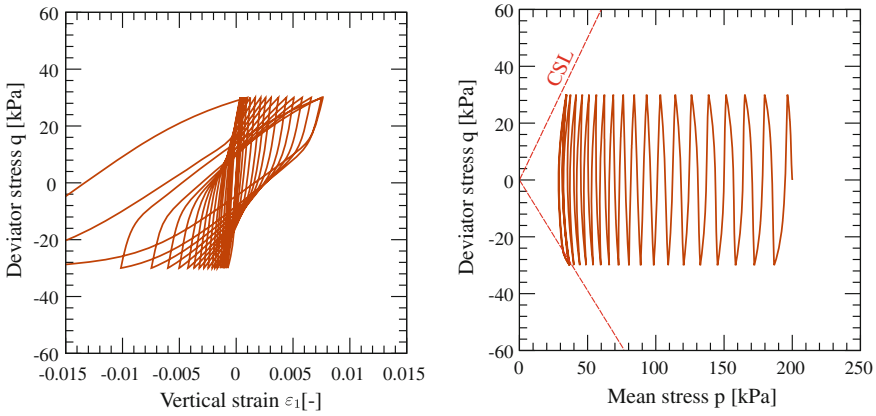

Fig. 6 Simulation with the ISA model for clays of a cyclic undrained triaxial test with constant deviator stress amplitude

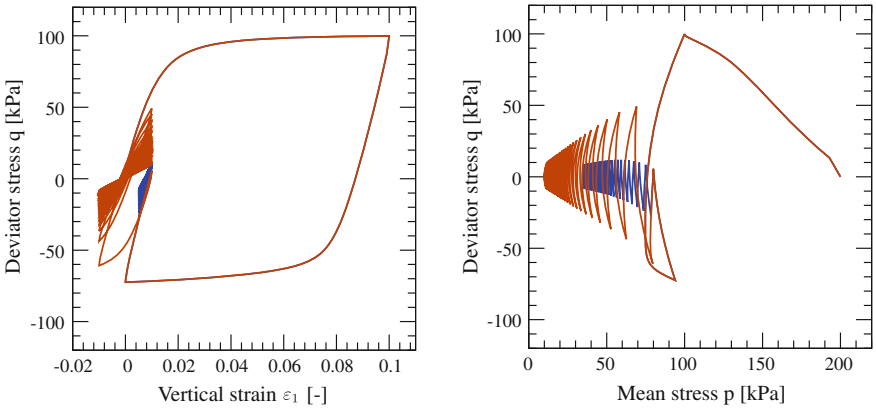

Fig. 7 Simulations with the ISA model for clays of a cyclic undrained triaxial test with constant strain amplitude (*blue* $|| \Delta\varepsilon || = 0.005$; *red* $|| \Delta\varepsilon || = 0.02$ and after a large cycle)

6 Closure and Outlook

In this article an ISA-type constitutive model for clays has been proposed. The model is based on the intergranular strain plasticity, which provides an alternative way to propose constitutive formulations describing the cyclic behavior of some soils. Similar relations as the ISA model for sands [4] were herein adopted and modified to simulate the clay behavior. The qualitative simulations showed that under some cyclic undrained loading paths, the attractors shown by the model are similar to those observed in many experiments. The next step, is to perform more validations through the simulation of experimental results and the incorporation of some effects as the material viscosity, partial saturation and cementation as well as the anisotropy.

References

1. Dafalias, Y.: Bounding surface plasticity. I: Mathematical foundation and hypoplasticity. J. Eng. Mech. ASCE **112**(9), 966–987 (1986)
2. Dafalias, Y., Manzari, M., Papadimitriou, A.: Saniclay: simple anisotropic clay plasticity model. Int. J. Num. Anal. Meth. Geomech. **30**, 1231–1257 (2006)
3. Fuentes, W.: Contributions in mechanical modelling of fill materials. PhD thesis, Karlsruhe Institute of Technology, KIT, Germany. Heft No. 179 (2014)
4. Fuentes, W., Triantafyllidis, T.: ISA model: a constitutive model for soils with yield surface in the intergranular strain space. Int. J. Num. Anal. Meth. Geomech. **39**, 1235–1254 (2015)
5. Fuentes, W., Triantafyllidis, T., Lizcano, A.: Hypoplastic model for sands with loading surface. Acta Geotech. **7**, 177–192 (2012)
6. Kolymbas, D.: Eine konstitutive Theorie für Boden und andere körnige Stoffe. Habilitation Thesis, Universität Karlsruhe, Germany. Institut für Boden- und Felsmechanik, Heft 109 (1988)
7. Leoni, M., Karstunen, M., Vermeer, P.: Anisotropic creep model for soft soils. Géotechnique **58**, 215–226 (2008)

8. Manzari, M., Dafalias, Y.: A critical state two-surface plasticity model for sands. Géotechnique **47**(2), 255–272 (1997)
9. Masin, D.: A hypoplastic constitutive model for clays. Int. J. Numer. Anal. Meth. Geomech. **29**(4), 311–336 (2005)
10. Niemunis, A.: Extended hypoplastic models for soils. Habilitation, Schriftenreihe des Institutes für Grundbau und Bodenmechanil der Ruhr-Universität Bochum, Germany. Heft 34 (2003)
11. Niemunis, A., Herle, I.: Hypoplastic model for cohesionless soils with elastic strain range. Mech. Cohesive-Frictional Mater. **2**, 279–299 (1997)
12. Niemunis, A., Prada-Sarmiento, L., Grandas-Tavera, C.: Paraelasticity. Acta Geotech. **6**, 1–14 (2011)
13. Wolffersdorff, V.: A hypoplastic relation for granular materials with a predefined limit state surface. Mech. Cohesive Frictional Mater. **1**, 251–271 (1996)

On the Use of Isotropic Hardening Plasticity to Model Cyclic Consolidation of Fine Grained Soils

Nina Müthing, Thomas Barciaga and Tom Schanz

Abstract Cyclic soil behavior plays an important role in geotechnical engineering, both in the installation phase as over the life span of constructions. Relevant application examples which find increasing attention nowadays are the dimensioning of on- and offshore foundation systems, the analysis of soil behavior due to mechanized tunneling processes as well as analyses of loading histories related to deep excavation walls. Thus, in the present paper fundamentals of cyclic soil behavior under partially drained, oedometric conditions are analyzed. Excess pore water pressure evolution and accumulated deformations are studied by both numerical and experimental approach. For this purpose, a new oedometer device is introduced which allows to measure complete stress state under transient loading. Additionally, by numerical experiments using FEM the influence of soil stiffness and permeability on the evolution of excess pore water pressures and accumulated deformations is studied. By comparison of numerical and laboratory experiments the ability of classical isotropic hardening plasticity to model cyclic consolidation phenomena is validated.

1 Introduction

Cyclically loaded structures are most common in different applications of geotechnical engineering. Typical structures as foundations of wind turbines or pipelines must be designed considering these nonmonotonic impacts. As structures are in contact with the surrounding soil understanding the soil-structure interaction as well as the underlying mechanisms is a major need. Thereby, an important role falls upon the constitutive behavior of cyclically loaded soils. This paper deals in particular with the cyclic behavior of fine grained soils as in fine grained soils excess pore water pressure build up and dissipation occurs and influencing the effective stresses and kinematics as well as the stability of the entire structure accordingly. Related to the

N. Müthing (✉) · T. Barciaga · T. Schanz
Chair of Foundation Engineering, Soil and Rock Mechanics,
Ruhr-Universität Bochum, 44780 Bochum, Germany
e-mail: nina.muething@rub.de

T. Triantafyllidis (ed.), *Holistic Simulation of Geotechnical Installation Processes*, Lecture Notes in Applied and Computational Mechanics 80, DOI 10.1007/978-3-319-23159-4_7

excess pore water pressures, the accumulation of settlements is of major interest. FEM simulations are a well-established tool to analyze this type of complex soil-structure interaction boundary value problems involving consolidation process and transient states accordingly.

Existing analytical solutions, see, e.g., [6, 7], consider cyclic loading conditions. However, in most cases these solutions are based on Terzaghi's classical theory assuming geometrical as well as constitutive linearity and therefore only rather idealized boundary value problems can be analyzed. Though, in reality with changing effective stresses and void ratio under cyclic loading conditions soil stiffness and permeability will also change.

In the present paper, partially drained consolidation of fine grained soils under cyclic loading condition is analyzed. Therefore, a newly developed one-dimensional compression cell is introduced and typical, experimental results for fine grained soils are discussed. This type of experiment involves several challenges as, for example, measuring only small amount of water inflow or outflow of the sample, measuring radial total stress and sealing the cell in order to measure and/or control pore water pressures in the samples. Furthermore, numerical experiments using FEM are carried out to study the influence of soil stiffness and permeability on the evolution of excess pore water pressures and accumulated deformations. The FEM simulations comprise one-dimensional tests involving isotropic hardening plasticity which is commonly used in engineering practice [9]. In the coupled hydraulic-mechanical analysis the soil stiffness is adapted according to the change in effective stress. Additionally soil stiffness is modeled as loading direction dependent. Plastic strains are determined based on a double hardening rule. Cap hardening is calibrated to result in realistic K_0 values under one-dimensional loading paths. Experimental results are qualitatively compared to the FEM simulations.

Summarizing, the main objective of this paper is to analyze whether classical hardening plasticity is an appropriate tool to model cyclic soil-structure interaction mechanisms involving underlying partially drained consolidation processes.

2 Experimental Study

In the experimental study partially drained, oedometric tests on soft Kaolin clay were carried out to study the cyclic consolidation behavior of fine grained soils. A new oedometer device was designed and constructed at Ruhr-Universität Bochum, introduced already in [4, 5]. In the following section the oedometer device is described regarding its technical features and testing procedure. Hydraulic boundary and loading conditions, which were used to perform cyclic tests, are given. Furthermore, the tested Spergau Kaolin clay samples are characterized and the sample preparation is described.

2.1 Oedometer Device

To experimentally analyze the consolidation behavior of fine grained soils under cyclic loading conditions a new oedometer device was implemented at Ruhr-Universität Bochum and introduced in [4]. In the new oedometer device cylindric samples of 20 mm height and 70 mm diameter are tested (see Fig. 1). The oedoemeter ring is sealed against the top and bottom plate by rubber rings. Therefore, it allows the measurement of pore water pressure and pore water volume, which is in the focus of this study. As top and bottom of the device can be set drained or undrained independently, tests under different hydraulic boundary conditions as well as undrained compression tests can be performed.

Supplementary to the functionality of a classical oedometer the following measurements are conducted: measurement of positive and negative pore water pressures up to 1000/−100 kPa at the bottom of the sample, lateral stress measurement up to 400 kPa allowed by strain gauges attached to the oedometer ring, determination of wall friction between sample and oedometer ring by measurement of vertical stress above and below the sample as well as volume measurement of the outflowing pore water.

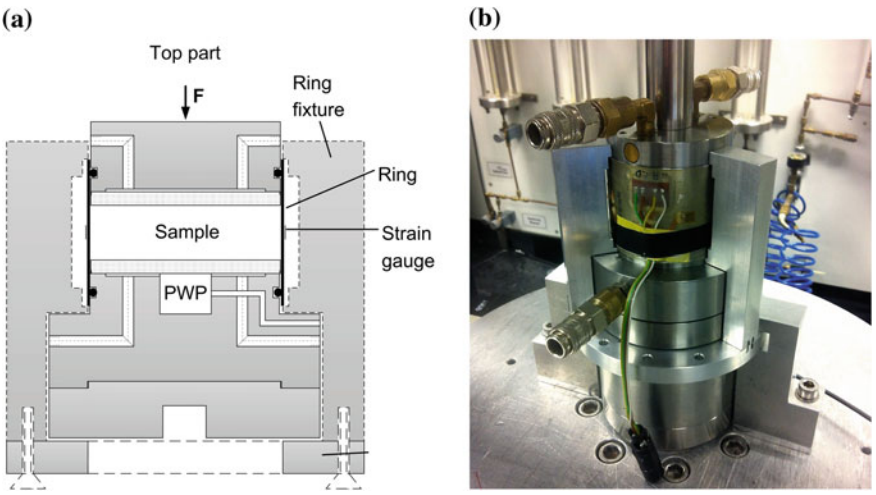

Fig. 1 **a** Sketch and **b** photograph of the new oedometer device [4]

Table 1 Plasticity of Spergau Kaolin

Liquid limit, w_L (%)	53.4
Plastic limit, w_P (%)	32.3
Shrinkage limit, w_S (%)	31.3
Plasticity index, I_P (%)	21.1

2.2 Testing Material and Sample Preparation

In the present study experiments were conducted on Spergau Kaolin clay. Spergau Kaolin is an inorganic clay of high plasticity [1]. Table 1 gives the Atterberg limit values for this clay.

The samples were prepared mixing Kaolin powder with water to a sample material with a water content slightly above liquid limit ($w = 1.1 \cdot w_L = 0.588$). The paste-like soil material with a density of $\rho = 1.63\,\mathrm{g/cm^3}$ was placed in the oedometer ring using a spattle between two deaired filter plates. Figure 2b shows an exemplary Kaolin sample.

The clay sample was saturated by streaming it from bottom to top. This procedure guarantees better saturation and allows the determination of the sample permeability, as a permeability test with variable pressure head is performed. Thereby, the mean values of the initial permeability of the samples were determined, for details see [4].

2.3 Hydraulic Boundary Conditions

The hydraulic boundary conditions in the experiment had to be chosen such that pore water pressures could be measured during the cyclic consolidation process. In a standard oedometer configuration, where usually both top and bottom of the sample are drained (abbreviated PTPB), the measurement of pore water pressure however

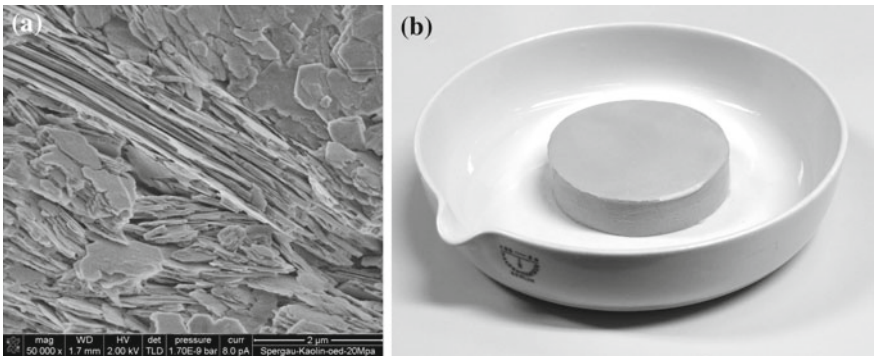

Fig. 2 **a** ESEM photograph of Spergau Kaolin [1] and **b** Spergau Kaolin sample

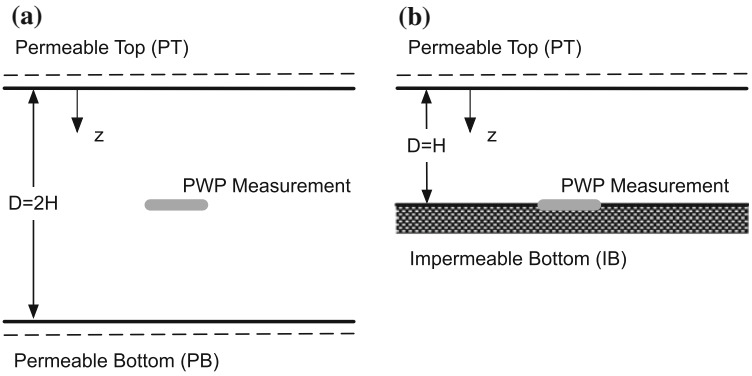

Fig. 3 Possible hydraulic boundary conditions and location of pore water pressure measurement: **a** PTPB, **b** PTIB

is rather difficult as pore water pressures have to be measured in the middle of the sample (see Fig. 3). Due to the minor height of the sample the implementation of a pore pressure transducer in this place would cause a strong disturbance of the sample and flow paths. Therefore, experiments were conducted with the following testing configuration: permeable top and impermeable bottom (abbreviated PTIB). This configuration is equivalent to a standard PTPB oedometer configuration considering that the height of the sample is halved. The hydraulic boundary conditions can be described by

$$u(z = H, t) = 0 \tag{1}$$

where z is the vertical coordinate starting from the bottom of the sample and H is the sample height.

2.4 Applied Loading

For the present study a cyclic loading function of sinusoidal type was selected according to [4, 7]:

$$L(t) = q \ \sin^2 \frac{\pi t}{d} \tag{2}$$

where $L(t)$ = applied loading as a function of time, q = load amplitude, t = time, and d = load period.

This haversine loading function was chosen considering that in geotechnical applications mostly compression loading is considered, while tensile loading is neglected.

In the present study the load amplitude q was set to 400 kPa accounting for the soft soil behavior and the short time range of load application. The load period d was

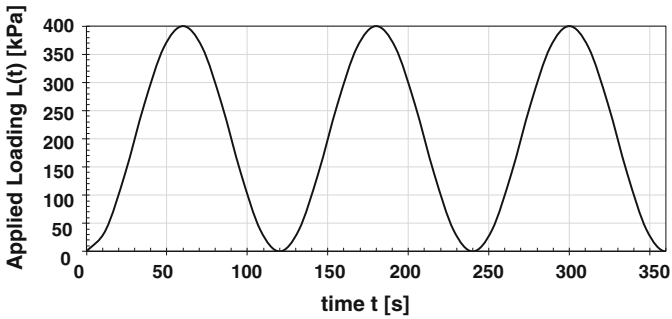

Fig. 4 Applied haversine loading function

chosen to be 15 % of the reference time t^{ref} ($T_0 = 1$), an equivalent sample (identical initial state) under static loading would need to completely consolidate:

$$d = \frac{T_0 \times H^2}{c_v} = \frac{0.15 \times (0.02\,\text{m})^2}{5 \times 10^{-7}\,\text{m}^2/\text{s}} = 120\,\text{s} \tag{3}$$

where T_0 is the chosen dimensionless period, c_V is the material-dependent coefficient of consolidation assumed to be a constant value determined from static consolidation tests on the same sample material. For details see [4].

Figure 4 shows the haversine loading function over time as applied in the experimental testing.

2.5 Experimental Results

In the following section selected results from the experimental study on Kaolin clay under haversine cyclic loading are presented. Thereby, the focus is set on the qualitative pore water dissipation behavior and evolution of settlements during the cyclic consolidation process.

2.5.1 Pore Water Dissipation Behavior

Figure 5 shows the evolution of excess pore water pressure u_{norm}, normalized with the applied load amplitude $q = 400\,\text{kPa}$, during the consolidation process. It can be observed that in the first cycles of the test the excess pore water pressure reaches values equal to 0.9. Considering the friction between soil sample and oedometer ring, which is among 5–10 % of the applied load, at the beginning almost the entire load is carried by the pore water pressure. With ongoing consolidation time the excess pore water pressure dissipates, reaching a quasi-stationary state after approximately

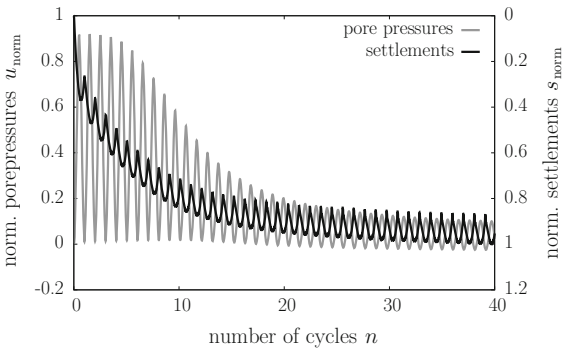

Fig. 5 Evolution of pore pressures and settlements from the experimental study

40 cycles. It is important to notice that the amplitude of excess pore water pressures u is strongly damped during the consolidation process. Moreover, the pore water pressures in the quasi-stationary state reach slight negative values at the beginning and end of a loading cycle, while the average value stays clearly above zero.

2.5.2 Evolution of Settlements

As displayed in Fig. 5, the settlements s_{norm}, normalized with the maximum consolidation settlement, during the cyclic consolidation process accumulate and just as the excess pore water pressures reach a quasi-stationary state after approximately 40 cycles. The increment of settlement accumulation is significantly decreasing from larger values in the first cycles to smaller ones in quasi-stationary state.

3 Numerical Modeling

The cyclic consolidation of normally consolidated Kaolin clay is numerically modeled using the finite element method (FEM). The FEM is an appropriate tool to solve geotechnical boundary value problems under defined complex initial and boundary conditions. Simulating the cyclic consolidation under partially drained conditions in a numerical model allows the investigation of the influence of constitutive soil parameter variation on model responses (e.g., pore water pressures and settlements).

3.1 Initial and Boundary Conditions

The geometry of the simulation model is chosen in accordance with the experimental setup using same diameter and height as the samples in the oedometer test device described above. For reasons of computational simplicity the cylindrical sample is

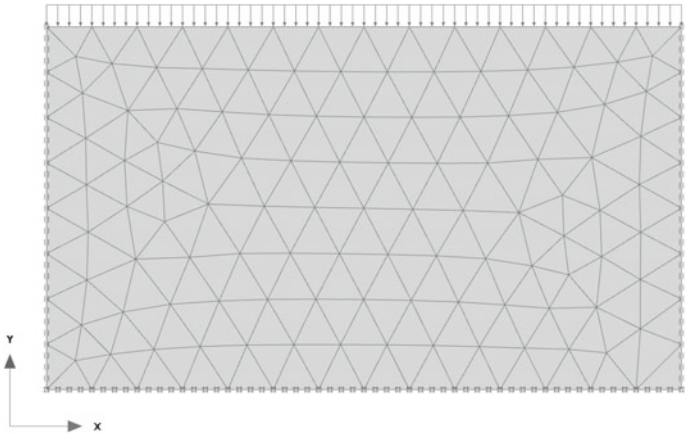

Fig. 6 Discretization for axis-symmetric FE simulation of oedometer tests ($H = 2$ cm, $D/2 = 3.5$ cm)

modeled using principles of axis symmetry with respect to the vertical centerline of the sample.

In the conducted research 15-node triangular finite elements are used for the discretization of the simulation model (see Fig. 6). Within coupled hydromechanical analyses of consolidation problems both settlements and pore water pressures are degrees-of-freedom for the nodes of a finite element.

The mechanical boundary conditions are applied with respect to the oedometer test conditions. Therefore, the prescribed boundary conditions allow for settlements of the soil sample in general, while the bottom is fixed in its vertical position. The lateral displacements are constraint at the side wall and in the symmetry axis. The numerical simulations are performed under stress controlled loading conditions. Whereat the cyclic load is applied at the top of the soil sample as a mechanical stress boundary condition referred to the haversine loading function from the laboratory experiments (same amplitude, load period, number of cycles, and equivalent consolidation coefficient).

In all conducted numerical tests, homogeneous material properties and isotropic permeabilities of the soil sample are assumed. The soil sample is fully water saturated. The chosen hydraulic boundary conditions are chosen according to the PTIB case in the experiment and therefore allow for drainage at the top of the soil sample and restrict the side wall, the bottom and the symmetry axis of the soil sample to be impermeable.

In general the numerical simulations start with a K_0 phase to initialize the total and effective stress conditions of the soil sample considering at-rest earth pressure and hydrostatic water pressure distributions. The initial density of the soil sample is initialized by introducing the initial void ratio e_0. In the subsequent coupled hydromechanical calculation phase, the cyclic load is applied in terms of the haversine

loading function described above while the consolidation process is numerically analyzed according to Biot's theory simultaneously, see [2, 3].

3.2 Constitutive Soil Model

For adequate modeling of the mechanical behavior of frictional soil, a sophisticated constitutive model, namely the hardening soil model is used. The hardening soil model has been developed in the framework of classical elastoplasticity, see [8, 9].

The highly nonlinear, hyberbolic stress–strain behavior of the soil is accurately modeled by introducing three loading path dependent stiffnesses. The tangent stiffness for primary oedometer loading $E_{\text{oed}}^{\text{ref}}$, the secant stiffness for primary triaxial loading E_{50}^{ref} and the un-/reloading stiffness $E_{\text{ur}}^{\text{ref}}$ correspond to a stress-dependent reference stiffness p^{ref}. Whereat the exponential correlation is controlled by a material parameter m.

The shear failure surface in the hardening soil model obeys Mohr–Coulomb failure criterion including constitutive strength parameters, namely friction angle φ and cohesion c.

The plasticity of the soil is modeled by introducing a double hardening yield surface shown in Fig. 7 which encloses the elastic region. The yield surface is not fixed in principle stress space and is allowed to isotropically expand due to deviatoric and volumetric plastic straining.

The plastic shear behavior of the soil is modeled by a deviatoric yield surface which is a function of the current stress state, the triaxial loading stiffness E_{50}^{ref}, the un-/reloading stiffness $E_{\text{ur}}^{\text{ref}}$, and the deviatoric plastic strains γ^{p} which are used as internal hardening parameters. The hardening expansion of the deviatoric yield surface is controlled by the evolution of γ^{p} as shown in Fig. 8. The deviatoric yield surface is allowed to expand up to the Mohr–Coulomb failure surface. For the cal-

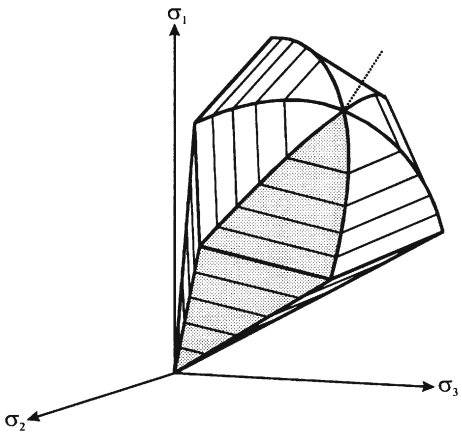

Fig. 7 Yield surface of the Hardening Soil Model in principle stress space [9]

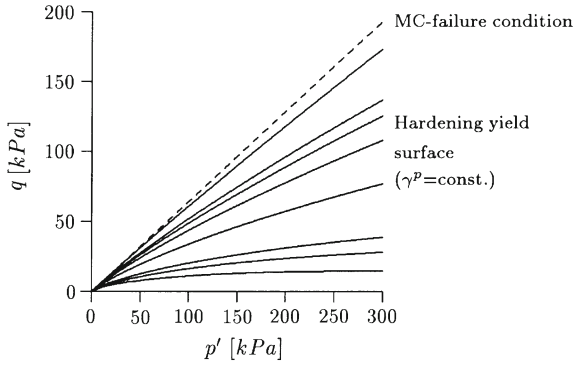

Fig. 8 Deviatoric hardening of the yield surface of the hardening soil model and Mohr–Coulomb failure surface [9]

culation of γ^{p} a nonassociated flow rule is assumed where the plastic potential is a function of the dilatancy angle ψ.

The volumetric soil behavior is controlled by a cap-yield surface which separates the elastic and plastic region in the direction of the effective mean stress p'. Whereat the size of the cap is defined by the effective preconsolidation pressure p'_{c} which accounts for the stress history of the soil. The p'_{c} is used as an internal state variable and is updated with respect to the evolution of volumetric plastic strains which are calculated using an associated flow rule. The initial elliptical shape of the cap is determined internally based on initial K_0-conditions where K_0 is the coefficient of earth pressure at rest.

3.3 Constitutive Material Parameters

The constitutive parameters for the hardening soil model are derived based on the mechanical and hydraulical parameters determined in standard laboratory tests (triaxial tests and static oedometer tests) on Kaolin clay with initial conditions equivalent to those in the experimental setup ($w = 1.1 \cdot w_L = 0.588$). An overview of the main constitutive parameters of the hardening soil model used in the numerical simulation of cyclic oedometer tests is given in Table 2.

3.4 Numerical Testing Concept and Program

Within the present research the focus is set on the analysis of the influence of consolidation coefficient c_{v}, permeability k, and oedometric stiffness E_{oed} on the model responses. For comparison of the numerical model responses with the experimental data of Kaolin clay the development of pore water pressures u at the bottom and settlements s at the top of the soil sample are evaluated. The numerical testing

Table 2 Main constitutive parameters for the hardening soil model

Parameter	Value	Unit
φ	22	(°)
ψ	0	(°)
c	5	(kN/m^2)
E_{50}^{ref}	1,750	(kN/m^2)
$E_{\mathrm{oed}}^{\mathrm{ref}}$	1,750	(kN/m^2)
$E_{\mathrm{ur}}^{\mathrm{ref}}$	5,250	(kN/m^2)
p^{ref}	100	(kN/m^2)
m	0.95	(−)
K_0	0.625	(−)
e_0	1.543	(−)
k	4×10^{-8}	(m/s)

program for analyzing the influence of varying the constitutive parameters on the model responses u and s is given in Table 3.

Case 1 is chosen as the reference case. The variation of the consolidation coefficient c_{v} is linearly controlled by the variation of the permeability k and the oedometric stiffness E_{oed} according to Eq. (4) where γ_{w} is the weight of water.

$$c_{\mathrm{v}} = \frac{k\, E_{\mathrm{oed}}}{\gamma_{\mathrm{w}}} \tag{4}$$

The permeability k and the oedometric stiffness at reference stress $E_{\mathrm{oed}}^{\mathrm{ref}}$ are varied by multiplication of the values from the reference test (case 1) with the factors $i = 2$ and $i = 1/2$. The cases 2 and 3 are conducted to investigate the influence of constant

Table 3 Numerical testing program—variation of constitutive parameters

Case	c_{v} (m^2/s)	k (m/s)	$E_{\mathrm{oed}}^{\mathrm{ref}}$ (kPa)
Reference test			
1	7×10^{-7}	4×10^{-8}	1,750
Constant c_{v} by variation of k and $E_{\mathrm{oed}}^{\mathrm{ref}}$			
2	7×10^{-7}	2×10^{-8}	3,500
3	7×10^{-7}	8×10^{-8}	875
Variation of c_{v} by variation of k and constant $E_{\mathrm{oed}}^{\mathrm{ref}}$			
4	3.5×10^{-7}	2×10^{-8}	1,750
5	1.4×10^{-6}	8×10^{-8}	1,750
Variation of c_{v} by variation of $E_{\mathrm{oed}}^{\mathrm{ref}}$ and constant k			
6	3.5×10^{-7}	4×10^{-8}	875
7	1.4×10^{-6}	4×10^{-8}	3,500

c_v on the model responses u and s while k and E_{oed}^{ref} are varying contrarily. The cases 4 and 5 are used to analyze the influence of c_v controlled by variation of k and constant E_{oed}^{ref}. In the cases 6 and 7 the c_v is influenced by variation of E_{oed}^{ref} and constant k.

Besides the variation of c_v, k, and E_{oed}^{ref}, the other parameters are kept constant in compliance with Table 2. It is assumed that during the variation of oedometric stiffness E_{oed}^{ref} the correlations $E_{50}^{ref} = E_{oed}^{ref}$ and $E_{ur}^{ref} = 3\ E_{oed}^{ref}$ are always valid.

To generalize the comparison of the different cases, all pore pressures are normalized to u_{norm} with the maximum total stress applied during the cyclic oedometer test. Furthermore, all settlements are normalized to s_{norm} with the maximum settlements from the reference case (case 1).

4 Numerical Test Results

In the following section the results of the numerical experiments simulating cyclically loaded oedometer tests with partially drained boundary conditions are analyzed. Thereby, the main focus is set on the influence of soil stiffness E_{oed}^{ref} and permeability k on the normalized excess pore pressure dissipation behavior $u_{norm}(t)$ at the bottom (undrained side) and the normalized accumulated settlements $s_{norm}(t)$ at the top of the samples (drained side). To do so case 1 is used as the reference configuration, using typical constitutive parameters of the soft Kaolin soil samples in the experimental study. As explained above cases 2–7 are derived from the reference case by changing one or two parameters (soil stiffness and/or permeability) while keeping all the other parameters the same for all cases as shown in Table 3.

Figure 9 gives the results for three cases with the same c_v but increasing and decreasing stiffness and permeability. First of all, it can be seen that for a constant value of c_v the excess pore water pressure dissipation is independent of soil stiffness E_{oed}^{ref} and permeability k. This observation holds for both the amplitude and the average value. Moreover, it can be observed that the final average settlement clearly depends on the reference oedometer stiffness E_{oed}^{ref} and that the stiffer the soil is the smaller is the deformation amplitude.

In Fig. 10 results showing the influence of the soil permeability k are displayed. As soil stiffness E_{oed}^{ref} remains constant final average settlements are the same for all three cases. However, the less permeable the soil is the smaller is also the amplitude of vertical deformation. Amplitude and average value of the excess pore water pressure are independent of the permeability. However, the more permeable the soil is the earlier the quasi-stationary state is reached.

In Fig. 11 results showing the influence of soil stiffness E_{oed}^{ref} are displayed. It can be seen that the final settlements s_{norm} linearly depend on the stiffness, while the amplitude of cyclic deformation increases with decreasing stiffness E_{oed}^{ref}. The dissipation of excess pore water pressure accelerates with increasing soil stiffness and increasing c_v, respectively.

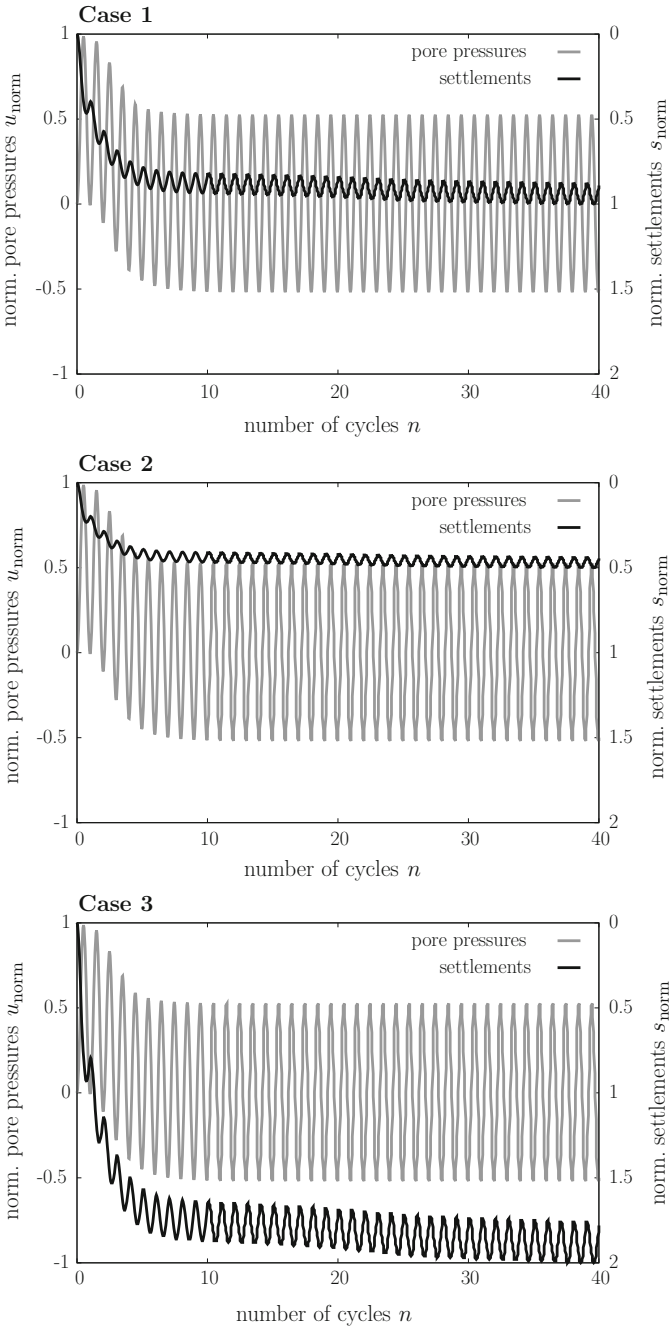

Fig. 9 Evolution of pore pressures and settlements during numerical cyclic loading test—variation of permeability and oedometric stiffness

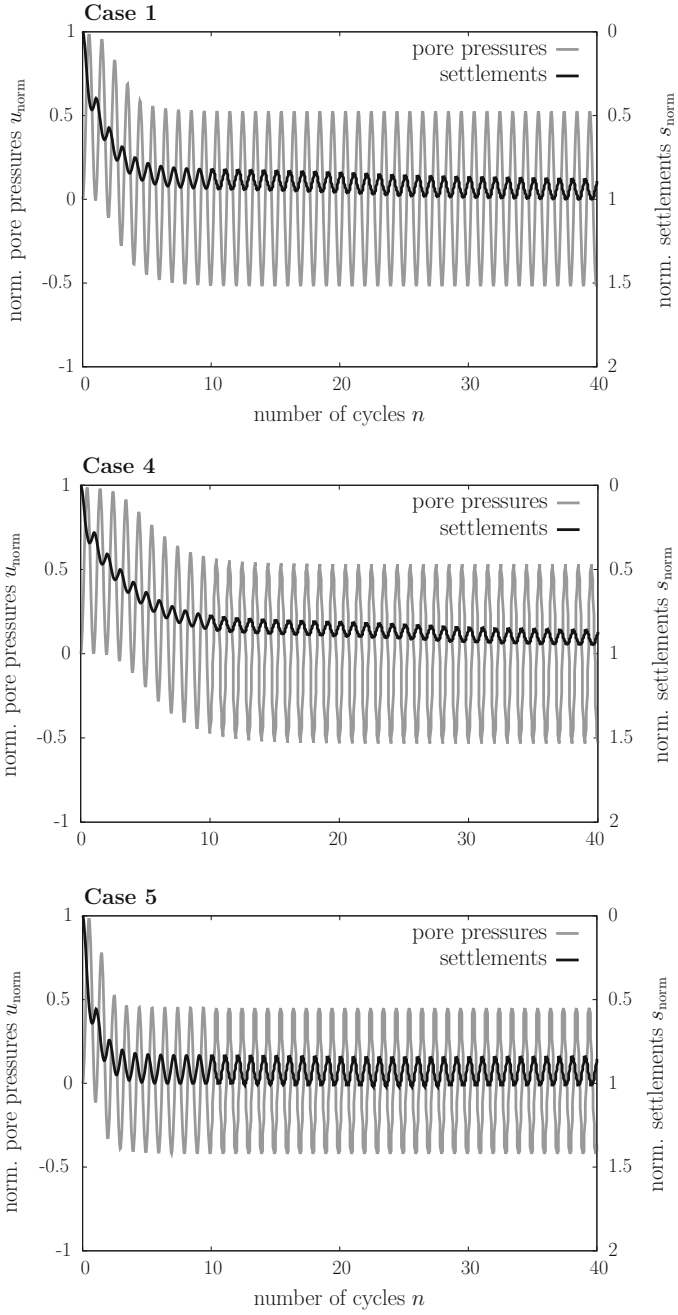

Fig. 10 Evolution of pore pressures and settlements during numerical cyclic loading test—variation of permeability

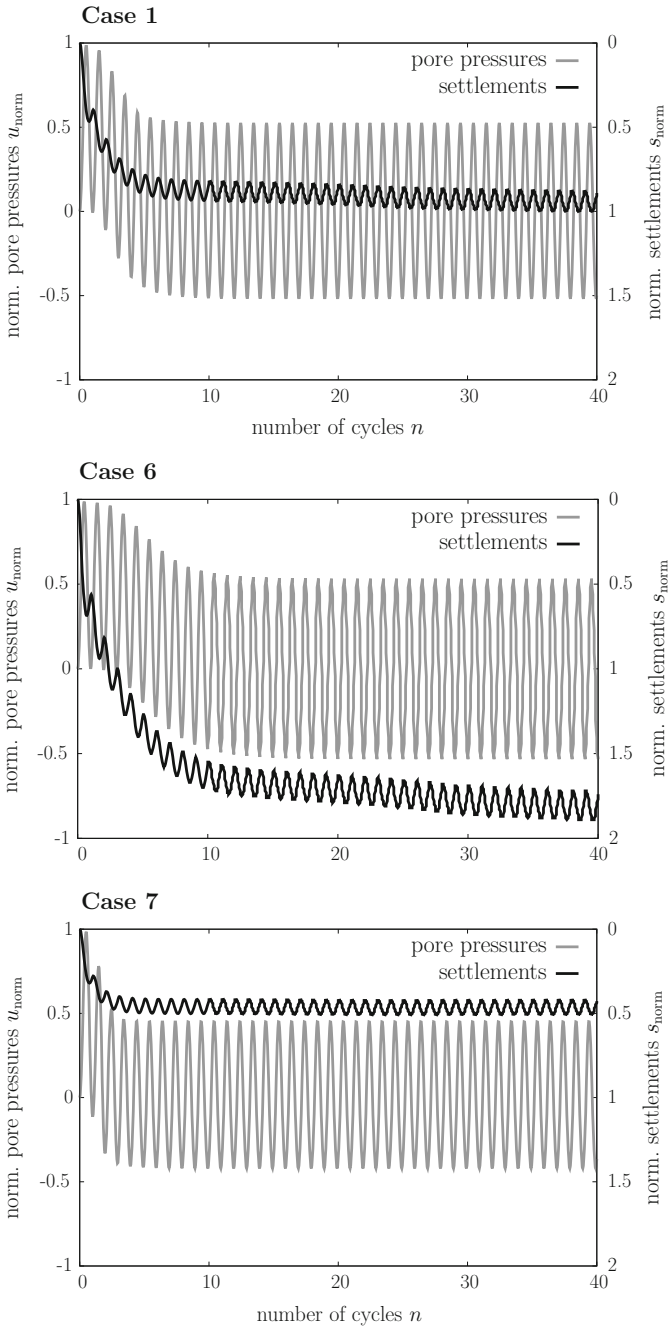

Fig. 11 Evolution of pore pressures and settlements during numerical cyclic loading test—variation of oedometric stiffness

In general it can be concluded that both—normalized excess pore water dissipation and normalized accumulation of settlements—depend on soil permeability and stiffness. The soil deformation is more significantly influenced by a change of the stiffness than the permeability, as a change in permeability with constant stiffness only effects the amplitude of the deformations but not the average value. The excess pore water dissipation is most significantly influenced by a change of c_v as for higher c_v the quasi-stationary state is reached earlier.

5 Validation of Numerical Results by Experiments

In the following section a validation of the constitutive model used is performed by a qualitative comparison of excess pore water dissipation and accumulation of settlements from the laboratory experiments. As typical numerical results for soft soils we use the reference case one, as displayed in Fig. 9a. From such a comparison it becomes obvious that accumulation of vertical settlements is captured rather well by the constitutive approach employed. For about 20 cycles amplitude of deformation decreases and quasi-stationary state seems to be reached for number of cycles larger than 40. On the other hand, a clear discrepancy must be stated when comparing results from excess pore water pressure dissipation. First of all, a significant damping of the amplitude can be observed for the experimental results. This results from a strong decrease of the maximum pore pressures reached during one cycle. Moreover, the excess pore water pressure minima only slightly reach the negative range with an average value for quasi-stationary state clearly different from zero. On the opposite, the numerical results show a remaining constant amplitude and an average of about zero for quasi-stationary state. Consequently, it can be concluded that constitutive models based on isotropic hardening plasticity are not adequate to simulate excess pore water pressure dissipation behavior during cyclic consolidation processes in a qualitatively realistic manner.

6 Conclusion and Outlook

In the present research the capability of isotropic hardening plasticity to model correctly the cyclic consolidation behavior under partially drained hydraulic boundary conditions was studied. In order to perform the experimental study a new oedometer cell was used allowing measurement of the complete stress state. Numerical experiments were conducted using FEM to model the coupled hydromechanical consolidation process. A well-established isotropic double hardening model was used to describe constitutive behavior of fine grained soil.

From the comparison of experimental and numerical results it can be concluded that the applied models based on isotropic hardening plasticity are not completely able to qualitatively simulate the excess pore water pressure dissipation behavior

during cyclic consolidation processes. This holds for the amplitude as well as for the average value in the quasi-stationary state. Final settlements in the quasi-stationary state are too large, as the accumulation of deformation is not modeled adequately. A decrease of deformation increment as observed from the experiments is not observed from the numerical simulations.

An alternative concept to simulate this type of cyclic consolidation processes is the use of constitutive models based on bounding surface plasticity. In further research, it will be studied whether this model class is able to represent accumulation of deformations and degradation of excess pore water pressure amplitude in a more realistic way.

Acknowledgments The second author acknowledges financial support provided by the German Science Foundation (DFG) in the framework of the Collaborative Research Center SFB 837 (subproject A5).

References

1. Baille, W.: Hydro-mechanical behaviour of clays—significance of mineralogy. Dissertation, Band 53, Schriftenreihe des Lehrstuhls für Grundbau, Boden- und Felsmechanik, Ruhr-Universität Bochum (2015)
2. Biot, M.A.: General theory of three-dimensional consolidation. J. Appl. Phys. **12**(2), 155–164 (1941)
3. Brinkgreve, R.B.J., Engin, E., Swolfs, W.M.: Plaxis 2014. PLAXIS b.v, The Netherlands (2014)
4. Müthing, N., Datcheva, M., Schanz, T.: On the influence of loading frequency on the pore-water dissipation behavior during cyclic consolidation of soft soils. In: Computer Methods and Recent Advances in Geomechanics, pp. 441–445. CRC Press 2014, Fusao Oka, Akira Murakami, Ryosuke Uzuoka, and Sayuri Kimoto (2014)
5. Müthing, N., Röchter, L., Datcheva, M., Schanz, T.: Cyclic consolidation of soft soils. Bochum. Aktuelle Forschung in der Bodenmechanik, Tagungsband zur 1. Deutschen Bodenmechanik Tagung Bochum (2013)
6. Razouki, S.S., Bonnier, P., Datcheva, M., Schanz, T.: Analytical solution for 1d consolidation under haversine cyclic loading. Int. J. Numer. Anal. Meth. Geomech. **37**(14), 2367–2372 (2013)
7. Razouki, S.S., Schanz, T.: One-dimensional consolidation under haversine repeated loading with rest period. Acta Geotech. **6**(1), 13–20 (2011)
8. Schanz, T.: Zur Modellierung des mechanischen Verhaltens von Reibungsmaterialien. Habilitationsschrift, Mitteilung 45, Institut für Geotechnik, Universität Stuttgart (1998)
9. Schanz, T., Vermeer, P.A., Bonnier, P.G.: The hardening soil model: formulation and verification. In: Beyond 2000 in Computational Geotechnics—10 years of Plaxis, pp. 281–296, Rotterdam, Balkema (1999)

Experimental and Numerical Element Tests for Granular Soils: Performance of Different Constitutive Models for Monotonous and Low-Cycle Loading

Stefanie Danne and Achim Hettler

Abstract It is known that some common constitutive models show deficits when predicting elastic and plastic deformations due to high- and low-cycle loading resulting for example from geotechnical installation processes. The object of part I of subproject 8 within the DFG research group FOR 1136 (GeoTech) is to show the performance of different constitutive models and to compare them to experimental laboratory test results and among each other. To look onto the incremental stress–strain behaviour of sand, series of drained, stress-controlled triaxial tests have been carried out to obtain strain response envelopes for monotonous loading. Here, a soil element is subjected to a constant stress increment in different directions and its strain responses are evaluated graphically. The presented laboratory tests were performed at different initial stress states. The accumulation of strains due to low cyclic loading ($N \leq 50$) has also been examined for different loading directions and different sizes of stress amplitudes. All experiments have been recalculated numerically with different constitutive models, amongst them some common as well as advanced constitutive models, which have been developed recently and partly within the research group GeoTech.

Keywords Low-cycle loading · Triaxial tests · Strain response envelopes · Incremental stress–strain behaviour · Granular soils

S. Danne (✉) · A. Hettler
Chair of Soil Mechanics and Foundation Engineering, Technical University of Dortmund, Dortmund, Germany
e-mail: stefanie.danne@tu-dortmund.de

T. Triantafyllidis (ed.), *Holistic Simulation of Geotechnical Installation Processes*, Lecture Notes in Applied and Computational Mechanics 80, DOI 10.1007/978-3-319-23159-4_8

1 Introduction

In practical applications, soil elements can be subject to monotonous as well as to stress or strain cycles with different magnitudes of amplitudes. Constitutive equations used to solve boundary value problems should generally be able to model all these loading situations and predict resulting stresses and deformations realistically.

Especially, when it comes to cyclic loading, occurring for example during geotechnical installation processes, it is well known that some common constitutive models show deficits when predicting elastic and plastic deformations with regard to magnitude as well as to accumulation.

In general, cyclic loading processes can be divided into high-cycle and low-cycle loading, depending on the number of cycles N. To avoid numerical errors and high computing time, it is often useful to calculate deformations due to high-cycle loading by means of explicit models, where irreversible strains are treated similar to creep deformations under constant loads [14]. In Wichtmann's High Cycle Accumulation model, the strain amplitudes are limited to $\Delta\varepsilon \leq 10^{-3}$. So it is appropriate to use other constitutive equations for low number of cycles, where the magnitude of strains is often $\geq 10^{-3}$. Low-cycle loading processes can be defined for a lower number of cycles with $N \leq 50$, [4]. In these cases, an implicit calculation of deformations is often appropriate.

After describing some fundamentals in Sect. 2 of this paper, numerical and experimental analyses of monotonous and low-cycle loading in triaxial testing are presented. The results of different monotonous loading paths are evaluated by means of response envelopes in Sect. 3. In Sect. 4, the stress–strain behaviour during low-cycle loading is examined, where the focus is set on the accumulation of plastic strains. A comprehensive study of quasi-elastic strains during low-cycle loading can be found in [5].

By comparing the experimental and numerical results, an attempt is made to show the performance of some common and advanced constitutive models.

2 Fundamentals

2.1 Response Envelopes

In axial symmetric conditions considered in this paper, index 1 denotes the axial component and index 3 the lateral component of stress or strain, respectively. The stress ratio η is defined by the quotient of the deviatoric stress $q = \sigma_1 - \sigma_3$ and the mean pressure $p = (\sigma_1 + 2\sigma_3)/3$ describing the stress state's position in the p–q plane.

To avoid distortion of two vectors in the p–q plane, which are orthogonal to each other in the three-dimensional principal stress space $\sigma_1 - \sigma_2 - \sigma_3$, stresses and strains in this paper are presented in the Rendulic plane, which is isomorphic. Its horizontal axis is $\sqrt{2}\sigma_3$ and $\sqrt{2}\varepsilon_3$, respectively, and the vertical axis σ_1 and ε_1 (Fig. 1).

So-called response envelopes are a useful tool for calibrating, validating and comparing constitutive equations [11]. The soil's incremental stress–strain behaviour can hereby be investigated during first loading as well as during un- and reloading processes. First basics of response envelopes were presented in the 1970s by [12]. A few years later, [9] used this concept in context with the development of constitutive equations.

To obtain a response envelope, a soil element is subjected to a certain stress or strain increment. Considering the concept of *strain*-response envelopes dealt with in this paper—subsequently referred to as "SREs"—a constant stress increment

$$\Delta\sigma = \sqrt{\Delta\sigma_1^2 + 2\Delta\sigma_3^2} \tag{1}$$

is applied in different directions α_σ, Fig. 1a.

The corresponding "response" of the soil in terms of either strain or stress is determined and presented graphically. The direction of the implied stress or strain increment with a constant absolute value is varied and leads to different stress or strain responses, endpoints of which are connected to a response envelope.

The strains are also plotted in the isomorphic rendulic diagram, in which the resulting total strain increment is

$$\Delta\varepsilon = \sqrt{\varepsilon_1^2 + 2\Delta\varepsilon_3^2} \tag{2}$$

The angles α_σ and α_ε shown in Fig. 1 are used herein to quantify the direction of incremental quantities. α_σ is the angle between stress probe vector and the positive $\sqrt{2}\sigma_3$-axis and α_ε is the angle between the strain increment vector and the positive $\sqrt{2}\varepsilon_3$-axis.

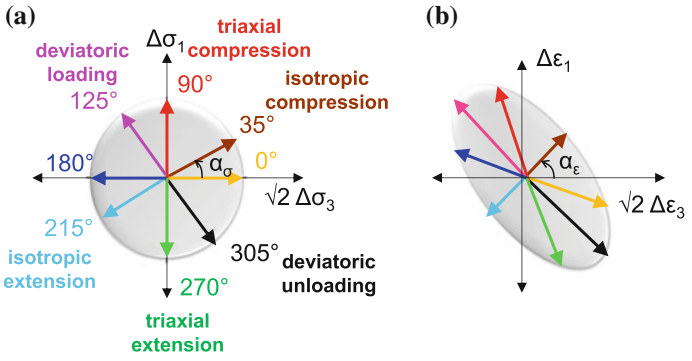

Fig. 1 Applied stress increments $\Delta\sigma$ (**a**) and corresponding strain responses (**b**) for different directions α_σ

Table 1 Initial stress states

Stress state	p (kPa)	q (kPa)	Stress-ratio $\eta = q/p$ [−]	Region
A	200	150	0.75	Compression
I	200	0	–	Isotropic
J	200	−100	−0.5	Extension

2.2 Triaxial Device and Testing Procedure

The triaxial device used for experiments presented in this paper is equipped with high-resolution measurement and control technology. The confining pressure as well as the axial force can be controlled independently, so that stress paths in different directions from any initial stress state can be performed.

The tested soil is a fine-grained sand with a low uniformity-index (C_U = 1.25, d_{50} = 0.15 mm), having a positive impact when it comes to avoid effects from membrane penetration. Height and diameter of the soil specimen are 10 cm.

The soil sample was fabricated by pluviating dry sand thereby maintaining a constant height. This specimen-preparation method was kept constant for all tests. The achieved relative densities I_D were well reproducible with small deviation (± 0.1). Starting with an isotropic stress, the predefined initial stress state was reached, either by increasing the vertical stress (for stress states in compression) or the horizontal stress (for stress states in extension). Then the soil sample was consolidated.

The experiments described in this paper are carried out with medium to dense soil samples ($I_D \approx 0.75$), consolidated at initial stress states shown in Table 1.

For all experiments and stress probe directions, one equally prepared and consolidated sample is used. The stress-controlled experiments are carried out under drained conditions. The rate and the frequency during low-cycle loading, respectively, are kept low to avoid pore water pressure. All stresses referred to in this paper are effective stresses ($\sigma = \sigma'$).

2.3 Considered Constitutive Equations

There are quite some constitutive models for granular soils, which are used to calculate boundary value problems for practical purposes. It is known, however, that some of them show deficits when predicting deformations due to high- and/or low-cycle loading processes.

In this paper, some of them are chosen exemplarily to compare them with each other and to the experiments, which have been carried out by the authors. The constitutive equations are

- Hypoplasticity with intergranular strain (IS);
- Hardening Soil model (HS);
- Intergranular Strain Anisotropy-model (ISA);
- Simple Anisotropic Sand Plasticity model (Sanisand).

The **hypoplastic constitutive model** describes the stress–strain behaviour of non-cohesive soils in rate form. Its present version was formulated by von Wolffersdorff [20]. Small strain stiffness formulation (so-called intergranular strain concept) was added by [13].

The **Hardening Soil model** developed by [16] is formulated in the framework of classical theory of plasticity. Total strains are calculated using a stress-dependent stiffness, different for first loading and un-/reloading. Plastic strains are calculated by introducing a multi-surface yield criterion. Hardening is assumed to be isotropic depending on both the plastic shear and the volumetric strain. For the frictional hardening, a non-associated and for the cap hardening an associated flow rule is assumed.

The elastoplastic **ISA model** recently introduced by [8] is based on the intergranular strain concept, but contrary to the existing formulations it proposes a yield function describing a surface within the intergranular strain space. It includes an elastic locus in the intergranular strain space.

The **Sanisand model** was developed within the framework of critical state soil mechanics and bounding surface plasticity [17]. As analytical description of a narrow but closed cone-type yield surface, which obeys rotational and isotropic hardening, an 8-curve equation is used.

The numerous material parameters needed for the different constitutive models for the used fine sand have either been determined experimentally by the authors or have been kindly provided by colleagues of the Karlsruhe Institute of Technology (KIT).

3 Experimental and Numerical Results from Monotonous Loading

To obtain a SRE from monotonous loading, once a chosen initial stress state is reached and consolidation is finished, and a stress path in one direction is applied until failure, Fig. 2.

Total strains $\Delta\varepsilon$ are evaluated for different stress increments $\Delta\sigma = 20$, 30, 40, 50 and 100 kPa (circles in Fig. 2a). The same procedure is repeated with an equally prepared new sample.

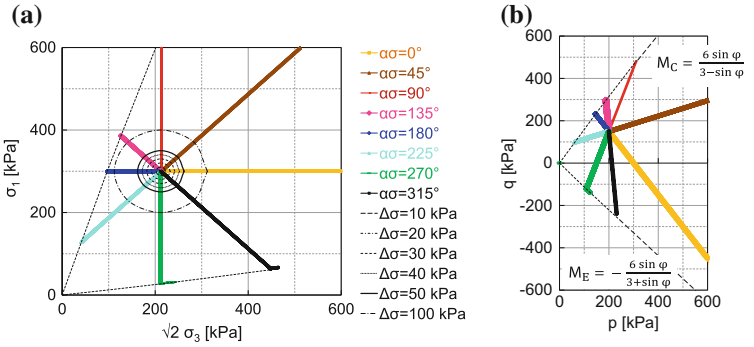

Fig. 2 Applying monotonous stress probes (here from stress state A) in the Rendulic plane (**a**) and in the p–q plane (**b**)

3.1 Experimental Results

There are few papers which report of experimental SREs for momentous loading, e.g. [1, 3, 6]. An overview can be found in [5].

Figure 3 shows SREs determined experimentally for three different initial stress states, Table 1.

For all stress states, it turns out that the size of the SREs non-linearly increases with increasing stress increment. It can also be seen that the SREs derived from stress states in extension (Fig. 3a) and compression (Fig. 3c) get longer and slimmer, the closer the stress increment approaches the failure lines shown in Fig. 2. Largest deformations occur for pure deviatoric loading ($\alpha_\sigma \approx 125°$) for the initial stress state located in compression and for deviatoric unloading ($\alpha_\sigma \approx 305°$) for the initial stress state located in extension.

For the stress state located on the isotropic axis (I), the shapes of the strain response envelopes for $\Delta\sigma \leq 50$ kPa are almost similar to symmetrical ellipses. For larger stress increments, the envelope becomes elongated towards extension region.

3.2 Numerical Results

The experiments described in Sect. 3.1 have been recalculated numerically with the aforementioned constitutive equations.

Figure 4 shows the numerically determined SREs for initial stress state A (compression). Except for the Sanisand model, the SREs' elongation and inclination are in good agreement with the experimental results shown in Fig. 3c. Regarding the size of the SREs, only the hypoplastic model seems to depict the adequate stiffness.

Figure 5 shows the numerically determined SREs for the isotropic initial stress state I. Approximate symmetrical envelopes for $\Delta\sigma \leq 50$ kPa can be found at the HS

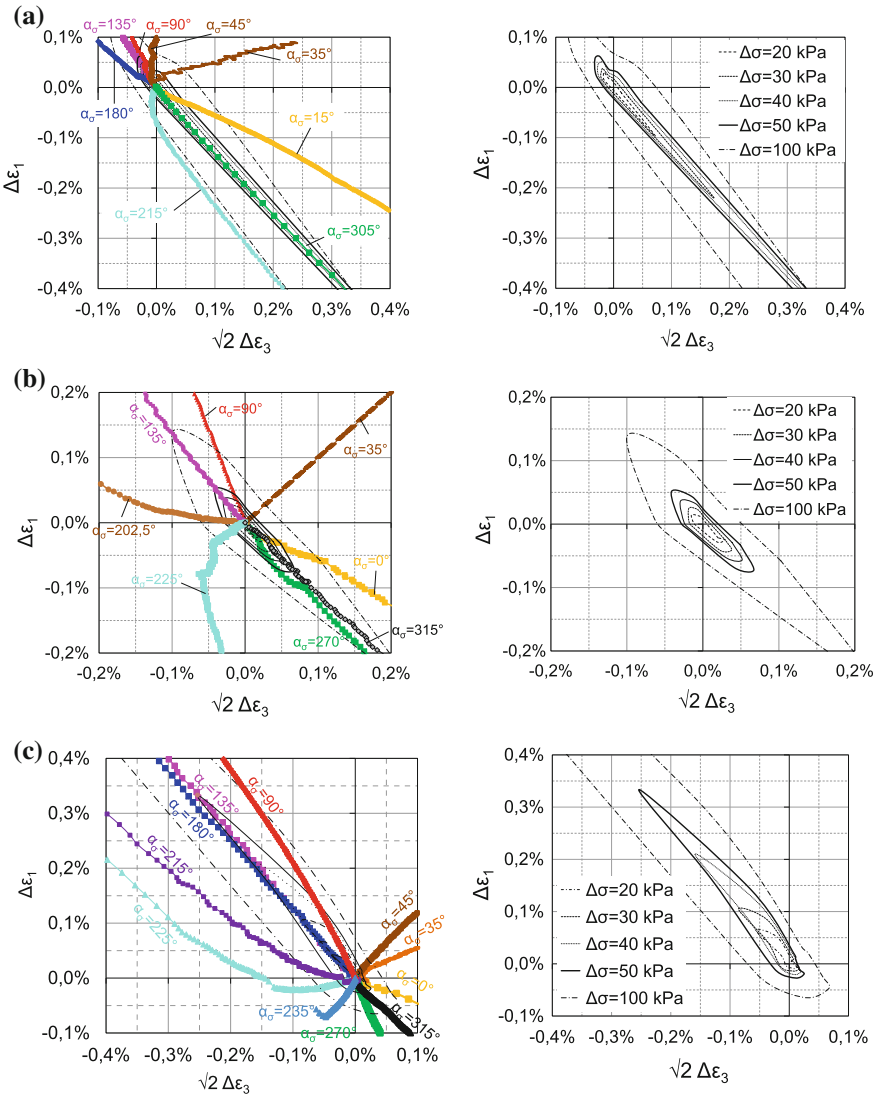

Fig. 3 Strain response envelopes for initial stress states *A* (**a**), *I* (**b**) and *J* (**c**)

and the Sanisand model, which is in good agreement with the experimental results shown in Fig. 3b.

For the SREs calculated from stress state *J* shown in Fig. 6, a significant difference between un- and reloading stress probes can be observed for the hypoplastic model (Fig. 6a). For isotropic unloading ($\alpha_\sigma \approx 215°$), the resulting strains are very small and lead to an asymmetrical shape of the envelopes. The elastoplastic SREs in

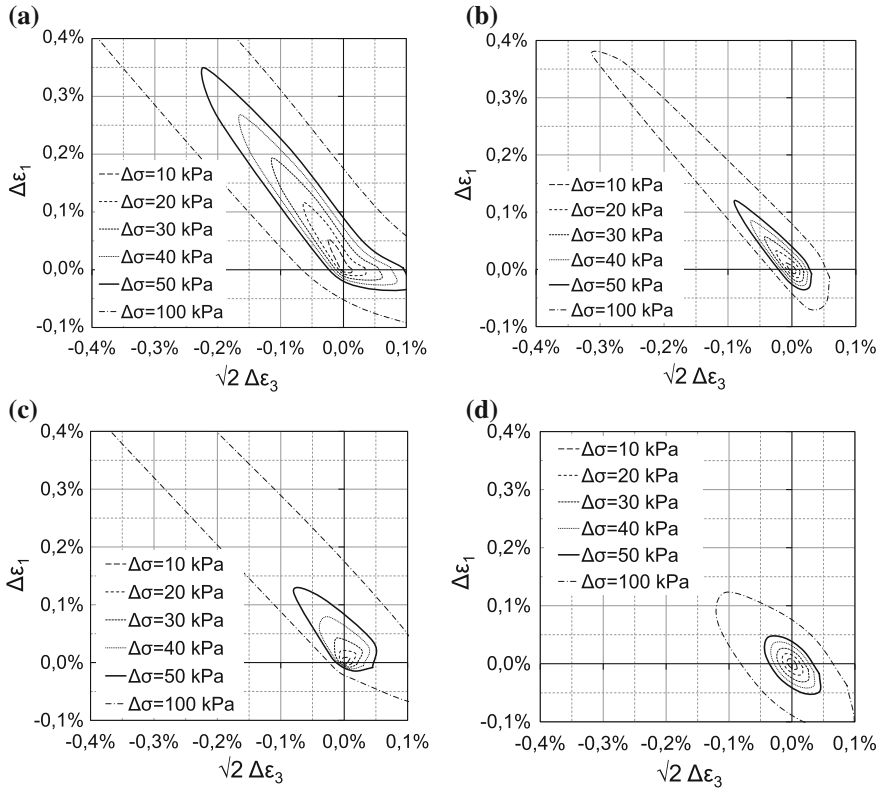

Fig. 4 Numerically determined SREs at initial stress state *A*: **a** Hypoplasticity (with IS), **b** Hardening Soil, **c** ISA, **d** Sanisand

Fig. 6b, d are quite similar but here again smaller, i.e. stiffer than the SREs obtained experimentally.

Numerical investigations of (other) different constitutive equations and their evaluation and comparison by means of SREs can be found in [2, 7, 15, 19].

4 Experimental and Numerical Results from Low-Cycle Loading

The strain accumulation during low-cycle loading has also been examined in this paper. Exemplarily, the results for different stress cycles with two different increment sizes each are presented in this paper:

- pure deviatoric loading ($\alpha_\sigma \approx 125°$): $\Delta q = 50$ kPa and $\Delta q = 200$ kPa with $\Delta p = 0$ and

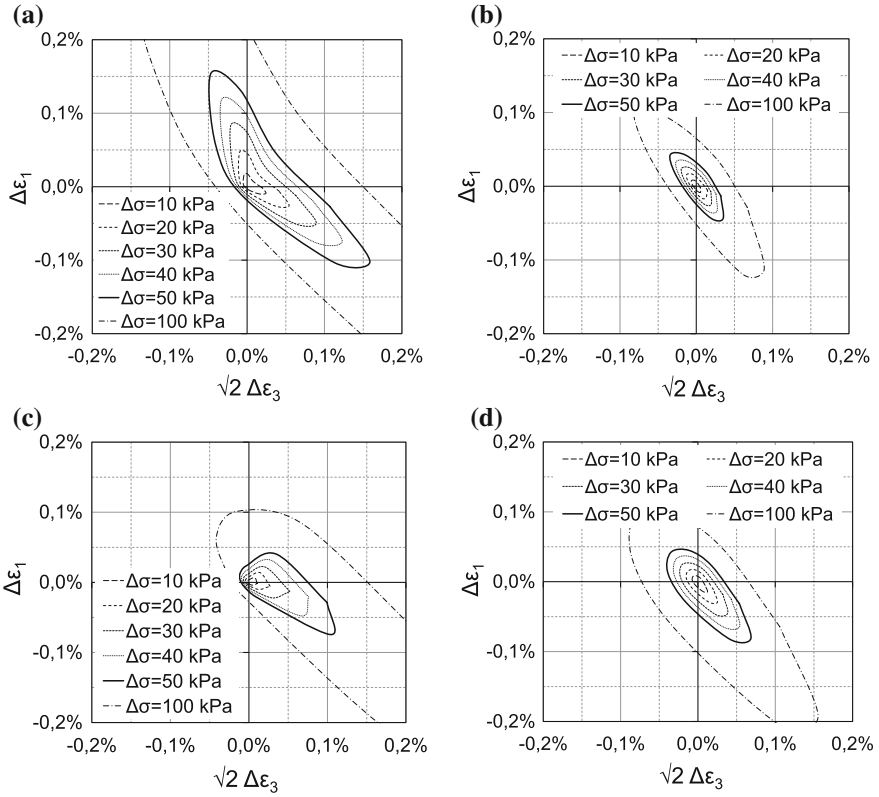

Fig. 5 Numerically determined SREs at initial stress state I: **a** Hypoplasticity (with IS), **b** Hardening Soil, **c** ISA, **d** Sanisand

- pure volumetric loading ($\alpha_\sigma \approx 35°$): $\Delta p = 50$ kPa and $\Delta p = 200$ kPa with $\Delta q = 0$

The cycles are applied on a soil specimen/element, starting from the isotropic stress state I (Table 1). The results are presented by plotting the total strains $\Delta\varepsilon$ over the number of cycles N.

In each case both increment sizes for the same direction are plotted in one figure. The solid lines show the total strains $\Delta\varepsilon$ during 20 cyclic stress increments of 200 kPa (magnitudes shown on the left axis of ordinates), and the dashed lines show the development of total strains during smaller stress cycles of 50 kPa (magnitudes shown on the right axis of ordinates).

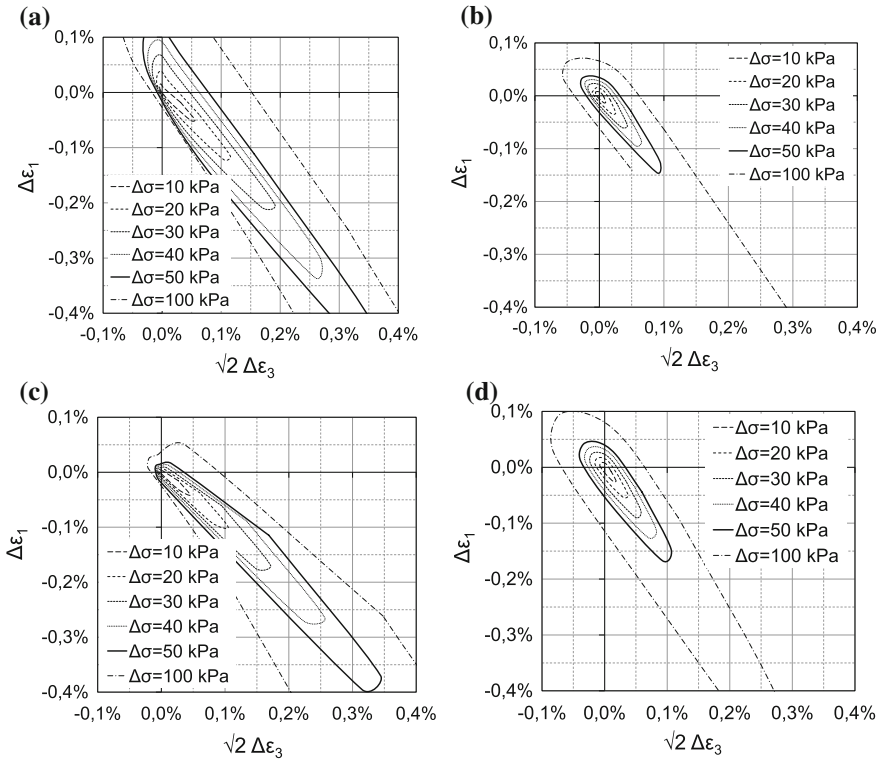

Fig. 6 Numerically determined SREs at initial stress state J: **a** Hypoplasticity (with IS), **b** Hardening Soil, **c** ISA, **d** Sanisand

4.1 Experimental Results

The experimental results are shown in Fig. 7. Both loading directions show that the largest strain increase occurs during first loading. Another similarity which attracts attention is the fact that after a few cycles, already the quasi-elastic strain, i.e. the difference between $\Delta\varepsilon_{\text{loading}} - \Delta\varepsilon_{\text{unloading}}$, seems to be constant and independent from the number of cycles N. Generally, the total and the quasi-elastic strains due to pure deviatoric loading (Fig. 7a) are larger than for an isotropically loaded soil element (Fig. 7b). A logarithmic increase of total strains can be observed here, which still slightly continues after 20 stress cycles.

In contrast to deviatoric loading, there is quasi-elastic behaviour for isotropically loaded samples after a low number of cycles already. In this case, no further increase of strains can be observed. For high-cycle loading, an increase may be noticeable for a large number of cycles ($N \gg 50$), see e.g. [18].

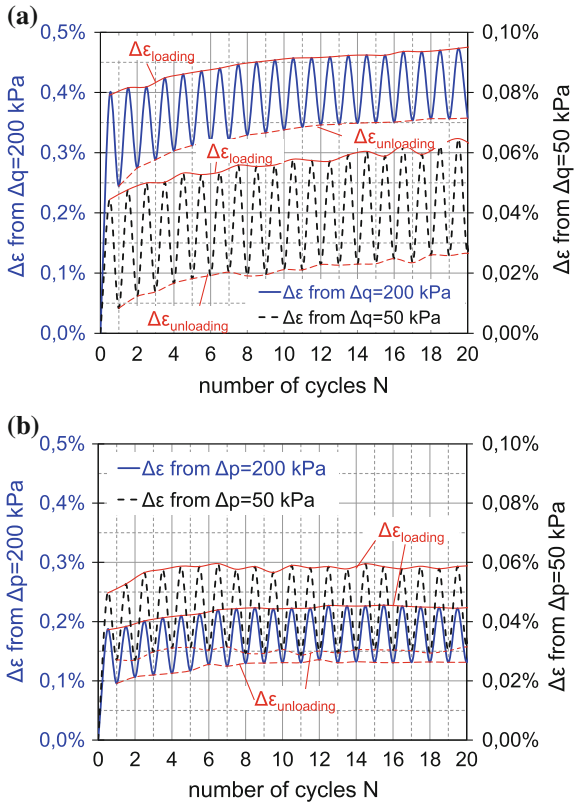

Fig. 7 Strain accumulation during 20 pure deviatoric stress cycles (**a**) and pure isotropic stress cycles (**b**)

4.2 Numerical Results

Figures 8 and 9 show the strain accumulation of the corresponding numerical calculations.

It can be observed that there is no strain accumulation at all after the second un- and reloading for the calculations carried out with the elastoplastic HS model, Figs. 8b and 9b. The largest strains are obtained for the calculations with the hypoplastic model for both deviatoric and volumetric loading conditions. While the strains due to $\Delta q = 50$ kPa seem to be almost elastic after the second un- and reloading, ratcheting occurs during larger stress cycles with $\Delta q = 200$ kPa, Fig. 8a. For large volumetric stress cycles in Fig. 9a this ratcheting-effect becomes significantly smaler, so that the calculated total strains for this loading direction are in good agreement to the experimental results shown in Fig. 7b. Fuente's ISA model provides an increasing tendency of strains for both amplitudes, and their magnitudes, however, seem to be either too large ($\Delta q = 200$ kPa) or too small ($\Delta q = 50$ kPa), Fig. 8c. The Sanisand model shows a constant strain increase with each $\Delta q = 200$ kPa-cycle, for $\Delta q = 50$ kPa there even seems to be a decrease of total and elastic strains.

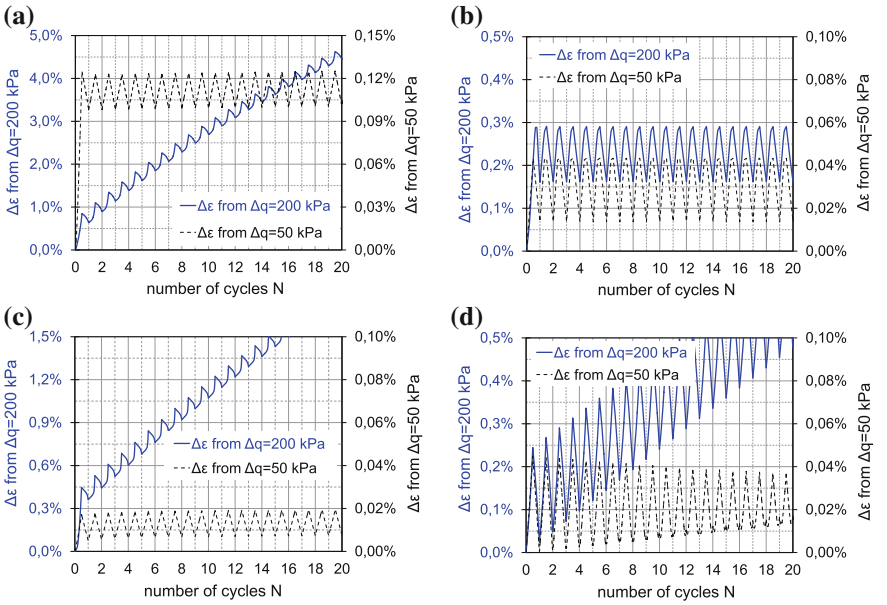

Fig. 8 Strain accumulation during 20 pure deviatoric stress cycles: **a** Hypoplasticity (with IS), **b** Hardening Soil, **c** ISA, **d** Sanisand

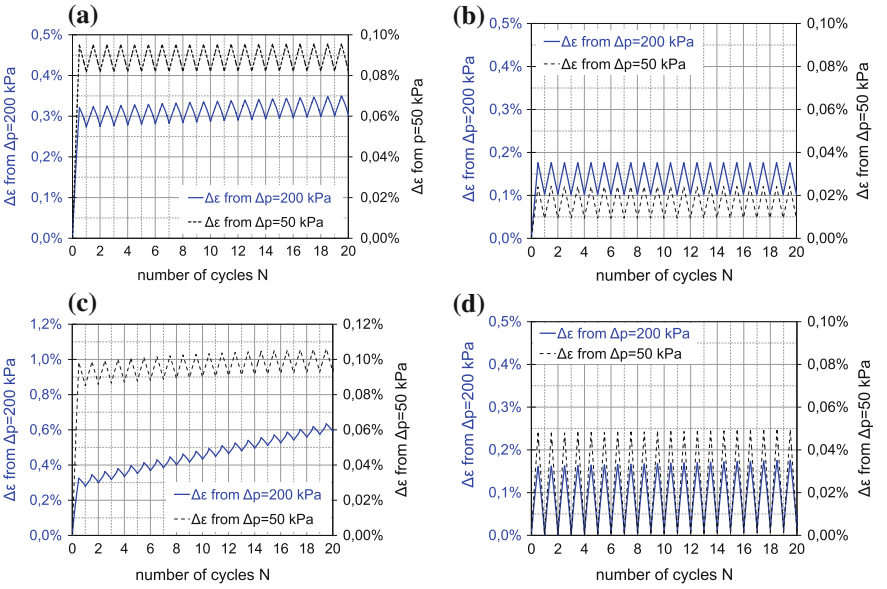

Fig. 9 Strain accumulation during 20 pure volumetric stress cycles: **a** Hypoplasticity (with IS), **b** Hardening Soil, **c** ISA, **d** Sanisand

Figure 9 shows the strain accumulation of the corresponding numerical calculations for pure volumetric stress cycles.

The results in this case are qualitatively in agreement with the ones from pure deviatoric un- and reloading.

5 Summary and Further Hints

When comparing the numerical and experimental results presented in this paper, fairly good agreements could be found considering monotonous loading.

Considerable differences, however, have been found when investigating the development of total and quasi-elastic strains during low-cycle loading. None of the four investigated constitutive models were able to simulate the strains for the investigated loading directions close to the experimental results. This means further research work is needed to improve existing incremental stress–strain relations. Especially, for low-cycle loading it is recommended to check thoroughly the stress paths dominating the actual boundary value problem and to choose a suitable constitutive model.

Acknowledgments The work presented in this paper was supported by the German Research Foundation (DFG) as subproject 8 "Incremental stress-strain-behaviour of sand at low-cycle loading and application on excavation-models" of the interdisciplinary research group FOR 1136 "Simulation of geotechnical installation processes with holistic consideration of the stress strain soil behaviour (GeoTech). The authors appreciate the financial support from the DFG. The authors also like to thank their colleagues of the Karlsruhe Institute of Technology (KIT) who provided the incremental driver, which was used to perform some of the numerical element tests.

References

1. Anandarajah, A., Sobhan, K., Kuganenthira, N.: Incremental stress-strain behaviour of granular soil. J. Geotech. Eng.—ASCE **121**(1), 57–68 (1995)
2. Calvetti, F., Viggiani, G., Tamagnini, C.: A numerical investigation of the incremental behaviour of granular soils. Rivista Italiana di Geotecnica 11–19 (2003)
3. Costanzo, D., Viggiani, G., Tamagnini, C.: Directional response of a reconstituted fine-grained soil—Part I: Experimental investigation. Int. J. Numer. Anal. Meth. Geomech. **13**, 1283–1301 (2006)
4. Danne, St., Hettler, A.: Verhalten von nichtbindigen Böden bei niederzyklischer Belastung. Geotechnik **36**, 19–29 (2013)
5. Danne, St., Hettler, A.: Experimental strain response-envelopes of granular materials for monotonous and low-cycle loading processes. In: Holistic Simulation of Geotechnical Installation Processes—Numerical and Physical Modelling. Lecture Notes in Applied and Computational Mechanics (77). Springer International Publishing, 229–250 (2015)
6. Doanh, T.: Strain response envelope: a complementary tool for evaluating hostun sand in triaxial compression and extension: experimental observations. In: Constitutive Modelling of Granular Materials. Springer, Berlin, 375–396 (2000)

7. Froiio, F., Roux, J.-N.: Incremental response of a model granular material by stress probing with DEM simulations. In: IUTAM-ISIMM Symposium on Mathematical Modelling and Physical Instances of Granular Flow, Reggio Calabria, Italy (2009)
8. Fuentes Lacouture, W.M.: Contributions in mechanical modelling of fill materials. Veröffentlichung des Institutes für Bodenmechanik und Felsmechanik am Karlsruher Institut für Technologie (KIT) (2014)
9. Gudehus, G.: A comparison of some constitutive laws for soils under radially symmetric loading and unloading. In: Wittke, W. (Ed.), Proceedings of the 3rd International Conference on Numerical Methods in Geomechanics, Balkema, 1309–1323 (1979)
10. Hettler, A., Danne, St.: Strain response envelopes for low-cycle loading processes. In: Proceedings of the 18th International Conference on Soil Mechanics and Geotechnical Engineering, Paris, 1491–1494 (2013)
11. Kolymbas, D.: Response-Envelopes: A useful tool, aus "Hypoplasticity then and now". In: Kolymbas, D. (ed.) Constit. Modell. Gran. Mater. 57–105. Springer-Verlag, Berlin (2000)
12. Lewin, P., Burland, J.: Stress-probe experiments on saturated normally consolidated clay. Géotechnique **20**(1), 38–56 (1970)
13. Niemunis, A., Herle, I.: Hypoplastic model for cohesionless soils with elastic strain range. Mech. Cohesive-Frictional Mater. **2**, 279–299 (1997)
14. Niemunis, A., Wichtmann, T., Triantafyllidis, T.: A high-cycle accumulation model for sand. Comput. Geotech. **32**(4), 245–263 (2005)
15. Royis, P., Doanh, T.: Theoretical analysis of strain response envelopes using incrementally non-linear constitutive equations. Int. J. Numer. Anal. Meth. Geomech. **22**(2), 97–132 (1998)
16. Schanz, T., Vermeer, P.A., Bonnier, P.G.: 1999. The hardening soil model: Formulation and verification. Beyond 2000 in Computational Geotechnics—10 Years of Plaxis. Balkema, Rotterdam (2000)
17. Taiebat, M., Dafalias, Y.: Sanisand, simple anisotropic sand plasticity model. Int. J. Numer. Anal. Meth. Geomech. **32**(8), 915–948 (2008)
18. Triantafyllidis, Th., Wichtmann, T., Niemunis, A.: Entwicklungen in der Bodenmechanik, Bodendynamik und Geotechnik. In: Dr.-Ing. Frank Rackwitz (Ed.) Festschrift zum 60. Geburtstag von Univ.-Professor Dr.-Ing. habil. Stavros A. Savidis, 173–191 (2006)
19. Tamagnini, C., Masın, D., Costanzo, D., Viggiani, G.: An evaluation of different constitutive models to predict the directional response of a reconstituted fine-grained soil. Modern Trends in Geomechanics, Springer, Berlin Heidelberg New York **106**, 143–157 (2006)
20. von Wolffersdorff, P.A.: A hypoplastic relation for granular materials with a predefined limit state surface. Mech. Cohesive-Frictional Mater. **1**, 251–271 (1996)

Towards the Holistic Simulation of Geotechnical Foundation Processes Using Vibro-Injection Piles

Wolfgang Ehlers, Maik Schenke and Bernd Markert

Abstract In civil engineering, the installation of a reliable foundation is essential for the stability of the emerging structure. Thus, already during the foundation process, a comprehensive survey of the mutual interactions between the preliminary established construction pit and the surrounding soil is indispensable, especially when building in the existing context. Addressing the simulation of geotechnical foundation processes using vibro-injection piles, complex initial-boundary-value problems are necessary. In particular, the numerical model is composed of several mutual interacting parts, such as retaining walls, anchors and vibro-injection piles, all interacting with the surrounding soil. Additionally, a fine mesh is required in order to adequately resolve local effects such as shear bands. However, when such complex simulations are inevitable, explicit time-integration schemes are advantageous over implicit schemes. In this regard, the present contribution addresses the development and application of a numerical soil model based on the Theory of Porous Media, which is suitable for simulations exploiting the explicit time-integration schemes of Abaqus/Explicit. The underlying numerical soil model is investigated in terms of accuracy and parallel efficiency.

Keywords Explicit scheme · Implicit scheme · Parallel computing · Soil dynamics · Theory of Porous Media

1 Introduction

During geotechnical foundation processes, the reliability of the often necessary construction pits are vital for the safety of people and the stability of the existing buildings in the immediate vicinity, especially when building in an existing context. In general,

W. Ehlers (✉) · M. Schenke
Institute of Applied Mechanics (CE), University of Stuttgart, Stuttgart, Germany
e-mail: ehlers@mechbau.uni-stuttgart.de

B. Markert
Institute of General Mechanics, RWTH Aachen University, Aachen, Germany

T. Triantafyllidis (ed.), *Holistic Simulation of Geotechnical Installation Processes*, Lecture Notes in Applied and Computational Mechanics 80, DOI 10.1007/978-3-319-23159-4_9

a construction pit is composed of retaining walls, which withstand the earth pressure acting from the outside of the pit, and of tiebacks, which act as additional retaining-wall anchor points. As both are embedded into the surrounding soil, the stability and reliability of the entire system strongly relies on the strength of the circumambient soil. In this regard, drawing the attention to a particular construction site, measurements at the construction pit at the Potsdamer Platz in Berlin have revealed significant displacements of the retaining walls during the foundation process, in particular, during the vibratory installation of foundation piles via so-called vibro-injection processes.

In order to ensure the stability of the construction pit during the foundation process, numerical simulations, in general based on the finite-element method, can be carried out to predict the response of the system. The reliability of these simulations strongly depends on the complexity of the numerical model. However, with increasing complexity, more robust algorithms are necessary. In this regard, numerical simulations based upon explicit time-integration schemes, such as the explicit (forward) *Euler* or the central-difference method, e.g. [17], are considered to be advantageous in comparison to implicit schemes, especially, for systems with strong nonlinearities. In particular, although implicit schemes are unconditionally stable, they require a converging iterative procedure, such as the *Newton-Raphson* method [25], to solve the in general nonlinear system of equations, which, however, may fail to converge for strong nonlinear systems. In this connection, explicit schemes are considered to be more robust for complex systems and are more efficient for large-scale problems but suffer from their only conditional stability. In particular, the maximum allowable time increment depends, on the one hand, on the physical properties of the system and, on the other hand, on the spatial discretisation, i.e. on the element size [5, 8]. Nevertheless, addressing complex and large-scale models, the advantages of explicit schemes predominate the drawbacks.

In this regard, the present contribution addresses the simulation of fully saturated soils under dynamic loading conditions exploiting explicit time-integration schemes. Therein, the governing soil model, which proceeds from the Theory of Porous Media (TPM) as a suitable modelling framework, incorporates a materially incompressible solid skeleton representing the soil grains and a materially compressible pore fluid describing the pore water. In particular, in contrast to other authors, e.g. [13], which proceeded from a materially incompressible pore water, the present contribution describes the pore fluid as an inseparable mixture of a trapped materially compressible gas and of a materially incompressible liquid, thereby, on the one hand, accounting for a more realistic pore-fluid description and, on the other hand, allowing for explicit time-integration schemes. The governing pore-fluid model proceeds from [19], where a relation for the pressure-dependent pore-fluid density has been derived. In contrast to the case of a materially incompressible pore fluid, which requires more complex solution strategies, such as decoupled solution procedures, e.g. [20, 27, 30], the solution procedure is more straightforward and, thus, allows for an embedding into the commercial FE package Abaqus. In particular, the governing equations are spatially and temporally discretised, where the latter, on the one hand, exploits the implicit *Hilber–Hughes–Taylor* (HHT) procedure [15] and, on the other

hand, the explicit central-difference together with the forward *Euler* method, e.g. [17]. Following this, the numerical model is implemented into the coupled finite-element solver PANDAS, which, however, is linked via a general interface to the commercial finite-element (FE) package Abaqus. This coupling allows for the definition of complex initial-boundary-value problems through Abaqus, thereby exploiting the material models of PANDAS. In order to evaluate the presented modelling approach in terms of accuracy and parallel efficiency (parallel scalability), several simulations are carried out.

2 Theory of Porous Media

In order to lay down a theoretical foundation, the basic concepts of the Theory of Porous Media (TPM) are briefly reviewed in the following chapter. For a more detailed insight into the governing theory, the interested reader is referred to the related literature, e.g. [2, 10], and references therein.

Within the macroscopic TPM approach, the overall system soil is treated as an immiscible mixture of various interacting components φ^α, which are assumed to be homogeneously distributed within a representative elementary volume (REV) $\mathrm{d}v$. In particular, within the scope of the present contribution, the fluid-saturated soil is composed of the solid skeleton ($\alpha = S$), assembled by the soil grains, and of the pore fluid ($\alpha = F$), which can be again a mixture of various interacting components φ^β, i.e. $\varphi^F = \bigcup_\beta \varphi^\beta$. The composition of the bulk volume element is defined through the respective volume fractions $n^\alpha = \mathrm{d}v^\alpha/\mathrm{d}v$, where $\mathrm{d}v^\alpha$ is the partial volume of the component φ^α within the REV. Note that the saturation condition $\sum_\alpha n^\alpha = n^S + n^F = 1$ must hold.

Following this, two density functions are defined. The material (realistic or effective) density $\rho^{\alpha R} = \mathrm{d}m^\alpha/\mathrm{d}v^\alpha$ relates the components local mass $\mathrm{d}m^\alpha$ to its volume $\mathrm{d}v^\alpha$, while the partial (global or bulk) density $\rho^\alpha = \mathrm{d}m^\alpha/\mathrm{d}v$ is associated with the bulk volume. Moreover, both density definitions are related to each other through $\rho^\alpha = n^\alpha \rho^{\alpha R}$. As we assume materially incompressible and uncrushable grains, the realistic density of the solid remains constant under the prescribed isothermal conditions, but the bulk density can still change through a changing volume fraction n^α.

2.1 Kinematics

In the framework of the TPM, the individual components φ^α are treated as superimposed continua where each spatial point is simultaneously occupied by particles of both components. Each component is moving according to its own motion function and, thus, has its own velocity and acceleration fields. In this regard, it is convenient to express the solid motion in the *Lagrange*an or material setting through the solid displacement $\mathbf{u}_S$ and the motion of the pore-fluid component φ^F in the *Euler*ian or spatial setting their respective seepage velocities $\mathbf{w}_F$ relative to the solid motion:

$$\begin{aligned} &\bullet \text{ solid:} \quad \mathbf{u}_S = \mathbf{x} - \mathbf{X}_S, \; \mathbf{v}_S = (\mathbf{u}_S)'_S = \overset{\prime}{\mathbf{x}}_S, \; (\mathbf{v}_S)'_S = \overset{\prime\prime}{\mathbf{x}}_S, \\ &\bullet \text{ pore fluid:} \quad \mathbf{w}_F = \mathbf{v}_F - \mathbf{v}_S, \quad (\mathbf{v}_F)'_F \approx (\mathbf{v}_F)'_S. \end{aligned} \tag{1}$$

Therein, $\mathbf{X}_S$ denotes the position of a solid material point in the reference configuration ($t = t_0$), while $\mathbf{x}$ is the position of a point in the current configuration ($t > t_0$). Moreover, $(\cdot)'_S$ and $(\cdot)'_F$ denote the material time derivatives following the motion of the solid skeleton and the pore fluid, respectively. Note that in the geometric linear case, which is the case within the scope of the present contribution, the nonlinear convective term $\operatorname{grad} \mathbf{v}_F \, \mathbf{w}_F$ can be neglected [29]. Thus, $(\mathbf{v}_F)'_F = (\mathbf{v}_F)'_S + \operatorname{grad} \mathbf{v}_F \, \mathbf{w}_F \approx (\mathbf{v}_F)'_S$.

2.2 Balance Relations

Within the TPM framework, the underlying balance equations proceed from the balance equations of classical continuum mechanics. They can be written for the individual components, yielding the so-called partial balance equations, or be summed up to obtain the balance equations of the overall aggregate. With respect to the scope of the present contribution, assuming isothermal conditions, the governing balance laws are the mass and momentum balance. Note that, in order to obtain a thermodynamically consistent model, the entropy inequality is additionally exploited. However, its evaluation is not carried out here, instead, only the final results are given and the interested reader is referred to [7, 9] and references therein. Based on the work of [10], the governing partial mass and momentum balances, neglecting mass-exchange processes between the individual components, are given by

$$\begin{aligned} &\bullet \text{ partial mass balance:} \quad (\rho^\alpha)'_\alpha + \rho^\alpha \operatorname{div} \overset{\prime}{\mathbf{x}}_\alpha = 0, \\ &\bullet \text{ partial momentum balance:} \quad \rho^\alpha (\mathbf{v}_\alpha)'_\alpha = \operatorname{div} \mathbf{T}^\alpha + \rho^\alpha \mathbf{b}^\alpha + \hat{\mathbf{p}}^\alpha. \end{aligned} \tag{2}$$

Therein, $\mathbf{T}^\alpha$ is the partial *Cauchy* stress tensor, $\mathbf{b}^\alpha$ the body-force vector and $\hat{\mathbf{p}}^\alpha$ the direct momentum production, which accounts for the local momentum exchange between the individual components.

3 Soil Model

3.1 Governing Balance Laws

The governing balance laws are the momentum balance of the overall aggregate and the convective-less momentum balance of the pore fluid [20], and the mass balance of the compressible pore fluid [10]. Thus,

$$\rho^S (\mathbf{v}_S)'_S + \rho^F (\mathbf{v}_F)'_S = \operatorname{div} (\mathbf{T}^S_E - p \, \mathbf{I}) + (\rho^S + \rho^F) \mathbf{b}, \tag{3}$$

$$\rho^F (\mathbf{v}_F)'_S = \operatorname{div}(-n^F p\, \mathbf{I}) + \rho^F \mathbf{b} - \frac{(n^F)^2 \gamma^{FR}}{k^F} \mathbf{w}_F + p \operatorname{grad} n^F, \tag{4}$$

$$(n^F \rho^{FR})'_S + n^F \rho^{FR} \operatorname{div} \mathbf{v}_S + \operatorname{div}(n^F \rho^{FR} \mathbf{w}_F) = 0. \tag{5}$$

Therein, $\mathbf{b}$ is the constant gravitation substituting $\mathbf{b}^\alpha$, k^F is the hydraulic conductivity (*Darcy* permeability), and $\gamma^{FR} = g\rho^{FR}$ is the effective fluid weight with $g = |\mathbf{b}| =$ constant. Moreover, $\mathbf{T}^S_E$ is the effective solid extras stress, p is the overall pore-fluid pressure, and $\mathbf{I}$ is the second-order identity tensor. Note that the sum of the individual direct production terms vanishes, i.e. $\hat{\mathbf{p}}^S + \hat{\mathbf{p}}^F = \mathbf{0}$, as the overall aggregate is momentum conserving. Additionally, it can be shown that fluid extra stresses can be neglected based on a dimensional analysis [12], i.e. $\mathbf{T}^F_E \approx \mathbf{0}$.

3.2 Solid Skeleton

Confined to the small strain regime, the linear solid strain reads as

$$\begin{aligned} &\varepsilon_S \approx \tfrac{1}{2} (\operatorname{grad} \mathbf{u}_S + \operatorname{grad}^T \mathbf{u}_S), \\ &\text{where} \qquad \operatorname{grad}(\cdot) = \partial(\cdot)/\partial x. \end{aligned} \tag{6}$$

Futhermore, the linearised solid volume fraction [7] is given as

$$n^S = n^S_{0S}(1 - \operatorname{div} \mathbf{u}_S), \tag{7}$$

where n^S_{0S} denotes the initial solid volume fraction. The solid extra stress can be described by the linear *Hooke* an elasticity law

$$\mathbf{T}^S_E = 2\mu^S \varepsilon_S + \lambda^S (\varepsilon_S \cdot \mathbf{I})\, \mathbf{I}. \tag{8}$$

Therein, μ^S and λ^S denote the macroscopic *Lamé* constants of the porous solid skeleton.

3.3 Pore Fluid

As was mentioned before, the pore fluid is treated as an inseparable mixture composed of a compressible gas and a incompressible liquid. Proceeding from the TPM, a relation for the pore-pressure-dependent density of the pore-fluid mixture can be derived (see [19] for details).

Proceeding from $(2)_1$ with the substitution $\beta \in \{L, G\}$, the partial mass balances of the pore liquid and the pore gas can be obtained. Moreover, assuming that both are following the same motion, in particular, with the barycentric velocity of the pore-fluid mixture, i.e. $\mathbf{v}_L = \mathbf{v}_G \equiv \mathbf{v}_F$ and $(\cdot)'_L = (\cdot)'_G \equiv (\cdot)'_F$, the mass balances can be recast to yield

$$\left.\begin{aligned} (\rho^L)'_F + \rho^L \operatorname{div} \mathbf{v}_F &= 0 \\ (\rho^G)'_F + \rho^G \operatorname{div} \mathbf{v}_F &= 0 \end{aligned}\right\} \;\rightarrow\; \frac{(\rho^L)'_F}{\rho^L} = \frac{(\rho^G)'_F}{\rho^G}. \tag{9}$$

Analytical integration results in a constant ratio between ρ^L and ρ^G are given by

$$\rho^L = C\,\rho^G \qquad \text{where} \qquad C = \left.\frac{n^L \rho^{LR}}{n^G \rho^{GR}}\right|_{t=t_0} = \frac{n^L_{0F} \rho^{LR}}{n^G_{0F} \rho^{GR}_{0F}}. \tag{10}$$

Therein, the integration constant C is not a material but a structural parameter conducting the composition of the pore-fluid mixture.

Finally, the addressed relation for the pressure-dependent pore-fluid density is obtained by recasting (10), with the help of the mixture density, $n^F \rho^{FR} = n^L \rho^{LR} + n^G \rho^{GR}$, and the saturation condition of the pore-fluid mixture, $n^F = n^G + n^L$. It reads as

$$\rho^{FR}(p) = \rho^{LR} \frac{1 + C}{C + \frac{\rho^{LR}}{\rho^{GR}(p)}} \qquad \text{with} \qquad \rho^{GR}(p) = \frac{p + p_0}{R\,\Theta}. \tag{11}$$

Therein, p_0 is the initial pressure of the gaseous phase, R is the specific gas constant of air and Θ is the temperature. Note that $(11)_1$ also comprises the case of a fully gas-saturated pore space by setting $n^L_{0F} = 0$ yielding $C = 0$ and, thus, $\rho^{FR} = \rho^{GR}$. In contrast, the case of a fully liquid-saturated pore space is obtained by setting $n^G_{0F} = 0$ resulting in $C \rightarrow \infty$ and, herewith, by exploiting the rule of *de l'Hôspital* [18], $\rho^{FR} = \rho^{LR}$.

4 Numerical Treatment

The following section addresses the numerical treatment of the governing soil model, in particular, the spatial and temporal discretisation of the unknown fields $\mathbf{u}_S$, $\mathbf{v}_F$ and p. Having a comparison of different time-integration schemes in mind, the latter is carried out, on the one hand, using an implicit procedure and, on the other hand, using an explicit scheme. Finally, some remarks related to the solution procedure of the coupled problem are given.

4.1 Spatial Discretisation

The spatial discretisation of the semi-infinite domain is based on the finite-element method (FEM). Following the *Bubnov-Galerkin* approach, the governing strong forms are multiplied with the test function $\delta\mathbf{u}_S$, $\delta\mathbf{v}_F$ and δp corresponding to the unknown fields and are integrated over the spatial domain Ω, thereby, exploiting the *Gauss* theorem. In particular, the governing weak forms are given as

$$0 = \int_{\Omega} \left\{ \rho^S (\mathbf{v}_S)'_S + \rho^F (\mathbf{v}_F)'_S - (\rho^S + \rho^F)\mathbf{b} \right\} \cdot \delta\mathbf{u}_S \, \mathrm{d}v + \int_{\Omega} (\mathbf{T}^S_E - p\,\mathbf{I}) \cdot \operatorname{grad} \delta\mathbf{u}_S \, \mathrm{d}v - \int_{\Gamma_{\mathbf{t}}} \bar{\mathbf{t}} \cdot \delta\mathbf{u}_S \, \mathrm{d}a, \tag{12}$$

$$0 = \int_{\Omega} \left[\rho^F (\mathbf{v}_F)'_S - \mathbf{b} \right] \cdot \delta\mathbf{v}_F \, \mathrm{d}v + \int_{\Omega} \left[\frac{(n^F)^2 \gamma^{FR}}{k^F} \mathbf{w}_F - p \operatorname{grad} n^F \right] \cdot \delta\mathbf{v}_F \, \mathrm{d}v + \int_{\Omega} (-n^F p) \operatorname{div} \delta\mathbf{v}_F \, \mathrm{d}v + \int_{\Gamma_{\mathbf{t}^F}} \bar{\mathbf{t}}^F \cdot \delta\mathbf{v}_F \, \mathrm{d}a, \tag{13}$$

$$0 = -\int_{\Omega} (n^F \rho^{FR} \mathbf{w}_F) \cdot \operatorname{grad} \delta p \, \mathrm{d}v + \int_{\Omega} \left[(\rho^{FR} n^F)'_S + \rho^{FR} n^F \operatorname{div} \mathbf{v}_S \right] \delta p \, \mathrm{d}v + \int_{\Gamma_v} \overline{m} \, \delta p \, \mathrm{d}a. \tag{14}$$

Therein, $\bar{\mathbf{t}} = (\mathbf{T}^S_E - p\,\mathbf{I})\mathbf{n}$ and $\bar{\mathbf{t}}^F = -n^F p\,\mathbf{n}$ denote the external loading vectors acting on the *Neumann* boundaries $\Gamma_{\mathbf{t}}$ and $\Gamma_{\mathbf{t}^F}$ of the overall aggregate and the pore fluid, respectively, and $\overline{m} = \rho^{FR} n^F \mathbf{w}_F \cdot \mathbf{n}$ is the mass efflux draining through the *Neumann* boundary Γ_v with $\mathbf{n}$ as the outward oriented unit surface normal.

In a second step, the unknown fields and the corresponding test functions of the weak forms are approximated by suitable test and ansatz functions, which, for the sake of a stable solution procedure, need to fulfil the *inf-sup* condition (*Ladyshenskaya-Babuška-Brezzi* (LBB) condition) [3]. In this connection, having an exploit of Abaqus/Explicit in mind, the solid displacements need to be approximated by linear ansatz functions, which, however, leads to pore-pressure oscillations in case of low *Darcy* permeabilities [20].

Following this, the resulting semi-discrete initial-boundary-value problem (IBVP) can be summarised as

$$\mathcal{G}(t, \boldsymbol{y}, \boldsymbol{y}', \boldsymbol{y}'', \boldsymbol{q}) = \boldsymbol{M}\boldsymbol{y}'' + \boldsymbol{r}(\boldsymbol{y}, \boldsymbol{y}', \boldsymbol{q}) - \boldsymbol{f} \stackrel{!}{=} \boldsymbol{0}. \tag{15}$$

Therein, $\boldsymbol{M}$ is the mass matrix, $\boldsymbol{r}$ the quasi-static residual vector and $\boldsymbol{f}$ the generalised force vector acting on the *Neumann* boundaries. Moreover, in order to keep the following remarks more general, a vector $\boldsymbol{q}$, which gathers the internal variables of an inelastic solid, such as inelastic strains, is introduced. Furthermore, $\boldsymbol{y} = [\hat{\mathbf{u}}_S\, \hat{\mathbf{u}}_F\, \hat{\mathbf{p}}]^T$ denotes a vector containing the nodal values of the unknown field variables, where, for the sake of convenience, the abbreviation $(\cdot)' = (\cdot)'_S$ is used. Note that, having an implementation in Abaqus/Explicit in mind, where due to its limitations regarding the additional degrees of freedom, the relation $\mathbf{v}_F = (\mathbf{u}_F)'_S$ has been used. Therein, $\mathbf{u}_F$ denotes the fictitious fluid displacements. Consequently, the fluid momentum balance, which was initially of first order in time, now becomes second order in time.

In order to illustrate the coupling nature of (15), the overall coupled system is expressed in matrix form as

$$\underbrace{\begin{bmatrix} M_{11} & M_{12} & 0 \\ 0 & M_{22} & 0 \\ 0 & 0 & 0 \end{bmatrix}}_{\boldsymbol{M}} \boldsymbol{y}'' + \underbrace{\begin{bmatrix} C_{11} & C_{12} & 0 \\ C_{21} & C_{22} & 0 \\ C_{31} & C_{32} & C_{33} \end{bmatrix}}_{\boldsymbol{C}} \boldsymbol{y}' + \underbrace{\begin{bmatrix} K_{11} & 0 & K_{13} \\ K_{21} & 0 & K_{23} \\ K_{31} & 0 & K_{33} \end{bmatrix}}_{\boldsymbol{K}} \boldsymbol{y} - \boldsymbol{f} = \mathbf{0}. \tag{16}$$

Therein, the matrices can be distinguished into coupling (highlighted) and non-coupling terms. From this representation, it can be concluded that monolithic explicit time-integration schemes are not applicable. This is seen from the singular submatrix $\boldsymbol{M}_{33}$ resulting in a non-invertible mass matrix $\boldsymbol{M}$. To cope with that, the problem will be decomposed into the smaller subsystems I (filled box) and II (framed box) according to the following scheme:

$$\begin{bmatrix} M_{11} & M_{12} & 0 \\ 0 & M_{22} & 0 \\ 0 & 0 & \boxed{0} \end{bmatrix} \boldsymbol{y}'' + \begin{bmatrix} C_{11} & C_{12} & 0 \\ C_{21} & C_{22} & 0 \\ C_{31} & C_{32} & \boxed{C_{33}} \end{bmatrix} \boldsymbol{y}' + \begin{bmatrix} K_{11} & 0 & K_{13} \\ K_{21} & 0 & K_{23} \\ K_{31} & 0 & \boxed{K_{33}} \end{bmatrix} \boldsymbol{y} - \boldsymbol{f} = \mathbf{0}. \tag{17}$$

Therein, the submatrices $\boldsymbol{C}_{31}$ and $\boldsymbol{C}_{32}$ are important for the decoupling procedure, as they govern the coupling strength (strong or weak) between subsystems I and II. The submatrices read as

$$\begin{aligned} \boldsymbol{C}_{31} &= \int_\Omega \nabla \boldsymbol{P}^T n^F \rho^{FR} \boldsymbol{U}_S \, \mathrm{d}v + \int_\Omega \boldsymbol{P}^T \rho^{FR} (n^F + n^S_{0S}) \boldsymbol{U}_S \, \mathrm{d}v, \\ \boldsymbol{C}_{32} &= -\int_\Omega \nabla \boldsymbol{P}^T n^F \rho^{FR} \boldsymbol{U}_F \, \mathrm{d}v. \end{aligned} \tag{18}$$

Therein, $\boldsymbol{U}_S$, $\boldsymbol{U}_F$ and $\boldsymbol{P}$ are matrices of the interpolation functions of the associated unknown fields, $\mathbf{u}_S$, $\mathbf{u}_F$ and p, and their corresponding test functions. Moreover,

$\nabla(\cdot) := \operatorname{grad}(\cdot)$ denotes the gradient operator. It can be seen that the coupling strength depends on the density of the fluid mixture and, thus, on the structural parameter C.

Assuming that the coupling is sufficiently weak, i.e. $\boldsymbol{C}_{31}$ and $\boldsymbol{C}_{32}$ are small in comparison to $\boldsymbol{C}_{33}$, the general nonlinear system (15) can be decoupled into subsystems I and II by setting $\boldsymbol{C}_{31} = \boldsymbol{C}_{32} \equiv \boldsymbol{0}$. The decoupled system can be summarised as

$$\begin{aligned} \mathcal{G}_I &= \boldsymbol{M}_{\mathrm{I}}\, \boldsymbol{y}_{\mathrm{I}}'' + \boldsymbol{r}_{\mathrm{I}}(\boldsymbol{y}, \boldsymbol{y}', \boldsymbol{q}) - \boldsymbol{f}_{\mathrm{I}} \stackrel{!}{=} \boldsymbol{0}, \\ \mathcal{G}_{\mathrm{II}} &= \boldsymbol{C}_{\mathrm{II}}\, \boldsymbol{y}_{\mathrm{II}}' + \boldsymbol{r}_{\mathrm{II}}(\boldsymbol{y}, \boldsymbol{q}) - \boldsymbol{f}_{\mathrm{II}} \stackrel{!}{=} \boldsymbol{0}. \end{aligned} \tag{19}$$

Therein, $\boldsymbol{M}_{\mathrm{I}}$ is the mass matrix of subsystem I, $\boldsymbol{C}_{\mathrm{II}} = \boldsymbol{C}_{33}$ is the capacitance matrix of subsystem II, and $\boldsymbol{r}_{\mathrm{I}}$ and $\boldsymbol{r}_{\mathrm{II}}$ are the quasi-static and static residual vector of subsystems I and II. Moreover, $\boldsymbol{y}_{\mathrm{I}}$ and $\boldsymbol{y}_{\mathrm{II}}$ denote the vectors of nodal unknowns and $\boldsymbol{f}_{\mathrm{I}}$ and $\boldsymbol{f}_{\mathrm{II}}$ the *Neumann* force vectors of the corresponding subsystems.

4.2 Temporal Discretisation

In the next step, the temporal discretisations of the semi-discrete coupled (15) and of the semi-discrete decoupled system (19) are carried out. In particular, having dynamic loading conditions in mind, the system can either be discretised by an implicit or explicit procedure.

4.2.1 Implicit Scheme

Exploiting the implicit *Hilber–Hughes-Taylor* (HHT) method [15], which is a generalisation of *Newmark*s method [21] but with a direct control of the numerical damping, the time-discrete form of (15) reads as

$$\begin{aligned} &\boldsymbol{\mathcal{R}}_{n+1} = \boldsymbol{M}\, \boldsymbol{y}_{n+1}'' + (1+\alpha)(\boldsymbol{r}_{n+1} - \boldsymbol{f}_{n+1}) - \alpha(\boldsymbol{r}_n - \boldsymbol{f}_n) \stackrel{!}{=} \boldsymbol{0} \\ &\text{with} \quad \boldsymbol{y}_{n+1} = \boldsymbol{y}_n + \Delta t\, \boldsymbol{y}_n' + \Delta t^2 \left(\left(\frac{1}{2} - \beta \right) \boldsymbol{y}_n'' + \beta\, \boldsymbol{y}_{n+1}'' \right), \\ &\qquad\quad \boldsymbol{y}_{n+1}' = \boldsymbol{y}_n' + \Delta t \left((1-\gamma)\, \boldsymbol{y}_n'' + \gamma\, \boldsymbol{y}_{n+1}'' \right). \end{aligned} \tag{20}$$

Therein, $\boldsymbol{r}_{n+1} = r(\boldsymbol{y}_{n+1}, \boldsymbol{y}_{n+1}', \boldsymbol{q}_{n+1})$ and $\boldsymbol{r}_n = r(\boldsymbol{y}_n, \boldsymbol{y}_n', \boldsymbol{q}_n)$ denote the quasi-static response of the system at the new (unknown) state t_{n+1} and at the previous (known) state t_n, respectively. The parameter α controls the numerical damping by governing the parameters β and γ via

$$\beta = \frac{1}{4}(1-\alpha)^2, \; \gamma = \frac{1}{2}(1-\alpha), \tag{21}$$

which are inherit from *Newmark*s method. A suitable choice of the parameter α ranges from $\alpha = -1/3$ (significant damping) to $\alpha = 0$ (no damping), where, in the latter, the trapezoidal rule ($\beta = 1/4$, $\gamma = 1/2$) is obtained. Note that a value of $\alpha = -0.05$ is in general considered a good choice as the inevitably time-stepping-induced high-frequency noise is quickly removed without a significant effect on the low-frequency response of the system.

4.2.2 Explicit Scheme

In contrast to the implicit scheme, the explicit procedure proceeds from the decomposed system (19), where, accounting for the temporal order of the governing subsystem, different explicit time-integration schemes are exploited. In particular, the subproblem I uses the central-difference method. In this regard, $(19)_1$ can be recast into

$$\begin{aligned} &\boldsymbol{M}\boldsymbol{y}_n'' + \boldsymbol{r}(\boldsymbol{y}_n, \boldsymbol{y}_n', \boldsymbol{q}_n) - \boldsymbol{f}_n \stackrel{!}{=} \boldsymbol{0} \\ &\text{with} \quad \boldsymbol{y}_n' \approx \boldsymbol{y}_{n-\frac{1}{2}}' = \frac{1}{\Delta t}(\boldsymbol{y}_n - \boldsymbol{y}_{n-1}), \;\; \boldsymbol{y}_{n+\frac{1}{2}}' = \frac{1}{\Delta t}(\boldsymbol{y}_{n+1} - \boldsymbol{y}_n) \\ &\qquad\quad \boldsymbol{y}_n'' = \frac{1}{\Delta t}\left(\boldsymbol{y}_{n+\frac{1}{2}}' - \boldsymbol{y}_{n-\frac{1}{2}}'\right) = \frac{1}{\Delta t^2}\left(\boldsymbol{y}_{n+1} - 2\,\boldsymbol{y}_n + \boldsymbol{y}_{n-1}\right). \end{aligned} \tag{22}$$

Note that for the sake of a clear representation, the previously introduced subsystem index I has been dropped. Moreover, it is important to point out that in the central difference method the velocities are computed at the intermediate steps, i.e. $\boldsymbol{y}'(t_{n-\frac{1}{2}}) = \boldsymbol{y}_{n-\frac{1}{2}}'$ and $\boldsymbol{y}'(t_{n+\frac{1}{2}}) = \boldsymbol{y}_{n+\frac{1}{2}}'$, where the former is used to approximate the velocity vector $\boldsymbol{y}_n'$.

Subsystem II can be adequately discretised by the explicit (forward) *Euler* method. In this regard, the discrete form of $(19)_2$ reads as

$$\boldsymbol{C}\boldsymbol{y}_n' + \boldsymbol{r}(\boldsymbol{y}_n, \boldsymbol{q}_n) - \boldsymbol{f}_n \stackrel{!}{=} \boldsymbol{0} \qquad \text{with} \qquad \boldsymbol{y}_n' = \frac{1}{\Delta t}(\boldsymbol{y}_{n+1} - \boldsymbol{y}_n). \tag{23}$$

As before, for the sake of a clear representation, the subsystem index II has been dropped.

4.3 Solution Procedure

Depending on the underlying time-integration scheme, the solution procedure is different. In particular, an implicit time integration yields a system of coupled algebraic equations, which needs to be solved, for instance, by the iterative *Newton-Raphson* method. In contrast, in order to exploit the advantage of explicit schemes, a matrix lumping technique is required, which diagonalises the matrix and, thus, decouples the

individual algebraic equations. The decoupled system of algebraic equations allows for a straightforward and, thus, a more efficient computation of the nodal unknowns.

4.3.1 Implicit Scheme

The nonlinear discrete system (20) is solved by the iterative *Newton-Raphson* method, where, at each temporal increment $n+1$ the system is linearised around the known state via

$$\begin{aligned} \boldsymbol{J}^i_{n+1} &= \frac{\mathrm{d}\boldsymbol{\mathcal{G}}^i_{n+1}}{\mathrm{d}\boldsymbol{y}_{n+1}} = \frac{\partial \boldsymbol{\mathcal{G}}^i_{n+1}}{\partial \boldsymbol{y}''_{n+1}} \frac{\partial \boldsymbol{y}''_{n+1}}{\partial \boldsymbol{y}_{n+1}} = \frac{1}{\Delta t^2\, \beta} \mathbf{M}^i_{n+1} + (1+\alpha)\left(\mathbf{K}^i_{n+1} + \frac{\gamma}{\Delta t\, \beta} \mathbf{C}^i_{n+1}\right), \\ \text{where} \quad \mathbf{K}^i_{n+1} &= \frac{\partial \boldsymbol{\mathcal{R}}^i_{n+1}}{\partial \boldsymbol{y}^i_{n+1}}, \; \mathbf{C}^i_{n+1} = \frac{\partial \boldsymbol{\mathcal{R}}^i_{n+1}}{\partial (\boldsymbol{y}')^i_{n+1}}, \; \mathbf{M}^i_{n+1} = \frac{\partial \boldsymbol{\mathcal{R}}^i_{n+1}}{\partial (\boldsymbol{y}'')^i_{n+1}}. \end{aligned} \tag{24}$$

Therein, $\boldsymbol{J}^i_{n+1}$ denotes the so-called *Jacobi*an matrix at the ith *Newton* increment, which will be used to compute the update to the solution via

$$\boldsymbol{J}^i_n \boldsymbol{y}^i_{n+1} = \boldsymbol{\mathcal{R}}^i_{n+1}, \tag{25}$$

until (25) satisfies a certain convergence criteria, e.g. $\|\|\boldsymbol{\mathcal{R}}^i_{n+1}\|\| < \epsilon$, with ϵ being the admissible numerical error. In a subsequent step, the velocity and acceleration can be computed from $(20)_2$ and $(20)_3$.

4.3.2 Explicit Scheme

The efficiency of explicit schemes originates from the matrix lumping technique, which, however, introduces a small numerical error (e.g. see [17]). A very common and efficient procedure is the method of row-sum lumping (RSL), where all components A_{ij} of a matrix $\mathbf{A}$ are concentrated to the diagonal element of row i via

$$\widetilde{\mathbf{A}} = \mathrm{diag}(\widetilde{A}_i) \qquad \text{with} \qquad \widetilde{A}_i = \sum_{j=1}^{m} A_{ij} \qquad i = 1, 2, ..., m. \tag{26}$$

Therein, m denotes the number of columns (equal to the number of rows), which corresponds to the degrees of freedom of the FE mesh. In this connection, it is important to point out that the RSL method cannot be applied to elements with quadratic ansatz functions, as the row sum yields negative diagonal terms [1, 4]. To cope with that, alternative lumping techniques, such as the HRZ method [16] or the nodal-quadrature method [11], can be applied.

With respect to the given problem, the RSL method is applied to the mass matrix $\boldsymbol{M}_{\mathrm{I}}$ of subproblem I and to the capacitance matrix $\boldsymbol{C}_{\mathrm{II}}$ of subproblem II, yielding the

corresponding diagonalised forms $\widetilde{\boldsymbol{M}}_{\mathrm{I}}$ and $\widetilde{\boldsymbol{C}}_{\mathrm{II}}$, respectively. With the diagonalised matrices at hand, subsystems I and II can be solved independently for the unknowns $(\boldsymbol{y}_{\mathrm{I}})''_n$ and $(\boldsymbol{y}_{\mathrm{II}})'_n$, from which, in a subsequent step, the unknown velocities and displacements of the individual subsystem can be computed with the help of $(22)_2$, $(22)_3$ and $(23)_2$.

4.4 Numerical Implementation

The discretised coupled system is implemented into the FE package PANDAS[1] and linked through a general interface to the commercial FE package Abaqus [26]. This software coupling allows for the definition of complex initial-boundary-value problems in terms of features, such as kinematic coupling and tie constraints, and in terms of large-scale analyses through parallelisation.

Basically, the coupling exploits the coupled-temperature-displacement procedures in Abaqus/Standard (implicit time-integration) as well as Abaqus/Explicit (explicit time-integration), where the temperature degrees of freedom are exploited as placeholders for the additional degrees of freedom, fictitious fluid displacement and pore pressure. Note that, in contrast to Abaqus/Standard, where up to 20 additional slots can be used, Abaqus/Explicit solely allows for one additional vector-valued and two additional scalar-valued degrees of freedom.

4.4.1 Coupling Workflow

The Abaqus-PANDAS linkage is based on the FORTRAN-coded user-defined element subroutine UEL of Abaqus/Standard, which serves to evaluate the element-wise contributions to the ride-hand-side vector and the *Jacobi*an matrix, and VUEL of Abaqus/Explicit, which needs to define the quasi-static residual vector, and the mass and capacitance matrices. However, within the current setting, the functionality of the UEL subroutine or the VUEL subroutine, respectively, is handed over to PANDAS (cf. Fig. 1). In particular, within the C-coded CUEL subroutine, PANDAS is initialised (only once per analysis), the input data is copied to a matching data format, the element-wise contributions are computed and, finally, converted back again. In subsequent steps, Abaqus gradually assembles the overall system of equations considering the boundary conditions and solves the system of equations at each time increment.

[1] Porous media Adaptive Nonlinear finite-element solver based on Differential Algebraic Systems, http://www.get-pandas.com.

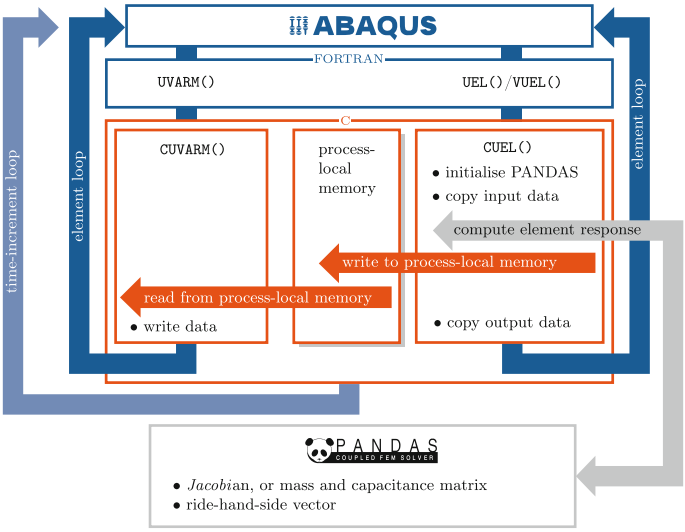

Fig. 1 Schematic sketch of the coupling workflow exploiting the overlay-element-based post-processing method

4.4.2 Post-processing Methods

A crucial point when performing Abaqus simulations incorporating user-defined elements is the post-processing of the analysis results, which originates from the fact that the ansatz functions and the method used to integrate the governing weak forms (e.g. via *Gauss* point quadrature) are solely defined within the user subroutine. However, in order to fill the lack of data, several methods are possible.

A naive approach is to store the integration-point data in a temporary database (e.g. text file, .fil file of Abaqus) [23, 26] and to merge its content, at the end of an increment or at the end of the analysis, into either the results database of Abaqus (.odb) or an external database suitable for third-party tools, such as Tecplot or Paraview.

Another very prominent method introduces so-called overlay (or dummy or ghost) elements, which solely serve as data container as they exhibit, in relation to the simulated process, negligible material properties. Therein, an Abaqus element with a similar element topology is connected in parallel to the user-defined element, thereby introducing ansatz functions for the nodal interpolation and integrations points to hold the dependent variables (e.g. stresses). In order to transfer the integration-point data between the overlay and the corresponding user-defined element, a process-local memory is exploited as a temporary data container, from which the CUVARM subroutine retrieves the integration-point data and writes them to the results data base of Abaqus. In this connection, it is important to note that, in a process-based parallelisation, which incorporates a decomposition of the simulated domain and a distribution of the partial domains onto the individual processes, it may be necessary to transfer the integration-point data between the processes (e.g. via MPI programming

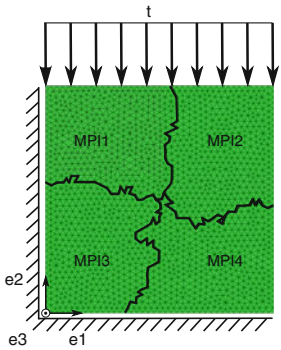

Fig. 2 Benchmark problem decomposed into four MPI domains

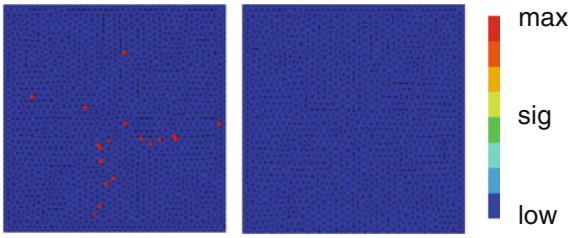

Fig. 3 Contour plot of σ_{22} for a simulation without (*left*) and with MPI-based communication (*right*) of integration point data

standard), as the domain-decomposition algorithm of Abaqus does not guarantee that the overlay element and its related user-defined element are attached to the same process.

In order to verify the overlay-element-based post-processing method in a parallel analysis, a benchmark problem has been investigated. Therein, a simple initial-boundary-value problem (IBVP) has been created, where the displacements at the right and bottom edges are constrained in normal direction and the upper edge is loaded by the surface load $\bar{t} = 1\,\mathrm{kN/m}$ (Fig. 2). The material behaviour is governed by single-phasic (non-porous) linear-elastic material law. The analysis has been carried out in parallel comprising a thread- and process-based parallelisation. In particular, the problem has been decomposed into four MPI domains, where each subdomain is split into two threads, i.e. the benchmark problem runs in parallel on eight computing cores.

The resulting stress distribution is depicted in Fig. 3. Therein, the previously mentioned non-matching processes assignment between the user-defined and the corresponding overlay element is clearly illustrated, as the stress distribution is not homogeneous (Fig. 3, left). In contrast, when incorporating an inter-process communication of the integration-point variables, a homogeneous stress field is obtained (Fig. 3, right). It is important to point out that the overlay-element method has two major drawbacks. On the one hand, it is not applicable to Abaqus/Explicit, as the necessary UVARM subroutine is only available in Abaqus/Standard and, thus, only nodal values can be visualised. On the other hand, it suffers from a significant computational overhead of approx. 90 % in case of the direct solver and of approx. 45 %

when using the iterative solver. Nevertheless, in comparison to the alternative methods, it is a convenient procedure, suitable for thread- and process-based parallel Abaqus simulations and, thus, the method of choice within the present contribution.

5 Simulations

The present section addresses the numerical simulation of the previously discussed soil model. In particular, in order to verify the presented decoupling procedure, which is essential for the explicit time-integration scheme, the influence of the coupling submatrices, which are governed by the initial gas and liquid fractions, is analysed. In a second step, the efficiency in parallel simulations of the implicit and the explicit time-integration scheme is investigated. Both sets of simulations are carried out with the governing material parameters summarised in Table 1. Note that the volume fractions of the liquid and gaseous phases, n^L_{0F} and n^G_{0F}, depend on the investigated problem. Please refer to the corresponding section for their respective values.

5.1 Explicit Versus Implicit Schemes

To start with, the first set of simulations addresses the investigation of the coupling strength between subsystems I and II (see Sect. 4.1). In this regard, the initial volume fraction n^G_{0F} of the gaseous phase and, in order to satisfy the saturation condition, the volume fraction n^L_{0F} of the liquid phase are varied. In particular, n^G_{0F} is set to $n^G_{0F} = 10^{-5} \equiv n^G_{\min}$, which corresponds to the maximum gas solubility in water at atmospheric conditions ($p_0 = 10^5\,\mathrm{N/m^2}$, $\Theta = 293\,\mathrm{K}$) [14], and to $n^G_{0F} = 2 \times 10^{-2} \equiv n^G_{\max}$, which is associated with the residual gas saturation of mudstones [24]. The governing initial-boundary-value problem is depicted in Fig. 4. Therein, a soil column (height 10 m, width 1 m, depth 1 m) is loaded by a prescribed displacement (Fig. 5) given by

$$\begin{aligned} &\overline{u}(t) = \overline{u}_0 \left[\frac{t}{\tau} H(t) - H(t-\tau) \right] + \overline{u}_0 \, H(t-\tau), \\ &\text{with} \qquad \overline{u}_0 = 0.1\,\mathrm{m}, \;\; \tau = 0.01\,\mathrm{s}, \;\; 0 \leq t \leq 0.2\,\mathrm{s}, \end{aligned} \tag{27}$$

which triggers a compressional wave (p-wave) propagating through the column. The simulations are carried out in Abaqus/Standard and Abaqus/Explicit. In this regard, in Abaqus/Standard the unknown fields, in particular, the solid displacement $\mathbf{u}_S$, the fictitious fluid displacement $\mathbf{u}_F$ and the pore pressure of the pore-fluid mixture p, are, on the one hand, approximated by linear ansatz functions (impl./LL), and, on the other hand, by so-called mixed finite elements, where quadric ansatz functions for $\mathbf{u}_S$ and linear ansatz functions for $\mathbf{u}_F$ and p (impl./QL) are used. In contrast, in

Table 1 Material parameters of the governing soil model

n^S_{0S}	n^L_{0F}	n^G_{0F}	μ^S	λ^S	ρ^{SR}	ρ^{LR}	γ^{FR}	Θ_0	R_{air}	p_0	k_F
0.6	Mutable	Mutable	5.6×10^6	8.4×10^6	2.7×10^3	10^3	10^4	293	287	10^5	10^{-4}
–	–	–	$\left(\frac{\text{N}}{\text{m}^2}\right)$	$\left(\frac{\text{N}}{\text{m}^2}\right)$	$\left(\frac{\text{kg}}{\text{m}^3}\right)$	$\left(\frac{\text{kg}}{\text{m}^3}\right)$	$\left(\frac{\text{N}}{\text{m}^3}\right)$	(K)	$\left(\frac{\text{J}}{\text{kg K}}\right)$	$\left(\frac{\text{N}}{\text{m}^2}\right)$	$\left(\frac{\text{m}}{\text{s}}\right)$

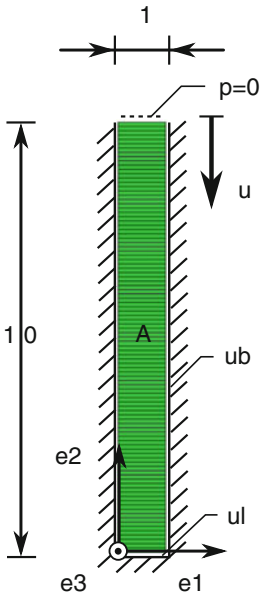

Fig. 4 IBVP for time-integration-scheme comparison

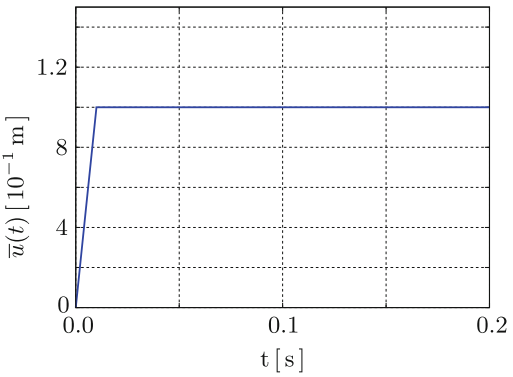

Fig. 5 Evolution of the prescribed displacement $\overline{u}(t)$ applied on top of the domain

Abaqus/Explicit, constrained by the overlay-element post-processing method, linear approximations for all field variables (expl./LL) are used.

In order to illustrate the differences between the different schemes, the evolution of the pore-pressure for the cases $n^G_{\min}$ and $n^G_{\max}$ at point A, located at the spatial coordinates (0 m, 5 m, 0 m), is recorded (Figs. 6 and 7). As can be seen in both cases, the initiated p-wave propagates through the domain and is reflected at the top and bottom of the column. Moreover, the influence of the amount of gas in the pore-fluid mixture is clearly illustrated. In particular, in the case of a low gas content ($n^G_{\min}$), the compression of the porous solid skeleton causes significant higher pore pressures compared to the case of a higher gas content ($n^G_{\max}$), as the incompressibility of the pore liquid exhibits stronger interaction with the motion of the solid skeleton.

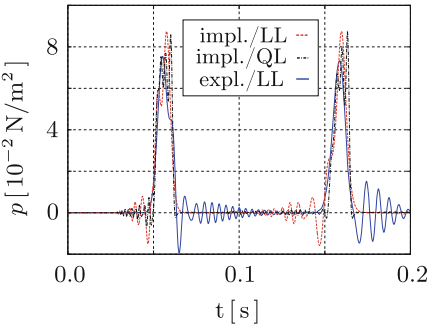

Fig. 6 Evolution of the pore-pressure p for the case of $n^G_{\min}$

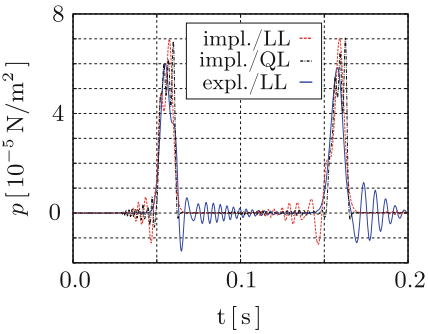

Fig. 7 Evolution of the pore-pressure p for the case of $n^G_{\max}$

Comparing the results for the different time-integration schemes and different spatial discretisations, although all methods show similar results, it is obvious that the explicit scheme exploiting linear ansatz functions (expl./LL) exhibits strong pore-pressure oscillations, which are owed to the unsatisfied LBB condition. Nevertheless, also the stable mixed finite elements (impl./QL) show small, but observable, oscillations, which suggest that the pressure oscillations are of physical nature. In order to avoid numerical oscillations when using linear–linear approximations, stabilisation techniques, e.g. [6], are necessary.

5.2 Parallel Benchmark

This section addresses a performance investigation between the previously introduced explicit and implicit time-integration schemes when carrying out parallel simulations. In this regard, preparing the numerical simulation of geotechnical installation processes using vibro-injections piles, the governing benchmark problem is inspired by a practically relevant scenario (cf. Fig. 8).

Therein, an ellipsoidal halfspace (first and second minor axes: 20 m, third minor axis: 10 m) with a drained top surface ($\overline{p} = 0$) is simplified to a one-fourth model by exploiting the symmetry of the problem and by introducing suitable boundary

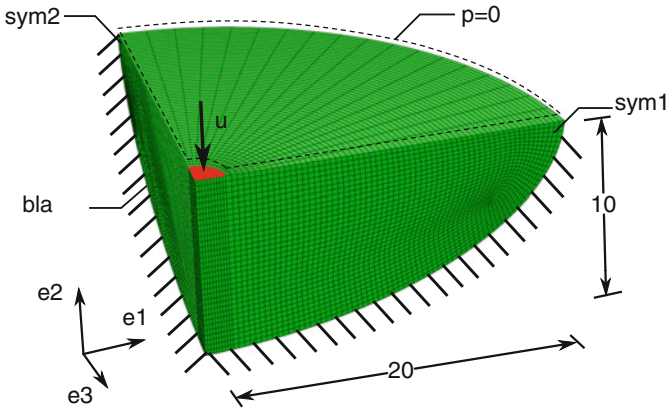

Fig. 8 Initial-boundary-value problem of the benchmark problem

conditions at the symmetry planes. Moreover, the load imposed by the vibrating pile is replaced by a single displacement impulse given

$$\begin{aligned} &\overline{u}(t) = \overline{u}_0 \sin(2\pi f t)[H(t) - H(t-\tau)], \\ &\text{with} \quad \overline{u}_0 = 0.05\,\text{m}, \;\; f = 10\,\text{Hz}, \;\; \tau = 0.05\,\text{s}, \;\; 0 \leq t \leq 0.5\,\text{s}. \end{aligned} \tag{28}$$

The governing material parameters are taken from Table 1, where the initial volume fraction of the liquid and the gaseous component are $n^L_{0F} = 0.399$ and $n^G_{0F} = 0.001$.

The resulting numerical model consists of approximately 38 295 elements (excluding overlay elements) with linear ansatz functions for the nodal unknowns and the corresponding test functions, which result in 294 056 degrees of freedom. For the investigation of the parallel performance of the implicit and the explicit schemes, the simulations have been carried out on a compute node[2] of a high-performance computing (HPC) cluster exploiting different numbers of processes, viz.p $\in \{2, 4, 8, 16, 32\}$. The simulations proceed from a thread-based parallelisation incorporating a LU-decomposition-based direct solver in Abaqus/Standard and from an MPI-based parallelisation in Abaqus/Explicit. For a comprehensive insight into the technical differences between the diverse parallelisation methods, the interested reader is referred to [22]. Note that the for large-scale problems more suitable *Krylov*-subspace-based iterative solvers are not available for the imposed HHT time-integration scheme in Abaqus/Standard. Moreover, the time increments are fixed to $\Delta t_{\text{impl.}} = 5 \cdot 10^{-4}\,\text{s}$ and $\Delta t_{\text{expl.}} = 5 \cdot 10^{-5}\,\text{s}$ in Abaqus/Standard and Abaqus/Explicit, respectively.

The simulation results are depicted in Fig. 9. Therein, a sequence of contour plots of the solid displacement in direction of $\mathbf{e}_2$, i. e. $u_{S2} = \mathbf{u}_S \cdot \mathbf{e}_2$, at different time steps is given. The loading impulse triggers two bulk-wave types, in particular, compressional

[2] A compute node consists of two AMD Opteron™ Processors (model 6328), each composed of 16 cores running at 3.2 GHz, and is equipped with 256 GB memory.

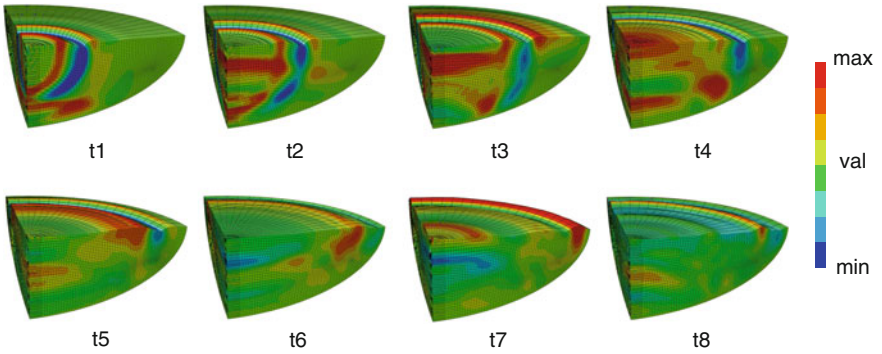

Fig. 9 Contour plots of the solid displacement in vertical direction u_{S2} on the deformed mesh (*scale factor* 1000) at different times

Table 2 Run-time comparison between the Abaqus/Standard and Abaqus/Explicit

	Number of threads/processes				
	$p = 2$	$p = 4$	$p = 8$	$p = 16$	$p = 32$
Run time Abaqus/Explicit (s)	16627	8801	4972	2612	1877
Run time Abaqus/Standard (s)	446056	247604	137444	79393	44114

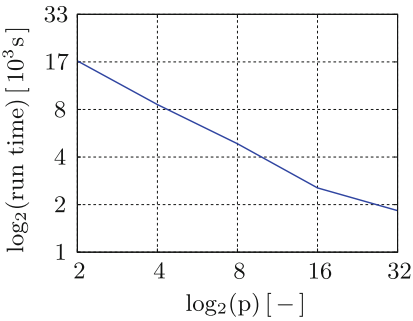

Fig. 10 Run-time comparison in Abaqus/Explicit for a different number p of parallel processes

waves (p-waves) and transverse shear waves (s-waves), which propagate through the domain and are reflected on the domain boundaries.

The run-time measurements are summarised in Table 2. Therein, the advantage of explicit scheme in comparison to the implicit scheme is clearly illustrated, as the simulation times in Abaqus/Explicit are significantly lower than for Abaqus/Standard. Moreover, it can be concluded from Figs. 10 and 11 that, at least within the test regime, both schemes exhibit a linear speed up with a speed-up factor of approximately 1.8. However, it is expected that with increasing model complexity, i.e. increasing number of degrees of freedom, the explicit scheme will show a better speed up, as the necessary number of floating-point operations to solve a system of equations of size $n \times n$ using on LU-decomposition-based method is approximately

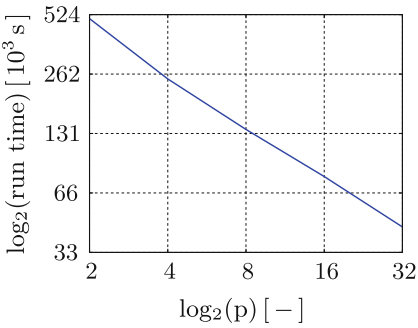

Fig. 11 Run-time comparison in Abaqus/Standard for a different number p of parallel processes

$2/3\,n^3$ [28], which is a nonlinear relation in n. Moreover, this effect will become even more pronounced if the system of equations needs to be distributed to different machines which, in order to account for the coupling of the nodal degrees of freedom, requires a machine-to-machine communication via the network interconnect.

6 Summary

This chapter investigated the possibility of exploiting the explicit time-integration scheme of Abaqus/Explicit to simulate complex and large-scale IBVP. In particular, the underlying fully-saturated soil model proceeds from the TPM incorporating a compressible pore fluid, treated as an inseparable mixture of a compressible trapped pore gas and an incompressible pore liquid leading to an compressible pore-fluid mixture. In a first step, the governing equations were spatially discretised through the finite-element method. In a second step, the temporal discretisation was carried out, on the one hand, by the implicit *Hilber–Hughes–Taylor* method and, on the other hand, via the explicit central-difference scheme together with the explicit *Euler* method, which required a decoupling of the coupled problem at hand.

The discretised equations have been implemented into PANDAS and linked to Abaqus via a general interface. The software coupling has been designed to account for a parallel-capable post-processing method, which is however only available for Abaqus/Standard. Finally, the presented approach has been tested with implicit and explicit time-integrations schemes in terms of accuracy and parallel performance. In particular, the first set of simulations reveals that all simulations show similar results. However, the linear–linear spatial approximations, which are a requirement of Abaqus/Explicit when exploiting the overlay-element-based post-processing method is used, suffer from significant numerical oscillations. Therefore, suitable stabilisation methods, available from the related literature, are necessary. The second set of simulations demonstrated the efficiency of the explicit schemes in comparision to the implicit schemes, especially in parallel simulations.

References

1. Bathe, K.: Finite Element Procedures. Prentice Hall (2006)
2. de Boer, R., Ehlers, W.: Theorie der Mehrkomponentenkontinua mit Anwendung auf bodenmechanische Probleme. Forschungsberichte aus dem Fachbereich Bauwesen, Heft 40, Universität-GH-Essen (1986)
3. Brezzi, F., Fortin, M.: Mixed and Hybrid Finite Element Methods. Springer-Verlag, New York (1991)
4. Cook, R.D.: Concepts and applications of finite element analysis, 4th edn. Wiley, New York (2002)
5. Courant, R., Friedrichs, K., Lewy, H.: Über die partiellen Differenzengleichungen der mathematischen Physik. Mathematische Annalen **100**, 32–74 (1928)
6. Donea, J., Huerta, A.: Finite Element Methods for Flow Problems. John Wiley & Sons, Chichester (2003)
7. Ehlers, W.: Foundations of multiphasic and porous materials. In: Ehlers, W., Bluhm, J. (eds.) Porous Media: Theory, Experiments and Numerical Applications, pp. 3–86. Springer-Verlag, Berlin (2002)
8. Ehlers, W., Zinatbakhsh, S., Markert, B.: Stability analysis of finite difference schemes revisited: a study of decoupled solution strategies for coupled multifield problems. Int. J. Numer. Methods Eng. **94**, 758–786 (2013)
9. Ehlers, W.: Poröse Medien - ein kontinuumsmechanisches Modell auf der Basis der Mischungstheorie. Habilitation, Forschungsberichte aus dem Fachbereich Bauwesen, Heft 47, Universität-GH-Essen (1989)
10. Ehlers, W.: Challanges of porous media models in geo- and biomechanical engineering including electro-chemically active polymers and gels. Int. J. Adv. Eng. Sci. Appl. Math. **1**, 1–24 (2009)
11. Fried, I., Malkus, D.S.: Finite element mass matrix lumping by numerical integration with no convergence rate loss. Int. J. Solids Struct. **11**, 461–466 (1975)
12. Hassanizadeh, S.M., Gray, W.G.: High velocity flow in porous media. Transport in Porous Media **2**, 521–531 (1987)
13. Heider, Y., Avci, O., Markert, B., Ehlers, W.: The dynamic response of fluid-saturated porous materials with application to seismically induced soil liquefaction. Soil Dyn. Earthq. Eng. **63**, 120–137 (2014)
14. Henry, W.: Experiments on the quantity of gases absorbed by water, at different temperatures, and under different pressures. Philos. Trans. R. Soc. Lond. **93**, 29–274 (1803)
15. Hilber, H.M., Hughes, T.J.R., Taylor, R.L.: Improved numerical dissipation for time integration algorithms in structural dynamics. Earthq. Eng. Struct. Dyn. **5**, 283–292 (1977)
16. Hinton, E., Rock, T., Zienkiewicz, O.C.: A note on mass lumping and related processes in the finite element method. Earthq. Eng. Struct. Dyn. **4**, 245–249 (1976)
17. Huebner, K.H., Thornton, E.A., Byrom, T.G.: The Finite Element Method for Engineers, 4th edn. Wiley, New York (2001)
18. de l'Hôspital, G.: Analyse des Infiniment Petits pour l'Intelligence des Lignes Courbes. L'imprimerie Royale, Paris (1696)
19. Mahnkopf, D.: Lokalisierung fluidgesättigter poröser Festkörper bei finiten elastoplastischen Deformationen. Dissertation, Bericht Nr. II-5 aus dem Institut für Mechanik (Bauwesen), Universität Stuttgart (2000)
20. Markert, B., Heider, Y., Ehlers, W.: Comparision of monolithic and splitting solutions schemes for dynamic porous media problems. Int. J. Numer. Methods Eng. **82**, 1341–1383 (2010)
21. Newmark, N.M.: A method of computation for structural dynamics. J. Eng. Mech. Div., ASCE (1959)
22. Rauber, T., Rünger, G.: Parallel Programming. Springer-Verlag, Heidelberg, New York, Dordrecht, London (2012)
23. Roth, S., Hütter, G., Mühlich, U., Nassauer, B., Zybell, L., Kuna, M.: Visualisation of user defined finite elements with abaqus/viewer. GACM-Rep. Summer **2012**, 7–14 (2012)

24. Rutqvist, J., Vasco, D.W., Myer, L.: Coupled reservoir-geomechanical analysis of CO_2 injection and ground deformations at in Salah, Algeria. Int. J. Greenhouse Gas Control **4**, 225–230 (2010)
25. Ryaben'kii, V.S., Tsynkov, S.V.: A Theoretical Introduction to Numerical Analysis. Taylor & Francis (2006)
26. Schenke, M., Ehlers, W.: On the analysis of soils using an abaqus-pandas interface. Proc. Appl. Math. Mech. **11**, 431–432 (2011)
27. Turek, S., Abdulrahman, O., Markert, B.: On a fully implicit, monolithic finite element method-multigrid solution approach for dynamic porous media problems. J. Coupled Syst. Multiscale Dyn. **1**, 224–240 (2013)
28. Vandenberghe, L.: Lecture Notes on Applied Numerical Computing. Technical Report, University of California, Los Angeles (2015)
29. Zienkiewicz, O.C., Chan, A.H.C., Pastor, M., Schrefler, B.A., Shiomi, T. (eds.): Computational Geomechanics with Special Reference to Earthquake Engineering. Wiley, Chichester (1999)
30. Zienkiewicz, O.C., Paul, P.D., Chan, A.H.C.: Unconditionally stable staggered solution procedure for soil-pore fluid interaction problems. Int. J. Numer. Methods Eng. **26**, 1039–1055 (1988)

Theory and Numerical Modeling of Geomechanical Multi-material Flow

Daniel Aubram, Stavros A. Savidis and Frank Rackwitz

Abstract Multi-material flow describes a situation where several distinct materials separated by sharp material interfaces undergo large deformations. The research presented in this paper addresses a particular class of multi-material flow situations encountered in geomechanics and geotechnical engineering which is characterized by a complex coupled behavior of saturated granular material as well as by a hierarchy of distinct spatial scales. Examples include geotechnical installation processes, liquefaction-induced soil failure, and debris flow. The most attractive numerical approaches to solve such problems use variants of arbitrary Lagrangian–Eulerian descriptions allowing interfaces and free surfaces to flow through the computational mesh. Mesh elements cut by interfaces (multi-material elements) necessarily arise which contain a heterogeneous mixture of two or more materials. The heterogeneous mixture is represented as an effective single-phase material using mixture theory. The paper outlines the specific three-scale mixture theory developed by the authors and the MMALE numerical method to model and simulate geomechanical multi-material flow. In contrast to traditional flow models which consider the motion of multiple single-phase materials or single multi-phase mixture, the present research succeeds in incorporating both the coupled behavior of saturated granular material and its interaction with other (pure) materials.

Keywords Multi-material flow · Large deformations · Mixture · Granular material · Sand · Volume averaging · Interface reconstruction · Volume of fluid method

D. Aubram (✉) · S.A. Savidis
Chair of Soil Mechanics and Geotechnical Engineering, Berlin University of Technology, Secr. TIB1-B7, Gustav-Meyer-Allee 25, 13355 Berlin, Germany
e-mail: daniel.aubram@tu-berlin.de

F. Rackwitz
Department of Geotechnical Engineering, Ostbayerische Technische Hochschule Regensburg, Prüfeninger Straße 58, 93049 Regensburg, Germany

T. Triantafyllidis (ed.), *Holistic Simulation of Geotechnical Installation Processes*, Lecture Notes in Applied and Computational Mechanics 80, DOI 10.1007/978-3-319-23159-4_10

1 Introduction

Geotechnical installation processes, which may include digging, mixing, displacement, or penetration, are characterized by large material deformations, moving material interfaces and free surfaces, changing contact conditions, and complex nonlinear soil mechanical behavior [112]. Soil generally is a mixture of solid grains and one or more pore fluids (liquid and/or gas). Its mechanical behavior results from the behavior of each constituent, the internal structure, and from the interfacial coupling due to mass and momentum transfer. The realistic simulation of such complex processes, either numerically or by experiments, is very challenging but at the same time of high practical relevance because geotechnical installation processes may significantly impact on the soil and the load bearing of nearby structures. This is particularly the case for the installation of vibro-injection piles [84, 92], which has recently been investigated by the authors [14, 98]; see also Fig. 1a.

There are several more situations encountered in geomechanics and geotechnical engineering that share the characteristics of geotechnical installation processes. Examples are liquefaction-induced soil failure [104, 105], natural hazards like landslides interacting with water [73, 78], and debris flow [63, 64]. Schematic views are shown in Fig. 1. To make their similarities clear, consider the liquefaction-induced failure of an earth-fill dam under seismic excitation (Fig. 1b). Usually, the details of the exact flow fields (e.g., motion of particular grains) are of secondary interest. However, the consideration of the liquefaction-prone, water-saturated fill material as a mixture of granular material and pore fluid is indispensable [120]. At the same time, the instantaneous water level and geometry of the dam (free surfaces and large-scale interfaces) must be taken into account because they govern the progress of failure. The initiation and evolution of the liquefied zone is generally unknown and could only be resolved in a direct numerical simulation of the problem. In this regard, major achievements have been made using Lagrangian or almost-Lagrangian descriptions in which mesh elements contain only one material throughout the calculation [81, 120, 121]. However, a simulation of the entire process from flow initiation to deposit consolidation will fail due to severe mesh distortion unless more sophisticated approaches will be employed.

We refer to each of the situations mentioned above as geomechanical multi-material flow. Multi-material flow generally contains several pure, physically distinct materials which are separated by sharp material interfaces and one or more of these materials undergo large deformations—void (empty space or atmosphere) is considered as material. In contrast to traditional multi-phase or multi-fluid flow, material strength and compressibility should be included in the description of multi-material flow, whereas mass transfer between the materials is usually of secondary interest. Moreover, in many situations momentum relaxation can be assumed infinitely fast, resulting in a velocity field common to all materials in the flow.

The notion of multi-material flow has emerged along with the development of efficient numerical simulation techniques [24, 75]. Problems that have traditionally been modeled include hypervelocity impact, detonation with structure–media

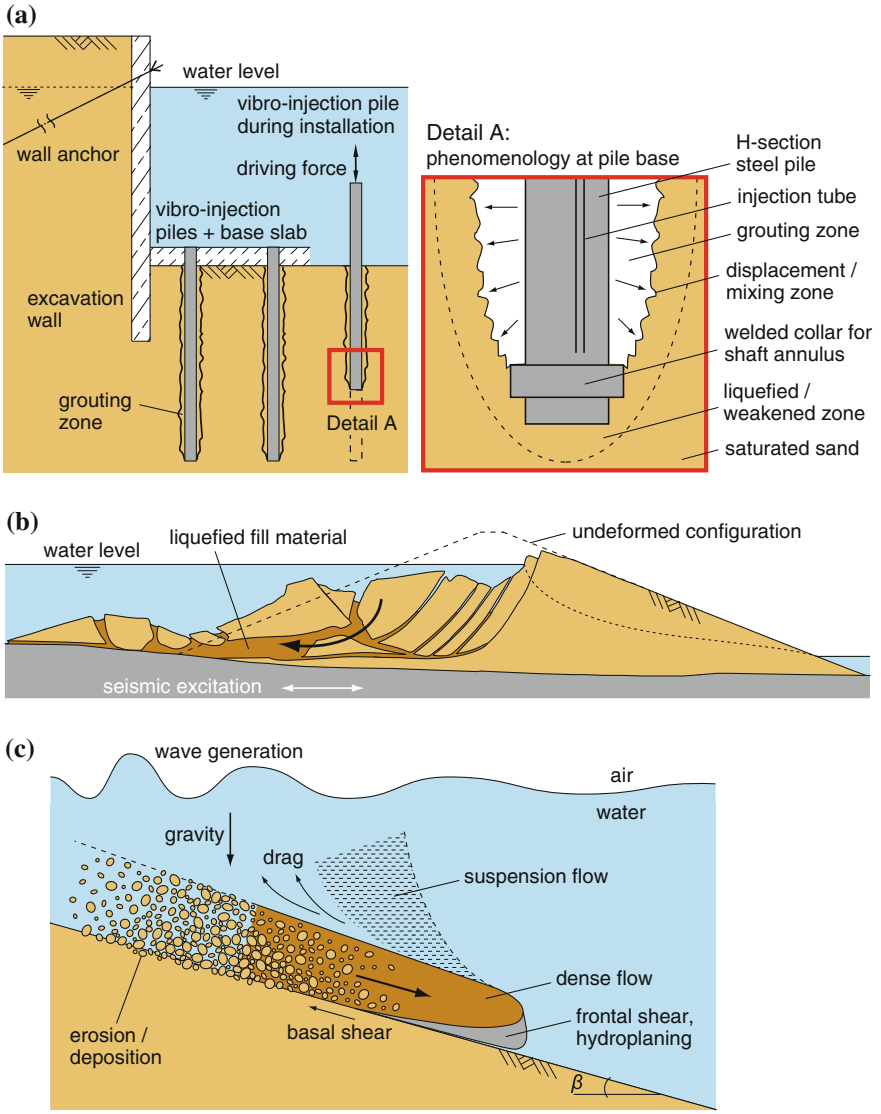

Fig. 1 Schematic of complex geomechanical multi-material flow situations. **a** Installation of vibro-injection piles to tie back the base slab of a deep excavation. **b** Liquefaction-induced failure of an earth-fill dam under seismic excitation; in accordance with [104]. **c** Submarine landslide; in accordance with [73]

interaction, dynamics of bubbles and droplets, material processing and manufacturing, as well as astrophysical events. The most attractive approaches use variants of the multi-material arbitrary Lagrangian–Eulerian (MMALE) description allowing interfaces and free surfaces to flow through the computational mesh [25, 26, 39, 46, 47, 74, 79, 88, 94, 98, 118]. MMALE methods generalize the classical approaches in which the mesh either follows the material motion (Lagrangian approach) or is fixed in space (Eulerian approach). Mesh elements cut by interfaces necessarily arise which contain a heterogeneous mixture of two or more materials. Because the mixture must be represented as an effective single-phase material (homogenized mixture), the underlying mixture theory is an essential ingredient.

Besides the characteristics common to all multi-material flows, geomechanical multi-material flows are characterized by a complex coupled behavior of the saturated granular material representing the soil or debris material as well as by a hierarchy of distinct spatial scales (grain diameter, scale of mixture continuum representation, characteristic size of bulk material interfaces, etc.). While certain aspects of geomechanical multi-material flow can be considered as well understood, a fully fledged flow model that is able to predict a time history of the material states for arbitrary compositions and configurations of the mixture is yet missing.

In two previous papers [14, 98], we have developed an MMALE finite element method accounting for the two-phase coupled response of saturated sand. The present paper goes into more detail about the three main features of the MMALE method for geomechanical problems, which are (i) the mixture theory for multi-material elements, (ii) the determination of the stress field, and (iii) the technique to resolve material interfaces. Accordingly, the paper has the following structure. Section 2 provides an overview of the MMALE method. The mathematical modeling of three-scale mixtures is addressed in Sect. 3, where we summarize the special mixture theory and the homogeneous equilibrium model derived in [14]. In Sect. 4, we focus on stress decompositions in saturated granular material resp. dense granular suspensions which enable the description of those arbitrary compositions and mixture configurations present in geomechanical multi-material flow. Section 5 is concerned with the treatment of material interfaces and their evolution (motion) from a non-Lagrangian point of view, i.e., in multi-material elements. After deriving the governing equations and introducing the basic discretization techniques, we outline the volume of fluid (VOF) interface reconstruction and propagation methods implemented into our MMALE code and present some preliminary results. The paper closes with concluding remarks and outlook in Sect. 6.

2 Overview of the MMALE Method

Our multi-material method is an extension of the single-material or simplified arbitrary Lagrangian–Eulerian (ALE) approach [9, 10, 12, 13, 97]. A detailed description is given in [98], so only the basic equations will be presented in this section. The continuum mechanical background can be found in [9, 19, 76, 113, 114].

The MMALE method addresses isothermal mechanical initial boundary value problems which are governed by conservation of mass

$$\dot{\rho} + \rho \operatorname{div} \boldsymbol{v} = 0, \tag{1}$$

and balance of momentum

$$\rho \dot{\boldsymbol{v}} = \rho \boldsymbol{b} + \operatorname{div} \boldsymbol{\sigma}. \tag{2}$$

The equations are written in updated Lagrangian form referring to the spatial domain $\mathcal{D} \subset \mathbb{R}^3$ instantaneously occupied by the materials at time $t \in [0, T]$. They are assumed to hold at all points $x \in \mathcal{D}$ and for all $t \in [0, T]$. The field $\boldsymbol{v} = \dot{\boldsymbol{u}}$ is the spatial image of the material velocity, $\boldsymbol{u}$ is the material displacement, ρ is the spatial mass density, $\boldsymbol{b}$ is a prescribed body force per unit mass (e.g., gravitational acceleration), and $\boldsymbol{\sigma} = \boldsymbol{\sigma}^{\mathrm{T}}$ is the symmetric Cauchy stress. The superscribed T refers to the transpose. Moreover, the superposed dot is shorthand for the material time derivative $\dot{q} = \frac{\partial}{\partial t} q + \boldsymbol{v} \cdot \boldsymbol{\nabla} q$ of a time-dependent spatial field q, div is the spatial divergence operator, $\otimes$ is the tensor product, and $\cdot$ denotes the single contraction of tensors.

The stress tensor is decomposed into a pressure stress and an extra stress according to

$$\boldsymbol{\sigma} = -p \boldsymbol{I} + \boldsymbol{s}, \tag{3}$$

where p is the pressure and $\boldsymbol{I}$ is the second-order unit tensor. We assume that the extra stress is always deviatoric such that $p = -\frac{1}{3} \operatorname{tr} \boldsymbol{\sigma}$ and $\boldsymbol{s} = \boldsymbol{\sigma}_{\mathrm{dev}}$, where $\boldsymbol{\sigma}_{\mathrm{dev}} = \boldsymbol{\sigma} - \frac{1}{3} (\operatorname{tr} \boldsymbol{\sigma}) \boldsymbol{I}$ is the deviatoric stress, $\operatorname{tr} \boldsymbol{a} = \boldsymbol{I} : \boldsymbol{a}$ returns the trace of a second-order tensor $\boldsymbol{a}$, and : indicates double contraction.

The rate of pressure is related to the rate of mass density through a compression model

$$-\frac{1}{V} \frac{\partial V}{\partial p}\bigg|_M = \frac{1}{\rho} \frac{\mathrm{d}\rho}{\mathrm{d}p} = \frac{1}{K} \qquad \text{resp.} \qquad \dot{p} = \frac{K}{\rho} \dot{\rho}. \tag{4}$$

K is the bulk modulus, V and $M = \rho V$ are the volume and mass of a bounded region, respectively, and $|_M$ means that mass is kept constant along with differentiation.

The balance equations (1) and (2) are rewritten using (3) and (4), treating $\boldsymbol{v}$ and p as the independent variables:

$$\rho \dot{\boldsymbol{v}} - \rho \boldsymbol{b} - \operatorname{div}(\boldsymbol{s} - p \boldsymbol{I}) = \boldsymbol{0}, \tag{5}$$

$$\dot{p} + K \operatorname{div} \boldsymbol{v} = 0. \tag{6}$$

The ALE formulation [8–10, 13, 24, 57] introduces a reference domain which may move in space at an arbitrary velocity $\boldsymbol{w}$. This velocity is referred to as the mesh velocity because the reference domain is represented by the computational mesh in numerical implementation. The difference $\boldsymbol{c} = \boldsymbol{v} - \boldsymbol{w}$ is called the convective

velocity. The relative volume change between the referential coordinate system and the spatial coordinate system is the Jacobian, J, and its rate of change is given by

$$\frac{\partial J}{\partial t} = J \operatorname{div} \boldsymbol{w}. \tag{7}$$

Moreover, if $\hat{q}$ is the description of a spatial field q in the referential coordinates, then the rate of $\hat{q}$ is related to the material time derivative through

$$\dot{q} = \frac{\partial \hat{q}}{\partial t} + \boldsymbol{c} \cdot \nabla q. \tag{8}$$

Substitution of (8) into the Eqs. (5) and (6), respectively, and using the product rule yields

$$\frac{\partial \hat{\rho}\hat{\boldsymbol{v}}}{\partial t} + \operatorname{div}(\rho \boldsymbol{v} \otimes \boldsymbol{c}) + \rho \boldsymbol{v} \operatorname{div} \boldsymbol{w} - \rho \boldsymbol{b} - \operatorname{div}(\boldsymbol{s} - p\boldsymbol{I}) = \boldsymbol{0}, \tag{9}$$

$$\frac{\partial \hat{p}}{\partial t} + \operatorname{div}(p\boldsymbol{c}) - p \operatorname{div} \boldsymbol{c} + K \operatorname{div} \boldsymbol{v} = 0. \tag{10}$$

Multiplication with J, substitution of (7), and arranging terms then results in the ALE conservation form of (5) and (6),

$$\frac{\partial \hat{\rho}\hat{\boldsymbol{v}} J}{\partial t} + J \operatorname{div}(\rho \boldsymbol{v} \otimes \boldsymbol{c}) = J(\rho \boldsymbol{b} + \operatorname{div}(\boldsymbol{s} - p\boldsymbol{I})), \tag{11}$$

$$\frac{\partial \hat{p} J}{\partial t} + J \operatorname{div}(p\boldsymbol{c}) = J(p - K) \operatorname{div} \boldsymbol{v}. \tag{12}$$

We write this set of equations in the compact form

$$\frac{\partial \hat{q} J}{\partial t} + J \operatorname{div} F = SJ, \tag{13}$$

where $q \in \{\rho \boldsymbol{v}, p\}$, F is the convective flux of q, and S is the source term.

The MMALE method is based on the common Lagrange–remap strategy which divides the incremental solution of the nonlinear problem into a Lagrangian step and remap step (Fig. 2). Conceptually, (13) is split into two sets of equations which are solved sequentially:

$$\frac{\partial \hat{q} J}{\partial t} = SJ, \tag{14}$$

$$\frac{\partial \hat{q} J}{\partial t} + J \operatorname{div} F = 0. \tag{15}$$

The first set of equations, (14), is associated with $\boldsymbol{c} = \boldsymbol{0}$ resp. $\boldsymbol{v} = \boldsymbol{w}$. Hence, it is equivalent to the set of Eqs. (5) and (6), and formalizes a Lagrangian description of motion. During the Lagrangian step, the set (14) is solved with standard finite

element methods for the two-field mixed element formulation by accounting for large deformations [71, 117, 121]. Accordingly, (5) and (6) are written in a weak form which is discretized in space using finite elements. The solution of the semi-discrete weak form of the governing equations is advanced implicitly in time using the Newmark-beta and generalized trapezoidal methods in conjunction with a damped Newton–Raphson method.

The solution of the second set of equations, (15), is associated with the remap step. The remap step first relocates the nodes to reduce mesh distortion and then transfers the solution variables onto the modified mesh using a conservative advection algorithm [9, 13]. Time is advanced only during the Lagrangian step, whereas the spatial distributions of the solution variables are fixed during the remap step. That is,

$$\boldsymbol{v} \equiv \mathbf{0} \quad \text{and} \quad \frac{\partial q}{\partial t} \equiv 0, \quad \text{but} \quad \boldsymbol{c} \neq \mathbf{0}, \tag{16}$$

so that $\dot{q} = 0$ holds but $\nabla q \neq \mathbf{0}$ in general. The overall Lagrange–remap solution procedure of the MMALE method is summarized in Algorithm 1.

Because the reference domain (finite element mesh) is moved relative to the "frozen" material during the remap step, elements may arise in MMALE methods which intersect with material interfaces and thus contain a mixture of two or more materials (Fig. 2). However, the spatial distribution of the elements' degrees of freedom is homogeneous, so that a lack of information arises within these multi-material elements. The main difficulties are to accurately determine the states of the individual material portions and the reaction of the element they will generate [103]. This is particularly true for geomechanical multi-material flows which exhibit several spatial scales. For that reason, we have developed a three-scale mixture theory and derived a homogeneous equilibrium model which provides reasonable, physically based mixing rules. These are summarized in the following section; the details are presented elsewhere [11, 14].

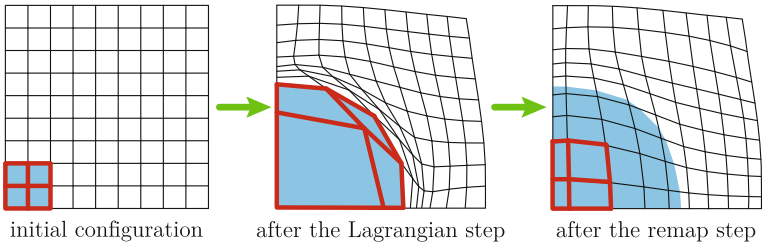

Fig. 2 Schematic diagram of the Lagrange–remap strategy in a calculational cycle of the MMALE method [98]. The *blue area* indicates a material zone whose initial configuration is assigned to an element patch highlighted in *red*. In the Lagrangian step, the governing equations are solved with respect to the mesh deforming with the material. During the remap step, the mesh distortion is reduced and the solution variables are transferred to the modified mesh. After the remap step, several elements intersect with the material interface. These elements contain a mixture of two materials (*blue* and *white*) and are called multi-material elements

3 Mathematical Modeling of Three-Scale Mixtures

3.1 Averaging Procedure

The three-scale (micro, meso, and macro) system of interest is illustrated in Fig. 3. A still image of the flow recorded through a spatially fixed and reasonably small observation window is shown above in the figure. The flow consists of a bulk solid (S), a bulk fluid (F), and a composite material representing a fluid-saturated granular material (G). The granular material by itself is an immiscible mixture consisting of a solid phase (s) and fluid phase (f). Void is considered as a particular fluid.

Algorithm 1: Overall solution procedure of the MMALE method.

Input: initial mesh, geometry, initial conditions, and boundary conditions
Output: velocity, pressure, mass density, stress, and material state

```
initialize time steps;
collect topological data required for remap;
while number of time steps n ≤ n_max do
    begin LAGRANGIAN STEP
        re-initialize finite element matrices and compute loads;
        while number of Newton iteration steps i ≤ i_max do
            determine number of materials per element;
            update volume fractions and porosity;
            integrate constitutive equations and compute material stiffness;
            update element averages of stress, stiffness, mass density etc.;
            compute internal loads and form vector of residuals;
            compute effective stiffness matrix;
            solve system of linearized equations;
            if convergence criterion met then exit;
            i ← i + 1;
        store solution variables;
        update and store geometry;
        reconstruct material interfaces using VOF method;
    begin REMAP STEP
        loop mesh elements and evaluate element quality Q;
        if Q < Q_min then flag nodes of the element;
        relocate flagged nodes to reduce mesh distortion;
        gather elements affected by mesh motion step;
        compute total transport volumes for affected elements;
        compute material transport volumes using reconstructed interface;
        advect and store volume fractions;
        advect and store remaining solution variables;
    n ← n + 1;
```

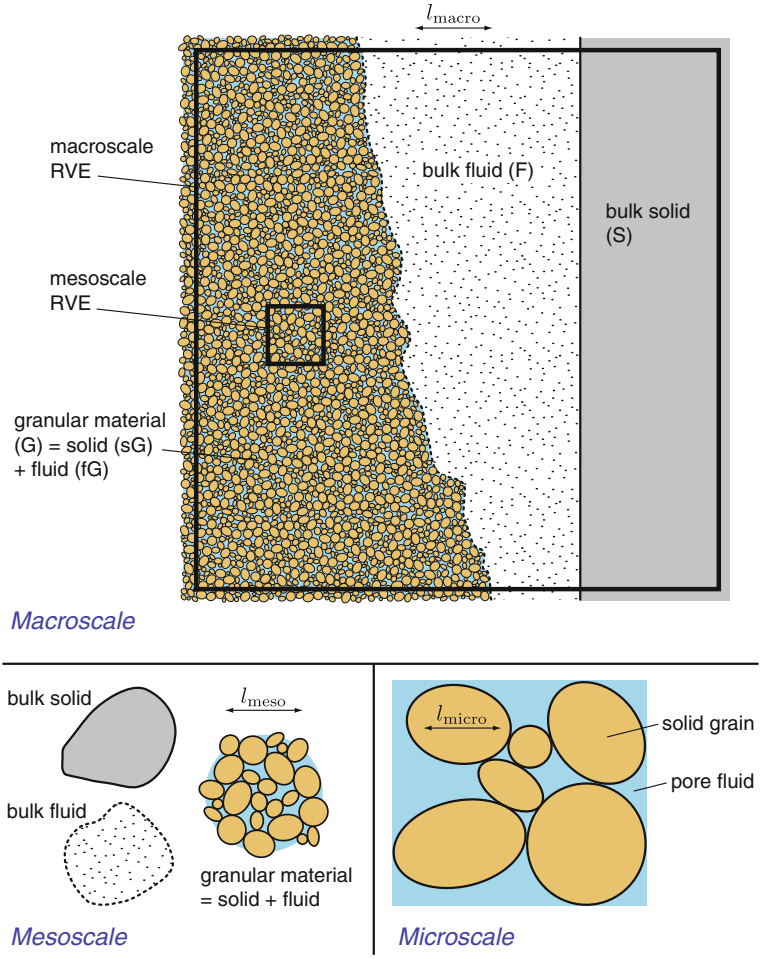

Fig. 3 Three spatial scales in a particular geomechanical multi-material flow

The granular material is constituted by an assembly of solid grains, whose typical diameter defines the microscale of the problem, l_{micro} (Fig. 3 below). The characteristic length at which the grain assembly can be represented by a continuum is introduced as the mesoscale l_{meso}. At the mesoscale, the bulk solid, the bulk fluid, and granular material can be regarded as homogeneous materials separated by sharp interfaces. Finally, at the macroscale the immiscible mixture of mesoscale continua (bulk solid, bulk fluid, and granular material) can be equivalently modeled as an effective single-phase material (homogenized immiscible mixture). Hence, we assume that the multi-material flow has a representative volume element (RVE) with characteristic length l_{macro} (Fig. 3 above). The real-world problem is modeled on an even larger scale.

To keep our theory as general as possible, each material $k \in \{\mathrm{S}, \mathrm{F}, \mathrm{G}\} \overset{\text{def}}{=} \{1, \ldots, M\}$ is initially viewed as containing the same phases $\alpha \in \{\mathrm{s}, \mathrm{f}\} \overset{\text{def}}{=} \{1, \ldots, N\}$, even though the fractional volume of one phase in a particular material might be zero. This means, for example, that the bulk solid is initially viewed as being composed of a solid phase and a fluid phase, even though the volume fraction of the fluid is zero. A particular phase α in a particular material k represents an individual, chemically independent constituent of the flow and will be denoted by αk. For the particular flow under consideration, we write $\mathrm{sS} \equiv \mathrm{S}$ and $\mathrm{fF} \equiv \mathrm{F}$ such that $\alpha k \in \{\mathrm{S}, \mathrm{F}, \mathrm{sG}, \mathrm{fG}\}$.

The flow takes place in a time interval $[0, T] \subset \mathbb{R}$ and in a three-dimensional modeling domain $\mathcal{D} \subset \mathbb{R}^3$ of the ambient Euclidian space. The subregions in $\mathcal{D}$ instantaneously occupied by the k-material and the α-phase at time $t \in [0, T]$ are denoted by $\mathcal{M}^k$ and $\mathcal{P}^\alpha$, respectively, with

$$\mathcal{D} = \bigcup_\alpha \mathcal{P}^\alpha = \bigcup_k \mathcal{M}^k. \tag{17}$$

The (possibly empty) domain of the α-phase in the k-material is given by the intersection $\mathcal{P}^\alpha \cap \mathcal{M}^k$. Based on the assumptions above, each two phases and each two materials do only intersect at their interface (if any).

Let χ^k be the material indicator function on $\mathcal{M}^k \subset \mathcal{D}$ and χ^α the phase indicator function on $\mathcal{P}^\alpha \subset \mathcal{D}$, with $\chi^k, \chi^\alpha : \mathcal{D} \times [0, T] \to \{0, 1\}$. The product of χ^k and χ^α defines another indicator function which picks out the generally time-dependent α-phase domain of the k-material domain in the modeling domain:

$$\chi^{\alpha k}(x, t) \overset{\text{def}}{=} (\chi^\alpha \chi^k)(x, t) = \begin{cases} 1 & \text{if } x \in (\mathcal{P}^\alpha \cap \mathcal{M}^k) \text{ at time } t, \\ 0 & \text{if } x \in \mathcal{D} \backslash (\mathcal{P}^\alpha \cap \mathcal{M}^k) \text{ at time } t. \end{cases} \tag{18}$$

This indicator function is unique to our mixture theory. It covers arbitrary flow compositions bounded between the classical cases of mixtures composed of single-phase materials ($\chi^\alpha = 1$) and mixtures represented by a single multi-phase material ($\chi^k = 1$).

Indicator functions represent distributions, and hence possess a weak derivative. Therefore, in accordance with Eqs. (17)–(22) of [41], it can be shown that the substantial time derivative of $\chi^{\alpha k}$ defined by (18) is given by the topological equation

$$\frac{\partial \chi^{\alpha k}}{\partial t} + \boldsymbol{v}_{\mathrm{I}}^{\alpha k} \cdot \boldsymbol{\nabla} \chi^{\alpha k} = 0, \qquad \text{with} \quad \boldsymbol{\nabla} \chi^{\alpha k} = \delta_{\mathrm{I}}^{\alpha k} \boldsymbol{n}_{\mathrm{I}}^{\alpha k}. \tag{19}$$

Here, $\boldsymbol{v}_{\mathrm{I}}^{\alpha k}$ is the velocity of the α-phase-k-material interface $\partial(\mathcal{P}^\alpha \cap \mathcal{M}^k)$, $\boldsymbol{n}_{\mathrm{I}}^{\alpha k}$ is the field of outward normals on that interface, and $\delta_{\mathrm{I}}^{\alpha k}$ is a Dirac delta function which picks out the α-phase-k-material interface in $\mathcal{D}$. Accordingly, $\boldsymbol{\nabla} \chi^{\alpha k}$ is everywhere zero except for $\partial(\mathcal{P}^\alpha \cap \mathcal{M}^k)$.

Upscaling information from lower to higher scales can be achieved by different types of approaches, and each has its advantages and disadvantages [18, 37, 55].

The approach followed here is known as hybrid mixture theory [1, 21, 22, 54, 55]. The basic idea is to apply local volume averaging [32, 41, 42] to the small-scale balance equations and to make the constitutive assumptions needed for closure at the large scale, that is, for the averaged balance equations. The closure relations can be obtained either by direct postulation of desirable equations, as done in [71] and in this paper, or based on thermodynamical considerations as in the continuum theory of mixtures and the theory of porous media [34, 40, 113].

Local volume averaging is carried out with respect to a macroscopic RVE of the flow at all points $x \in \mathcal{D}$, which is defined through a spatially fixed and time-independent subset $\mathcal{H}(x) \subset \mathbb{R}^3$. At each instant t, the RVE intersects with the current configuration of materials and phases as well as with their boundaries. The subregion of the RVE occupied by the k-material is $\mathcal{M}^k \cap \mathcal{H} \stackrel{\text{def}}{=} \mathcal{H}^k$, and $(\mathcal{P}^\alpha \cap \mathcal{M}^k) \cap \mathcal{H} \stackrel{\text{def}}{=} \mathcal{H}^{\alpha k}$ is the subregion occupied by the α-phase of the k-material, with $\mathcal{H} = \bigcup_k \mathcal{H}^k = \bigcup_k \bigcup_\alpha \mathcal{H}^{\alpha k}$ by (17). The $\mathcal{H}$-average of an arbitrary time-dependent spatial microscopic field $q(x,t)$ is then defined through

$$\langle q \rangle(x,t) \stackrel{\text{def}}{=} \frac{1}{H} \int_{\mathcal{H}} q(x + \boldsymbol{a}, t)\, \mathrm{d}v \qquad \text{for all } \boldsymbol{x} \in \mathcal{D} \text{ and } t \in [0,T], \tag{20}$$

in which $\boldsymbol{a}$ is a vector on $\mathcal{H}$, $\mathrm{d}v$ is the volume density on $\mathbb{R}^3$, and $H \stackrel{\text{def}}{=} \int_{\mathcal{H}} 1\, \mathrm{d}v = \text{const}$ is the volume measure of $\mathcal{H}$.

Particular examples of the local volume average defined by (20) are the volume fractions

$$f^k \stackrel{\text{def}}{=} \langle \chi^k \rangle = \frac{H^k}{H} \qquad \text{and} \qquad \pi^{\alpha k} \stackrel{\text{def}}{=} \frac{1}{f^k} \langle \chi^{\alpha k} \rangle = \frac{H^{\alpha k}}{H^k} \qquad \in [0,1], \tag{21}$$

where $H^k \stackrel{\text{def}}{=} \int_{\mathcal{H}^k} 1\, \mathrm{d}v = \int_{\mathcal{H}} \chi^k\, \mathrm{d}v$ and $H^{\alpha k} \stackrel{\text{def}}{=} \int_{\mathcal{H}^{\alpha k}} 1\, \mathrm{d}v = \int_{\mathcal{H}} \chi^{\alpha k}\, \mathrm{d}v$. While f^k is the volume fraction of the k-material with respect to the RVE, $\pi^{\alpha k}$ represents the macroscale volume fraction of the α-phase intrinsic to the k-material. The topology present in $\mathcal{H}$ entails the fundamental properties

$$\sum_k f^k = 1 \qquad \text{and} \qquad \sum_\alpha \pi^{\alpha k} = 1 \qquad \text{for all } k \in \{1, \ldots, M\} \tag{22}$$

since phase or material overlaps are precluded. If the physical field $q(x,t)$ is defined per unit volume, then

$$\langle q \rangle = \sum_k f^k q^k = \sum_k \sum_\alpha f^k \pi^{\alpha k} q^{\alpha k}, \qquad \text{with} \quad q^{\alpha k} \stackrel{\text{def}}{=} \frac{\langle \chi^{\alpha k} q \rangle}{f^k \pi^{\alpha k}}, \tag{23}$$

follows immediately from (22) and the averaging operator (20). For example, if $q = \rho$ is the microscopic spatial mass density, then the intrinsic or true mass density $\rho^{\alpha k}$

represents the mass of the constituent αk per unit volume of that constituent, $\pi^{\alpha k}\rho^{\alpha k}$ is the mass of the constituent αk per unit volume of the k-material, and $f^k\pi^{\alpha k}\rho^{\alpha k}$ denotes its mass per unit volume of the mixture. Therefore, the latter two are bulk mass densities.

3.2 Macroscopic Balance Equations

On the microscale, all constituents of the mixture are regarded as compressible continua, governed by the equations of continuum mechanics [76, 113, 114]. The balance principles of the problems under consideration are conservation of mass, (1), and balance of momentum, (2), in conjunction with the interface jump conditions. We currently do not take care of any thermodynamical issue. Mass is neither supplied in the interior of any constituent nor at the interfaces. Moreover, there is no interfacial momentum supply due to surface tension.

Each term of the microscopic balance equations is averaged by using the procedure outlined in the previous section; see [11, 14, 41, 42] for details. This results in the α-phase-k-material macroscopic conservation of mass

$$\frac{\partial f^k\pi^{\alpha k}\rho^{\alpha k}}{\partial t} + \operatorname{div}(f^k\pi^{\alpha k}\rho^{\alpha k}\boldsymbol{v}^{\alpha k}) = \Lambda^{\alpha k} \tag{24}$$

and macroscopic balance of momentum

$$\begin{aligned}&\frac{\partial f^k\pi^{\alpha k}\rho^{\alpha k}\boldsymbol{v}^{\alpha k}}{\partial t} + \operatorname{div}(f^k\pi^{\alpha k}\rho^{\alpha k}\boldsymbol{v}^{\alpha k}\otimes\boldsymbol{v}^{\alpha k})\\ &= f^k\pi^{\alpha k}\rho^{\alpha k}\boldsymbol{b}^{\alpha k} + \operatorname{div}(f^k\pi^{\alpha k}\boldsymbol{\sigma}^{\alpha k}) + \Lambda^{\alpha k}\boldsymbol{v}_{\mathrm{I}}^{\mathrm{m}} + \boldsymbol{\Gamma}^{\alpha k},\end{aligned} \tag{25}$$

where

$$\Lambda^{\alpha k} \overset{\text{def}}{=} \left\langle (\rho(\boldsymbol{v}-\boldsymbol{v}_{\mathrm{I}}))^{[\alpha k]}\cdot\boldsymbol{n}_{\mathrm{I}}^{\alpha k}\right\rangle, \tag{26}$$

$$\Lambda^{\alpha k}\boldsymbol{v}_{\mathrm{I}}^{\mathrm{m}} \overset{\text{def}}{=} \left\langle (\rho\boldsymbol{v}\otimes(\boldsymbol{v}-\boldsymbol{v}_{\mathrm{I}}))^{[\alpha k]}\cdot\boldsymbol{n}_{\mathrm{I}}^{\alpha k}\right\rangle, \qquad \text{and} \tag{27}$$

$$\boldsymbol{\Gamma}^{\alpha k} \overset{\text{def}}{=} -\langle\boldsymbol{\sigma}^{[\alpha k]}\cdot\boldsymbol{n}_{\mathrm{I}}^{\alpha k}\rangle. \tag{28}$$

The superscribed αk denotes macroscopic (i.e., $\mathcal{H}$-averaged) fields related to the α-phase in the k-material. The mass transfer term $\Lambda^{\alpha k}$ denotes the rate of mass supply per unit volume via the α-phase-k-material interface. The momentum transfer term $\boldsymbol{\Gamma}^{\alpha k}$ includes drag forces per unit volume generated by the relative motion of the constituents. Note that $\boldsymbol{\Gamma}^{\alpha k}$ accounts for surface forces, but not for momentum exchange owing to transfer of inertial mass which is described by the term $\Lambda^{\alpha k}\boldsymbol{v}_{\mathrm{I}}^{\mathrm{m}}$. Total mass and momentum of the mixture is conserved. Hence, the sum of the transfer terms over all constituents must vanish:

$$\sum_k \sum_\alpha \Lambda^{\alpha k} = 0 \quad \text{and} \quad \sum_k \sum_\alpha \left(\Lambda^{\alpha k} \boldsymbol{v}_{\mathrm{I}}^{\mathrm{m}} + \boldsymbol{\Gamma}^{\alpha k} \right) = \mathbf{0}. \tag{29}$$

From this and the conditions (23), summation of (24) and (25) over all phases $\alpha \in \{1, \ldots, N\}$ and all materials $k \in \{1, \ldots, M\}$ finally yield the macroscopic conservation of mass and macroscopic balance of momentum of the mixture:

$$\frac{\partial \langle \rho \rangle}{\partial t} + \operatorname{div} \langle \rho \boldsymbol{v} \rangle = 0 \quad \text{and} \quad \frac{\partial \langle \rho \boldsymbol{v} \rangle}{\partial t} + \operatorname{div} \langle \rho \boldsymbol{v} \otimes \boldsymbol{v} \rangle = \langle \rho \boldsymbol{b} \rangle + \operatorname{div} \langle \boldsymbol{\sigma} \rangle. \tag{30}$$

The macroscopic balance equations (30) in conjunction with the jump conditions (29) and the balance equations (24) and (25) provide unified description of non-reactive isothermal flow of an immiscible mixture of M materials consisting of N phases. They hold at each spatial point and at all interfaces and refer to a spatial reference volume instantaneously occupied by the mixture on the macroscale. A single spatial point is viewed as being simultaneously occupied by all materials and all phases, that is, the mixture after averaging is viewed as being composed of overlapping continua.

The equations explicitly account for volume fractions of each bulk material and for volume fractions of each phase in the bulk materials. Moreover, the equations include separate physical quantities for each constituent and separate terms representing the interaction between the constituents. The mechanical behavior of the mixture is a consequence of the mechanical behavior of its individual constituents, their volume fractions as well as of their interactions. Therefore, the macroscopic equations can explicitly represent diverse compositions or evolving configurations of multi-material flow.

3.3 Homogeneous Equilibrium Model

The particular geomechanical multi-material flow of interest can be locally described as a mixture consisting of a bulk solid (S), a bulk fluid (F), and a fluid-saturated granular material (G) composed of a solid phase (sG) and a fluid phase (fG); cf. Fig. 3. Hence, the materials generally represent binary immiscible mixtures, solely composed of a solid phase and a fluid phase such that $\alpha \in \{\mathrm{s}, \mathrm{f}\}$. We denote the fluid fraction or porosity of the k-material, $k \in \{\mathrm{S}, \mathrm{F}, \mathrm{G}\}$, by

$$n^k \overset{\text{def}}{=} \pi^{\mathrm{f}k}, \tag{31}$$

so the solid fraction within the k-material becomes $\pi^{\mathrm{s}k} = 1 - n^k$ by using $(22)_2$. We remark that in cases where the k-material consists of a solid without significant porosity ($k = \mathrm{S}$) one has $n^{\mathrm{S}} = 0$. If on the other hand the k-material is a fluid ($k = \mathrm{F}$), then $n^{\mathrm{F}} = 1$ applies. The mixture represented by a single fluid-saturated granular material is characterized by $f^k \equiv f^{\mathrm{G}} = 1$ and $0 < n^{\mathrm{G}} < 1$.

Modeling of a particular multi-material flow requires closure of the set of balance equations, which is otherwise underdetermined. Generally, the following closure relations have to be specified [32, 33]:

1. Transfer relations expressing the physics at the material interfaces.
2. Topological relations accounting for the evolution of the interfacial structure.
3. Constitutive relations characterizing the physical behavior of each material.

Concerning the first group of closure relations, we take the simplest approach by assuming zero mass and momentum exchange, so that $\Lambda^{\alpha k} = 0$ and $\mathbf{\Gamma}^{\alpha k} = \mathbf{0}$ for all $\alpha \in \{\mathrm{s}, \mathrm{f}\}$ and $k \in \{\mathrm{S}, \mathrm{F}, \mathrm{G}\}$. The former complies with the assumption of no phase change and no chemical reaction at interfaces. The assumption of zero momentum transfer, on the other hand, may contradict flow situations in reality in which interactions, e.g., based on viscous drag, play an important role. Moreover, a granular material in the mixture, by this assumption, must be either dry ($\rho^{\mathrm{fG}} = 0$) or locally undrained (no consolidation effects).

The topological closure relations restore the information of the flow structure lost by the application of volume averaging [32, 33]. For the flow situation under consideration, the only relations required are those that account for the evolution of the material volume fractions f^k. A proper closure relation for volume fraction has to specify how the volumetric distribution of the bulk solid, the bulk fluid, and the saturated granular medium evolves during the particular geomechanical multi-material flow under consideration. Because further research is needed to establish such a physics-based topological closure law, we have simply assumed homogeneous distributions of pressure and velocity between the materials:

$$p^k = \langle p \rangle \quad \text{and} \quad \boldsymbol{v}^k = \langle \boldsymbol{v} \rangle \qquad \text{for all} \;\; k \in \{\mathrm{S}, \mathrm{F}, \mathrm{G}\} \;\; \text{and} \;\; t \in [0, T]. \tag{32}$$

From a physical viewpoint, this means that everything is in homogeneous thermodynamic equilibrium [35, 80], and its limitations are discussed in [14].

The description of material behavior and the development of constitutive relations are major concerns in continuum mechanics. Restrictions on the form of the closure relations result from the principles of constitutive theory [42, 76, 114]. In order to treat all materials and material compositions that might be present in geomechanical multi-material flow in a unified fashion, the stress tensor of any material is decomposed into a pressure stress $-p^{\alpha k}\boldsymbol{I}$ and an extra stress $\boldsymbol{s}^{\alpha k}$ [76, 114], in accordance with (3):

$$\boldsymbol{\sigma}^{\alpha k} = -p^{\alpha k}\boldsymbol{I} + \boldsymbol{s}^{\alpha k}. \tag{33}$$

We assume that the extra stress is always deviatoric such that $p^{\alpha k} = -\frac{1}{3}\,\mathrm{tr}\,\boldsymbol{\sigma}^{\alpha k}$, and that all constituents of the flow are compressible, including both the grains and the fluid phase of the granular material.

A rather long but almost straightforward derivation using all the ingredients yields the following homogeneous equilibrium model for geomechanical multi-material flow which is consistent with the set of Eqs. (5) and (6) for a single-material problem [11, 14]:

$$\langle\rho\rangle\langle\dot{\boldsymbol{v}}\rangle - \langle\rho\boldsymbol{b}\rangle - \mathrm{div}\langle\boldsymbol{s} - p\boldsymbol{I}\rangle = \boldsymbol{0} \tag{34}$$

$$\langle\dot{p}\rangle + \langle K\rangle\mathrm{div}\langle\boldsymbol{v}\rangle = 0, \tag{35}$$

where

$$\langle\boldsymbol{s}\rangle = \sum_k f^k\boldsymbol{s}^k = f^{\mathrm{S}}\boldsymbol{s}^{\mathrm{S}} + f^{\mathrm{F}}\boldsymbol{s}^{\mathrm{F}} + f^{\mathrm{G}}\left(\boldsymbol{s}^{\mathrm{G}'} + n^{\mathrm{G}}\boldsymbol{s}^{\mathrm{fG}}\right), \tag{36}$$

$$\langle p\rangle = \sum_k f^k p^k = f^{\mathrm{S}}p^{\mathrm{S}} + f^{\mathrm{F}}p^{\mathrm{F}} + f^{\mathrm{G}}\left(p^{\mathrm{G}'} + p^{\mathrm{fG}}\right), \tag{37}$$

$$\langle\rho\rangle = \sum_k f^k\rho^k = f^{\mathrm{S}}\rho^{\mathrm{S}} + f^{\mathrm{F}}\rho^{\mathrm{F}} + f^{\mathrm{G}}\left((1-n^{\mathrm{G}})\rho^{\mathrm{sG}} + n^{\mathrm{G}}\rho^{\mathrm{fG}}\right), \tag{38}$$

$$\frac{1}{\langle K\rangle} = \sum_k \frac{f^k}{K^k} = \frac{f^{\mathrm{S}}}{K^{\mathrm{S}}} + \frac{f^{\mathrm{F}}}{K^{\mathrm{F}}} + \frac{f^{\mathrm{G}}}{K^{\mathrm{G}}}, \qquad \zeta^{\mathrm{G}} = 1 - \frac{K^{\mathrm{G}}_{\mathrm{dr}}}{K^{\mathrm{sG}}}, \tag{39}$$

$$\text{and} \quad K^{\mathrm{G}} = K^{\mathrm{G}}_{\mathrm{dr}}\left(1 + \frac{(\zeta^{\mathrm{G}})^2}{\zeta^{\mathrm{G}}K^{\mathrm{G}}_{\mathrm{dr}}/K^{\mathrm{sG}} + n^{\mathrm{G}}\left(K^{\mathrm{G}}_{\mathrm{dr}}/K^{\mathrm{fG}} - K^{\mathrm{G}}_{\mathrm{dr}}/K^{\mathrm{sG}}\right)}\right). \tag{40}$$

The model is closed by the constitutive equations for the bulk solid ($\alpha k \equiv k = \mathrm{S}$), the bulk fluid ($\alpha k \equiv k = \mathrm{F}$), the granular material ($k = \mathrm{G}$) including the solid phase ($\alpha k = \mathrm{sG}$) and fluid phase ($\alpha k = \mathrm{fG}$), by the evolution equations for the porosity,

$$\dot{n}^{\mathrm{G}} = (1-n^{\mathrm{G}})\left(\frac{\dot{p}^{\mathrm{sG}}}{K^{\mathrm{sG}}} + \mathrm{div}\langle\boldsymbol{v}\rangle\right), \qquad \text{with} \quad \dot{p}^{\mathrm{sG}} = \dot{p}^{\mathrm{G}'}\frac{K^{\mathrm{sG}}}{K^{\mathrm{G}}_{\mathrm{dr}}} + \dot{p}^{\mathrm{fG}}, \tag{41}$$

and volume fractions,

$$\dot{f}^k = f^k\left(\frac{\langle K\rangle}{K^k} - 1\right)\mathrm{div}\langle\boldsymbol{v}\rangle, \tag{42}$$

and by the compression models for each constituent,

$$\dot{\rho}^{\mathrm{S}} = \frac{\rho^{\mathrm{S}}}{K^{\mathrm{S}}}\langle\dot{p}\rangle, \quad \dot{\rho}^{\mathrm{F}} = \frac{\rho^{\mathrm{F}}}{K^{\mathrm{F}}}\langle\dot{p}\rangle, \quad \dot{\rho}^{\mathrm{sG}} = \frac{\rho^{\mathrm{sG}}}{K^{\mathrm{sG}}}\dot{p}^{\mathrm{sG}}, \quad \dot{\rho}^{\mathrm{fG}} = \frac{\rho^{\mathrm{fG}}}{K^{\mathrm{fG}}}\dot{p}^{\mathrm{fG}}. \tag{43}$$

Besides the quantities already defined, $p^{\mathrm{G}'}$ and $\boldsymbol{s}^{\mathrm{G}'}$ are the effective pressure and effective deviatoric stress, respectively, in the granular material which will be defined in the subsequent section, $\langle K\rangle$ is the bulk modulus of the mixture, K^k is the bulk modulus of the k-material, with $k \in \{\mathrm{S}, \mathrm{F}, \mathrm{G}\}$, K^{sG} and K^{sG} are intrinsic bulk moduli of the granular material solid phase and fluid phase, respectively, $K^{\mathrm{G}}_{\mathrm{dr}}$ is the bulk modulus of the drained granular material, $K^{\mathrm{G}}_{\mathrm{uj}} \approx K^{\mathrm{sG}}$ is the unjacketed bulk modulus [20], and ζ^{G} is the Biot-Willis coefficient [29, 30].

For the stress tensors in the bulk solid and in the bulk fluid, the common constitutive equations can be substituted [19, 42, 76, 114]; effects of turbulence in the bulk fluid are currently neglected. However, the stress tensor in the granular material ($k = \mathrm{G}$) needs to be analyzed in more detail. In particular, we have to justify our motivation to express the extra stress of the granular material in (36) by $\boldsymbol{s}^{\mathrm{G}} = \boldsymbol{s}^{\mathrm{G}'} + n^{\mathrm{G}}\boldsymbol{s}^{\mathrm{fG}}$.

4 Stress in Granular Materials and Suspensions

The specific granular material of interest is a cohesionless granular material in which a single fluid fills the intersticial space. From a formal rheological viewpoint, the material can be addressed as a dense (high concentration) grain–fluid mixture or "granular suspension" [3]. Our current research is particularly concerned with cohesionless soil (sand). The smallest diameter of the solid grains is generally larger than 0.075 mm and the solid volume fraction resp. volume concentration is basically higher than 50 % (porosity $n^{\mathrm{G}} < 0.5$) [38]. We assume for simplicity that the grains are permanent, i.e., they are non-abrasive and cannot crush. The fluid can be gas, liquid, or a suspension (slurry) of liquid and dispersed fines (grain diameter < 0.075 mm).

According to [7, 59, 96], two limiting regimes of dry granular flow have to be considered. Under static or quasi-static loads, the grains are in close contact and form a network. The contact forces acting between the grains are dominated by the mean stress and dry friction (granular solid). Grain inertia effects are negligible, and the material response is rate-independent plastic. This is called the frictional or quasi-static regime, and it is the granular flow regime extensively studied in soil mechanics [102]. At the other extreme characterized by high rates of shear deformation and smaller solid volume fractions, the material behaves rate-dependent "viscous" (granular liquid). Grain inertia and instantaneous grain contacts through collision dominate [15], and hence this flow regime is called the collisional or dynamic regime. In many practical flow situations, frictional and collisional interactions are roughly of the same order, and the contributions of each to the bulk stress of the mixture cannot be clearly distinguished. However, relatively little is known about this intermediate flow regime, called the frictional–collisional regime, from both theoretical and experimental viewpoints [4–6, 65].

Furthermore, complexity is introduced by the interstitial fluid in granular materials. Fluid–solid coupling by Stokes' drag resulting from the relative velocity has been recognized for a long time in soil mechanics because it is responsible for consolidation [29, 110]. Besides this, indirect grain interactions generally occur through lubricated contacts [3, 4, 6, 36]. Lubricated contact is characterized by repulsive viscous forces due to squeezing and shearing of the interstitial fluid; the shear-thickening effect is an exemplary consequence of this phenomenon [36]. The rate of shear at which lubricational (or macros-viscous [15]) flow may take place at otherwise equal conditions ranges between those present in the frictional and collisional regimes. In general, all three flow regimes have to be considered in the analysis of debris flows [60, 63] and liquefaction-induced flow of soils [69]. However, the description

of the mechanical behavior of a dense grain–fluid mixture for a wide range of flow conditions and material properties is still an open problem [6].

Based on (23), the bulk stress in a saturated granular material can be generally expressed as

$$\boldsymbol{\sigma}^{\mathrm{G}} = (1 - n^{\mathrm{G}})\boldsymbol{\sigma}^{\mathrm{sG}} + n^{\mathrm{G}}\boldsymbol{\sigma}^{\mathrm{fG}} \stackrel{\text{def}}{=} \tilde{\boldsymbol{\sigma}}^{\mathrm{sG}} + \tilde{\boldsymbol{\sigma}}^{\mathrm{fG}}, \tag{44}$$

with a fluid fraction resp. porosity $0 < n^{\mathrm{G}} < 1$, and taking $f^{\mathrm{G}} \equiv 1$. The tensors $\tilde{\boldsymbol{\sigma}}^{\mathrm{sG}}, \tilde{\boldsymbol{\sigma}}^{\mathrm{fG}}$ on the right are referred to as the partial stresses. These amalgamated stress tensors are used in many models for saturated porous media [34, 40, 43] and debris flows [6, 60, 63, 64, 90, 91], particularly those derived from the continuum theory of mixtures.

In order to model the full frictional–collisional regime, the stress tensors of the solid and fluid phases are represented as the linear sum of a rate-independent frictional contribution and a rate-dependent viscous contribution [7, 59, 60, 116]:

$$\boldsymbol{\sigma}^{\alpha\mathrm{G}} \stackrel{\text{def}}{=} \boldsymbol{\sigma}^{\alpha\mathrm{G}}_{\mathrm{fr}} + \boldsymbol{\sigma}^{\alpha\mathrm{G}}_{\mathrm{vi}}, \qquad \text{with} \quad \alpha \in \{\mathrm{s}, \mathrm{f}\}, \tag{45}$$

so that $\boldsymbol{\sigma}^{\mathrm{G}} = \boldsymbol{\sigma}^{\mathrm{G}}_{\mathrm{fr}} + \boldsymbol{\sigma}^{\mathrm{G}}_{\mathrm{vi}}$ likewise. We then assume

$$\operatorname{tr}\boldsymbol{\sigma}^{\mathrm{sG}}_{\mathrm{fr}} = -3p^{\mathrm{sG}}, \qquad \boldsymbol{\sigma}^{\mathrm{fG}}_{\mathrm{fr}} = -p^{\mathrm{fG}}\boldsymbol{I}, \qquad \text{and} \qquad \operatorname{tr}\boldsymbol{\sigma}^{\mathrm{fG}}_{\mathrm{vi}} = 0. \tag{46}$$

The first assumption formalizes that the solid-phase constituent is not subject to internal constraints [114]. The second is the interpretation of a saturated intersticial space [60], and the third assumption is because volume viscosity is usually neglected in porous media and debris flow theories. The latter two assumptions result in $\boldsymbol{\sigma}^{\mathrm{fG}}_{\mathrm{vi}} = \boldsymbol{s}^{\mathrm{fG}}$.

In accordance with [23], we introduce Terzaghi's effective stress $\boldsymbol{\sigma}^{\mathrm{G}'}_{\mathrm{fr}}$ as the frictional partial stress of the solid phase in which the pressure has been replaced with the excess pressure $p^{\mathrm{sG}} - p^{\mathrm{fG}}$. Clearly,

$$\frac{\boldsymbol{\sigma}^{\mathrm{G}'}_{\mathrm{fr}}}{1 - n^{\mathrm{G}}} \stackrel{\text{def}}{=} -(p^{\mathrm{sG}} - p^{\mathrm{fG}})\boldsymbol{I} + \boldsymbol{s}^{\mathrm{sG}}_{\mathrm{fr}} \qquad \text{and} \qquad \frac{p^{\mathrm{G}'}}{1 - n^{\mathrm{G}}} = p^{\mathrm{sG}} - p^{\mathrm{fG}}, \tag{47}$$

where $p^{\mathrm{G}'} \stackrel{\text{def}}{=} -\frac{1}{3}\operatorname{tr}\boldsymbol{\sigma}^{\mathrm{G}'}_{\mathrm{fr}}$ is called the mean effective stress and $\boldsymbol{s}^{\mathrm{sG}}_{\mathrm{fr}} = (\boldsymbol{\sigma}^{\mathrm{sG}}_{\mathrm{fr}})_{\mathrm{dev}}$ by $(46)_1$. Note that in a suspension without grain contacts each grain would be completely surrounded by water, resulting in $p^{\mathrm{sG}} = p^{\mathrm{fG}}$ and $p^{\mathrm{G}'} = 0$. In the light of (46) and (47), the total frictional (quasi-static) stress part of the saturated granular medium can be calculated from

$$\boldsymbol{\sigma}^{\mathrm{G}}_{\mathrm{fr}} = \boldsymbol{\sigma}^{\mathrm{G}'}_{\mathrm{fr}} - p^{\mathrm{fG}}\boldsymbol{I}, \tag{48}$$

which is known as Terzaghi's principle of effective stress [38, 110, 121].

In contrast to the frictional part, we postulate that the effective stress for the collisional (dynamic) regime remains unaffected by fluid stresses, i.e., $\boldsymbol{\sigma}_{\mathrm{vi}}^{\mathrm{G}'} = (1 - n^{\mathrm{G}})\boldsymbol{\sigma}_{\mathrm{vi}}^{\mathrm{sG}}$. Therefore, by taking into account (45), the assumptions (46), and the principle (48), the representation (44) of the total Cauchy stress can be recast into

$$\begin{aligned} \boldsymbol{\sigma}^{\mathrm{G}} &= \boldsymbol{\sigma}_{\mathrm{fr}}^{\mathrm{G}'} + \boldsymbol{\sigma}_{\mathrm{vi}}^{\mathrm{G}'} + \boldsymbol{\sigma}_{\mathrm{fr}}^{\mathrm{fG}} + n^{\mathrm{G}}\boldsymbol{\sigma}_{\mathrm{vi}}^{\mathrm{fG}} \\ &= \boldsymbol{\sigma}^{\mathrm{G}'} - p^{\mathrm{fG}}\boldsymbol{I} + n^{\mathrm{G}}\boldsymbol{s}^{\mathrm{fG}}, \end{aligned} \tag{49}$$

with $\boldsymbol{\sigma}^{\mathrm{G}'} = \boldsymbol{\sigma}_{\mathrm{fr}}^{\mathrm{G}'} + \boldsymbol{\sigma}_{\mathrm{vi}}^{\mathrm{G}'}$. We refer to (49) as the principle of effective stress for a general saturated grain–fluid mixture. The same relation is used in [64] in a continuum mixture theory to describe the flow of variably fluidized granular masses (debris flow, rock avalanches, etc.).

Based on the general principle of effective stress (49), and the discussion at the beginning of this section concerned with the different flow regimes of dense grain–fluid mixtures, constitutive equations have to be specified for the fluid-phase stress and for the frictional and viscous parts of the effective stress.

For simplicity, the interstitial fluid (pore fluid) is represented by a Newtonian fluid with deviatoric viscous stress. Hence, the constitutive behavior can be described by the standard Navier–Poisson relation together with the Stokes condition [76], leading to

$$\boldsymbol{\sigma}^{\mathrm{fG}} = \boldsymbol{\sigma}_{\mathrm{fr}}^{\mathrm{fG}} + \boldsymbol{\sigma}_{\mathrm{vi}}^{\mathrm{fG}} \overset{\mathrm{def}}{=} -p^{\mathrm{fG}}\boldsymbol{I} + 2\mu^{\mathrm{fG}}\boldsymbol{d}_{\mathrm{dev}}^{\mathrm{fG}}, \tag{50}$$

where $\boldsymbol{d} \overset{\mathrm{def}}{=} \frac{1}{2}(\boldsymbol{\nabla}\boldsymbol{v} + (\boldsymbol{\nabla}\boldsymbol{v})^{\mathrm{T}})$ is the spatial rate of deformation tensor and μ^{fG} is the dynamic shear viscosity. Effects of turbulence are again neglected. In cases where the fluid phase does not represent pure liquid but a suspension with moderate concentrations of dispersed fines, estimates for μ^{fG} can be found in [82]. Moreover, in order to account for the fact that the fluid phase fills the interstitial space of the distributed granular material, we define $\mu^{\mathrm{fG}}(n^{\mathrm{G}}) \overset{\mathrm{def}}{=} (n^{\mathrm{G}})^2\mu_0^{\mathrm{fG}}$ in accordance with [86], where μ_0^{fG} is the shear viscosity of the fluid for $n^{\mathrm{G}} = 1$ (pure fluid).

Compared to the fluid phase, the mechanical behavior of cohesionless granular material is very complex and has several distinctive features [48, 59, 60, 68, 99, 102, 111, 121]. Different approaches can be employed to model this behavior on the mesoscale. Here, we are interested in exploring fundamental behavior of complex phenomena in geomechanics and geotechnical engineering. In this regard, phenomenological two-phase models relying on a continuum representation of granular material and not on micromechanics are eminently suited [6, 45, 48, 60, 121]. The application to general geomechanical multi-material flows calls for constitutive relations which need only a single set of material constants and then are able to simulate the mechanical behavior of granular material under complex loading paths over a wide range of densities and stress states. However, a constitutive relation accounting for all features and over the entire frictional–collisional regime is still out of reach.

Constitutive equations should be prescribed for the effective stress $\boldsymbol{\sigma}^{\mathrm{G}'} = \boldsymbol{\sigma}_{\mathrm{fr}}^{\mathrm{G}'} + \boldsymbol{\sigma}_{\mathrm{vi}}^{\mathrm{G}'}$. Concerning the quasi-static frictional stress contribution $\boldsymbol{\sigma}_{\mathrm{fr}}^{\mathrm{G}'}$, attractive models have been proposed for applications in soil mechanics and fall into the categories of elasto-plastic [72, 77, 87, 109] or hypoplastic [17, 51, 83, 115] rate constitutive equations. All of them determine an objective rate of the effective stress as a function of the rate of deformation, the effective stress, the porosity n^{G} or void ratio $e^{\mathrm{G}} \overset{\mathrm{def}}{=} n^{\mathrm{G}}/(1 - n^{\mathrm{G}})$, and a (possibly empty) set of additional state variables $\boldsymbol{h}^{\mathrm{G}} \overset{\mathrm{def}}{=} \{h_1^{\mathrm{G}}, \ldots, h_m^{\mathrm{G}}\}$. As an example, we consider the generic rate constitutive equation

$$\begin{aligned} \overset{\triangledown}{\boldsymbol{\sigma}}{}_{\mathrm{fr}}^{\mathrm{G}'} &\overset{\mathrm{def}}{=} \boldsymbol{c}_{\mathrm{fr}}^{\mathrm{G}'}(\boldsymbol{\sigma}_{\mathrm{fr}}^{\mathrm{G}'}, n^{\mathrm{G}}, \boldsymbol{h}^{\mathrm{G}}) : (\boldsymbol{d}^{\mathrm{sG}} - \dot{\varepsilon}^{\mathrm{sG}}\boldsymbol{I}) \\ &\overset{\mathrm{def}}{=} \overset{\triangledown}{\boldsymbol{\sigma}}{}_{\mathrm{fr}}^{\mathrm{G}''} - \dot{\varepsilon}^{\mathrm{sG}}\boldsymbol{c}_{\mathrm{fr}}^{\mathrm{G}'} : \boldsymbol{I}, \end{aligned} \tag{51}$$

in which $\overset{\triangledown}{\boldsymbol{\sigma}} \overset{\mathrm{def}}{=} \dot{\boldsymbol{\sigma}} + \boldsymbol{\sigma}\cdot\boldsymbol{\omega} - \boldsymbol{\omega}\cdot\boldsymbol{\sigma}$ denotes the Zaremba–Jaumann rate of Cauchy stress and $\boldsymbol{\omega} \overset{\mathrm{def}}{=} \frac{1}{2}(\nabla\boldsymbol{v} - (\nabla\boldsymbol{v})^{\mathrm{T}})$ is the vorticity tensor. In (51), we subtracted from the solid-phase rate of deformation $\boldsymbol{d}^{\mathrm{sG}}$ the average volumetric strain rate $\dot{\varepsilon}^{\mathrm{sG}}\boldsymbol{I}$ of the compressible solid phase due to fluid phase pressure rate $\dot{p}^{\mathrm{fG}}$. The stress tensor $\boldsymbol{\sigma}_{\mathrm{fr}}^{\mathrm{G}''}$ is responsible for all deformation of the solid phase, including the compression of grains. We should remark that the spatial gradient of solid-phase volume fraction has been detected as fundamental in describing the quasi-static mechanical behavior of granular materials [49, 59, 86, 96], and hence should be included in the list of arguments of $\boldsymbol{c}_{\mathrm{fr}}^{\mathrm{G}'}$. However, for simplicity we assume here that this gradient is zero (homogeneous granular material).

It remains to specify a constitutive relation for the dynamic contribution $\boldsymbol{\sigma}_{\mathrm{vi}}^{\mathrm{G}'} = (1-n^{\mathrm{G}})\boldsymbol{\sigma}_{\mathrm{vi}}^{\mathrm{sG}} = \tilde{\boldsymbol{\sigma}}_{\mathrm{vi}}^{\mathrm{sG}}$ of the effective bulk stress in the dense grain–fluid mixture representing the saturated granular material. Different approaches are available, but most of them are restricted to particular flow conditions or to narrow ranges of material properties. In the present research, we adopt a simple model formulation suggested by Passman et al. [86] and further investigated in [61, 116]. Its representation in rate form has been adopted in [31] to model silo discharge:

$$\overset{\triangledown}{\boldsymbol{\sigma}}{}_{\mathrm{vi}}^{\mathrm{G}'} \overset{\mathrm{def}}{=} 2\mu^{\mathrm{G}'}\overset{\triangledown}{\boldsymbol{d}}{}^{\mathrm{sG}} = \mu_{\mathrm{vol}}^{\mathrm{G}'}(\mathrm{tr}\overset{\triangledown}{\boldsymbol{d}}{}^{\mathrm{sG}})\boldsymbol{I} + 2\mu^{\mathrm{G}'}\overset{\triangledown}{\boldsymbol{d}}{}^{\mathrm{sG}}{}_{\mathrm{dev}}. \tag{52}$$

Such a form was also used in [56]. The first term on the right expresses the rate of stress change due to volume viscosity $\mu_{\mathrm{vol}}^{\mathrm{G}'}$. The dynamic shear viscosity $\mu^{\mathrm{G}'}$ is generally a function of the void ratio (porosity) and shear rate. Relations have been proposed for different flow situations resp. flow geometries [6, 15, 31, 45, 49, 59, 60, 65, 66, 86]. However, decision on which one is the most appropriate for the present class of problems requires further investigation.

5 Interface Reconstruction and Propagation

5.1 Governing Equations

One of the main features of the MMALE method is that material interfaces are not necessarily aligned with boundaries of the computational cells but may flow through the mesh (Fig. 2). The interface position needs to be known at each time step in order to achieve a reasonable accuracy of the overall method (Algorithm 1). Different approaches are available in this context, as reviewed in [27, 62, 100]. The widely used volume of fluid (VOF) methods [39, 52, 58, 89, 93, 95, 118, 119] do not track the interface directly, but instead track the fractional material volume in a mesh element using an approximation to the interface. The interfaces are reconstructed ab initio element by element from the solution data. Once the interface locations in each multi-material element have been determined, the material transport volumes across the element boundaries can be computed as truncation volumes. Finally, the fractional material volumes are integrated to a new time level to propagate the interface (Algorithm 2). The actual calculation is largely geometrical in nature, as will be shown in the remainder of this paper.

Algorithm 2: VOF interface reconstruction and propagation.

Input: mesh, velocity field, discrete material volume fraction data
Output: reconstructed material interface, advected volume fraction data

1 reconstruct material interface for each element using volume fraction data;
2 compute material transport volumes as truncation volumes;
3 update fractional material volume by summing material transport volumes;

VOF methods are typically discussed with regard to a fixed, structured computational mesh of finite difference type. The descriptions use volume coordinates and, in two dimensions, reduce the element to a unit square [24]. Concerning the present research, two points have to be considered. First, we seek to apply VOF methods to unstructured finite element meshes. This requires special data structures and coordinate systems which allow to resemble the classical descriptions. For example, in an unstructured quadrilateral mesh the parametric coordinates of the parent square element are equivalent to volume coordinates. Second, the mesh in MMALE methods is not fixed.

When using a Lagrangian–remap strategy, Algorithm 2 is implemented by reconstructing the material interfaces in the Lagrangian elements prior to the remap; see also Algorithm 1. The amount of transported material is usually defined as the regions swept out by the element facets during mesh relocation truncated by the interfaces. The interfaces that should be reconstructed in our MMALE method are not the microscopic interfaces between the grains and the pore fluid in the granular material, but the interfaces between the bulk materials on the macroscale (Fig. 3). For this rea-

son, the material volume fraction f^k has been introduced as a basic variable of our three-scale mixture theory. It naturally carries information based on which material interfaces can be reconstructed using VOF methods.

Recall the situation and the basic notation introduced in Sect. 3.1. For reasons of simplification, the present study is restricted to two-dimensional problems in Cartesian coordinates. Moreover, we consider the flow of only two materials $k \in \{1, 2\}$, say, a light material and a dark material, which are separated by a sharp material interface. The flow takes place in a time interval $[0, T] \subset \mathbb{R}$ and in a modeling domain $\mathcal{D} \subset \mathbb{R}^2$ of the ambient Euclidian space. A point in $\mathcal{D}$ is identified with its coordinate vector $\boldsymbol{x} = [x, y]^{\mathrm{T}} \in \mathbb{R}^2$. Velocities are assumed continuous at the interface, that is,

$$\boldsymbol{v}_1 = \boldsymbol{v}_2 \equiv \bar{\boldsymbol{v}}. \tag{53}$$

No slip is currently taken into account. Hence, the interface velocity is the velocity normal to the interface [100]:

$$\boldsymbol{v}_{\mathrm{I}} = v_{\mathrm{I}}\, \boldsymbol{n}_{\mathrm{I}} = (\bar{\boldsymbol{v}} \cdot \boldsymbol{n}_{\mathrm{I}})\, \boldsymbol{n}_{\mathrm{I}}, \tag{54}$$

where $\boldsymbol{n}_{\mathrm{I}}$ is the field of unit normals on the interface, pointing outward the dark material.

Let χ be the material indicator function on the dark material in accordance with (18), then (19) and the application of (54) yield

$$\frac{\partial \chi}{\partial t} + \bar{\boldsymbol{v}} \cdot \boldsymbol{\nabla} \chi = 0. \tag{55}$$

Taking the volume[1] average resp. $\mathcal{H}$-average of this equation as defined in Sect. 3.1 and respecting the averaging rules [41, 42] results in

$$\frac{\partial f}{\partial t} + \boldsymbol{v} \cdot \boldsymbol{\nabla} f = 0, \qquad \text{or equivalently} \qquad \dot{f} = 0, \tag{56}$$

where f is the material volume fraction and $\boldsymbol{v}$ is an averaged velocity field, referred to as the (common) material velocity in what follows. Comparison with Eq. (42) of the homogeneous equilibrium model derived in Sect. 3.3 indeed shows that the right sides of (56) are not zero in case of compressible materials. Therefore,

$$\dot{f} = f \left(\frac{\langle K \rangle}{K} - 1 \right) \operatorname{div} \boldsymbol{v} \tag{57}$$

is taken as the basic equation.

[1] We use the term "volume" and "surface area" even though the present section is restricted to two-dimensional problems. In fact, area and length in two dimensions can be regarded as volume and surface area per unit depth in three dimensions.

The material volume fraction is considered as the primary variable of VOF methods as it naturally carries information based on which material interfaces can be reconstructed. In fact, if $f = 1$ then the zone is filled with dark material, and if $f = 0$ the zone is filled with light material. A value $0 < f < 1$ indicates that the interface lies within that zone.

Following the derivations of Sect. 2, the ALE formulation of (57) is

$$\frac{\partial \hat{f} J}{\partial t} + J \operatorname{div}(f \boldsymbol{c}) = \frac{\langle K \rangle}{K} f J \operatorname{div} \boldsymbol{v} \tag{58}$$

and the operator split associated with the Lagrange–remap strategy gives the two equations

$$\frac{\partial \hat{f} J}{\partial t} = \frac{\langle K \rangle}{K} f J \operatorname{div} \boldsymbol{v}, \tag{59}$$

$$\frac{\partial \hat{f} J}{\partial t} + J \operatorname{div}(f \boldsymbol{c}) = 0. \tag{60}$$

Again, (59) is equivalent to (57), but its integration in time is left unconsidered here. We just keep in mind that volume fraction might change during the Lagrangian step of the MMALE method. The second equation, (60), constitutes a conservation law and has to be solved during the remap step with respect to a given finite element mesh. This is outlined in the next sections.

5.2 Basic Topological and Geometrical Functions

The topological and geometrical information required for VOF interface reconstruction and propagation must be gathered from a given finite element mesh, consisting of n_{el} two-dimensional elements Ω_e. The unique element number, e, is occasionally dropped. Each element is a simple polygon and represents a discrete portion of the reference domain moving and deforming in space. It is defined by nodes $I \in \{1, \ldots, n_{\mathrm{en}}\}$ and edges $\Gamma_{e,I}$ connecting the nodes I and $I + 1$. Nodes are numbered in counter-clockwise order of their occurrence along the element's perimeter, and the node $I = n_{\mathrm{en}} + 1$ coincides with $I = 1$. The global node number is denoted by X, and for each element e and local node I, there is a unique number $X(I, e)$. The total number of nodal points in the mesh is n_{np}. We assume for simplicity that global node numbering and element numbering is contiguous, so that n_{np} and n_{el} are equal to the largest node number and largest element number in the mesh, respectively. In other words, $X \in \{1, \ldots, n_{\mathrm{np}}\}$ and $e \in \{1, \ldots, n_{\mathrm{el}}\}$.

The numerical implementation of Algorithm 2 requires topological information of the adjacent elements to an element, fundamental boolean set-theoretic operations

applied to lines and polygons, also called clipping, as well as geometrical functions. In summary, the following functions are required:

1. Adjacent elements
2. Segment–segment intersection
3. Point-in-polygon test
4. Clipped polygon collection
5. Polygon volume

5.2.1 Adjacent Elements

The transport resp. advection of material between elements requires the list of elements adjacent to each element. Data structures and the implementation of functions to determine these lists in unstructured quadrilateral meshes have been suggested in [28]. The basic information required in that reference is the two-dimensional connectivity array associated with the mesh. A modified approach is taken here.

In unstructured meshes, working with dynamic structures like linked lists and pointer variables (available in Fortran 90 and above) is more practical than using fixed dimensional arrays. Beyond that, the current Fortran implementation adopts a somewhat object-oriented programming. Elements and nodes, for example, are derived data types which are comparable to those C++ objects defined in [88]. Pointers to other data types resp. objects are stored within these data types, enabling the creation of a linked list with an arbitrary number of entries. By taking advantage of this option, the list of elements connected to a node is easily generated (Algorithm 3).

Algorithm 3: List of elements connected to all nodes.

Input: mesh elements, nodes connected to each element
Output: list of elements connected to all $X \in \{1, \ldots, n_{\mathrm{np}}\}$

```
1 while node X ≤ n_np do disassociate pointer to list of elements;
2 while element e ≤ n_el do
3 |   while element node I ≤ n_en do
4 |   |   add element e to list of X(I, e);
5 while node X ≤ n_np do associate pointer with first list entry;
```

The element data type has an identifier $e \in \{1, \ldots, n_{\mathrm{el}}\}$, the element number, and points to an array of the local nodes $I \in \{1, \ldots, n_{\mathrm{en}}\}$ defining the element, and to an array of adjacent elements. Nodes are defined by a global node number $X \in \{1, \ldots, n_{\mathrm{np}}\}$ and a coordinate array. The global node number $X(I, e)$ assigned to the local node I of an element e has been traditionally defined as an entry of a mesh connectivity matrix. Because of their frequent use, the next node and the

previous node of a particular node are also stored. The best way to do this is to store arrays containing the corresponding permutations of the local node numbers, $\mathrm{next}(I) = I + 1$ and $\mathrm{prev}(I) = I - 1$, respectively, in the definition of the element data type.

Once the list of elements connected to all nodes has been generated, the elements adjacent to an element can be determined according to the following procedure [28]. Edge Γ_I of element e is defined by node I and the node counter-clockwise from it, $\mathrm{next}(I) = I + 1$. The edge is shared by only two elements, the current element e, and the adjacent element, $\mathrm{adj}(e, I)$, sharing the edge with index I. A search on the lists of elements connected to the two nodes of the edge is carried out in order to determine the two elements in common. The element which is not the current element is the adjacent element (Algorithm 4).

For the interface normal calculation outlined below, all the adjacent elements connected to all nodes of an element need to be known. Since the elements adjacent to an edge are known through Algorithm 4, only the corner elements have to be determined. An easy way to generate this list is to copy the list resulting from Algorithm 3 to the local nodes of all elements and to delete the current element and the elements adjacent to an edge.

5.2.2 Segment–Segment Intersection

One basic function frequently used in VOF methods is the determination of the intersection point of line segments, i.e., between the interface and the element edges. A line segment, in contrast to infinite lines, has a finite length. Hence, there might be no intersection even if the segments are not parallel (invalid intersection). Several other cases generally have to be considered. We refer to [85, Sect. 7.2] and [107] for further details and implementation.

Algorithm 4: Elements adjacent to edges for all elements.

Input: elements, nodes connected to each element, elements connected to each node
Output: elements adjacent to edges for all elements

```
1 while element e ≤ n_el do
2     while element node I ≤ n_en do
3         forall the elements a connected to X(I, e) do
4             if a ≠ e then
5                 forall the elements b connected to X(next(I), e) do
6                     if b = a then store adj(e, I) = a;
```

5.2.3 Point-in-Polygon Test

The point-in-polygon test is needed to determine whether a particular point or node lies inside a material zone. It is a basic operation frequently applied in computer graphics and other areas dealing with processing of geometrical data. One of the fastest solution strategies that requires only negligible amount of polygon data pre-processing is the crossing test [53]. A ray is shot from the test point commonly along an axis. Then, either the even/odd crossing number or winding number is computed to classify the point for arbitrary closed polygons [2, 44, 53, 85, 101].

5.2.4 Clipped Polygon Collection

VOF methods must frequently determine the partial material volumes (subzones) in the mesh elements or in the polygonal transport volumes across the element edges. Mathematically spoken, the subzone is the set-theoretic intersection of the domains enclosed by two polygons, or by one polygon and a half-plane. In computer graphics, this is called polygon clipping [44, 108]. The mesh represents a collection of clip polygons and the total material domain is represented by the subject polygon or half-plane.

In fact, not the polygon itself but only the vertices of its polygonal boundary line are stored. Polygon clipping has to determine the line segments belonging to the boundary of the subzone through intersection and has to merge these segments to close the boundary line; this decisive latter step is sometimes called "capping" in the literature. Hence, polygon clipping requires elaborate data structures and has to implement different boolean operations on polygons.

The data structures and clipping algorithm used in the present research have been developed in [50] and extended in [67] to handle degenerate cases. In both neither the clip nor the subject polygon needs to be convex, and they may have self-intersections. The each input and output polygon is efficiently represented as a doubly linked edge list, referred to as the half-edge data structure. First, the segment–segment intersection points between the two input polygons are determined, then these are assigned specific flags to indicate relative orientation of the polygon edges, and finally the intersection points are merged into the data structure of the clipped subject polygons.

5.2.5 Polygon Volume

The signed volume of a two-dimensional polygon defined by vertices $I \in \{1, \ldots, M\}$, with $M + 1 = 1$, can be calculated from [44, 85, 101, 106]

$$V = \frac{1}{2} \sum_{I=1}^{M} (x_I y_{I+1} - x_{I+1} y_I) = \frac{1}{2} \sum_{I=1}^{M} x_I (y_{I+1} - y_{I-1}). \tag{61}$$

The first summation requires $2M$ multiplications and $(2M-1)$ additions, while the second summation requires only M multiplications and $(2M-1)$ additions [106]. Note that the signed volume is positive, i.e., $|V| = V$, if the vertices are placed in counter-clockwise order along the perimeter, otherwise it is negative.

It should be emphasized that the formula (61) can also be used to calculate the signed volume of a self-intersecting polygon. In this case, the partial volumes adjacent to an intersection have opposite signs. For example, twisting a rectangle so that it looks like a Fig. 8 results in two triangular regions. Their volumes sum up to zero, which is the total signed volume of the twisted rectangle according to (61).

5.3 Interface Reconstruction

Common state-of-the-art VOF methods approximate the interface in each multi-material element by a straight line; see reviews in [27, 89, 93]. One of the earliest two-dimensional methods is due to Youngs [118], which forms a basis for the developments of the present research. Our implementation relies on that described in [95] because the original paper provides little detail of the interface reconstruction procedure. An alternative implementation is presented in [27].

A linear interface can be generally described by the Hesse normal form

$$\boldsymbol{n} \cdot \boldsymbol{x} - d = 0, \tag{62}$$

in which $\boldsymbol{x}$ is an arbitrary point on the interface, $\boldsymbol{n} = [n^x, n^y]^{\mathrm{T}} \in \mathbb{R}^2$ is the unit normal on that interface (the index I has been dropped for notational brevity), and d is the line constant representing the shortest distance between the interface and the origin. Most volume of fluid methods determine a linear reconstruction of the interface for each element in two steps: (i) estimate $\boldsymbol{n}$ and (ii) determine d such that the volume fraction of the material lying behind the interface matches the known value.

Since we choose the normal to point outward of the material, (62) returns a positive number if $\boldsymbol{x}$ lies outside of the material. From the viewpoint of implementation, it proves convenient to introduce the gradient of the volume fraction, $\boldsymbol{m} = [m^x, m^y]^{\mathrm{T}}$, for which $\boldsymbol{n} = -\boldsymbol{m}/\|\boldsymbol{m}\|$. The slope of the interface, s, is related to the normal by $s = -m^x/m^y = -n^x/n^y$.

Youngs' method [118] has been developed for finite difference type uniform meshes of square elements with edge lengths $\Delta x = \Delta y$; the original paper uses a mesh of unit squares. The interface slope is estimated based on the volume fraction data in the current element and its eight neighbors. Figure 4 shows the notation for the element-centered volume fractions using the principal points of the compass. According to [95], the components of the volume fraction gradient in the current element of a uniform mesh can be approximated by the stencil

$$
\begin{aligned}
m_x &= \frac{1}{\Delta x}\left(f_{\mathrm{NE}} + 2f_{\mathrm{E}} + f_{\mathrm{SE}} - f_{\mathrm{NW}} - 2f_{\mathrm{W}} - f_{\mathrm{SW}}\right), \\
m_y &= \frac{1}{\Delta y}\left(f_{\mathrm{NE}} + 2f_{\mathrm{N}} + f_{\mathrm{NW}} - f_{\mathrm{SE}} - 2f_{\mathrm{S}} - f_{\mathrm{SW}}\right).
\end{aligned}
\tag{63}
$$

The slope angle $\beta = \tan^{-1} s = \tan^{-1}(-m_x/m_y)$ lies in the range $-\pi/2 < \beta < \pi/2$. The stencil assumes that the elements are all unit volume. It would be not optimal, though practical to use the same stencil in structured quadrilateral meshes where the elements have different sizes. When using an gradient estimation according to (63), the interface reconstruction is only first-order accurate and linear interfaces are reproduced exactly only in certain isolated cases [27, 89, 93, 95].

Elements located at mesh boundaries require special treatment because one or more of the neighbors indicated in Fig. 4 might not exist. In this case, the missing neighbors are substituted by the so-called ghost elements, and the volume fraction of the current element is just copied to the ghost elements. The use of ghost elements also allows boundary conditions (e.g., inflow, outflow) to be handled efficiently in MMALE methods.

Once the slope or normal direction of the material interface is known, its location has to be determined by some procedure. The interface truncates the element domain, and the truncated volume behind the interface represents the partial material volume. Volume is conserved, i.e., the right location of the interface has been determined, if the partial volume divided by the element volume matches the given volume fraction data of that element. The matching can either be achieved through iteration of the distance parameter d, as done in [93], or by deriving an explicit expression that relates the truncated element volume to d or to other parameters that locate the interface. The second approach has been pursued in [27, 52, 119]. We particularly follow the derivation of [95] again, implementing the original method [118].

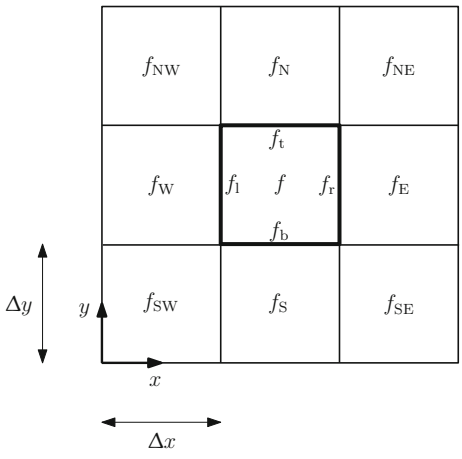

Fig. 4 Notation of adjacent element volume fractions and side fractions used for interface slope calculation

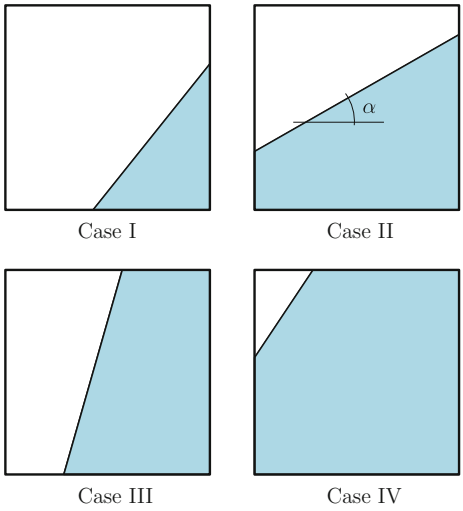

Fig. 5 Four principal configurations of reconstructed interface for Youngs' method; after [95]

If the element is a square, four principal cases of how the interface is located generally have to be considered (Fig. 5). In each case, the interface intersects a particular pair of element edges under an angle

$$\alpha = \tan^{-1}\left(\frac{\Delta x}{\Delta y}\frac{-m_x}{m_y}\right), \qquad \text{with} \quad 0 \leq \alpha \leq \pi/2. \tag{64}$$

The 3×3 block of elements eventually has to be rotated in such a way that α lies within the indicated range. The factor $\Delta x/\Delta y$ in the expression is only necessary if m_x, m_y have been evaluated based on $\Delta x \neq \Delta y$. After the case has been determined using α and the volume fraction f of the element under consideration, the side fractions f_b, f_r, f_t, and f_l at the bottom, right, top, and left edges, respectively, of the current element can be calculated (Fig. 4). The side fractions $f_\sigma \in [0, 1]$, $\sigma \in \{\mathrm{b}, \mathrm{r}, \mathrm{t}, \mathrm{l}\}$, are the fractions of the edges that lie within the material and uniquely determine the intersections of the interface with the element boundary. The logic to determine the case according to Fig. 5 and the calculation of the side fractions have been presented in [95][2] and are summarized in Algorithm 5.

As a simple example providing an analytical solution, we consider a linear interface on a fixed mesh of unit squares. The problem statement and mesh, including the element and global node numbers, is shown in Fig. 6. Application of the interface reconstruction algorithm described above to elements along the mesh boundary (element numbers 1, 2, 6, etc.) requires a layer of ghost elements to complete the

[2] Table V in the original paper [95] has typos in the formulas for the side fractions for case IV, in which C should be in fact $1 - C$, where C is the volume fraction. The correct formulas are in Algorithm 5.

set of element neighbors for a real element. However, these ghost elements are not shown in Fig. 6 and in the following figures. The unit normal to the interface pointing outward the dark material is readily available through

$$\boldsymbol{n} = \left\| \begin{matrix} 5.0 \\ 4.0 \end{matrix} \right\|^{-1} \begin{bmatrix} 5.0 \\ 4.0 \end{bmatrix} = \begin{bmatrix} 0.780871 \\ 0.624697 \end{bmatrix}. \tag{65}$$

The exact coordinates of the intersection points between the interface and the mesh in the initial configuration as well as the resulting volume fractions for all elements are plotted in Fig. 7. Since the volume of the elements is one, the volume fraction of an element is equal to the volume of the intersection between the dark material half-plane (triangular domain) and the element domain.

Algorithm 5: Case-by-case volume fraction matching using side fractions; after [95].

Input: f and α for current element
Output: side fractions f_b, f_r, f_t, and f_l

if $\alpha < \pi/4$ **then**
  if $f \leq \frac{1}{2}\tan\alpha$ **then**
    Case I: $f_\mathrm{b} = (2f\cot\alpha)^{1/2}$, $f_\mathrm{r} = (2f\tan\alpha)^{1/2}$, $f_\mathrm{t} = 0$, $f_\mathrm{l} = 0$;
  else if $f \leq 1 - \frac{1}{2}\tan\alpha$ **then**
    Case II: $f_\mathrm{b} = 1$, $f_\mathrm{r} = f + \frac{1}{2}\tan\alpha$, $f_\mathrm{t} = 0$, $f_\mathrm{l} = f - \frac{1}{2}\tan\alpha$;
  else
    Case IV: $f_\mathrm{b} = 1$, $f_\mathrm{r} = 1$, $f_\mathrm{t} = 1 - (2(1-f)\cot\alpha)^{1/2}$,
    $f_\mathrm{l} = 1 - (2(1-f)\tan\alpha)^{1/2}$;
else
  if $f \leq \frac{1}{2}\cot\alpha$ **then**
    Case I: $f_\mathrm{b} = (2f\cot\alpha)^{1/2}$, $f_\mathrm{r} = (2f\tan\alpha)^{1/2}$, $f_\mathrm{t} = 0$, $f_\mathrm{l} = 0$;
  else if $f \leq 1 - \frac{1}{2}\cot\alpha$ **then**
    Case III: $f_\mathrm{b} = f + \frac{1}{2}\cot\alpha$, $f_\mathrm{r} = 1$, $f_\mathrm{t} = f - \frac{1}{2}\cot\alpha$, $f_\mathrm{l} = 0$;
  else
    Case IV: $f_\mathrm{b} = 1$, $f_\mathrm{r} = 1$, $f_\mathrm{t} = 1 - (2(1-f)\cot\alpha)^{1/2}$,
    $f_\mathrm{l} = 1 - (2(1-f)\tan\alpha)^{1/2}$;

The interface is reconstructed by looping all real elements in the mesh and applying (63) and Algorithm 5. The exact and reconstructed material interface using this method are compared in Fig. 8. Note that the reconstructed interface is not continuous across element boundaries because VOF methods work on a local level for reasons of efficiency. The element volume fractions are exactly matched by the reconstruction, but the interface slopes differ. The relative error of the slope angle, $E_\beta = \frac{2}{\pi}\,||\beta_\mathrm{recon}| - |\beta_\mathrm{exact}||$, are listed in Table 1. It can be seen that the error is larger for elements located at mesh boundaries. This is because the volume fraction states in the ghost element neighbors are assigned the values of that element, which is only a

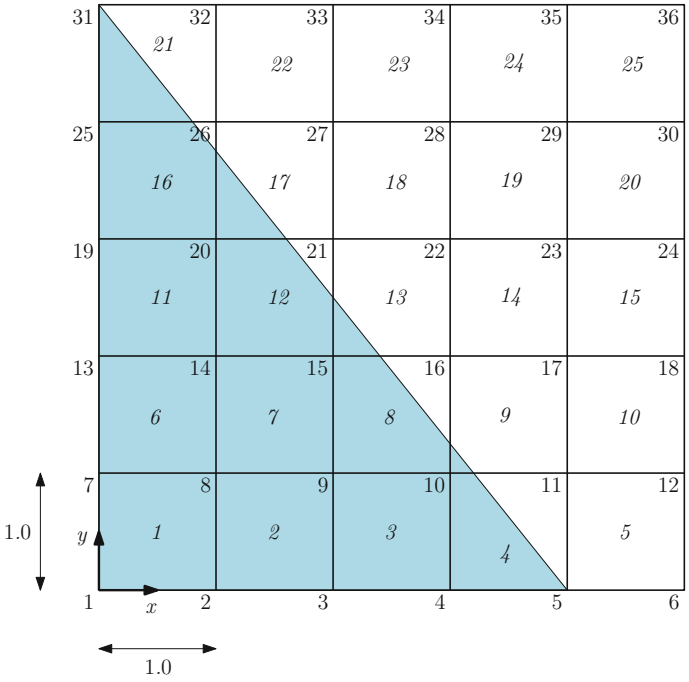

Fig. 6 Problem statement and mesh for linear interface reconstruction. The ghost elements along the mesh boundary are not shown

Table 1 Relative error of slope angle for elements with $0 < f < 1$

Element no.	4	8	9	12	13	16	17	21
E_β (%)	20.72	1.21	0.29	0.65	0.65	16.46	1.21	7.05

rough approximation to the "true" state expected for an interface continuing beyond the mesh boundary.

5.4 Interface Propagation

For a Lagrange–remap MMALE strategy, the interface is propagated through the mesh by transporting the fractional material volume across the element boundaries during the remap step. The time associated with the end of the Lagrangian step is denoted by t^-, while time associated with the end of remap step is t^+. The constant time increment is $\Delta t = t^+ - t^-$; however, there is actually no physical time associated with it. On occasion, quantities related to the Lagrangian step and to the

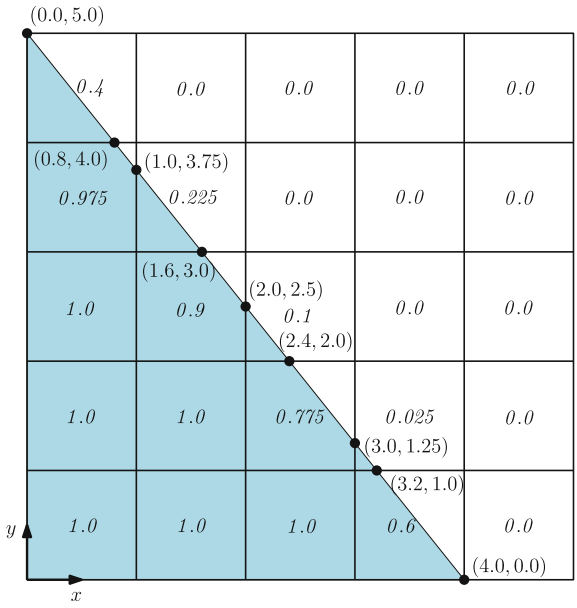

Fig. 7 Interface-mesh intersections (*numbers in parentheses*) and initial volume fractions (*slanted numbers in the elements*)

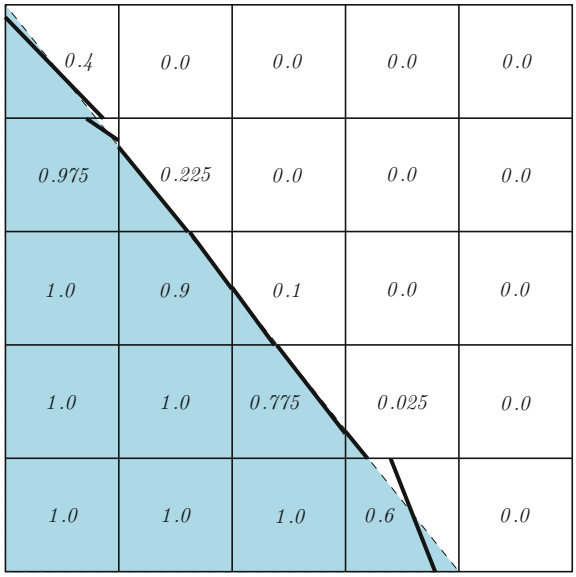

Fig. 8 Comparison of exact (*dashed line*) and reconstructed material interface (*solid line*) using Youngs' method [95, 118]. *Numbers* in the elements denote the material volume fractions, which are exactly matched by the reconstruction

remap step are superscribed with $-$ and $+$, respectively. Given the distorted geometry $\boldsymbol{x}^-$ after the Lagrangian step and relocated geometry $\boldsymbol{x}^+$, the convective velocity is simply approximated by the finite difference formula $\boldsymbol{c} = (\boldsymbol{x}^- - \boldsymbol{x}^+)/\Delta t$. Data assumed to be given in the remap step includes both $\boldsymbol{x}^-$ and $\boldsymbol{x}^+$ as well as the material

volume fraction distribution f^- constant in each element. If $\boldsymbol{x}^+ \equiv \boldsymbol{x}_0$ is the original geometry at time $t = 0$, then a Eulerian method is obtained [24].

Owing to (60), the remap takes the form of an advection problem subject to the initial condition $f|_{t=t^-} = f^-$. Its numerical solution is done by a kind of finite volume method [16, 70]. These methods are conservative by definition because they solve the integral form of (60). They work on a control volume tessellation which, in this paper, is assumed to coincide with the underlying finite element mesh. Therefore, the terms "control volume" and "element" can be used interchangeably.

The element boundary $\partial\Omega_e$ is piecewise oriented and C^1-continuous by definition. It is throughout assumed that the orientation of the boundary $\partial\Omega_e$ is compatible with the orientation of Ω_e such that the unit normals to $\partial\Omega_e$, denoted by $\boldsymbol{n}$, point outward. In the context of finite volume methods, the control volume resp. element boundary is approximated by the set of edges $\Gamma_{e,I}$ of element Ω_e, i.e.,

$$\partial\Omega_e \approx \bigcup_{I=1}^{n_{\text{en}}} \Gamma_{e,I} \equiv \bigcup_{I} \Gamma_{e,I}. \tag{66}$$

Since overlaps and gaps of the mesh are precluded, there is a unique element $\Omega_{\text{adj}(e,I)}$ adjacent to the edge $\Gamma_{e,I}$. If a vertex or edge of Ω_e is aligned with the boundary of the computational domain, a ghost element Ω_j is added such that the intersection $\Omega_e \cap \Omega_j$ is non-zero.

Based on the previous definitions, we seek an approximate solution to the integral form of the ALE conservation law (60) with respect to each control volume:

$$\frac{\mathrm{d}}{\mathrm{d}t} \int_{\Omega_e} f \,\mathrm{d}v + \sum_I \int_{\Gamma_{e,I}} f\boldsymbol{c} \cdot \boldsymbol{n} \,\mathrm{d}a = 0, \qquad \text{subject to} \quad f|_{t=t^-} = f^-. \tag{67}$$

The product $f\boldsymbol{c}$ in the second term on the left side is the convective flux of the field f, and $\mathrm{d}a$ is the surface area density on $\mathbb{R}^2$ (representing the differential arc length). In solving the problem defined through (67), the method approximates the evolution of the element average

$$f_e = \frac{1}{V_e} \int_{\Omega_e} f \,\mathrm{d}v\,, \qquad \text{with} \quad V_e = \int_{\Omega_e} 1 \,\mathrm{d}v > 0 \quad \text{and} \quad e \in \{1, \ldots, n_{\text{el}}\}\,, \tag{68}$$

over the pseudo-time interval $[t^-, t^+]$. The averaged convective volume flux across a moving and deforming element edge $\Gamma_{e,I}$ is defined by

$$F^V_{e,I} = \frac{1}{S_{e,I}} \int_{\Gamma_{e,I}} \boldsymbol{c} \cdot \boldsymbol{n} \,\mathrm{d}a, \qquad \text{where} \quad S_{e,I} = \int_{\Gamma_{e,I}} 1 \,\mathrm{d}a > 0. \tag{69}$$

Note that volume flux is positive if material leaves the moving element through the boundary. The measure $S_{e,I}$ is the surface area of the edge $\Gamma_{e,I}$.

For every pair of adjacent elements $(\Omega_e, \Omega_{\text{adj}(e,I)})$, the true averaged convective flux of the field f across the edge $\Gamma_{e,I} = \Omega_e \cap \Omega_{\text{adj}(e,I)}$ is replaced by a numerical averaged convective flux

$$F^f_{e,I} \approx \frac{1}{S_{e,I}} \int_{\Gamma_{e,I}} f \boldsymbol{c} \cdot \boldsymbol{n} \, \mathrm{d}a. \tag{70}$$

We require $F^{f=1}_{e,I} = F^V_{e,I}$ for reasons of consistency. This is most easily achieved by defining

$$F^f_{e,I} = \eta^\star_{e,I} \, F^V_{e,I}, \tag{71}$$

where $\eta^\star_{e,I}$ represents a particular volume fraction at the element edge $\Gamma_{e,I}$ determined by an appropriate volume of fluid algorithm.

Now, substitution of (68)–(71) into (67) yields the space-discrete problem

$$\frac{\mathrm{d}}{\mathrm{d}t} (f_e V_e) + \sum_I \eta^\star_{e,I} S_{e,I} F^V_{e,I} = 0 \tag{72}$$

for all $e \in \{1, \ldots, n_{\text{el}}\}$ and subject to $f|_{t=t^-} = f^-$. Discretization in time for solid mechanical applications is commonly done by first-order accurate explicit integration methods. In particular, application of the forward Euler method to (72) results in the advection algorithm

$$f^+_e = \frac{f^-_e V^-_e - \sum_I \Delta V^f_{e,I}}{V^+_e}, \qquad \text{with} \quad V^+_e = V^-_e - \sum_I \Delta V_{e,I}, \tag{73}$$

$\Delta V_{e,I} = S_{e,I} F^V_{e,I} \, \Delta t$, and $\Delta V^f_{e,I} = \eta^\star_{e,I} \, \Delta V_{e,I}$. Here, V^-_e is the volume of the deformed element in the Lagrangian mesh, V^+_e is the element volume in the relocated mesh, $\Delta V_{e,I}$ is the total transported volume across the edge $\Gamma_{e,I}$ between Ω_e and the element $\Omega_{\text{adj}(e,I)}$ adjacent to $\Gamma_{e,I}$, and $\Delta V^f_{e,I}$ represents the material transport volume across that edge. $\Delta V_{e,I}$ is defined positive if the nodes defining the edge are moved further into the element's region, that is, if the transport volume is leaving the element.

Explicit advection algorithms, like (73), give rise to stability issues. Stability of a numerical algorithm ensures that the local errors introduced by the approximate solution are not amplified and that the global error produced by the algorithm after several time steps is bounded. A necessary stability condition for any transport algorithm is the CFL condition [46]

$$0 \leq \quad Co = \frac{\|\boldsymbol{c}\,\Delta t\|}{h} \quad \leq 1. \tag{74}$$

Here, $h > 0$ is a characteristic element length and Co is called the CFL number. The CFL condition phrases that a material particle must not pass an element within one step. Concerning the remap step of the MMALE method, the condition (74) constrains the difference of nodal positions before and after the remap through $\|\boldsymbol{x}^- - \boldsymbol{x}^+\| \leq h$.

The amount of material transported across an element edge is represented by the flux term $\Delta V^f_{e,I}$ in the generic advection algorithm (73). This flux term can be calculated without interface reconstruction once a particular advection scheme has been assigned [95]. However, it is more common, and yet more accurate, to incorporate the geometry of the interface and to compute the material transport volumes as truncation volumes [27, 39, 46, 52, 88, 93, 118]. In this second approach, the total transport volume across an element edge is the signed volume swept out by that edge between its two configurations after the Lagrangian step and after the remap. The material transport volume is simply the set-theoretic intersection of the total transport volume and the material domain on the left of the interface (for a normal pointing outward resp. to the right). However, the actual implementation is more complicated.

The pseudocode of a suitable implementation of the volume fraction update in the remap step using (73) is provided in Algorithm 6, and it is based on a procedure outlined in [28]. Note that a negative total transport volume is set to zero, and a volume subtracted from element e is added to element $\mathrm{adj}(e, I)$ adjacent to edge I to avoid double counts. Moreover, the value of the total and material volume update is calculated only once if the total transport volume is positive. This eliminates half of the remap operations.

6 Conclusions and Outlook

An innovative theoretical and numerical framework has been presented which accounts for the large deformations and evolving material interfaces as well as for the complex coupled material behavior of saturated granular material present in geomechanical multi-material flow. In order to model the large-scale motions and interactions of materials in such flow situations, an arbitrary Lagrangian–Eulerian method has been developed in which multi-material elements carry the information of the material interfaces and free surfaces (MMALE method).

The states of the individual materials in multi-material elements are derived from a practical three-scale mixture theory and a homogeneous equilibrium model developed during this research. In contrast to common two-scale theories, the proposed three-scale approach is able to incorporate both the evolution of bulk material interfaces as well as the two-phase phenomena associated with saturated granular mate-

rial. The essential closure relations are specified with respect to the macroscale. We have considered an example flow consisting of a bulk solid, a bulk fluid, and a fluid-saturated granular material with compressible constituents. The mixture approach allows for the use of phenomenological constitutive models describing granular material response for the full frictional–collisional flow regime. Accordingly, the apparent stress tensors in the dense grain–fluid mixture have been split into rate-independent and rate-dependent parts.

Algorithm 6: Volume fraction transport algorithm for interface propagation; based on [28].

Input: V_e^-, f_e^-, and adjacent elements for all elements, mesh at times t^-, t^+
Output: V_e^+, f_e^+ for all elements

set $V_e = V_e^-$ and $f_e = f_e^-$;
while *element* $e \leq n_{\text{el}}$ **do**
  compute $\Phi_e = f_e V_e$;
  while *element edge* $I \leq n_{\text{en}}$ **do**
    calculate total transport volume $\Delta V_{e,I}$;
    set $\Delta V_{e,I}^* = \max(0, \Delta V_{e,I})$;
    if $\Delta V_{e,I}^* > 0$ **then**
      $V_e \leftarrow V_e - \Delta V_{e,I}^*$;
      $V_{\text{adj}(e,I)} \leftarrow V_{\text{adj}(e,I)} + \Delta V_{e,I}^*$;
      calculate material transport volume $\Delta V_{e,I}^f$;
      $\Phi_e \leftarrow \Phi_e - \Delta V_{e,I}^f$;
      $\Phi_{\text{adj}(e,I)} \leftarrow \Phi_{\text{adj}(e,I)} + \Delta V_{e,I}^f$;
  $V_e^+ = V_e$ and $f_e^+ = \Phi_e / V_e^+$;

In the MMALE method, material interfaces are reconstructed ab initio and propagated through the computational mesh using a volume of fluid (VOF) approach. It has been shown that the governing equations are consistent with the developed three-scale mixture theory and with the Lagrange–remap MMALE strategy. The geometrical and topological functions required for the VOF method have been outlined and efficient algorithms have been presented. The basic features were tested using a simple example for which an analytical solution is available. Future work will focus on the extension to unstructured triangle meshes, the implementation into the MMALE method, and on the solution of full-scale large deformation problems in geomechanics and geotechnical engineering, including geotechnical installation processes.

Nomenclature

Operators and Special Notations

$\cdot, :, \otimes$	Single contraction, double contraction, tensor product
$\cup, \cap, \setminus$	Union, intersection, and difference of sets
$\lvert\cdot\rvert, \lVert\cdot\rVert$	Absolute value, Euclidean length
$\langle\cdot\rangle$	Spatial average
$\dot{(\cdot)}, \dot{(\cdot)}^{\alpha k}$	Material time derivative, of an αk-related field
$\hat{(\cdot)}$	Referential, ALE description
$(\cdot)^{\alpha k}$	αk-intrinsic average
$(\cdot)^{[\alpha k]}$	Limit value at αk-boundary
$\overset{\triangledown}{(\cdot)}$	Zaremba–Jaumann rate
$\boldsymbol{\nabla}(\cdot)$	Covariant derivative, gradient
$\partial(\cdot)$	Boundary
$\mathrm{div}(\cdot)$	Divergence
$\mathrm{tr}(\cdot)$	Trace of a second-order tensor

Superscripts and Subscripts

$-, +$	Associated with Lagrangian step, remap step
adj	Adjacent
dev	Deviator of a second-order tensor
dr	Drained
f, fG, fk	Fluid phase, in granular material, in k-material
fr	Frictional (rate-independent) contribution
F	Bulk fluid; F $\equiv$ fF
G	Fluid-saturated granular material
G′	Related to effective stress in granular material
k	k-material; $k \in \{\mathrm{S}, \mathrm{F}, \mathrm{G}\} = \{1, \ldots, M\}$
s, sG, sk	Solid phase, in granular material, in k-material
S	Bulk solid; S $\equiv$ sS
T	Transpose of a tensor
uj	Unjacketed
vi	Viscous (rate-dependent) contribution
vol	Volume
α	α-phase; $\alpha \in \{\mathrm{s}, \mathrm{f}\} = \{1, \ldots, N\}$
αk	α-phase in k-material; $\alpha k \in \{\mathrm{S}, \mathrm{F}, \mathrm{sG}, \mathrm{fG}\}$

Latin Symbols

$\boldsymbol{b}, \boldsymbol{b}^{\alpha k}, \langle \boldsymbol{b} \rangle$	Body force per unit mass
$\boldsymbol{c}$	Convective velocity
$\boldsymbol{c}_{\mathrm{fr}}^{\mathrm{G}'}$	Fourth-order material tangent tensor
Co	CFL number
$\boldsymbol{d}, \boldsymbol{d}^{\alpha k}$	Spatial rate of deformation
$\mathrm{d}a, \mathrm{d}v$	Surface area density, volume density
d	Line constant
$\mathcal{D}$	Modeling domain in the ambient space
e	Element
e^{G}	Void ratio
$f, f^k, f^{\alpha k}, f_e$	Volume fractions, of k, αk, in element
$f_{\mathrm{b}}, f_{\mathrm{r}}, f_{\mathrm{t}}, f_{\mathrm{l}}$	Side fractions
$F, F_{e,I}^V, F_{e,I}^f$	Convective flux, of V_e, f_e across $\Gamma_{e,I}$
$\boldsymbol{h}^{\mathrm{G}'}$	Set of material state variables
$H, H^k, H^{\alpha k}$	Volume measures of $\mathcal{H}, \mathcal{H}^k, \mathcal{H}^{\alpha k}$
$\mathcal{H}$	Representative volume element (RVE)
$\mathcal{H}^k, \mathcal{H}^{\alpha k}$	Portions of k, αk in $\mathcal{H}$
I	Local node, vertex, edge
$\boldsymbol{I}$	Second-order unit tensor
J	Jacobian
$K, K^k, K^{\alpha k}, \langle K \rangle$	Bulk modulus
$l_{\mathrm{micro}}, l_{\mathrm{meso}}, l_{\mathrm{macro}}$	Microscale, mesoscale, macroscale
$\boldsymbol{m}$	Volume fraction gradient
M	Number of materials in the mixture
$\mathcal{M}^k$	k-material domain in $\mathcal{D}$
n, n^k, n^{G}	Fluid fraction, porosity
$n_{\mathrm{el}}, n_{\mathrm{en}}, n_{np}$	Number of elements, element nodes, nodal points
$\boldsymbol{n}, \boldsymbol{n}^{\alpha k}$	Outward normals on interface
N	Number of phases in the mixture
$p^{\alpha k}, p^k, \langle p \rangle$	Pressure
$p^{\mathrm{G}'}$	Mean effective stress
$\mathcal{P}^{\alpha}$	α-phase domain in $\mathcal{D}$
$q, q^k, q^{\alpha k}$	Generic spatial field
$\mathbb{R}, \mathbb{R}^2, \mathbb{R}^3$	Real numbers, ambient Euclidian space
s	Slope
$\boldsymbol{s}^k, \boldsymbol{s}^{\alpha k}, \langle \boldsymbol{s} \rangle$	Extra stress
$S_{e,I}$	Surface area of $\Gamma_{e,I}$
t, t^-, t^+	Time
$\boldsymbol{v}, \boldsymbol{v}^k, \boldsymbol{v}^{\alpha k}, \langle \boldsymbol{v} \rangle$	Spatial velocity
$\boldsymbol{v}_{\mathrm{I}}, \boldsymbol{v}_{\mathrm{I}}^{\mathrm{m}}$	Interface velocity
V_e	Element volume
$\boldsymbol{w}$	Mesh velocity

$x, \boldsymbol{x}$	Point in the ambient space
x, y	Spatial coordinate directions; $\boldsymbol{x} = [x, y]^{\mathrm{T}}$
X	Global node number

Greek Symbols

α, β	Slope angle
$\Gamma_I, \Gamma_{e,I}$	Edge, element edge
$\mathbf{\Gamma}^{\alpha k}$	Rate of momentum supply due to drag via $\partial\mathcal{H}^{\alpha k}$
$\delta_{\mathrm{I}}^{\alpha k}$	Dirac delta picking out the αk-interface
$\Delta V_{e,I}, \Delta V_{e,I}^{f}$	Total transport volume, material transport volume
Δt	Time increment
$\Delta x, \Delta y$	Element dimensions
$\dot{\varepsilon}^{\mathrm{sG}}$	Solid phase volumetric strain rate due to $\dot{p}^{\mathrm{fG}}$
ζ^{G}	Biot-Willis coefficient
$\eta_{e,I}^{\star}$	Volume fraction at $\Gamma_{e,I}$
$\Lambda^{\alpha k}$	Rate of mass supply via $\partial\mathcal{H}^{\alpha k}$
$\mu^{\mathrm{fF}}, \mu^{\mathrm{G}'}$	Dynamic shear viscosity
$\mu_{\mathrm{vol}}^{\mathrm{G}'}$	Volume viscosity
$\pi^{\alpha k}$	Volume fraction of α with respect to $\mathcal{H}^{k}$
$\rho, \rho^{k}, \rho^{\alpha k}, \langle\rho\rangle$	Spatial mass density
$\boldsymbol{\sigma}, \boldsymbol{\sigma}^{k}, \boldsymbol{\sigma}^{\alpha k}, \langle\boldsymbol{\sigma}\rangle$	(Cauchy) stress
$\boldsymbol{\sigma}^{\mathrm{G}'}$	Effective stress
$\chi^{k}, \chi^{\alpha}, \chi^{\alpha k}$	Indicator function
$\boldsymbol{\omega}$	Vorticity tensor
Ω_e	Element domain, control volume

Acknowledgments The presented work was carried out under the financial support from the German Research Foundation (DFG; Grant SA 310/26-2) as part of the DFG Research Unit FOR 1136, which is gratefully acknowledged. The authors would like to thank their colleagues in this research unit for collaboration and continuously discussing our work. Special thanks go to Prof. David J. Benson and the Department of Structural Engineering at the University of California, San Diego (UCSD) for the opportunity to undertake collaborative research on MMALE methods.

References

1. Achanta, S., Cushman, J.H., Okos, M.R.: On multicomponent, multiphase thermomechanics with interfaces. Int. J. Eng. Sci. **32**(11), 1717–1738 (1994)
2. Alciatore, D., Miranda, R.: A Winding Number and Point-In-Polygon Algorithm. Glaxo Virtual Anatomy Project Research Report, Department of Mechanical Engineering, Colorado State University, (1995)

3. Ancey, C., Coussot, P., Evesque, P.: A theoretical framework for granular suspensions in a steady simple shear flow. J. Rheol. **43**(6), 1673–1699 (1999)
4. Ancey, C., Evesque, P.: Frictional-collisional regime for granular suspension flows down an inclined channel. Phys. Rev. E **62**(6), 8349–8360 (2000)
5. Ancey, C.: Dry granular flows down an inclined channel: experimental investigations on the frictional-collisional regime. Phys. Rev. E **65**(011304) (2001)
6. Ancey, C.: Plasticity and geophysical flows: a review. J. Non-Newton. Fluid Mech. **142**, 4–35 (2007)
7. Anderson, K.G., Jackson, R.: A comparison of the solutions of some proposed equations of motion of granular materials for fully developed flow down inclined planes. Ind. Eng. Chem. Fundam. **241**, 145–168 (1992)
8. Aubram, D.: Differential Geometry Applied to Continuum Mechanics. In: Veröffentlichungen des Grundbauinstitutes der Technischen Universität Berlin, vol. 44. Shaker Verlag, Aachen (2009). http://opus.kobv.de/tuberlin/volltexte/2009/2270/
9. Aubram, D.: An Arbitrary Lagrangian-Eulerian Method for Penetration into Sand at Finite Deformation. In: Veröffentlichungen des Grundbauinstitutes der Technischen Universität Berlin, vol. 62. Shaker Verlag, Aachen (2013). http://opus4.kobv.de/opus4-tuberlin/frontdoor/index/index/docId/4755
10. Aubram, D.: Development and experimental validation of an arbitrary Lagrangian-Eulerian (ALE) method for soil mechanics. Geotechnik **38**(3),193–204 (2015). http://dx.doi.org/10.1002/gete.201400030
11. Aubram, D.: Homogeneous Equilibrium Model for Geomechanical Multi-Material Flow with Compressible Constituents (in preparation)
12. Aubram, D., Rackwitz, F., Savidis, S.A.: An ALE finite element method for cohesionless soil at large strains: computational aspects and applications. In: Benz, T., Nordal, S. (eds.) Proceedings 7th European Conference on Numerical Methods in Geotechnical Engineering (NUMGE), pp. 245–250. CRC Press, Boca Raton (2010)
13. Aubram, D., Rackwitz, F., Wriggers, P., Savidis, S.A.: An ALE method for penetration into sand utilizing optimization-based mesh motion. Comput. Geotech. **65** 241–249 (2015). http://dx.doi.org/10.1016/j.compgeo.2014.12.012
14. Aubram, D., Rackwitz, F., Savidis, S.A.: Vibro-injection pile installation in sand: part I-interpretation as multi-material flow. In: Triantyfyllidis, Th. (ed) Holistic Simulation of Geotechnical Installation Processes—Numerical and Physical Modelling, pp. 73–102. Springer International Publishing, Switzerland (2015). http://dx.doi.org/10.1007/978-3-319-18170-7_5
15. Bagnold, R.A.: Experiments on a gravity-free dispersion of large solid spheres in a newtonian fluid under shear. Proc. Royal Soc. Lond. A **225**, 49–63 (1954)
16. Barth, T., Ohlberger, M.: Finite volume methods: foundation and analysis. In: Encyclopedia of Computational Mechanics, vol. 1, chap. 15. Wiley, Chichester (2004)
17. Bauer, E.: Calibration of a comprehensive constitutive equation for granular materials. Soils Found. **36**(1), 13–26 (1996)
18. Bedford, A., Drumheller, D.S.: Theories of immiscible and structured mixtures. Int. J. Eng. Sci. **21**(8), 863–960 (1983)
19. Belytschko, T., Liu, W.K., Moran, D.: Nonlinear finite elements for continua and structures. Wiley, Chichester (2000)
20. Bennethum, L.S.: Compressibility moduli for porous materials incorporating volume fraction. J. Eng. Mech. **132**, 1205–1214 (2006)
21. Bennethum, L.S., Cushman, J.H.: Multiscale, hybrid mixture theory for swelling systems-I. Balance laws. Int. J. Eng. Sci. **34**(2), 125–145 (1996)
22. Bennethum, L.S., Cushman, J.H.: Multiscale, hybrid mixture theory for swelling systems-II. Constitutive theory. Int. J. Eng. Sci. **34**(2), 147–169 (1996)
23. Bennethum, L.S., Weinstein, T.: Three pressures in porous media. Transp. Porous Med. **54**, 1–34 (2004)

24. Benson, D.J.: Computational methods in Lagrangian and Eulerian hydrocodes. Comput. Methods Appl. Mech. Eng. **99**, 235–394 (1992)
25. Benson, D.J.: A multi-material Eulerian formulation for the efficient solution of impact and penetration problems. Comput. Mech. **15**, 558–571 (1995)
26. Benson, D.J.: An implicit multi-material Eulerian formulation. Int. J. Numer. Methods Eng. **48**, 475–499 (2000)
27. Benson, D.J.: Volume of fluid interface reconstruction methods for multi-material problems. Appl. Mech. Rev. **55**(2), 151–165 (2002)
28. Benson, D.J.: Momentum advection on unstructured staggered quadrilateral meshes. Int. J. Numer. Methods Eng. **75**, 1549–1580 (2008)
29. Biot, M.A.: General theory of three-dimensional consolidation. J. Appl. Phys. **12**, 155–164 (1941)
30. Biot, M.A., Willis, D.G.: The elastic coefficients of the theory of consolidation. J. Appl. Mech. **24**, 594–601 (1957)
31. Böhrnsen, J.U., Antes, H., Ostendorf, M., Schwedes, J.: Silo discharge: measurement and simulation of dynamic behavior in bulk solids. Chem. Eng. Technol. **27**, 71–76 (2004)
32. Bouré, J.A., Delhaye, J.M.: General equations and two-phase flow modeling Section 1.2. In: Hetsroni, G. (ed.) Handbook of Multiphase Systems. Hemisphere Publishing Corporation, Washington (1982)
33. Bouré, J.A.: Two-phase flow models: the closure issue. Multiph. Sci. Technol. **3**(1–4), 3–30 (1987)
34. Bowen, R.M.: Compressible porous media models by use of the theory of mixtures. Int. J. Eng. Sci. **20**(6), 697–735 (1982)
35. Colella, P., Glaz, H.M., Ferguson, R.E.: Multifluid algorithms for Eulerian finite difference methods. (1997) (unpublished manuscript)
36. Coussot, P., Ancey, C.: Rheophysical classification of concentrated suspensions and granular pastes. Phys. Rev. E **59**(4), 4445–4457 (1999)
37. Cushman, J.H., Bennethum, L.S., Hu, B.X.: A primer on upscaling tools for porous media. Adv. Water Resour. **25**, 1043–1067 (2002)
38. Das, B.M.: Advanced Soil Mechanics, 3rd edn. Taylor & Francis, USA (2008)
39. DeBar, R.B.: Fundamentals of the KRAKEN Code. Technical Report UCID-17366, Lawrence Livermore Laboratory, Livermore, USA (1974)
40. De Boer, R.: Theory Porous Media. Springer, Berlin (2000)
41. Drew, D.A.: Mathematical modeling of two-phase flow. Annu. Rev. Fluid Mech. **15**, 261–291 (1983)
42. Drew, D.A., Passman, S.L.: Theory of Multicomponent Fluids. Springer, New York (1999)
43. Drumheller, D.S.: A theory for dynamic compaction of wet porous solids. Int. J. Solids Struct. **23**, 211–237 (1987)
44. Foley, J.D., van Dam, A., Feiner, S.K., Hughes, J.F.: Computer Graphics: Principles and Practice, 2nd edn. Addison-Wesley Professional, Reading (1995)
45. Forterre, Y., Pouliquen, O.: Flows of dense granular media. Ann. Rev. Fluid Mech. **40**, 1–24 (2008)
46. Freßmann, D., Wriggers, P.: Advection approaches for single-and multi-material arbitrary Lagrangian-Eulerian finite element procedures. Comput. Mech. **39**, 153–190 (2007)
47. Galera, S., Maire, P.-H., Breil, J.: A two-dimensional unstructured cell-centered multi-material ale scheme using VOF interface reconstruction. J. Comput. Phys. **229**, 5755–5787 (2010)
48. Goddard, J.D.: Continuum modeling of granular media. Appl. Mech. Rev. **66**(050801) (2014)
49. Goodman, M.A., Cowin, S.C.: A continuum theory for granular materials. Archive Ration. Mech. Anal. **44**, 249–266 (1972)
50. Greiner, G., Hormann, K.: Efficient clipping of arbitrary polygons. ACM Trans. Gr. **17**(2), 71–83 (1998)
51. Gudehus, G.: A comprehensive constitutive equation for granular materials. Soils Found. **36**(1), 1–12 (1996)

52. Gueyffier, D., Li, J., Nadim, A., Scardovelli, R., Zaleski, S.: Volume-of-fluid interface tracking with smoothed surface stress methods for three-dimensional flows. J. Comput. Phys. **152**(2), 423–456 (1999)
53. Haines, E.: Point in Polygon Strategies. In: Graphics Gems, vol. IV, pp. 24–46. Academic Press, Boston (1994)
54. Hassanizadeh, M., Gray, W.G.: General conservation equations for multi-phase systems: 1 averaging procedure. Adv. Water Resour. **2**, 131–144 (1979)
55. Hassanizadeh, M., Gray, W.G.: Mechanics and thermodynamics of multiphase flow in porous media including interphase boundaries. Adv. Water Resour. **13**(4), 169–186 (1990)
56. Häussler, U., Eibl, J.: Numerical investigations on discharging silos. J. Eng. Mech. **110**(6), 957–971 (1984)
57. Hirt, C.W., Amsden, A.A., Cook, J.L.: An arbitrary Lagrangian-Eulerian computing method for all flow speeds. J. Comput. Phys. **14**, 227–253 (1974)
58. Hirt, C.W., Nichols, B.D.: Volume of fluid (VOF) method for the dynamics of free boundaries. J. Comput. Phys. **39**, 201–225 (1981)
59. Hutter, K., Rajagopal, K.R.: On flows of granular materials. Contin. Mech. Thermodyn. **6**, 81–139 (1994)
60. Hutter, K., Svendsen, B., Rickenmann, D.: Debris flow modeling: a review. Contin. Mech. Thermodyn. **8**, 1–35 (1996)
61. Hwang, H., Hutter, K.: A new kinetic model for rapid granular flow. Contin. Mech. Thermodyn. **7**, 357–384 (1995)
62. Hyman, J.M.: Numerical methods for tracking interfaces. Physica D **12**, 396–407 (1984)
63. Iverson, R.M.: The physics of debris flows. Rev. Geophys. **35**(3), 245–296 (1997)
64. Iverson, R.M., Denlinger, R.P.: Flow of variably fluidized granular masses across three-dimensional terrain. 1. Coulomb mixture theory. J. Geophys. Res. **106**(B1), 537–552 (2001)
65. Johnson, P.C., Jackson, R.: Frictional-collisional constitutive relations for granular materials, with application to plane shearing. J. Fluid Mech. **176**, 67–93 (1987)
66. Jop, P., Forterre, Y., Pouliquen, O.: A constitutive law for dense granular flows. Nature **441**, 727–730 (2006)
67. Kim, D.H., Kim, M.-J.: An extension of polygon clipping to resolve degenerate cases. Comput.-Aided Des. Appl. **3**(1–4), 447–456 (2006)
68. Kolymbas, D.: Const. Model. Granul. Mater. Springer, Berlin Heidelberg (2000)
69. Kramer, S.L., Byers, M.B., Wang, C.H.: Experimental measurement of the residual strength of particulate materials. In: Lade, P.V., Yamamuro, J.A. (eds.) Physics and Mechanics of Soil Liquefaction, pp. 249–260. A.A. Balkema, Rotterdam, The Netherlands (1999)
70. LeVeque, R.J.: Finite Volume Methods for Hyperbolic Problems, 3rd edn. Cambridge University Press, Cambridge (2002)
71. Lewis, R.W., Schrefler, B.A.: The Finite Element Method in the Static and Dynamic Deformation and Consolidation of Porous Media, 2nd edn. Wiley, Chichester (1998)
72. Li, X.S.: A sand model with state-dependent dilatancy. Géotechnique **52**(3), 173–186 (2002)
73. Locat, J., Lee, H.J.: Submarine landslides: advances and challenges. Can. Geotech. J. **39**, 193–212 (2002)
74. Luttwak, G., Rabie, R.L.: The Multi Material Arbitrary Lagrangian Eulerian Code MMALE and Its Application to Some Problems of Penetration and Impact. Technical Report LA-UR-85-2311, Los Alamos National Laboratory, Los Alamos, New Mexico (1985)
75. Mair, H.U.: Review: hydrocodes for structural response to underwater explosions. Shock Vibr. **6**, 81–96 (1999)
76. Malvern, L.E.: Introduction to the Mechanics of a Continuous Medium. Prentice Hall, New Jersey (1969)
77. Manzari, M.T., Dafalias, Y.F.: A critical state two-surface plasticity model for sands. Géotechnique **47**(2), 255–272 (1997)
78. Masson, D.G., Harbitz, C.B., Wynn, R.B., Pedersen, G., Løvholt, F.: Submarine landslides: processes, triggers and hazard prediction. Philos. Trans. Royal Soc. Lond. A **364**, 2009–2039 (2006)

79. McGlaun, J.M., Thompson, S.L.: CTH: a three-dimensional shock wave physics code. Int. J. Impact Eng. **10**, 351–360 (1990)
80. Miller, G.H., Puckett, E.G.: A high-order Godunov method for multiple condensed phases. J. Comput. Phys. **128**, 134–164 (1996)
81. Ming, H.Y., Li, X.S.: Fully coupled analysis of failure and remediation of lower San Fernando Dam. J. Geotech. Geoenviron. Eng. **129**(4), 336–348 (2003)
82. Mooney, M.: The viscosity of a concentrated suspension of spherical particles. J. Colloid Sci. **6**(2), 162–170 (1951)
83. Niemunis, A., Herle, I.: Hypoplastic model for cohesionless soils with elastic strain range. Mech. Cohesive-Frictional Mater. **2**, 279–299 (1997)
84. Nikolinakou, M.A., Whittle, A.J., Savidis, S.A., Schran, U.: Prediction and interpretation of the performance of a deep excavation in Berlin sand. J. Geotech. Geoenviron. Eng. **137**(11), 1047–1061 (2011)
85. O'Rourke, J.: Comput. Geom. C, 2nd edn. Cambridge University Press, New York (1998)
86. Passman, S.L., Nunziato, J.W., Bailey, P.B., Reed, K.W.: Shearing motion of a fluid-saturated granular material. J. Rheol. **30**(1), 167–192 (1986)
87. Pastor, M., Zienkiewicz, O.C., Chan, A.H.C.: Generalized plasticity and the modelling of soil behaviour. Int. J. Numer. Anal. Methods Geomech. **14**, 151–190 (1990)
88. Peery, J.S., Carroll, D.E.: Multi-material ALE methods in unstructured grids. Comput. Methods Appl. Mech. Eng. **187**, 591–619 (2000)
89. Pilliod, J.E., Puckett, E.G.: Second-order accurate volume-of-fluid algorithms for tracking material interfaces. J. Comput. Phys. **199**, 465–502 (2004)
90. Pudasaini, S.P., Wang, Y., Hutter, K.: Modelling debris flows down general channels. Nat. Hazards Earth Syst. Sci. **5**, 799–819 (2005)
91. Pudasaini, S.P.: A general two-phase debris flow model. J. Geophys. Res. **117**(F03010) (2012)
92. Rackwitz, F., Savidis, S.A.: Numerische Untersuchungen zum Tragverhalten von Zugpfählen in Berliner Sand. Bauingenieur **79**(9), 375–383 (2004)
93. Rider, W.J., Kothe, D.B.: Reconstructing volume tracking. J. Comput. Phys. **141**, 112–152 (1998)
94. Rider, W.J., Love, E., Wong, M.K., Strack, O.E., Petney, S.V., Labreche, D.A.: Adaptive methods for multi-material ALE hydrodynamics. Int. J. Numer. Methods Fluids **65**, 1325–1337 (2011)
95. Rudman, M.: Volume-tracking methods for interfacial flow calculations. Int. J. Numer. Methods Fluids **24**(7), 671–691 (1997)
96. Savage, S.B., Hutter, K.: The motion of a finite mass of granular material down a rough incline. J. Fluid Mech. **199**, 21–24 (1989)
97. Savidis, S.A., Aubram, D., Rackwitz, F.: Arbitrary Lagrangian-Eulerian finite element formulation for geotechnical construction processes. J. Theor. Appl. Mech. **38**(1–2), 165–194 (2008)
98. Savidis, S.A., Aubram, D., Rackwitz, F.: Vibro-injection pile installation in sand: part ii-numerical and experimental investigation. In: Triantyfyllidis, Th. (ed): Holistic Simulation of Geotechnical Installation Processes—Numerical and Physical Modelling, pp. 103–131. Springer, 2015. http://dx.doi.org/10.1007/978-3-319-18170-7_6
99. Sawicki, A., Mierczyński, J.: Developments in modeling liquefaction of granular soils, caused by cyclic loads. Appl. Mech. Rev. **59**, 91–106 (2006)
100. Scardovelli, R., Zaleski, S.: Direct numerical simulation of free-surface and interfacial flow. Ann. Rev. Fluid Mech. **31**, 567–603 (1999)
101. Schneider, P.J., Eberly, D.H.: Geometric Tools for Computer Graphics. Morgan Kaufmann (2003)
102. Schofield, A.N., Wroth, C.P.: Critical State Soil Mechanics. McGraw-Hill, New York (1968)
103. Shashkov, M.: Closure models for multimaterial cells in arbitrary Lagrangian-Eulerian hydrocodes. Int. J. Numer. Methods Fluids **56**(8), 1497–1504 (2008)
104. Seed, H.B., Lee, K.L., Idriss, I.M., Makdisi, F.I.: The slides in the San Fernando Dams during the earthquake of February 9, 1971. J. Geotech. Eng. Division, ASCE **101**(7), 651–688 (1975)

105. Seed, R.B., Cetin, K.O., Moss, R.E.S., Kammerer, A.M., Wu, J., Pestana, J.M., Riemer, M.F., Sancio, R.B., Bray, J.D., Kayen, R.E., Faris, A.: Recent Advances in Soil Liquefaction Engineering: A Unified and Consistent Framework. Technical Report EERC 2003–2006, University of California, Berkeley, California, USA (2003)
106. Sunday, D.: Fast polygon area and Newell normal computation. J Gr. Tools **7**(2), 9–13 (2002). http://geomalgorithms.com
107. Sunday, D.: Geometry Algorithms: Line and Segment Intersections. http://geomalgorithms.com/a05-_intersect-1.html, June 2015
108. Sutherland, I.E., Hodgman, G.W.: Reentrant polygon clipping. Commun. ACM **17**(1), 32–42 (1974)
109. Taiebat, M., Dafalias, Y.F.: SANISAND: simple anisotropic sand plasticity model. Int. J. Numer. Anal. Methods Geomech. **32**, 915–948 (2008)
110. Terzaghi, K.: Theor. Soil Mech. Wiley, New York (1943)
111. Triantafyllidis, Th: Cyclic Behaviour of Soils and Liquefaction Phenomena. A.A. Balkema, The Netherlands (2004)
112. Triantafyllidis, Th.: Holistic Simulation of Geotechnical Installation Processes—Numerical and Physical Modelling, vol. 77. In: Lecture Notes in Applied and Computational Mechanics. Springer, Switzerland (2015). http://dx.doi.org/10.1007/978-3-319-18170-7
113. Truesdell, C., Toupin, R.A.: Encyclopedia of Physics. Bd. III/1: The Classical Field Theories, pp. 226–793. Springer, Berlin (1960)
114. Truesdell, C., Noll, W.: The Non-Linear Field Theories of Mechanics, 3rd edn. Springer, Berlin (2004)
115. von Wolffersdorff, P.-A.: A hypoplastic relation for granular materials with a predefined limit state surface. Mech. Cohesive-Frictional Mater. **1**, 251–271 (1996)
116. Wang, Y., Hutter, K.: A constitutive model of multiphase mixtures and its application in shearing flows of saturated solid-fluid mixtures. Granul. Matter **1**, 163–181 (1999)
117. Wriggers, P.: Nonlinear Finite Element Methods. Springer, Berlin (2008)
118. Youngs, D.L.: Time-dependent multi-material flow with large fluid distortion, pp. 273–285. In: Morton, K.W., Baines, M.J. (eds.) Numerical Methods for Fluid Dynamics. Academic Press, London (1982)
119. Youngs, D.L.: An Interface Tracking Method for a 3D Eulerian Hydrodynamics Code. Technical Report AWRE/44/92/35, Atomic Weapons Research Establishment, Aldermaston, UK (1987)
120. Zienkiewicz, O.C., Chan, A.H.C., Pastor, M., Paul, D.K., Shiomi, T.: Static and dynamic behaviour of soils: a rational approach to quantitative solutions. I. Fully saturated problems. Proc. Royal Soc. Lond. A **429**, 285–309 (1990)
121. Zienkiewicz, O.C., Chan, A.H.C., Pastor, M., Schrefler, B.A., Shiomi, T.: Computational Geomechanics—With Special Reference to Earthquake Engineering. Wiley, Chichester (1999)

Prediction of Construction-Induced Deformations of Deep Excavation Walls by the Use of a Holistic 3D-Finite-Element Model

Andrea Thom and Achim Hettler

Abstract In the course of research group FOR 1136 GEOTECH the task of subproject 8 (TP 8, part II) is to generate a holistic three-dimensional finite-element model to give improved predictions of construction-induced deformations of deep excavation walls. For this purpose, the results of the other subprojects dealing with contact elements, describing material behaviour and the modelling of soil liquefaction around a vibrating pile should be implemented. This contribution presents the framework of the 3D-model, in which the results of the other subprojects can be adopted at a later stage. The deep excavation at Potsdamer Platz in Berlin in the 1990s serves as reference for the model, since unexpected deformations of the diaphragm walls arised after pile driving. First numerical studies are presented to demonstrate the possibilities of the model.

Keywords Finite-element modelling · Construction-induced deformations

1 Introduction

In October 1993, a broad construction process was started in the inner city of Berlin. After the destruction in World War 2, the Potsdamer Platz became again a centre for economy, culture and tourism. The required logistics like parking lots, delivery channels and technical facilities were realized with several floors underground. Large and deep excavation pits with a span up to 200 m and depth up to 25 m were needed. Since the groundwater level is only 3–4 m below surface in the inner city of Berlin, the excavations were constructed as trough-type excavations with an anchored underwater concrete bottom slab and tied-back diaphragm walls. As there was limited experience for such oversized excavations, comprehensive measurement devices were installed for monitoring and quality management in one of them. Figure 1 shows the ground

A. Thom (✉) · A. Hettler
Chair of Soil Mechanics and Foundation Engineering, TU Dortmund University, Dortmund, Germany
e-mail: andrea.thom@tu-dortmund.de

T. Triantafyllidis (ed.), *Holistic Simulation of Geotechnical Installation Processes*, Lecture Notes in Applied and Computational Mechanics 80, DOI 10.1007/978-3-319-23159-4_11

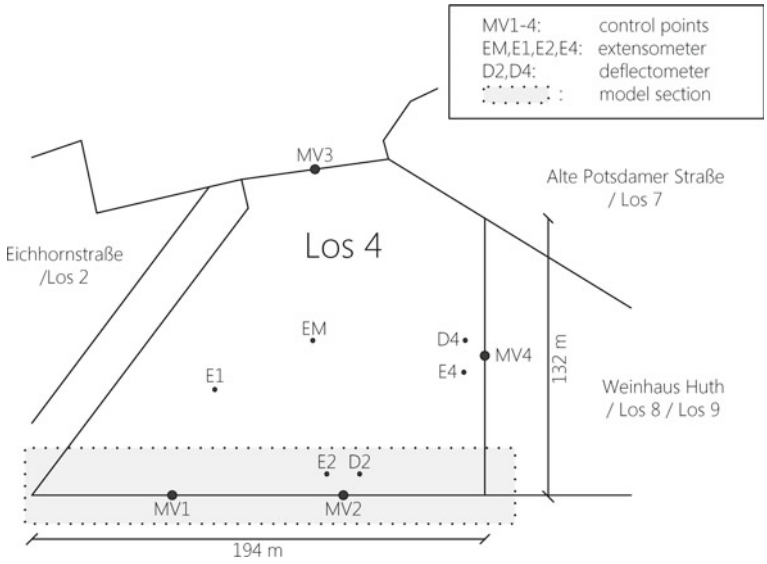

Fig. 1 Ground plan of instrumented Debis excavation section (Los 4) with control points and marked model section, cf. [11]

plan of the instrumented Debis excavation with the installation of the control points. For more detailed information see [11].

The construction process of the pits can be divided into different phases as illustrated in Fig. 2. As it turned out, the installation of the so-called vibrated RI-piles (H-section steel profiles vibrated into the ground) caused horizontal displacements of the diaphragm wall, which were up to 4 times higher than predicted by a classical analysis carried out in advance, cf. [11]. Figure 3 shows the development of the horizontal displacements at the control points MV1 and MV2 compared with the cross-section of the excavation and diaphragm wall. The significant difference

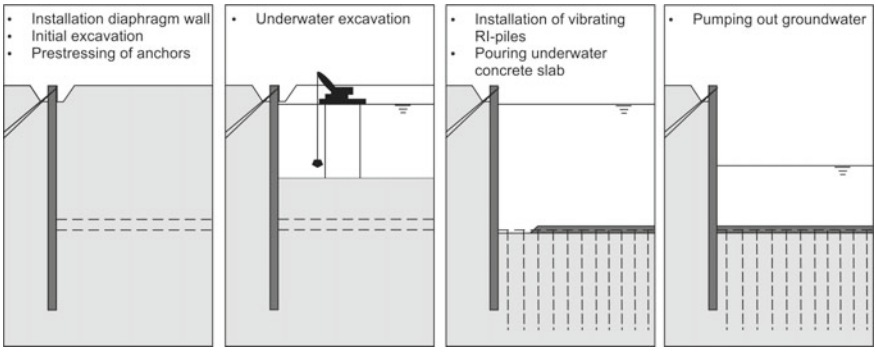

Fig. 2 Staged construction process

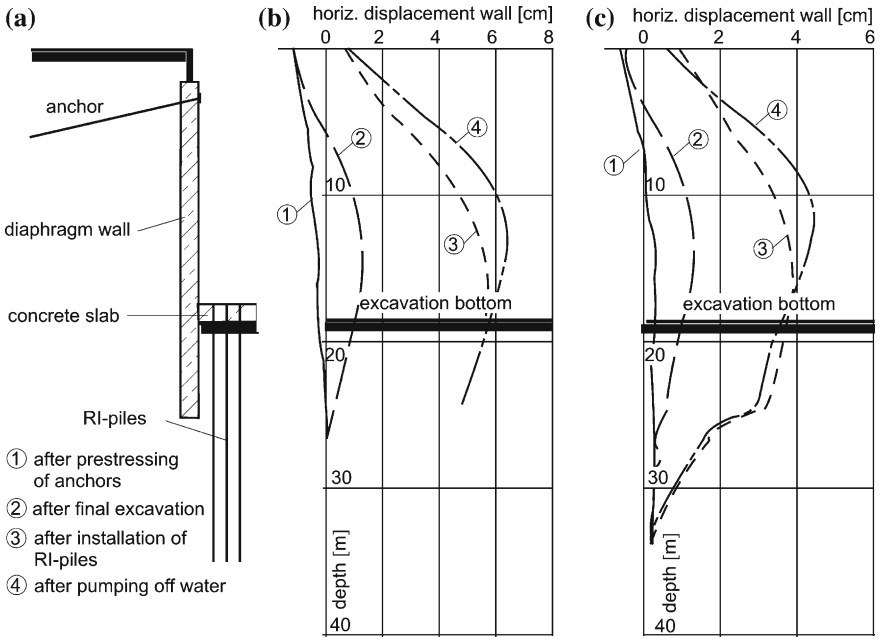

Fig. 3 Debis excavation at Potsdamer Platz. **a** Cross-section of excavation, **b** displacements in cross-section MV1, **c** displacements in cross-section MV2, cf. [4]

between the displacements at MV1 and MV2 can not be explained by different geologies, but with the installation direction of the piles: at MV1, the piles were installed parallel to the wall; on the contrary they were installed orthogonal to the wall at MV2. An explanation for the unexpected horizontal displacements is soil liquefaction. The installation of bored or vibrated piles close to retaining walls can lead to a temporary softening of the soil caused by a temporary increase of the pore pressure, cf. [11].

This contribution reports about the development of a holistic 3D-finite-element model for an improved prediction of construction-induced deformations. For that, the different construction stages

- Installation of diaphragm wall
- Initial excavation
- Prestressing of anchors
- Final excavation
- Installation of vibrated RI-piles

are taken into consideration with some simplifications. The diaphragm wall is modelled as 'wished-in-place' loaded with its own weight, since the modelling of the detailed installation is not crucial for this investigation, see also [2, 8]. The prestressing of anchors is replaced in that way that displacements are impeded in normal direction at the relevant nodes at the diaphragm wall. The simplified modelling of the installation of the RI-piles is described in Sect. 3.1.

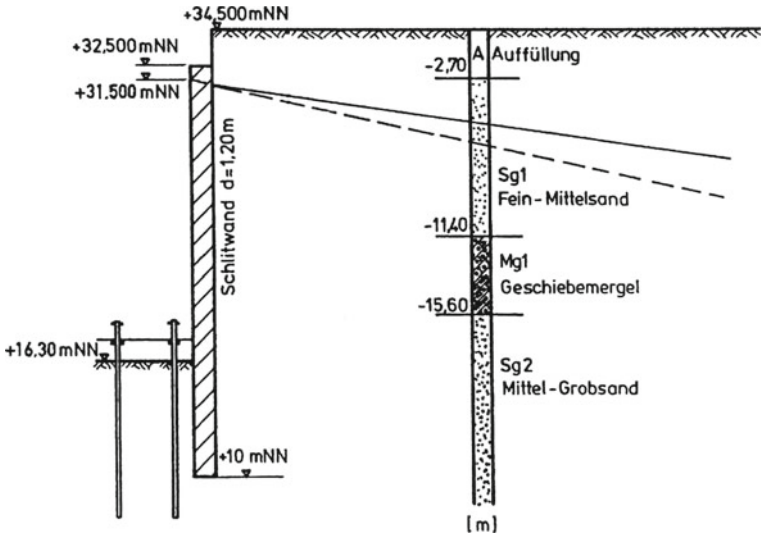

Fig. 4 Cross-section of excavation and soil profile, cf. [12]

2 Geological Situation and Structure of Excavation

Figure 4 shows the soil profile of typical Berlin sands. The soil consists of two sand layers (Sg1 and Sg2), which are separated by a layer of boulder clay (Mg1) with a thickness of 4.2 m.

The groundwater level in the greater area of Berlin is at approximately 3–4 m below ground level, so that the basement has to be protected against surrounding ground water in a long-term manner, and the excavation pits were constructed in a trough design. Therefore, diaphragm walls with a thickness of 1.2 m were installed with an embedment depth of 6.3 m at the foot of the wall, see Fig. 4. The walls were tied back with a single-anchor row 1.0 m below top edge at an interval of 0.6–0.9 m with an initial prestressing of 1 MN. The underwater concrete slab was made of steel fibre concrete with a thickness of 1.2 m; for buoyancy protection, the slab was anchored by vibrated RI-piles based on a 3×3 m grid. The excavation depth at the investigated cross-section is 18.2 m.

3 Numerical Model and Simulation

The 3D-model is created with the finite-element-programm *ABAQUS*. Figure 1 shows the relevant section of the diaphragm wall including the monitoring positions. In order to keep the model in a manageable scope, only a part of the section is modelled. This is reasonable, since the modelling of the total length of 194 m

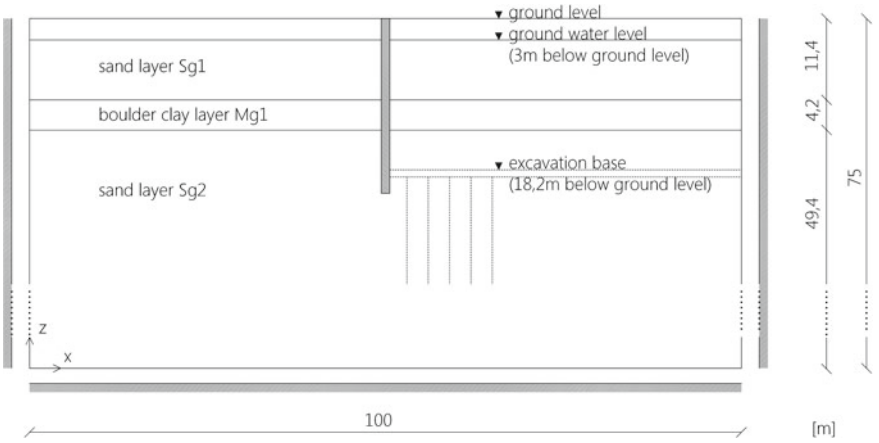

Fig. 5 Cross-section of static system of 3D-FE model in the x–z-plane

would not reveal further influences in the longitudinal direction. Figure 5 displays the cross-section of the chosen model section. In accordance to the recommendations of the DGGT (Deutsche Gesellschaft für Geotechnik), cf. [9], the dimension of the model was chosen with $100 \times 75 \times 47$ m (width × depth × length) in order to minimize the influences of the boundary conditions on the field quantities. Except for the positive x–y-plane, the whole model is fixed in perpendicular direction at the exterior surfaces.

After generating the undeformed geostatic state (geostatic step) and activating the diaphragm wall with its weight, the soil elements are deactivated stepwise. The first step comprises the elements to the anchor row 3 m below ground level; after that, all elements until the bottom slab are deactivated. Between these two steps, the anchor row is activated and modelled with fixed degrees of freedom in normal direction of the diaphragm wall. Since the soil is unilaterally relieved through the excavation, different vertical movements in the range of the diaphragm wall are expected. For that, a contact surface is defined, which allows independent displacements to both sides of the soil, see Fig. 6. The normal and tangential forces are transmitted using the friction law by Mohr-Coulomb. The horizontal x–y-plane between soil and excavation is fixed via the multiple-constraint condition, so that no relative movement can occur.

In order to check the model performance, we start with a hypoplastic material law for the description of the soil behaviour according to von Wolffersdorff [13], whereby the extension of intergranular strain according to Niemunis and Herle [7] is used. Thereafter the new developed material routines like Neo-Hypoplasticity or ISA will be adopted. The material parameters for Berlin sand are taken from Mayer [6]. The diaphragm wall is modelled using a linear-elastic material law. The soil layers are modelled with 3D continuum elements (C3D8R), whereas the diaphragm wall is modelled with shell elements (S4R). Figure 7 shows the calculated horizontal displacements after the final excavation step (Fig. 3, stage 2). One can see, that the

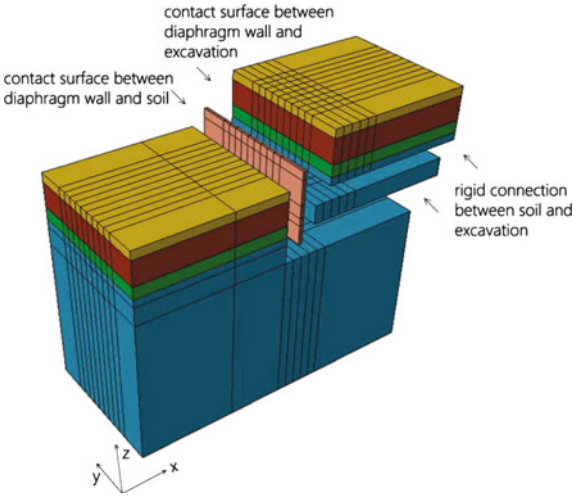

Fig. 6 Overview of the 3D-FE model and chosen contact surfaces

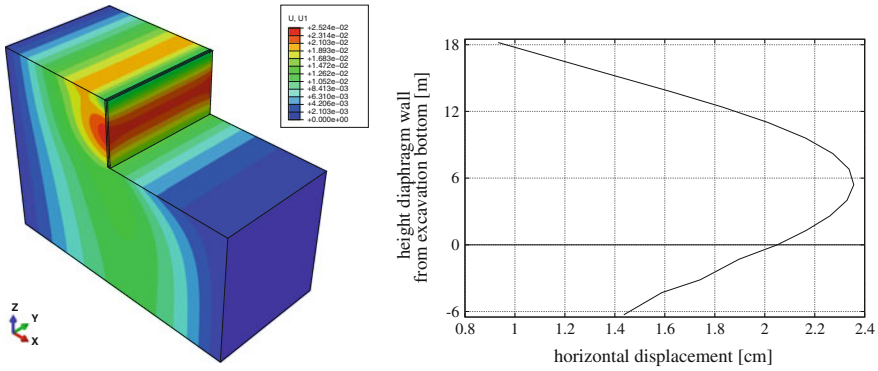

Fig. 7 Horizontal displacements u1 (positive x-direction) after final excavation step

diaphragm wall already deflected with horizontal displacements of approximately 2.4 cm, which is about 1.0 cm more than the measured ones, but the course of deflection is in good agreement. The overestimation of the displacements can be explained by the fact that the prestressing of anchors is replaced by the simplified modelling with fixed nodal displacements (activated after the initial excavation step), whereby the nodes at the geometric location of the anchors already shifted with about 1.0 cm during the initial excavation step. This configuration serves as the initial state for the next step, the installation of the RI-piles, for which also some simplifying assumptions have to be made as described in the following.

3.1 RI-Piles 'Wished-in-Place' with Dynamic Loading

Approaching the realistic procedure of vibrating RI-piles by performing a dynamic simulation is one variant for the holistic 3D-Model. Grabe et al. performed two- and three-dimensional simulations of vibrating a single RI-pile, also dealing with conditions as at Potsdamer Platz, see [1, 3]. For the requirements of TP 8 in FOR 1136 this methodical approach is not expedient, since the detailed meshing and detailed pile driving is not manageable with the large 3D-model. Dimensions of 1 mm to 30 cm of the pile-mesh would not match with element dimensions of the overall model with edge lengths up to 1–5 m.

Hence, the RI-piles are modelled 'wished-in-place' with a dynamic loading representing the vibration frequency in undrained conditions. For that, a vertical row of nodes at the geometric location of the pile (Fig. 9) is loaded with a speed-controlled amplitude, which is equivalent to a path-controlled amplitude of 2 mm in vertical z-direction, see Fig. 8, left. Applying a speed-controlled amplitude was necessary, since an amplitude of 2 mm should be applied on the pre-deformed soil of about 4 mm. The sinusoidal vibration frequency is equal to the realistic vibration frequency of $f = 34$ Hz. The pile driving was simulated for 0.25 s with a fixed increment size of 0.0005 s. This led to a calculation time on a i7-2600 processor (3.4 GHz, 16 GB RAM) of 15 h. Figure 8 (right) also displays the additional horizontal displacements of the diaphragm wall calculated during the dynamic step evaluated at node P1, marked in Fig. 9. It can be said that the model shows a good tendency to approach the additional displacements caused by the dynamic loading of the RI-piles, even though the simulation time of 0.25 s is not even approaching the realistic pile driving time of 20–30 min.

Considering the calculation time, the dynamic simulation of the RI-piles is not expedient, since a whole group of piles should be simulated for studies of the pile driving parallel or orthogonal to the wall and its effects on the pore pressure. Hence, an alternative for the simulation of the piles is considered, see Sect. 4.

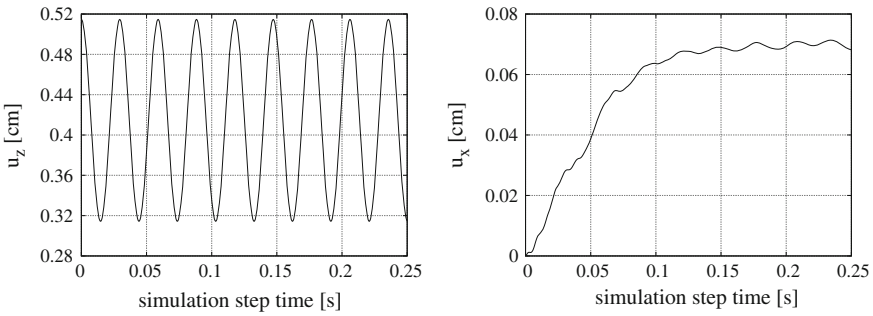

Fig. 8 *Left* Dynamic loading versus simulation time (amplitude = 2 mm, $f = 34$ Hz). *Right* Relative horizontal displacements Δu_x at node P1 of diaphragm wall caused by pile driving versus simulation time

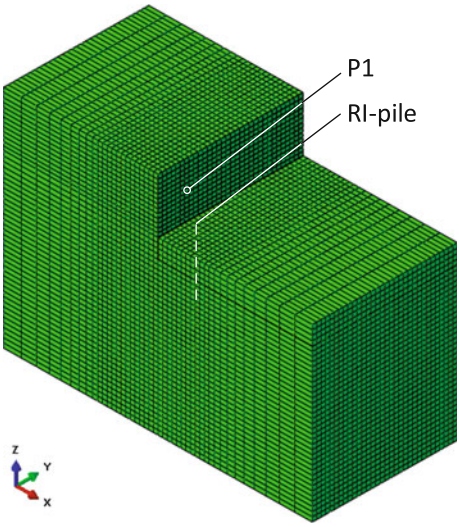

Fig. 9 Overview of model with evaluation point P1 and location of nodes for dynamic loading

4 Discussion and Outlook

Since the vibrating of the RI-piles caused the largest part of the horizontal displacements at the diaphragm walls at Berlin, Potsdamer Platz, a focus is laid on modelling this construction step. Applying a path-controlled amplitude as a dynamic loading on a nodal row is a promising approach which led to suitable first results. But in consideration of the fact, that comprehensive numerical studies of pile groups should be performed, the calculation time is a problem, so that an alternative is required.

As described in Sect. 1 a temporary softening of the soil caused by a temporary increase of the pore pressure is expected to be the reason for the additional horizontal displacements during the pile driving. Thus, as a possible approach, the modelling of the piles can be simplified by taking the soil liquefaction around the vibrating pile as a boundary condition for the pore pressure in a quasi-static analysis. The pile itself is not modelled anymore. With this, the long calculation time of the dynamic step can be avoided, but still the assumed reason for the additional displacements is investigated. This approach is currently being pursued and first investigations look promising.

Once the final step of simulating the pile driving in an appropriate manner is accomplished, the model should be enhanced by using contact elements provided by the research group as well as an improved hypoplastic material law. The model then should be investigated and evaluated under drained and undrained conditions.

References

1. Grabe, J., Henke, S., Schürmann, B.: Numerische Simulation von Rammarbeiten im Erdwiderstandsbereich von Baugrubenwänden. Bautechnik **84**(8), 519–524 (2007)
2. Grandas Tavera, C.-E.: A study on failure modes of corner slurry trenches using anisotropic visco-hypoplasticity. Veröffentlichungen des Instituts für Bodenmechanik und Felsmechanik der Universität Karlsruhe, Heft **178** (2013)
3. Henke, S., Grabe, J.: Simulation der Pfahleinbringung mittels dreidimensionaler Finite-Elemente-Analysen. Vorträge zum 14. Darmstädter Geotechnik-Kolloquium. Mitteilungen des Instituts und der Versuchsanstalt für Geotechnik der Technischen Universität Darmstadt, H. 76, 155–166 (2007)
4. Hettler, A., Triantafyllidis, Th.: Deformations of deep excavation walls induced by construction processes. In: Proceedings of 17th International Conference on Soil Mechanics and Geotechnical Engineering (ICSMGE), pp. 2457–2460. Millpress, IOS Press, Amsterdam, vol. III (2009)
5. Hettler, A., Borchert, K.-M.: Herstellbedingte Verformungen bei tiefen Baugruben. In: Baugrundtagung München, pp. 35–42. Deutsche Gesellschaft für Geotechnik (Hrsg.) (2010)
6. Mayer, P.-M.: Verformungen und Spannungsänderungen im Boden durch Schlitzwandherstellung und Baugrubenaushub. Veröffentlichungen des Instituts für Bodenmechanik und Felsmechanik der Universität Karlsruhe, Heft **151** (2001)
7. Niemunis, A., Herle, I.: Hypoplastic model for cohesionless soils with elastic strain range. Mech. Cohesive-Frictional Mater. **2**, 279–299 (1997)
8. Schäfer, R.: Einfluss der Herstellungsmethode auf das Verformungsverhalten von Schlitzwänden in weichen bindigen Böden. Schriftenreihe des Instituts für Grundbau und Bodenmechanik der Ruhr-Universität Bochum, Heft **36** (2004)
9. Schanz, T.: Standsicherheitsberechnungen von Baugruben - Berechnungsbeispiele. Geotechnik **29**(4), 359–369 (2006)
10. Schran, U.: Untersuchung zu Verschiebungen von Schlitzwänden beim Unterwasseraushub in Berliner Sanden. Veröffentlichungen des Grundbauinstituts der TU Berlin, Heft **23** (2003)
11. Triantafyllidis, Th.: Neue Erkenntnisse aus Messungen an tiefen Baugruben am Potsdamer Platz in Berlin. Bautechnik **75**(3), 133–154 (1998)
12. Triantafyllidis, Th.: Ein einfaches Modell zur Abschätzung von Setzungen bei der Herstellung von Rüttelinjektionspfählen. Bautechnik **77**(3), 161–168 (2000)
13. von Wolffersdorff, P.-A.: A hypoplastic relation for granular materials with a predefined limit state surface. Mech. Cohesive-Frictional Mater. **1**, 251–271 (1996)

Mesoscale Modeling and Properties of Clay Aggregates

Andrew J. Whittle, Davoud Ebrahimi and Roland J.-M. Pellenq

Abstract The clay phase of many natural soils comprises a micro-structure of clay aggregates. These can be formed during sedimentation, due to van der Waals attraction between negatively charged particle surfaces in saltwater environments, or can occur in partially saturated soils where colloidal iron acts as a cementing agent. In order to understand the formation of clay aggregates and their role in affecting properties at the macroscale/continuum level, we have carried out multiscale analyses, initially considering the formation and properties of the aggregates. Nanoscale numerical simulations consider interactions between two clay platelets. The analyses focus on Wyoming montmorillonite (Na-smectite) and use the CLAYFF force field to describe pairwise interactions between ions within the clay and surrounding bulk water (i.e., Coulombic and van der Waals forces). The analyses establish the potential of mean force at different spacings between the layers for edge-to-edge and face-to-face interactions. The results are then used to calibrate the Gay-Berne (GB) potential that represents each platelet as a single-site ellipsoidal body. It is then possible to simulate the process of aggregation for an assembly of clay platelets in mesoscale simulations. These simulations find that aggregates of Na-smectite typically form in face-to-face stacks with 3–8 platelets. The particle assemblies become more ordered

A.J. Whittle (✉) · D. Ebrahimi · R.J.-M. Pellenq
Department of Civil and Environmental Engineering ,
Massachusetts Institute of Technology, Cambridge, MA 02139, USA
e-mail: ajwhittl@mit.edu

R.J.-M. Pellenq
Centre Interdisciplinaire de Nanosciences de Marseille, Aix-Marseille Université, CNRS,
Campus de Luminy, 13288 Marseille Cedex 09, France

R.J.-M. Pellenq
<MSE>^{2}, UMI 3466, CNRS-MIT, Cambridge, MA 02139, USA

T. Triantafyllidis (ed.), *Holistic Simulation of Geotechnical Installation Processes*, Lecture Notes in Applied and Computational Mechanics 80, DOI 10.1007/978-3-319-23159-4_12

and exhibit more pronounced elastic anisotropy at higher confining pressures. The computed elastic stiffness properties are in good agreement with previously measured nanoindentation moduli over a wide range of clay-packing densities.

Keywords Multiscale analysis · Mesoscale modeling · Potential of mean force · Clay aggregates · Elastic stiffness

1 Introduction

It is well established that clays and sands both behave as particulate materials, and that their macroscopic (continuum) engineering properties derive from the 'micro-scale' particle interactions. For coarse-grained granular soils (i.e., sand and gravel size fractions with particle length scales O(mm)), major advances in understanding mechanical behavior have been achieved through grain-scale discrete analysis methods (notably the Discrete Element Method; DEM [5]). These methods are able to represent the evolution of particle contacts for complex particle shapes and distributions and assume relatively simple constitutive laws at particle contacts (elastic Hertzian contact and Coulomb friction), while more complex models of comminution have also been introduced to represent particle crushing [17]). While particle analyses provide direct insights into the behavior of granular systems, they become prohibitively expensive (computationally) when representing the massive numbers of particles often needed for practical engineering problems (length scales O(m-km)). This has led to extensive recent research on a variety of multiscale methods for bridging between the micro- and macroscale systems including hierarchical methods that use information from small scale within larger scale (FEM) models (e.g., coupling between DEM and finite element methods (FEM) (e.g., [19]) to concurrent methods where models at different scales are run concurrently (e.g., [2]).

In comparison to the work on granular soils, there has been much less progress in understanding the behavior of clays as particulate materials. This is due in large part, to the complex surface properties of clay minerals and resulting surface/interfacial forces (e.g., surface charges, interactions with water and dissolved ions to form electrical double layers). It is well known that the fine-grained cohesive soils exhibit multimodal particle size distributions when formed through sedimentation in marine or coastal environments. For example, [15] report that volume fractions of particles in a coastal sediment (measured by in situ laser scattering), Fig. 1a, can be characterized by four levels of PSDs (described by log-normal distribution functions) ranging from primary particles (0.2–2.5 μm) to microflocs or 'floccules' (10–20 μm), macrofloc (20–200 μm), and megaflocs (>200 μm). Lee et al. [15] note that the primary particles include clays, organic matter, plankton, and bacteria, while the flocculi consist of strongly bound clay minerals. Figure 1b shows the representative microstructure of weathered Old Alluvium (tropical residual soil) reported by [26, 27] using a combination of environmental scanning electron microscopy, selective chemical dissolution and particle size analyses, and Cation Exchange Capacity. Although the geological

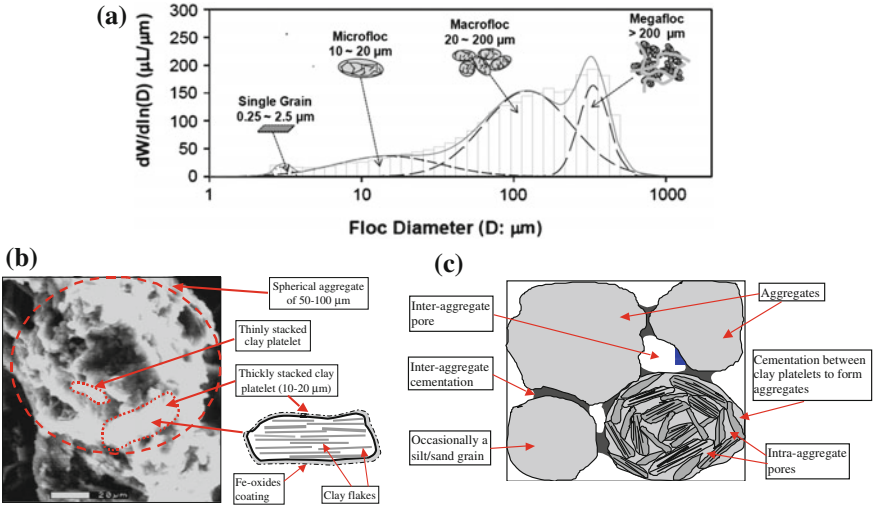

Fig. 1 Multimodal characteristics of fine-grained cohesive soils. **a** Multimodel PSD of coastal sediment (reproduced with permission from [15]. Copyright 2012 by the American Geophysical Union). **b** ESEM observations of weathered Old Alluvium. **c** Representative microstructure of weathered Old Alluvium (**b** and **c** reproduced with permission from [27]. Copyright 2004 by Thomas Telford Ltd.)

origins of the Old Alluvium differ markedly from the coastal zone, the basic building block consists of aggregates of clay platelets (10–20 μm) that are cemented by iron oxides and clustered to form a higher level of macroaggregates (50–100 μm). Both sets of observations suggest that the essential building blocks or essential primary structural units are the flocculi or aggregates of clay platelets that are strongly bound together.

Bottom-up modeling of clay behavior usually proceeds by considering the interaction between individual clay layers. All clay minerals are phyllo-silicates comprising two-dimensional sheets of silicon tetrahedra and aluminum octahedra as basic molecular units. The current work focuses on Na montmorillonite, a member of the smectite group that comprises two tetrahedral silicate sheets each with unshared oxygen, O, atoms around a central octahedral hydroxide sheet which has two planes of unshared O atoms and additional hydroxyl groups, OH, to form the base lamellae. Due to isomorphous substitutions of metal ions within the clay sheets, each lamella has a net negative charge that is compensated by positive exchangeable interlayer cations. Adsorption of water molecules by this system is accompanied by a large increase in the basal layer spacing.

Interactions between individual clay lamellae have often been considered using classical DLVO theory [8, 25] based on electrostatic mean field approximations for charged flat-plate geometries and van der Waals forces. This approach fails to explain the short-range repulsion associated with structured layers of water attracted to the surface of the clay [13, 20] and hence, is not able to simulate the process of clay

aggregation. In contrast, molecular dynamics (MD) is a highly versatile computational method that can be used to understand the interactions between clay particles without any of these limitations. Here, we use MD simulations with CLAYFF force fields [6] to represent the interactions between two layers of Wyoming montmorillonite (Na-smectite) in bulk water. The analyses are used to establish the potential of mean force (i.e., free energy) as a function of the distance between the centers of two particles for edge-to-edge and face-to-face interactions.

In order to represent clay aggregates with mesopores and grain boundaries, the model must be scaled to micron length scale. This exceeds the computational possibilities of full atomistic models and motivates a multiscale approach. Previous attempts to study clay aggregates were based on using quadrupoles [9] or pseudo-charge sites to represent individual clay platelets (e.g., [14]). The current research uses the interactions between nanoscale clay platelets to calibrate the Gay-Berne potential function [12] that represents each platelet as a single-site ellipsoidal body. A coarse-graining upscaling approach then uses the GB potentials and molecular dynamics to represent the mesoscale aggregation of clay platelets. This paper illustrates geometric properties of the resulting aggregates and evaluates their elastic stiffness properties.

2 Nanoscale Modeling of Interactions Between Two Clay Platelets

The current research focuses on Wyoming Na montmorillonite, a 2:1 smectite with isomorphous substitutions in both tetrahedral and octahedral sheets resulting in a chemical composition: $Na_{0.75}nH_2O[Si_{7.75}Al_{0.25}][Al_{3.5}Mg_{0.5}]O_{20}(OH)_4$. The crystallography of the mineral has been reported from ab initio calculations by [22]. The mineral has a cation exchange capacity, CEC = 102 meq/100 g. Our analyses assume random locations of the isomorphous substituted ions within each clay sheet (constrained by Lowenstein's rule for the distribution of defects), while the net negative charge of the clay is balanced by Na^+ ions in liquid water. The CLAYFF force field [6] is used to represent bonded interactions within the clay (stretching and angle bending) and non-bonded interactions including long-range electrostatic (Coulombic) and short-range (van der Waals—represented by the Lennard-Jones potential) forces through pairwise interactions, while water molecules are represented by the Simple Point Charge model [23]. Full atomistic MD simulations were carried out using the GROMACS program [24] with 1 fs time steps and using in-built thermostat (Nose–Hoover) and barostats (Parrinello–Rahman) to control temperature and pressure, respectively. Our methodology considers the free energy along a reaction coordinate, r_i, corresponding to the spacing between two clay platelets in either a face–face or an edge–edge configuration, Fig. 2.

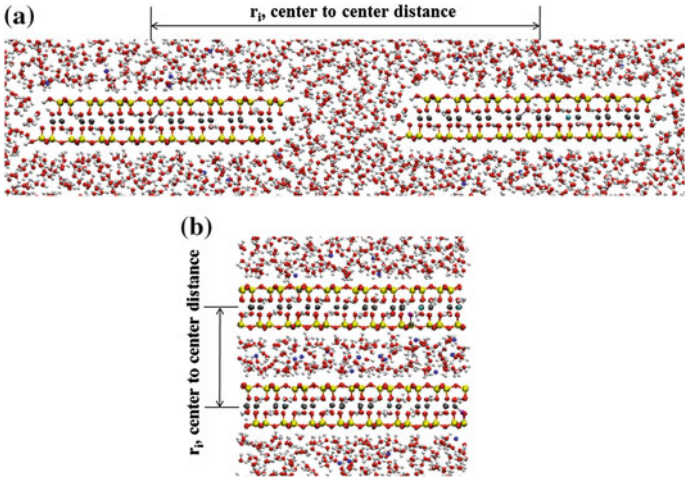

Fig. 2 Part of the typical simulation setup for studying interactions between two clay platelets in **a** edge-to-edge and **b** face-to-face configurations (reproduced with permission from [10]. Copyright 2014, AIP Publishing LLC.)

In order to calculate the change in free energy of the system from state A, when clay platelets are far from each other, to state B, when they are in close proximity, we define several intermediate states covering the change from A to B in small increments to enhance sampling of the phase space. Using distance-splitting strategy, successive states are separated by low-energy barriers such that the phase space is fully explored enabling statistical averaging of the states. We construct series of MD trajectories, each one representing one value of center to center distance. The trajectory of the MD simulation at one state is perturbed along the reaction coordinate to the target state, while all other degrees of freedom are frozen. Free energy differences between two successive reference and target thermodynamic states are then calculated and added along the transformation path from state A to state B. Following [28], the Gibbs free energy difference between a reference state, r_i and the updated target state, r_{i-1}, can be calculated using free energy perturbation theory:

$$\Delta G(r_i \rightarrow r_{i\pm1}) = G(r_{i\pm1}) - G(r_i) = \frac{-1}{\beta} \ln \langle \exp(-\beta \Delta U) \rangle_i \qquad (1)$$

where ΔU is the change of potential energy of the system, $\beta = 1/(k_B T)$, T is the temperature, and k_B is Boltzmann's constant; the $\langle \cdot \rangle$ brackets indicate a canonical ensemble average over the trajectory and subscript i indicates that the average is taken in the reference state. We calculated 172 free energy differences between successive states. In order to eliminate systematic sampling bias due to exponential averaging, we used simple overlap sampling of the forward and reverse perturbation [16].

Figure 3a summarizes the free energy for face–face interactions between two identical clay platelets computed at intervals, Δr_i = 0.25 Å. The same total number

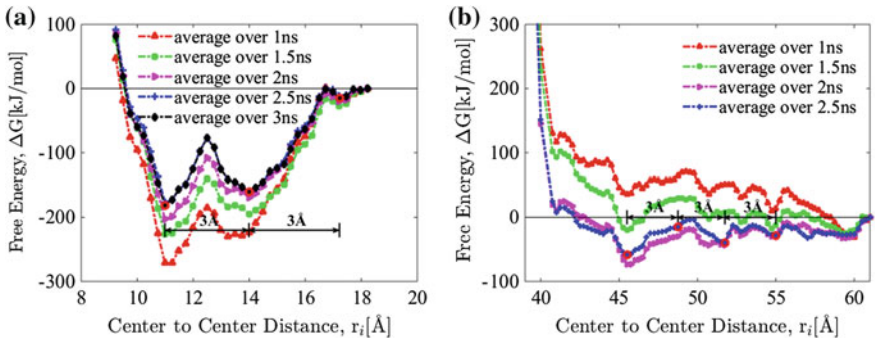

Fig. 3 Potential of mean force for interactions between two identical clay platelets. **a** Face–face configuration. **b** Edge–edge configuration (reproduced with permission from [10]. Copyright 2014, AIP Publishing LLC.)

of water molecules (3914 and Na^+ ions) are included in each of the 38 simulations in the canonical (NVT) ensemble (at $T = 300$ K). The total potential of mean force at each separation distance was calculated by sequentially summing up all the free energy changes from the largest separation to the state of interest ($r = r_i$) assuming zero value for the free energy of the system at the largest separation ($r = 18.47$ Å). The results show convergence of the free energy after 3 ns. The results show two local energy minima in free energy at $r \approx 11$ and 14 Å (i.e., the periodicity between minima is comparable to the diameter of a water molecule). Repulsion dominates for separations less than 11 Å indicating that it is not favorable to remove further water molecules from between the two clay platelets (at this state, there are 18 molecules between the two platelets).

Figure 3b shows similar results obtained from the analyses of edge–edge interactions between two clay platelets. In this case, there is one distinct minimum free energy at $r = 45.5$ Å (the average length of the clay platelet is 40 Å, Fig. 2a).

3 Calibration of GB Potential

The generalized interactions between two clay platelets in water (Fig. 4a) can be approximated as an equivalent single-site potential function, the Gay-Berne (GB) potential [12] that approximates the geometry of each platelet by an ellipsoidal (oblate) body, Fig. 4b. The GB potential is an anisotropic form of the Lennard-Jones potential with potential energy defined by

$$U = 4\varepsilon \left\{ \left(\frac{\sigma}{h_{12} + \sigma} \right)^{12} - \left(\frac{\sigma}{h_{12} + \sigma} \right)^{6} \right\} \eta_{12} \chi_{12} \tag{2}$$

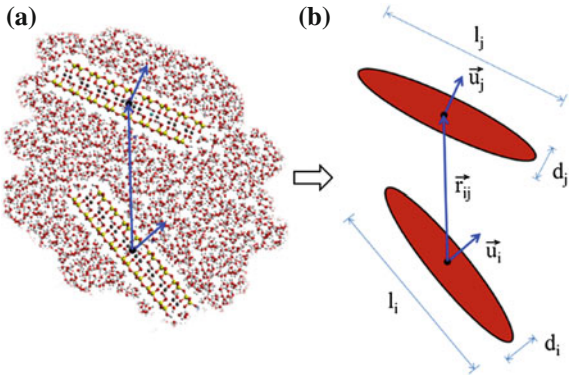

Fig. 4 Approximation of generalized interactions between two clay platelets by single-site potential functions for an ellipsoidal body

where $\varepsilon = 1$ determines the energy scale, σ is the atomic interaction radius, and h_{12} is a function that approximates the anisotropic interparticle distance (i.e., $h_{12} = r - \sigma_{12}$). The GB potential can be defined from four characteristic input parameters (Fig. 5a):

1. Energy well depth, $P_1 = -\varepsilon\eta_{12}\chi_{12}$;
2. Separation distance, $P_2 = \sigma_{12} + 0.1225\sigma$;
3. Soft contact distance, $P_3 = \sigma_{12}$;
4. Characteristic well depth, $P_4 = 0.3508\sigma$.

Optimized values of these parameters were obtained through fitting to the face–face (FF) and edge–edge (EE) free energy profiles presented previously. This was accomplished by first normalizing the free energy (per surface area for FF and per unit length of EE) and then minimizing a cost function as described by [10]. Figure 5b illustrates the resulting match between the calibrated GB potential and the free energy from the FF and EE atomistic models for the case of clay particles with length, $l = 500$ Å. In this example, the FF interactions are matched to the first energy well (r

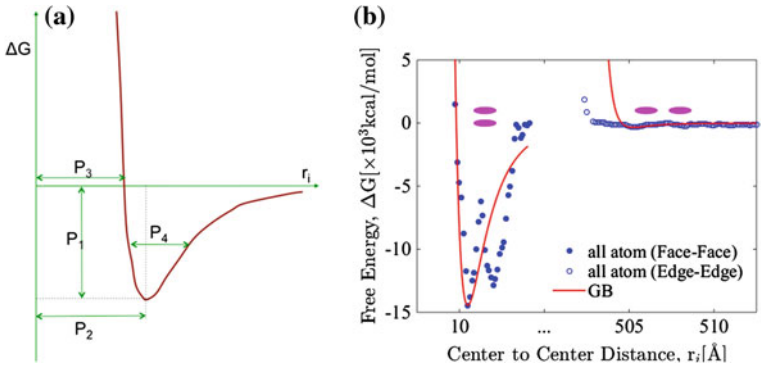

Fig. 5 Free energy for interaction of two ellipsoidal clay particles using GB potential. **a** Input parameters for GB potential. **b** Calibration of parameters for particles with length, $l = 500$ Å

= 11 Å, Fig. 3a). Ebrahimi et al. [10] have shown that this choice of calibration has only a small effect on subsequent simulation of clay aggregate geometry and elastic properties.

4 Mesoscale Modeling

Using the calibrated GB potential, it is now possible to simulate interactions between large numbers of clay platelets (this corresponds to upscaling using a coarse-graining approach). To date, we have focused on monodisperse assemblies of 1000 platelets (of varying sizes, l = 100–1000 Å) that are initially randomly distributed and are allowed to equilibrate (i.e., reach a 'jammed configuration') under isothermal–isobaric conditions (NPT ensemble) at selected pressures (p = 1–800 atm) at T = 300 K. The analyses were conducted using the MD program LAMMPS [21] and typically require up to 1000 ns to reach the jammed state. Figure 6 shows three snapshots for one typical simulation (l = 1000 Å, p = 1 atm) obtained using QMGA molecular graphics software [11]. These results are color coded according to particle orientation, ϕ (relative to the z-axis), and clearly show a progression toward a smaller range of preferred orientations and aggregation of platelets.

Following [4] two criteria are used to determine if two clay platelets can be considered part of the same aggregate (i.e., are stacked upon each other). The first requires that the interlayer distance is less than a threshold value, r_u = 13.75 Å (i.e., 1.25P_2, where P_2 is the soft contact distance defined in Fig. 5a), while the second requires the dot product of the normal vectors $n_1 \times n_2 > 0.95$. Using these definitions, we then derive distributions of aggregate stacks sizes for sets of 10 mesoscale simulations. Figure 7b shows typical results for monodisperse assemblies with l = 500 Å (at p = 1 atm) in which the stack size can be characterized by a log-normal distribution function with average stack size, N = 3.33.

Ebrahimi et al. [10] introduce a scalar order parameter, S, to characterize the orientation of the clay platelets:

$$S = \left\langle \frac{3\cos^2\theta - 1}{2} \right\rangle \tag{3}$$

where θ is angle between the normal vector of a platelet and the director of the system (i.e., a measure of the average orientation of all particles in the system). For a completely isotropic and randomly oriented system S = 0, while perfectly aligned systems have S = 1.

Figure 8 summarizes the order parameter and mean aggregate stack size, N, from mesoscale simulations of monodisperse systems with a range of particle sizes and pressures. These results show that aggregates of Na montmorillonite typically form stacks with 3–8 clay platelets in face–face configurations. This result is in good agreement with X-ray diffraction experiments for Na-smectites (e.g., [18]) who report N = 3–10. Increasing the confining pressure has a significant effect on ordering of the system. For l = 1000 Å, S increases from 0.23 at 1 atm to a maximum value of

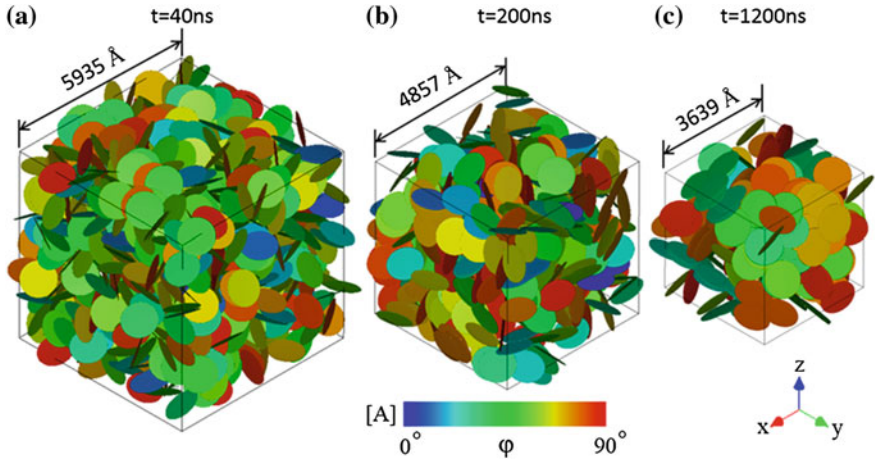

Fig. 6 Mesoscale simulation of clay aggregation for monodisperse assembly of 1000 clay platelets with $l = 1000$ Å at $p = 1$ atm. The results show snapshots of the assembly at selected times **a** 40 ns, **b** 200 ns, and **c** 1200 ns (reproduced with permission from [10]. Copyright 2014, AIP Publishing LLC.)

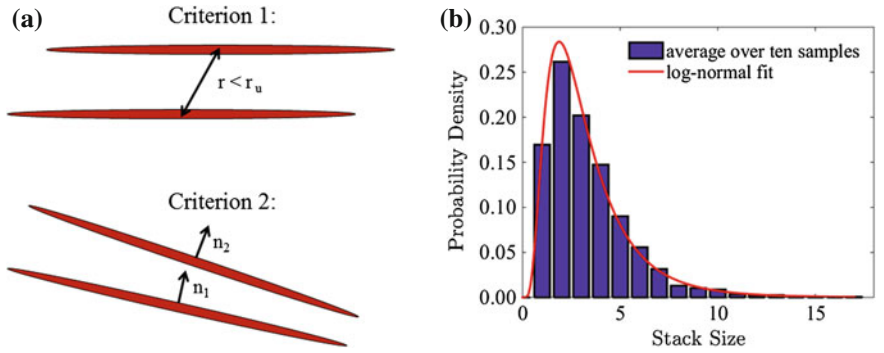

Fig. 7 Aggregation of clay particles from mesoscale simulations. **a** Definition of aggregate stack. **b** Histogram of stack sizes for $l = 500$ Å, $p = 1$ atm (reproduced with permission from [10]. Copyright 2014, AIP Publishing LLC.)

0.64 at 50 atm and remains approximately constant at higher pressures. The maximum stack size also occurs at around $p = 50$ atm.

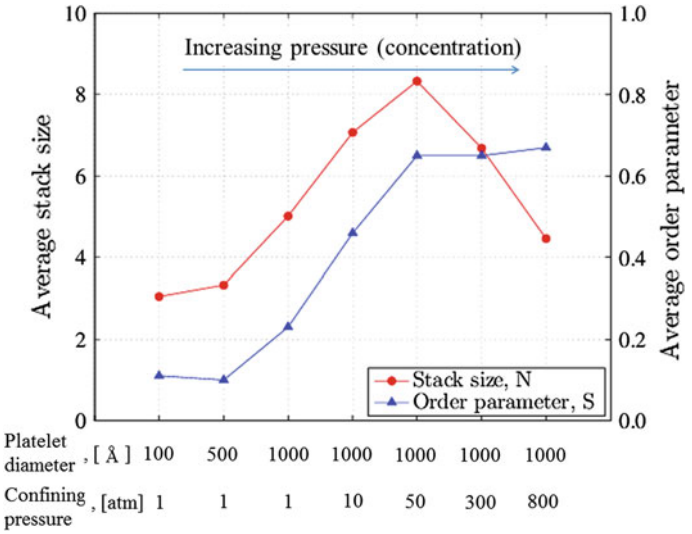

Fig. 8 Summary of geometric parameters from mesoscale simulations on monodisperse clay aggregates

5 Elastic Stiffness Properties

The stress–strain properties of the particle assemblies have been studied using a quasi-static method (after [1]) involving (1) application of a small homogeneous strain to the system; and (2) relaxing the strain step over a time period using an NVT ensemble (at $T = 0.01$ K). Components of the internal stress tensor are determined by averaging over the last 10 % of the relaxation time period for each of the six independent strain modes as follows:

$$\sigma_{ij} = \frac{1}{V} \sum_{\alpha} \left(m^{\alpha} v_i^{\alpha} v_j^{\alpha} + \sum_{\beta} f_i^{\alpha\beta} r_j^{\alpha\beta} \right) \tag{4}$$

where m^{α} and v^{α} are the mass and velocity of platelet α, $f_i^{\alpha\beta}$ is the force acting on platelet α by platelet β acting in the i-direction, and $r_j^{\alpha\beta}$ is the Cartesian component of the vector from platelet β on platelet α in the j-direction.

Elastic constants were obtained from a linear fit over the initial part of the stress–strain curve representing values from $\varepsilon = 0$–0.01 % for 500 Å platelets and $\varepsilon = 0$–0.03 % for 1000 Å platelets. Ebrahimi et al. [10] show that the full elasticity tensor can be well approximated for all particle assemblies by considering cubic symmetry with three independent coefficients, C_{11}, C_{12}, and C_{44} (using standard Voigt notation). Table 1 summarizes the resulting cubic averaged properties from the mesoscale particle assemblies. By increasing size of the platelets, the normal stiffness, $\overline{C}_{11}$,

Table 1 Cubic averaged elastic stiffness properties (GPa) for mesoscale particle assemblies with different platelet sizes and confining pressures

D (Å)	500	1000	1000	1000	1000	1000
P (atm)	1	1	10	50	300	800
$\overline{C}_{11}$	0.51	0.98	4.07	6.42	14.17	29.16
$\overline{C}_{12}$	0.13	0.14	0.53	1.24	4.12	8.80
$\overline{C}_{44}$	0.10	0.08	0.44	0.66	1.94	4.68

increases (from 0.51 to 0.98 GPa) but the shear stiffness ($\overline{C}_{44}$) and the stiffness component related to the Poisson's effect ($\overline{C}_{12}$) show negligible change. All elastic constants increase with increasing confining pressure as expected.

In order to validate mechanical properties, we calculated indentation modulus from the elastic constants (*Cij*) using the derivation by [7] for an orthotropic solid and compared the mesoscale model predictions with experimental indentation moduli on shale and clay samples reported by [3]. The mean indentation modulus shows good agreement with measured values and follows the same trend with packing density as shown in Fig. 9.

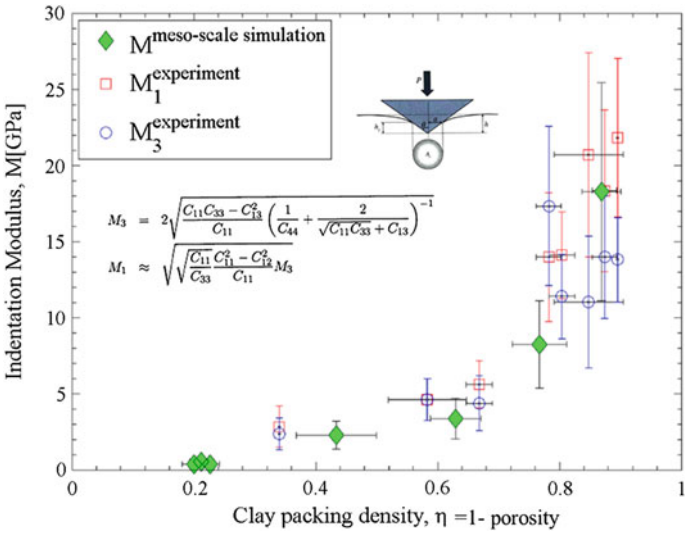

Fig. 9 Comparison of computed indentation modulus from mesoscale particle assemblies with experimental nanoindentation data for clays and shales (from [3]). Subscripts *1* and *3* indicate indentation parallel and normal to the bedding plane (reproduced with permission from [10]. Copyright 2014, AIP Publishing LLC.)

6 Conclusions

This paper has described a new methodology to study aggregation of clay particles at the mesoscale based on the atomistic interaction between two clay platelets in an aqueous environment. Full atomistic simulation of the clay (Na-Wyoming montmorillonite)—water system for edge-to-edge and face-to-face interaction of clay platelets was used to calculate changes in free energy as a function of the separation distance using perturbation theory. At the mesoscale, clay platelets were approximated by ellipsoidal particles and their interactions for different orientations were defined using the Gay-Berne potential calibrated to results of atomistic simulations for edge-to-edge and face-to-face configurations.

Results of the simulations show an increase in the average aggregate size by increasing platelet diameter. An increase in the confining pressure creates a more ordered system and average aggregate size increases until reaching to a maximum ordered state. Further increase of pressure results in decrease in average aggregate size since orientation of platelets remains constant and they start to slide against each other. The computed mean stack size (3–8) for Na-smectite is in good agreement with published experimental data. The mesoscale model is also able to match quite closely the measured elastic indentation modulus for shale and clay specimens over a wide range of packing density.

The current analyses are limited to a single species of smectite (Na-Wyoming montmorillonite) with cation exchange capacity, CEC = 102 meq/100 g and monodisperse assemblies of platelets. The method can be used to study the effect of amount and type of isomorphous substitution on the microstructure and mechanical properties of clay aggregates. The heterogeneity of the platelet sizes at the mesoscale can change the distribution of aggregate sizes. The research can be extended to study effects of polydisperse assemblies of clay platelets.

Acknowledgments The computational resources used for this project have been provided by the National Science Foundation through the Extreme Science and Engineering Discovery Environment (XSEDE) and the Texas Advanced Computing Center under Grant No. TG-DMR100028.

References

1. Aghaei, A., Qomi, M.A., Kazemi, M., Khoei, A.: Stability and size-dependency of Cauchy-Born hypothesis in three-dimensional applications. Int. J. Solids Struct. **46**, 1925–1936 (2009)
2. Andrade, J.E., Tu, X.: Multiscale framework for behavior prediction in granular media. Mech. Mater. **41**, 652–669 (2009)
3. Bobko, C., Ulm, F.-J.: The nano-mechanical morphology of shale. Mech. Mater. **40**, 318–337 (2008)
4. Chen, C.-T., Ball, V., de Almeida Gracio, J.J., SINGH, M.K., Toniazzo, V., Ruch, D., Buehler, M.J.: Self-assembly of tetramers of 5, 6-dihydroxyindole explains the primary physical properties of eumelanin: Experiment, simulation, and design. ACS Nano **7**, 1524–1532 (2013)
5. Cundall, P.A., Strack, O.: The development of constitutive laws for soil using the distinct element method. Numer. Methods Geomech. **1**, 289–317 (1979)

6. Cygan, R.T., Liang, J.-J., Kalinichev, A.G.: Molecular models of hydroxide, oxyhydroxide, and clay phases and the development of a general force field. J. Phys. Chem. B **108**, 1255–1266 (2004)
7. Delafargue, A., Ulm, F.-J.: Explicit approximations of the indentation modulus of elastically orthotropic solids for conical indenters. Int. J. Solids Struct. **41**, 7351–7360 (2004)
8. Derjaguin, B. V., and L. Landau.: The theory of stability of highly charged lyophobic sols and coalescence of highly charged particles in electrolyte solutions. Acta Phys. URSS **14**, 633–52 (1941)
9. Dijkstra, M., Hansen, J., Madden, P.: Gelation of a clay colloid suspension. Phys. Rev. Lett. **75**, 2236 (1995)
10. Ebrahimi, D., Whittle, A.J., Pellenq, R.J.-M.: Mesoscale properties of clay aggregates from potential of mean force representation of interactions between nanoplatelets. J. Chem. Phys. **140**, 154309 (2014)
11. Gabriel, A.T., Meyer, T., Germano, G.: Molecular graphics of convex body fluids. J. Chem. Theory Comput. **4**, 468–476 (2008)
12. Gay, J., Berne, B.: Modification of the overlap potential to mimic a linear site-site potential. J. Chem. Phys. **74**, 3316–3319 (1981)
13. Israelachvili, J.N., Pashley, R.M. Molecular layering of water at surfaces and origin of repulsive hydration forces. Nature. **306**(5940):249–250 (1983)
14. Kutter, S., Hansen, J.-P., Sprik, M., Boek, E.: Structure and phase behavior of a model clay dispersion: a molecular-dynamics investigation. J. Chem. Phys. **112**, 311–322 (2000)
15. Lee, B.J., Fettweis, M., Toorman, E., Molz, F.J.: Multimodality of a particle size distribution of cohesive suspended particulate matters in a coastal zone. J. Geophys. Res.: Oceans **1978–2012**, 117 (2012)
16. Lee, C., Scott, H.: The surface tension of water: a Monte Carlo calculation using an umbrella sampling algorithm. J. Chem. Phys. **73**, 4591–4596 (1980)
17. McDowell, G., Bolton, M.: On the micromechanics of crushable aggregates. Geotechnique **48**, 667–679 (1998)
18. Mystkowski, K., Środoń, J., Elsass, F.: Mean thickness and thickness distribution of smectite crystallites. Clay Miner. **35**, 545–557 (2000)
19. Nitka, M., Combe, G., Dascalu, C., Desrues, J.: Two-scale modeling of granular materials: a DEM-FEM approach. Granular Matter **13**, 277–281 (2011)
20. Pashley R.M., and Jacob N.I.: Molecular layering of water in thin films between mica surfaces and its relation to hydration forces. J. Colloid Interf Sci. **101**(2) , 511–523 (1984)
21. Plimpton, S.: Fast parallel algorithms for short-range molecular dynamics. J. Computat. Phys. **117**, 1–19 (1995)
22. Refson, K., Park, S.-H., Sposito, G.: Ab initio computational crystallography of 2: 1 clay minerals: 1. Pyrophyllite-1Tc. J. Phys. Chem. B **107**, 13376–13383 (2003)
23. Teleman, O., Jönsson, B., Engström, S.: A molecular dynamics simulation of a water model with intramolecular degrees of freedom. Mol. Phys. **60**, 193–203 (1987)
24. van der Spoel, D., Lindahl, E., Hess, B., Groenhof, G., Mark, A.E., Berendsen, H.J.: GROMACS: fast, flexible, and free. J. Comput. Chem. **26**, 1701–1718 (2005)
25. Verwey, E. J. W., and J. Th G. Overbeek.: Theory of the stability of lyophobic colloids. Journal of Colloid Science **10**(2):224–225 (1955)
26. Zhang, G., Germaine, J., Whittle, A., Ladd, C.: Index properties of a highly weathered old alluvium. Geotechnique **54**, 441–451 (2004a)
27. Zhang, G., Germaine, J., Whittle, A., Ladd, C.: Soil structure of a highly weathered old alluvium. Geotechnique **54**, 453–466 (2004b)
28. Zwanzig, R.W.: High-temperature equation of state by a perturbation method. I. nonpolar gases. J. Chem. Phys. **22**, 1420–1426 (1954)